

**Electrochemistry, acid-base
chemistry, synthesis and
characterization of TCNQF and
TCNQF₂-based materials –
A comparison between four
derivatives TCNQF_n (n=0, 1, 2, 4)**

**Nguyen Thang Vo
(M.Sc.)**

A thesis submitted to the Faculty of Science
Monash University, in fulfilment of the
requirements for the degree of
DOCTOR OF PHILOSOPHY

School of Chemistry,
Monash University

June 2016

Copyright Notice

© Nguyen Thang Vo (2016). Except as provided in the Copyright Act 1968, this thesis may not be reproduced in any form without the written permission of the author.

I certify that I have made all reasonable efforts to secure copyright permissions for third-party content included in this thesis and have not knowingly added copyright content to my work without the owner's permission.

Table of Contents

Table of Contents	i
Abbreviations	vi
Abstract	viii
General declaration	x
Publications during enrolment	xi
Acknowledgements	xii
Chapter 1	
Introduction	1
1.1. Introduction and recent studies on TCNQ and TCNQF ₄	1
1.2. TCNQF and TCNQF ₂ – Electrical and structural properties – A comparison to TCNQ and TCNQF ₄ derivative	7
1.3. Studies on TCNQF and TCNQF ₂ complexes	10
1.4. Thesis objectives	11
Chapter 2	
Investigation of the redox and acid-base properties of TCNQF and TCNQF ₂ – Electrochemistry, vibrational spectroscopy and substituent effects	17
2.1. Introduction	17
2.2. Experiments	19
2.2.1. Chemicals	19
2.2.2. Electrochemistry	20
2.2.3. Simulation software	20
2.2.4. DFT calculation of IR and Raman spectra	20
2.2.5. Other instrumentation	21
2.3. Result and discussion	21
2.3.1. Electrochemistry of TCNQF and TCNQF ₂ in CH ₃ CN in comparison with TCNQ and TCNQF ₄	21
2.3.2. UV-Vis spectroscopy of TCNQF _n and the anions in acetonitrile	24
2.3.3. Electrochemistry of TCNQF _n , TCNQF _n ⁻ and TCNQF _n ²⁻ in acetonitrile in the presence of trifluoroacetic acid (n = 1, 2)	27
2.3.4. Simulation of the voltammetry of TCNQF _n and its anions in the presence of TFA	33

2.3.5. Comparison of the redox and acid base chemistry of the TCNQF _n derivatives	38
2.3.6. Vibrational spectroscopy of TCNQF _n (n=1,2)	39
2.4. Conclusion	45
Chapter 3	
Electrochemistry of TCNQF ₂ in acetonitrile in the presence of [Cu(CH ₃ CN) ₄] ⁺ - The formation of CuTCNQF ₂ and its catalytic activity	48
3.1. Introduction	48
3.2. Experimental	49
3.2.1. Chemicals	49
3.2.2. Electrochemistry	49
3.2.3. Synthesis of CuTCNQF ₂	50
3.2.4. Conductivity measurement of CuTCNQF ₂	50
3.2.5. Other instrumentations	51
3.3. Result and discussion	52
3.3.1. Cyclic voltammetry of the TCNQF ₂ ^{0/-} process in the presence of [Cu(CH ₃ CN) ₄] ⁺	52
3.3.2. Cyclic Voltammometry of TCNQF ₂ in the presence of [Cu(CH ₃ CN) ₄] ⁺ , the second redox process	55
3.3.3. Cyclic voltammetry of Cu-TCNQF ₂ ²⁻ solid in the presence of [Cu(CH ₃ CN) ₄] ⁺	58
3.3.4. Powder X-Ray Crystallography	59
3.3.5. Spectroscopic characterization	60
3.3.6. Elemental microanalysis	62
3.3.7. Scanning electron microscopy	62
3.3.8. Solubility of CuTCNQF ₂	63
3.3.9. Conductivity of CuTCNQF ₂	63
3.4. Conclusion	64
Chapter 4	
Electrochemistry of TCNQF in the presence of [Cu(MeCN) ₄] ⁺ - A comparative study of the catalytic activity of TCNQF _n derivatives	68
4.1. Introduction	68
4.2. Experimental	69

4.2.1.	Chemicals	69
4.2.2.	Electrochemistry	69
4.2.3.	Synthesis of CuTCNQF	70
4.2.4.	Catalytic experiment	70
4.2.5.	Other instrumentations	71
4.3.	Result and discussion	72
4.3.1.	Voltammetry of TCNQF in the presence of $[\text{Cu}(\text{CH}_3\text{CN})_4]^+$, the first reduction process	72
4.3.2.	Cyclic voltammetry of $\text{TCNQF}^{-/2-}$ process in the presence of $[\text{Cu}(\text{MeCN})_4]^+$	77
4.3.3.	Spectroscopic characterization	81
4.3.4.	Elemental microanalysis for CuTCNQF material	82
4.3.5.	Morphology of CuTCNQF	83
4.3.6.	Catalytic activity	85
4.3.7.	Comparison between the four derivatives TCNQF_n ($n = 0, 1, 2, 4$)	89
4.4.	Conclusion	91
Chapter 5		
Electrochemical synthesis of M^{2+} -TCNQF materials (M=Ni, Co): Voltammetric, spectroscopic and microscopic evidence		93
5.1.	Introduction	93
5.2.	Experimental	93
5.2.1.	Chemicals	93
5.2.2.	Electrochemistry	94
5.2.3.	Synthesis of $\text{M}(\text{TCNQF})_2$ and MTCNQF where $\text{M} = \text{Ni}^{2+}$ and Co^{2+}	94
5.2.4.	Other instrumentations	94
5.3.	Result and discussion	95
5.3.1.	Cyclic voltammetry of the $\text{TCNQF}^{0/}$ process in the presence of M^{2+}	95
5.3.2.	Cyclic voltammetry of the $\text{TCNQF}^{-/2-}$ process in the presence of M^{2+}	99
5.3.3.	Elemental microanalysis	102

5.3.4.	Solubility of $M(\text{TCNQF}_2)_2$ materials	103
5.3.5.	IR and Raman spectroscopy	103
5.3.6.	Morphology of TCNQF-based material	106
5.4.	Conclusion	107
Chapter 6		
	Electrochemical synthesis of Ni^{2+} and Co^{2+} TCNQF ₂ -based in acetonitrile	109
6.1.	Introduction	109
6.2.	Experimental	109
6.2.1.	Chemicals	109
6.2.2.	Electrochemistry	109
6.2.3.	Synthesis of $M(\text{TCNQF}_2)_2$ and $M\text{TCNQF}_2$, where $M = \text{Ni}^{2+}, \text{Co}^{2+}$	110
6.2.4.	Other instrumentation	110
6.3.	Result and discussion	111
6.3.1.	Voltammetry of TCNQF ₂ in the presence of $M(\text{ClO}_4)_2$ ($M: \text{Co}, \text{Ni}$)	111
6.3.2.	Formation of $M\text{-TCNQF}_2^{2-}$ material on the electrode surface	115
6.3.3.	Cyclic voltammetry of TCNQF ₂ ^{-/-} in the presence of M^{2+} - The formation of $M\text{TCNQF}_2$ solid	117
6.3.4.	IR and Raman characterization of TCNQF ₂ - based material	121
6.3.5.	Elemental and thermogravimetric analysis	125
6.3.6.	Solubility measurements	125
6.3.7.	Morphologies of $M\text{-TCNQF}_2$ materials	126
6.3.8.	Interpretation of the cyclic voltammetry of TCNQ in the presence of Co^{2+}	128
6.4.	Conclusion	130
Chapter 7		
	Chemistry and electrochemistry of TCNQF and TCNQF ₄ in the presence of Zn^{2+}	132
7.1.	Disproportionation of $\text{TCNQF}^{\text{n-}}$ in the presence of Zn^{2+} in acetonitrile	132
7.1.1.	Introduction	132
7.1.2.	Experimental	134
7.1.2.1.	Chemicals	134
7.1.2.2.	Procedures	135

7.1.2.3. Electrochemistry	135
7.1.2.4. Other Instrumentations	136
7.1.3. Result and discussion	136
7.1.3.1. Characterization of the solid products of Zn ²⁺ -TCNQF _n	140
7.1.4. Conclusion	142
7.2. The preparation of [M(DMF) ₂ TCNQF ₄] ₂ DMF materials	142
7.2.1. Introduction	142
7.2.2. Experimental	143
7.2.2.1. Chemicals	143
7.2.2.2. Electrochemistry	143
7.2.2.3. Synthesis of [ZnTCNQF ₄ (DMF) ₂] ₂ ·(DMF) ₂	144
7.2.2.4. Crystallography	144
7.2.2.5. Other instrumentation	144
7.2.3. Results and discussion	144
7.2.3.1. Cyclic Voltammetry of TCNQF ₄ in the presence of M ²⁺ in the mixed MeCN/DMF solvents	144
7.2.3.2. X-ray structural characterization of ZnTCNQF ₄ (DMF) ₂ ·2DMF	153
7.2.3.3. Bulk electro-generation of the M ²⁺ -TCNQF ₄ material in the MeCN/DMF mixture	154
7.2.4. Conclusion	157
Conclusions and future work	159
8.1. Investigation of the redox and acid-base properties of TCNQF and TCNQF ₂ – Electrochemistry, vibrational spectroscopy and substituent effects	160
8.2. Electrochemistry of TCNQF and TCNQF ₂ in acetonitrile in the presence of [Cu(MeCN) ₄] ⁺ - The formation of Cu-TCNQF _n ⁻ materials and a comparative study on the catalytic activity of TCNQF _n derivatives	161
8.3. Electrochemical synthesis of M(TCNQF _n) ₂ and MTCNQF _n (M=Ni, Co): Voltammetric, spectroscopic and microscopic evidence	162
8.4. Disportionation of TCNQF _n ⁻ in the presence of Zn ²⁺ - The preparation of [M(DMF) ₂ TCNQF ₄] ₂ DMF materials	163
Future work	165
Appendix	166

Abbreviations

A	electrode area
BAS	Bioanalytical systems
C	concentration
D	diffusion coefficient
DB-TTF	dibenzo tetrathiafulvalene
DC	direct current
DCTC	dicyano-p-toluoylcyanide
DFT	density functional theory
DMF	dimethylformamide
E^0	formal potential
$E_{1/2}$	half-wave potential
EDS	energy dispersive spectroscopy
EDT-TTF	ethylenedithiotetrathiafulvalene
E_m	midpoint potential
E_p	peak potential
E_p^{ox}	oxidation peak potential
E_p^{red}	reduction peak potential
F	Faraday constant
FTIR	Fourier transform infrared spectroscopy
FTO	fluorine tin oxide
GC	Glassy carbon
IR	Infrared
i_p	peak current
IR	Infrared
ITO	indium tin oxide
K_{eq}	equilibrium constant
MeCN	acetonitrile
OCP	open circuit potential
R	gas constant
RE	reference electrode
SEM	scanning electron microscopy

T	temperature (K)
TCNQ	7,7,8,8-tetracyanoquinodimethane
TCNQF	monofluoro-7,7,8,8-tetracyanoquinodimethane
TCNQF ₂	2,5-difluoro-7,7,8,8-tetracyanoquinodimethane
TCNQF ₄	2,3,5,6-tetrafluoro-7,7,8,8 tetracyanoquinodimethane
TFA	trifluoroacetic acid
TGA	thermogravimetric analysis
TTF	tetrathiafulvalene
UV-Vis	Ultraviolet – Visible
XRD	X-Ray diffraction
ΔE	peak separation ($ E_p^{ox} - E_p^{red} $)
λ_{max}	maximum absorption wavelength
ν	scan rate
ρ	charge transfer degree
σ	Hammett constant

Abstract

Electrochemistry of monofluoro-7,7,8,8-tetracyanoquinodimethane (TCNQF) and 2,5-difluoro-7,7,8,8-tetracyanoquinodimethane (TCNQF₂) (denoted by TCNQF_n) have been studied. In an analogous manner to TCNQ and the tetrafluoro derivatives TCNQF₄, they both undergo two electrochemically and chemically reversible one-electron reduction steps in acetonitrile (0.1 M Bu₄NPF₆). The formal potentials for the two processes are 0.035 and -0.502 mV for TCNQF, and 0.129 and -0.408 mV for TCNQF₂, which are in an ideal linear relationship with the number of fluorine substituents, taking into account the other two derivatives. The substitution effect also plays an important role in the acid-base chemistry of TCNQF and TCNQF₂. In the presence of trifluoroacetic acid TFA, while the reduction TCNQF_n^{0/-} is not modified, TCNQF_n⁻ species undergo a disproportionation reaction generating TCNQF_n and H₂TCNQF_n; and TCNQF_n²⁻ is protonated to form H₂TCNQF_n. The equilibrium constants for those chemical steps derived from digital simulations demonstrate a great effect of strong electron withdrawing substituent, fluorine, on the stability and basicity of the anions. The more fluorine substituents there are, the more stable and less basic the anions are. DFT calculation assists the prediction of vibrational spectroscopies, which are diagnostic for each neutral or anion moieties. With a good agreement between calculation and experimental spectra of neutral TCNQF_n, DFT calculation on vibrational absorbance offers a reliable resource of spectroscopic characterization for TCNQF_n-based materials.

Electrochemistry of TCNQF_n in the presence of Cu⁺, Zn²⁺, Co²⁺ and Ni²⁺ as well as chemical and electrochemical synthesis of TCNQF_n-based materials have been investigated. Both reduction steps are voltammetrically accessible for probing the formation of corresponding solid provided that suitable concentration ranges are chosen. However, attempts to grow single crystals suitable for crystallography studies were unsuccessful. The use of voltammetric, spectroscopic and microscopic methods together confirm the presence of variable morphologies of both mono and dianionic materials with different metal ions. Powder X-Ray diffraction pattern of CuTCNQF₂ solid was found to resemble that of CuTCNQ phase

II, and interestingly conductivity of the bulk material is close to that of CuTCNQ phase II. An exciting catalytic activity of CuTCNQF_n film on a copper foil has been investigated and compared to CuTCNQ and CuTCNQF₄. The presence of two fluorine substituents significantly enhances the catalytic activity of CuTCNQF₂ on the redox reaction between ferricyanide and thiosulfate, compared to CuTCNQF.

In this thesis, detection of the formation of TCNQF_n⁻-based materials with divalent metal cations (Co²⁺, Ni²⁺) on voltammetric time scale has been reported with the use of high concentration of studied mixtures. These results also assist the revision of the interpretation of voltammetric data on TCNQ-Co²⁺ system.

Although all TCNQF_n⁻-based materials are aerobically stable, M-TCNQF_n²⁻ materials are not stable in the air as evident from colour change and spectroscopic data.

In the presence of Zn²⁺, TCNQF_n⁻ disproportionate to form TCNQF_n and ZnTCNQF_n precipitate in an analogous manner with what was found for TCNQ and TCNQF₄. The disproportionation is inhibited by the addition of a small amount of water.

Electrochemistry of TCNQF₄ in the presence of Zn²⁺, Co²⁺ and Mn²⁺ in MeCN/DMF solvent mixture has been investigated. Interestingly, the disproportionation of TCNQF₄⁻ wasn't observed in this solvent mixture. The formation of M²⁺-TCNQF₄²⁻ solid has been detected in voltammetric experiments and it was synthesized electrochemically. Crystal structure of [ZnTCNQF₄(DMF)₂]₂DMF has also been reported. Spectroscopy and powder X-Ray diffraction pattern confirm that two synthesis pathways generate identical material.

General declaration

I hereby declare that this thesis contains no material which has been accepted for the award of any other degree or diploma at any university or equivalent institution and that, to the best of my knowledge and belief, this thesis contains no material previously published or written by another person, except where due to reference is made in the text of the thesis.

Signed



Full name NGUYEN THANG VO

Date 24/10/2016

Publications during enrolment

1. Role of Water in the Dynamic Disproportionation of Zn-Based TCNQ(F₄) Coordination Polymers (TCNQ = Tetracyanoquinodimethane), Ayman Nafady, Thanh Hai Le, Nguyen Vo, Naomi L. Haworth, Alan M. Bond, and Lisandra L. Martin, *Inorganic chemistry*, 2014, 53, 2268-2275
2. Diagnosis of the Redox Levels of TCNQF₄ Compounds Using Vibrational Spectroscopy, Dr. Naomi L. Haworth, Dr. Jinzhen Lu, Nguyen Vo, Dr. Thanh Hai Le, Dr. Christopher D. Thompson, Prof. Alan M. Bond and Assoc. Prof. Lisandra L. Martin, *Chempluschem*, 2014, 79, 962-972
3. Voltammetric reduction and re-oxidation of solid coordination polymers of dihydroxybenzoquinone, Brendan F. Abrahams, Alan M. Bond, Thanh H. Le, Laura J. McCormick, Ayman Nafady, Richard Robson and Nguyen Vo, *Chemical communications*, 2012, 48, 11422-11424

Acknowledgements

I would like to express my gratitude to many people who are in one way or another have contributed in making this thesis achievable.

I gratefully acknowledge that Monash International Postgraduate Research Scholarship and Monash Graduate Scholarship have assisted me during my PhD studies.

I wish to thank my former high school teacher and also my first mentor as a PhD candidate, Dr. Thanh Hai Le, who was the first person to introduce me to join the group. He was one of the most inspiring and enthusiastic scientists that I have ever worked with. I deeply appreciate his help from the very first days I started my journey at Monash University.

It cannot find words to express my gratitude to my supervisors, Associate Professor Lisandra L. Martin and Professor Alan M. Bond, who were always supportive and encouraging during my PhD. I have learnt much from them not only within the PhD project but also about other aspects of doing science.

My PhD studies would not be this memorable without the support and discussion from the other members of the Bond and Martin groups. A thank you to Dr. Joyee Chun In Yeung, Dr. Stefania Piantavigna, Dr. Jinzhen Lu, Mingdeng Luo, Rajiv Thapa.

I want to thank Mr. Finlay Shanks for helping me on the use of FT-IR and Raman instrumentation, Dr. Xi-ya Fang at Monash Centre for Electron Microscopy for training and assisting with scanning electron microscopy instrumentation.

My studies in Melbourne would be boring without the friendship with my friends from my former high school. It has made me feel more like home with them around.

Finally and most importantly, I owe my deepest gratitude to my family who always love and support me unconditionally. I would like to dedicate this thesis to my parent who has been working hard, teaching and loving so that I become a me today. A big thank you to my lovely sister who has been sharing all the “rainy” as well as “sunny” time with me all these years.

I am indebted to my beloved husband who has always been patient and supportive. No word can express my appreciation for you, sharing the housework,

taking care of our little son, Ben and cooking for me when I was under deadline pressure. Last but not least, I want to say thank you to our son, Ben, a real “project”, for coming into our life. He has made the end of my PhD studies so meaningful.

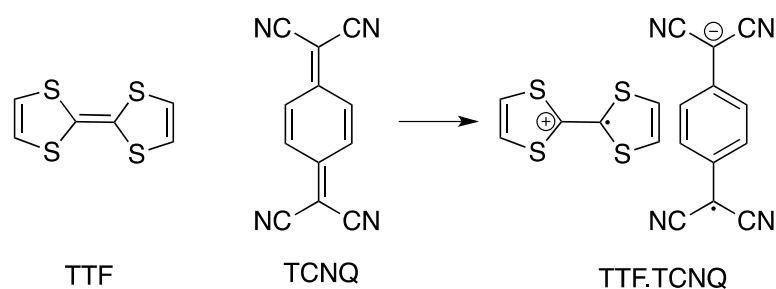
Chapter 1

Introduction

1.1. Introduction and recent studies on TCNQ and TCNQF₄

Electrochemistry has opened the door to a wide range of practical applications, since its development over two hundred years ago.¹ These include practical uses such as lead-acid battery, extraction and refining of metals from ores and fuels cell, through to more recent developments, such as solar cells, the glucose biosensor and bionic devices.²⁻⁵ Dynamic electrochemistry, which is of relevant to this thesis is based on redox reactions at an electrode, which cause a current to flow. This behaviour is measured and interpreted based on the relationships of current, potential and time.

TCNQ (TCNQ = 7,7,8,8-tetracyanoquinodimethane) and its derivatives (TCNQ(X)_n) have been widely investigated for many years as they have interesting electronic properties. The family of TCNQ-based materials includes some of the best electron acceptors known among organic redox compounds. The electrochemistry of TCNQ(X)_n and the synthesis of TCNQ(X)_n-based charge-transfer complexes have been reported since the 1970s with the most famous example of an organic charge-transfer complex being the TTF.TCNQ complex (Scheme 1),⁶⁻⁸ (where TTF = Tetrathiafulvalene) which was shown to behave like a metallic conductor at low temperatures.⁹⁻¹¹ In this material, TCNQ acts as an electron acceptor and TTF is an electron donor. This 1D conductor initiated the quest for superconductivity in organic compounds and led to a whole new era of organic conductors not only with TCNQ itself but also with many other derivatives. Among these derivatives, the halogenated TCNQX_n has shown promise for future research activity as the halogen substituents enhance the stability of the molecules as well as their charge transfer complexes.¹²⁻¹⁶



Scheme 1. The formation of charge transfer complex TTF.TCNQ

Most TCNQ-based conductors are charge transfer salts formed from TCNQ^{•-} anionic radical and a suitable cation, i.e. metals, organometallic complexes or organic cations.^{17,18} The reduced form TCNQ^{•-} is an excellent ligand for the synthesis of coordination polymers and metal-organic frameworks via the reaction with transition metal. Representative examples, including charge-transfer complexes of TCNQ with transition metal ions, such as copper or silver, have shown good conductivity and been utilized in optical, electrical and magnetic devices.¹⁹⁻³¹ These materials have been applied in a wide range of applications such as optical and electrical memory devices, sensors, catalysis and magnetic devices.^{19,21}

The properties of the fluorinated derivatives of TCNQ especially the TCNQF₄-based materials (TCNQF₄ = 2,3,5,6-tetrafluoro-7,7,8,8-tetracyanoquinodimethane) have also been studied recently (see Figure 1).³² The presence of four fluorine atoms on the ring significantly enhances the electron affinity of TCNQF₄, which consequentially makes it easier to be reduced as well as increases the stability of its anions, especially the dianion. Indeed, a number of TCNQF₄²⁻-based materials have been electrochemically generated in the air,^{12-14,33} while those of TCNQ needs to be synthesized under an inert environment.³⁴⁻³⁶ This enhanced stability of the fluorinated compound therefore provides a more feasible approach to explore new dianionic materials. Thus, as part of a study for new materials of TCNQ and the dihalogenated derivatives, several examples of the dibromo, dichloro and difluoro complexes have been reported,^{15,37-39} however this remains an area that still needs further investigation.

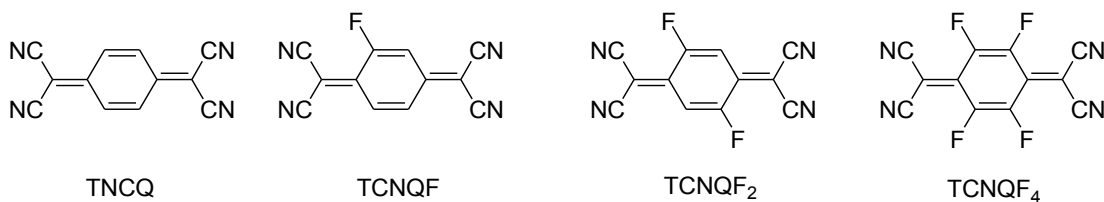


Figure 1. Molecular structure of TCNQF_n (n = 0, 1, 2, 4)

Most applications for TCNQ-based materials are based their unique electrical properties as organic conductors, from the pure organic charge transfer complex TTF-TCNQ⁹ to coordination polymers such as CuTCNQ. Interestingly, these TCNQ-based materials can be synthesized chemically as well as electrochemically due to the facile reduction potential of TCNQ. Although chemical synthesis is more promising to provide good crystalline products for structural analysis^{16,40}, electrochemical approaches offers a feasible method for understanding the formation of the materials in different morphologies on a convenient time scale, which in turn gives an opportunity to tune the properties of the products.^{13,41-46}

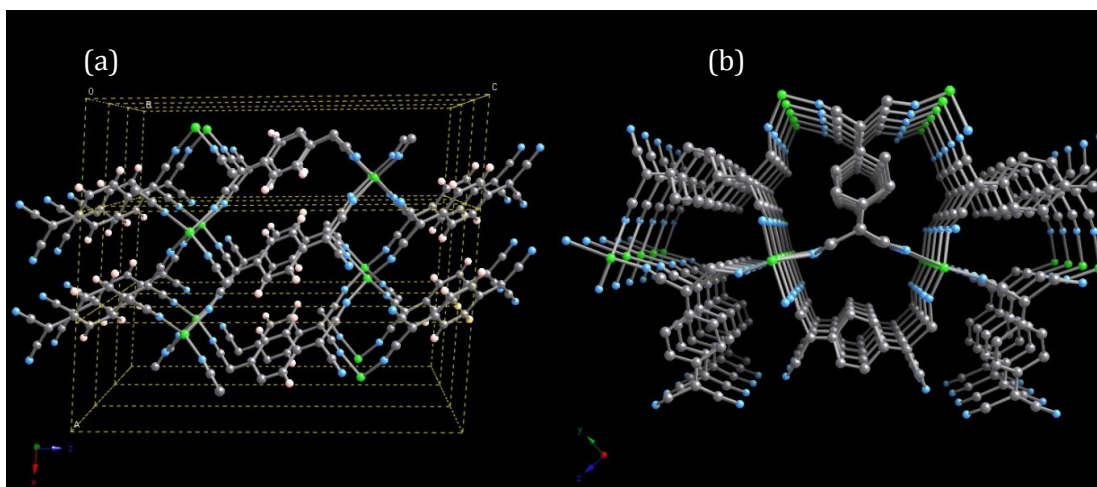
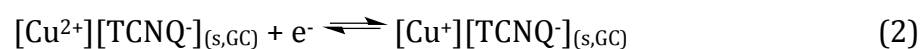
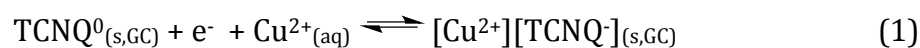


Figure 2. Crystal structure of CuTCNQ that exists in two different morphologies; (a) phase 1 and (b) phase 2 crystallized by Dunbar et. al⁴⁰

CuTCNQ was successfully crystallized from chemical synthesis from LiTCNQ and Cu(MeCN)₄ by Dunbar et. al in 1999.⁴⁰ It was reported that CuTCNQ exists as two different phases with significant conductivity difference (Figure 2). This property is due to the packing differences of the TCNQ⁻ moieties in crystal structures, that enhances the movement of electrons. Although they are both polymeric, neighbouring TCNQ molecules in phase I are rotated 90° with respect to each

other, while in phase II, there are infinite arrays of coplanar TCNQ molecules that are oriented in the same direction, but in two perpendicular planes. The stacking motif in phase I gives columnar stacks of TCNQ moieties with the closest distance between layers being 3.24 Å. In phase II structure, no π -stacking occurs between quinone rings and the closest distance between parallel TCNQ units is 6.8 Å. The identification of the two phases of CuTCNQ motivated electrochemists to study the mechanistic aspects of their formation. Although CuTCNQ had been electrocrystallized since 1980s,⁴⁷ only recently was cyclic voltammetry employed, allowing the kinetic as well as the thermodynamic aspects of their formation to be explored.^{41,42} CuTCNQ can be electrocrystallized either in aqueous media or in acetonitrile solution. In aqueous media, it is formed via solid-solid transformation when TCNQ is attached onto an electrode surface where it can be reduced in solid form in the presence of Cu^{2+} . The reduction potential was carefully chosen so that copper deposition can be avoided. The formation of CuTCNQ is proposed via two steps as described in equation 1 and 2.⁴¹

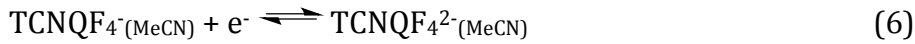


However, the limitation of using aqueous media is that Cu^+ easily disproportionates to Cu^{2+} and Cu . Cyclic voltammetry of TCNQ in acetonitrile in the presence of $[\text{Cu}(\text{MeCN})_4]^+$ provides further analysis and more kinetic and thermodynamic information. Interestingly, the reduction and oxidation of Cu^+ , i.e. $\text{Cu}^{+/0}$ and $\text{Cu}^{2+}/+$ processes, occur at potentials that are well removed from the first reduction step of TCNQ, hence the voltammetric studies are conveniently undertaken. Voltammetric evidence has revealed that the formation of CuTCNQ occurs via two processes in which the step at potentials more negative than the $E^{0'}$ value for the $\text{TCNQ}^{0/-}$ process is kinetically controlled via a nucleation-growth process.⁴² Furthermore, the voltammetric, spectroscopic and SEM imaging data suggested that the reduction of TCNQ at an electrode surface in the presence of $[\text{Cu}(\text{MeCN})_4]^+$ forms only phase I CuTCNQ (equation 3, 4) via these two processes, which generate precipitates with different morphologies either discrete large needles or smaller plates that cover most of the surface.

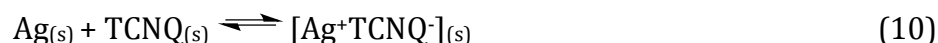




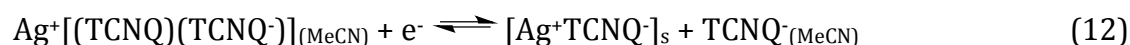
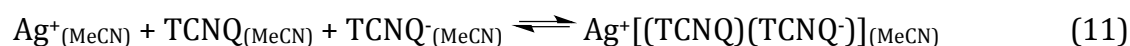
Using the fluorinated analogue, CuTCNQF₄ was also investigated electrochemically.¹⁴ It is interesting to note that in this study, not only was CuTCNQF₄ formed but also the TCNQF₄²⁻-based material, Cu₂TCNQF₄, was reported for the first time (equation 5-8). The formation of solid CuTCNQF₄ occurs electrochemically when the concentration of Cu(MeCN)₄⁺ and TCNQF₄ exceed the solubility product of CuTCNQF₄. Importantly, the solubility of Cu₂TCNQF₄ is significantly lower than that of CuTCNQF₄, hence voltammetry studies of the second reduction process do not interfere with the formation of solid CuTCNQF₄ at the electrode surface. When the cyclic voltammetry of TCNQF₄ includes the second reduction process, i.e. forming TCNQF₄²⁻ with Cu(MeCN)₄⁺ present, two stripping oxidation processes were detected after the solid Cu₂TCNQF₄ has been precipitated on the electrode surface, depending on scan rates. Although, there is no microscopic evidence, it was proposed based on the voltammetric responses and supported by simulations, that there are two phases of Cu₂TCNQF₄ which are oxidized at different potentials. Unfortunately, to date there is no single crystal structure reported for Cu₂TCNQF₄.



Ag-TCNQ based materials have also been studied using an analogous approach to Cu-TCNQ. Both AgTCNQ and AgTCNQF₄ have been synthesized chemically and crystallized as well as prepared by electrocrystallization.^{16,43,45} Electrochemically, AgTCNQ can be generated via solid-solid transformation if TCNQ is on an electrode surface and reduced in an aqueous solution containing Ag⁺ ions. However, the mechanism proposed for the formation of AgTCNQ is slightly different from what was observed in the CuTCNQ case. Because the standard potential of Ag^{+/0} is more positive than that of TCNQ^{0/-}, the formation of AgTCNQ was proposed via the redox reaction between Ag and TCNQ once Ag is oxidized onto the electrode surface (equation 9, 10).

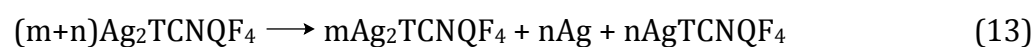


The electrocrystallization of AgTCNQ in acetonitrile shows that product morphology is dependent on the electrocrystallization potential and the deposition time, which is analogous to CuTCNQ system. That is, either longer deposition times or more negative potentials generates a film of 'blue crystals' of AgTCNQ on the electrode surface, while in the opposite case, discrete red needles are formed. The mechanism was postulated to involve the stabilization of (TCNQ)(TCNQ⁻) dimer by Ag⁺ followed by the reduction of TCNQ to TCNQ⁻ to form final product AgTCNQ (equation 11, 12).⁴³



However, cyclic voltammetry is not able to distinguish between these two phases of AgTCNQ synthesized chemically. Differing from two phases of CuTCNQ, which are convertible as kinetically and thermodynamically favoured products, two morphologies of AgTCNQ cannot be interconverted, so being obtained via different chemical synthesis pathways.¹⁶

Cyclic voltammetry of TCNQF₄ in the presence of Ag⁺ ions in acetonitrile has also been studied. In this case, as electrocrystallization of AgTCNQF₄ occurred, the ratio of the TCNQF₄^{0/-} reduction and oxidation peak currents decreased as expected, but there was no obvious solid state stripping process. Now, due to the much more positive redox potential of the second reduction process compared to that of TCNQ, the TCNQF₄^{2-/-} occurs before the Ag⁺ reduction process thus allowing the electrocrystallization of Ag₂TCNQF₄ to be achieved within the extended potential range at more negative values. The formation of TCNQF₄^{2-/-}-based materials in voltammetric time scale is a remarkable discovery due to the stabilization effect of four fluorine substituents on the TCNQ molecule. However, Ag₂TCNQF₄ material is not stable and decomposes as described in equation 13.⁴⁵



In addition to novel applications for electronic devices due to the switching behavior of TCNQF_n based materials, O'Mullane and co-workers recently proposed

their use as heterogeneous catalysts for redox reaction between $[\text{Fe}(\text{CN})_6]^{3-}$ and $\text{S}_2\text{O}_8^{2-}$.⁴⁸ It was found that a copper foil coated with CuTCNQF_n ($n = 0, 4$) or AgTCNQ_n ($n = 0, 4$) facilitates this redox reaction at variable rates depending on the nature of the catalyst. Interestingly, although the conductivity are considerably lower, the fluorinated derivatives significantly enhance the rate of the reduction of $[\text{Fe}(\text{CN})_6]^{3-}$ with $\text{S}_2\text{O}_8^{2-}$, compared to TCNQ based catalyst. The catalysts can be reused up to 50 cycles with a constant activity. Recently, the catalytic activity of TCNQF_n base materials was illustrated by the complex $[(\text{NH}_3)_4\text{Pt}](\text{TCNQF}_4)_2 \cdot (\text{DMF})_4$ employing the same redox system of $[\text{Fe}(\text{CN})_6]^{3-}$ and $\text{S}_2\text{O}_8^{2-}$.⁴⁹ The catalytic mechanism involves the replacement of $\text{S}_2\text{O}_8^{2-}$ with DMF solvate when the crystal is soaked in aqueous solution. This facilitates the reduction of TCNQF_4^- to TCNQF_4^{2-} and then a redox reaction between TCNQF_4^{2-} and $[\text{Fe}(\text{CN})_6]^{3-}$ generating $[\text{Fe}(\text{CN})_6]^{4-}$. From these studies it is noticeable that the fluorine substituents on the TCNQ moiety not only enhance the stability of the anions but also improve the catalyst activity. Although the electron withdrawing effects of fluorine substituents on the TCNQ ring is not the only factor, it plays an important role in the enhancing of the catalytic activity.

1.2. TCNQF and TCNQF₂ – Electrical and structural properties – A comparison to TCNQ and TCNQF₄ derivative

The mono- TCNQF (TCNQF = fluoro-7,7,8,8-tetracyanoquinodimethane) and difluoro-substituted, TCNQF₂ (TCNQF₂ = 2,5-difluoro-7,7,8,8-tetracyanoquinodimethane) (see Figure 1) are expected to possess intermediate electron transfer properties compared with TCNQ and TCNQF₄. As for quinone systems, the increase in the number electron withdrawing substituent shifts the redox potentials of the quinone derivatives.^{50,51} Indeed, the electron affinities of TCNQF and TCNQF₂ were reported to be 2.95 and 3.02 eV respectively, which lies midway between that of TCNQ and TCNQF₄, which are 2.85 and 3.20 eV, respectively.^{52,53} Thus, the substituent effect is related to the properties of TCNQF_n and can be described using a Hammett plot. In previous studies on TCNQF₄ - the four fluorine substituents derivatives - the reversible potentials for both $\text{TCNQF}_n^{0/-}$ / $^{2-}$ processes shifted positively so the stability of the dianion is significant enhanced in comparison with those of TCNQ.¹²⁻¹⁴ Inclusion of one and two fluorine

substituents on the TCNQ is expected that the redox chemistry will exhibit intermediate properties, between that of TCNQ and TCNQF₄.

The crystal, molecular and electronic structures of TCNQF and TCNQF₂ have been investigated and compared with those of TCNQ and TCNQF₄.⁵²⁻⁵⁵ The space group among four derivatives is listed in table 1. Among these four molecules, the 2,5-TCNQF₂ has a highly symmetric structure which is monoclinic C_{2h} symmetry. In contrast, TCNQF is the only compound in the family that is asymmetric which gives rise to a permanent molecule dipole moment.

Table 1. Crystallography space group of TCNQF_n(n = 0-2, 4)

	TCNQ	TCNQF	TCNQF ₂	TCNQF ₄
Space group	C2/c	P2 ₁ /m	C2/m	Pbca

Representative intramolecular bond lengths of the four TCNQ derivatives are shown in Figure 3. The bond lengths vary in each derivative; however, the fluoro-substituent effect only has a minor influence on these intramolecular bond lengths. In contrast, the variation of specific bond angles greatly reflects the number of fluorine atoms in the molecules. As can be seen from Table 2, bond angle C3-C4-C5 decreases, while C1-C3-C2 and C5-C4-C6 bond angles increase with the increase of the degree of fluorine substituents.

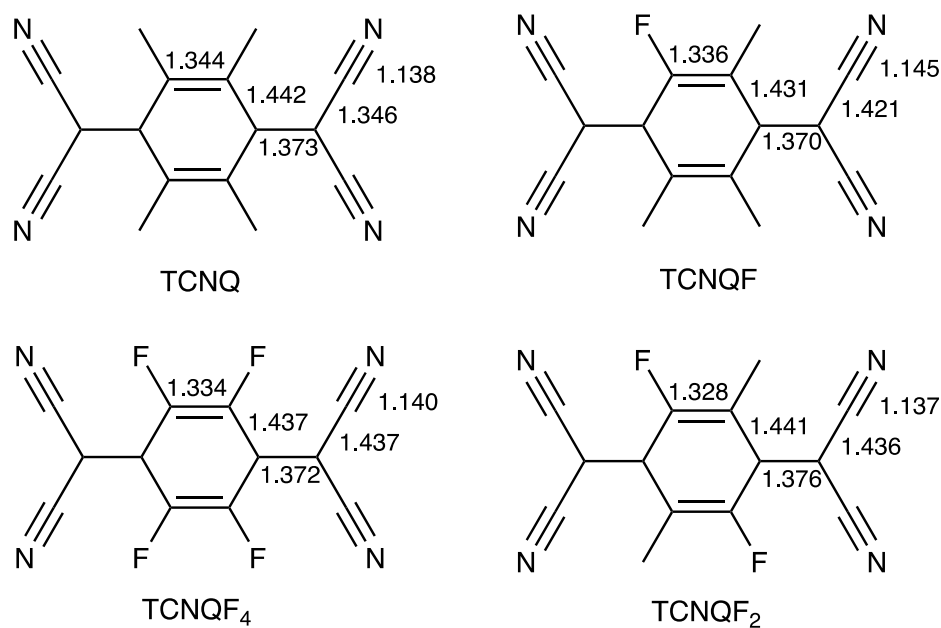
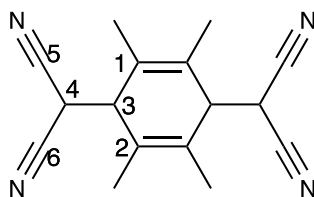


Figure 3. Representative bond lengths in crystal structure of TCNQF_n (n = 0-2, 4)⁵⁶

Table 2. Representative bond angles in crystal structure of TCNQF_n (n = 0-2, 4)



Bond angle (°)	TCNQ	TCNQF	TCNQF ₂	TCNQF ₄
C3-C4-C5	122.1	123.3	124.8	124.4
C5-C4-C6	115.9	115.6	114.8	112.4
C1-C3-C2	118.3	115.9	115.5	113.7

The single crystal structure of TCNQ is described to be dominated by intermolecular stacking interaction between quinone rings. Whereas, TCNQF₄ is considered as amphoteric molecule, which can act as both a base through the electron rich cyano group and an acid through electron-deficient fluorinated ring C atoms, due to the main intermolecular interaction being N...C-F, as described in Figure 4.^{52,55} Similar to TCNQ crystallography, both TCNQF and TCNQF₂ all contain arrays of parallel-aligned molecules. However, the antiparallel cyano-cyano coupling was found in TCNQF and TCNQF₂ (Figure 4). The coupling of local dipole moments in the crystal structure of TCNQF involves an internal interleaving of molecules, while that in the crystal structure of 2,5-TCNQF₂ is external.

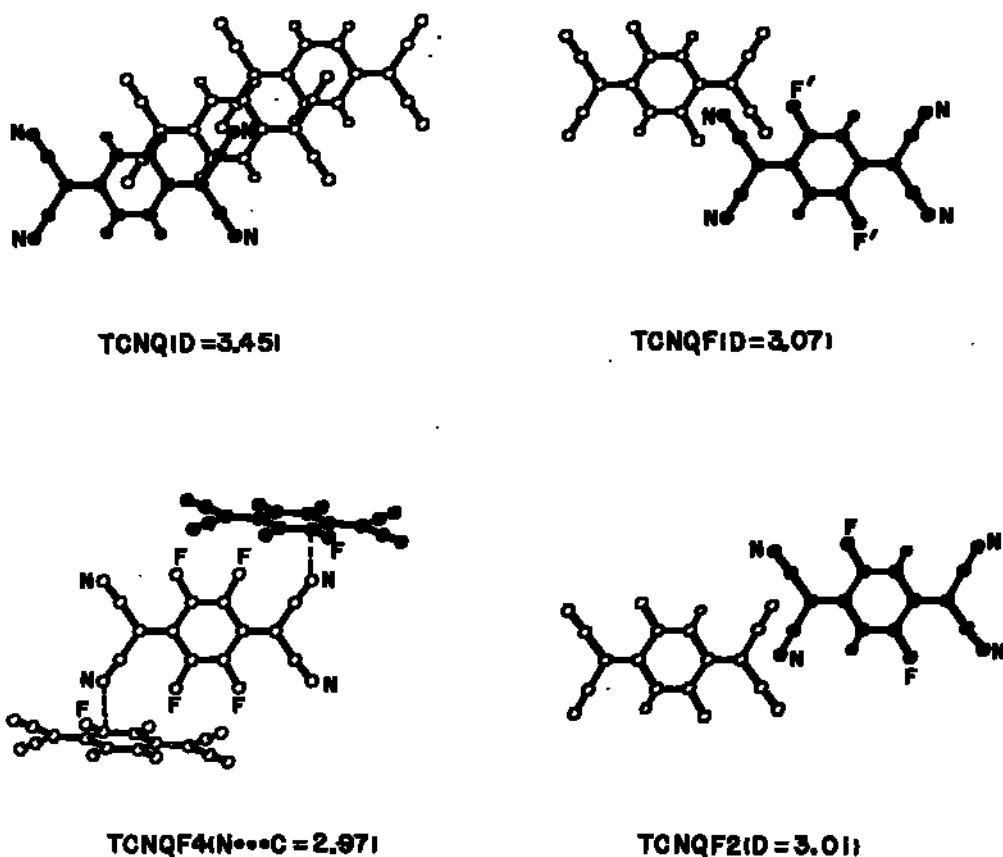


Figure 4. Dominant intermolecular interactions in crystal structure of TCNQF_n (n = 0-2, 4). D is the interplanar distance between two neighbouring layers. Adapted from ref 57.⁵⁶

1.3. Studies on TCNQF and TCNQF₂ complexes

In a study on the formation of charge transfer salts between a TCNQ fluoro derivative with an iodinated tetrathiafulvalene derivative, EDT-TTF-I (see Figure 5), an increase in the number of fluoro substituents on TCNQ leads to an enhanced ionicity in these complexes.^{37,57} For example, the complexes with TCNQF₄ were obtained with a degree of charge transfer of +1, while that of TCNQF₂ had a charge of 0.5. Interestingly, TCNQ can also form charge transfer complexes with either $\rho = 0.5$ or neutral 2:1 complex $\rho = 0$ (where ρ is the degree of charge transfer). Unfortunately, more detailed investigation on the TCNQF salt was limited by the small quantities of materials available and poor crystallinity. In another study at 150^oK, where EDT-TTF-I was replaced by EDT-TTF₂, the complex formed with TCNQ showed a charge ρ of 0, while that of TCNQF formed a complex with ρ of -0.1, the charge of TCNQF₂ was report to be 1.1. These studies support an increase

of ionicity in charge transfer salts that increase with the number of fluoro substituents.

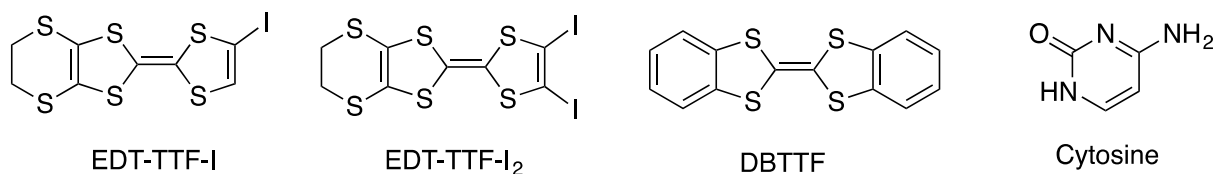


Figure 5. Molecular structure of EDT-TTF-I, EDT-TTF-I₂, DBTTF and cytosine

Further studies on the charge-assisted halogen bonding within donor-acceptor complexes were done by Liefbrig et. al. They described the effect of increase the number of fluorine substituents on the halogen bond distance as well as on the charge transfer degree in EDTTTFI₂-TCNQF_n. An increase of fluorine substituents not only drives the charge transfer degree of TCNQF_n⁻ to fully ionic but also shortens the C-I ... N=C halogen bond. In terms of resistivity of these charge transfer complexes at 293⁰K, TCNQF₂-based complexes possess the lowest resistivity while the TCNQ complex is most resistant.⁵⁷

Crystal structures of several complexes of TCNQF₂ with TTF derivatives also have been reported.³⁷⁻³⁹ Dimer stacking was observed in the structure of DBTTF-TCNQF₂. More interestingly, a complex of TCNQF₂ and a nucleobase, cytosine, showed a fully ionic material of the monoanion TCNQF₂⁻ and the cytosine cation.⁵⁸

Another TCNQF complex reported is a heterospin single-chain magnet (valpn)CuTb(TCNQF)₂(H₂O)₄·[TCNQF]·CH₃OH·6H₂O demonstrating a single chain magnet which involves stacking interaction of TCNQF⁻ radicals (H₂valpn is the Schiff base from the condensation of o-vanillin with 1,3-diaminopropane).⁵⁹

In summary, although a few TCNQF and TCNQF₂-based materials have been synthesized as noted before and some properties assessed, fundamental understanding has yet to be undertaken and is addressed for the first time in this thesis, and compare with results available for TCNQ and TCNQF₄.

1.4. Thesis objectives

The primary aim of this thesis is to investigate the chemistry and redox properties of TCNQF and TCNQF₂ in comparison with TCNQ and TCNQF₄ derivatives:

1. To understand the kinetics, thermodynamics and mechanism associated with reduction of TCNQF and TCNQF₂ in acetonitrile in the presence or absence of an acid or a metal cation and compare with TCNQ and TCNQF₄.
2. To understand the substituent effect on the chemistry and electrochemistry of TCNQF_n derivatives (n = 0, 1, 2, 4).
3. To electrochemically and chemically synthesize new materials based on the monoanions and dianions of TCNQF, TCNQF₂ and TCNQF₄
4. To characterize the structures, conductivities, morphologies and catalytic activity of the new materials.

References

- (1) Bond, A. M. *Broadening Electrochemical Horizons: Principles and Illustration of Voltammetric and Related Techniques*; Oxford University Press Inc.: New York 2002.
- (2) Grieshaber, D.; MacKenzie, R.; Vörös, J.; Reimhult, E. *Sensors (Basel, Switzerland)* **2008**, *8*, 1400.
- (3) Badawy, W. A. *Journal of Advanced Research* **2015**, *6*, 123.
- (4) Lewis, P. M.; Ackland, H. M.; Lowery, A. J.; Rosenfeld, J. V. *Brain Research* **2015**, *1595*, 51.
- (5) O'Donnell, J.; Kim, M.; Yoon, H.-S. *Journal of Manufacturing Science and Engineering* **2016**, *139*, 1.
- (6) Harrer, W.; Grampp, G.; Jaenicke, W. *Chemical Physics Letters* **1984**, *112*, 263.
- (7) Jérôme, D. *Chemical Reviews* **2004**, *104*, 5565.
- (8) Kepler, R. G.; Bierstedt, P. E.; Merrifield, R. E. *Physical Review Letters* **1960**, *5*, 503.
- (9) Ferraris, J.; Cowan, D. O.; Walatka, V.; Perlstein, J. H. *Journal of the American Chemical Society* **1973**, *95*, 948.
- (10) Coleman, L. B.; Cohen, M. J.; Sandman, D. J.; Yamagishi, F. G.; Garito, A. F.; Heeger, A. J. *Solid State Communications* **1973**, *12*, 1125.
- (11) Thomas, G. A.; Schafer, D. E.; Wudl, F.; Horn, P. M.; Rimai, D.; Cook, J. W.; Glocker, D. A.; Skove, M. J.; Chu, C. W.; Groff, R. P.; Gillson, J. L.; Wheland, R. C.; Melby, L. R.; Salamon, M. B.; Craven, R. A.; De Pasquali, G.; Bloch, A. N.; Cowan, D. O.; Walatka, V. V.; Pyle, R. E.; Gemmer, R.; Poehler, T. O.; Johnson, G. R.; Miles, M. G.; Wilson, J. D.; Ferraris, J. P.; Finnegan, T. F.; Warmack, R. J.; Raaen, V. F.; Jerome, D. *Physical Review B* **1976**, *13*, 5105.
- (12) Le, T.; O'Mullane, A.; Martin, L.; Bond, A. J. *Solid State Chem.* **2011**, *15*, 2293.
- (13) Le, T. H.; Nafady, A.; Bond, A. M.; Martin, L. L. *European Journal of Inorganic Chemistry* **2012**, *2012*, 5534.
- (14) Le, T. H.; Nafady, A.; Vo, N. T.; Elliott, R. W.; Hudson, T. A.; Robson, R.; Abrahams, B. F.; Martin, L. L.; Bond, A. M. *Inorganic Chemistry* **2014**, *53*, 3230.

- (15) Lopez, N.; Zhao, H. H.; Prosvirin, A. V.; Wernsdorfer, W.; Dunbar, K. R. *Dalton Trans.* **2010**, 39, 4341.
- (16) O'Kane, S. A.; Clérac, R.; Zhao, H.; Ouyang, X.; Galán-Mascarós, J. R.; Heintz, R.; Dunbar, K. R. *Journal of Solid State Chemistry* **2000**, 152, 159.
- (17) Qu, X.; Lu, J.; Zhao, C.; Boas, J. F.; Moubaraki, B.; Murray, K. S.; Siriwardana, A.; Bond, A. M.; Martin, L. L. *Angewandte Chemie International Edition* **2011**, 50, 1589.
- (18) Lu, J.; Qu, X.; Peleckis, G.; Boas, J. F.; Bond, A. M.; Martin, L. L. *The Journal of Organic Chemistry* **2011**, 76, 10078.
- (19) Nafady, A.; Bond, A. M.; Bilyk, A.; Harris, A. R.; Bhatt, A. I.; O'Mullane, A. P.; De Marco, R. *J. Am. Chem. Soc.* **2007**, 129, 2369.
- (20) Nafady, A.; O'Mullane, A. P.; Bond, A. M.; Neufeld, A. K. *Chem. Mater.* **2006**, 18, 4375.
- (21) Ran, C. B.; Peng, H. L.; Zhou, W.; Yu, X. C.; Liu, Z. F. *J. Phys. Chem. B* **2005**, 109, 22486.
- (22) Peng, H. L.; Ran, C. B.; Yu, X. C.; Zhang, R.; Liu, Z. F. *Adv. Mater.* **2005**, 17, 459.
- (23) Valade, L.; De Caro, D.; Malfant, I.; Ouahab, L., Yagubskii, E., Eds.; Kluwer Academic Publisher: Corfu, GREECE, 2003, p 241.
- (24) Yasuda, A.; Seto, J. *J. Electroanal. Chem.* **1988**, 247, 193.
- (25) Yamaguchi, S.; Potember, R. S. *Synth. Met.* **1996**, 78, 117.
- (26) Pandey, P. C.; Upadhyay, S.; Sharma, S. *Electroanalysis* **2003**, 15, 1115.
- (27) Llopis, X.; Merkoci, A.; del Valle, M.; Alegret, S. *Sens. Actuators, B* **2005**, 107, 742.
- (28) Kim, J. S.; Cho, O. K.; Min, K. S.; Park, K. Y. *Mol. Cryst. Liq. Cryst.* **1995**, 267, 375.
- (29) Kim, J.; Cho, O.; Min, K.; Park, K. *Synth. Met.* **1995**, 71, 2215.
- (30) Cho, O. K.; Park, K. Y. *Mol. Cryst. Liq. Cryst.* **1995**, 267, 393.
- (31) Cano, M.; Palenzuela, B.; Rodriguez-Amaro, R. *Electroanalysis* **2006**, 18, 1068.
- (32) Nafady, A.; O'Mullane, A. P.; Bond, A. M. *Coordination Chemistry Reviews* **2014**, 268, 101.
- (33) Nafady, A.; Le, T. H.; Vo, N.; Haworth, N. L.; Bond, A. M.; Martin, L. L. *Inorganic Chemistry* **2014**, 53, 2268.

- (34) Grosseil, M. C.; Duke, A. J.; Hibbert, D. B.; Lewis, I. K.; Seddon, E. A.; Horton, P. N.; Weston, S. C. *Chem. Mater.* **2000**, *12*, 2319.
- (35) Lombardo, A.; Fico, T. R. *J. Org. Chem.* **1979**, *44*, 209.
- (36) Suchanski, M. R.; Vanduyne, R. P. *J. Am. Chem. Soc.* **1976**, *98*, 250.
- (37) Lieffrig, J.; Jeannin, O.; Guizouarn, T.; Auban-Senzier, P.; Fourmigué, M. *Crystal Growth and Design* **2012**, *12*, 4248.
- (38) Miyasaka, H.; Motokawa, N.; Matsunaga, S.; Yamashita, M.; Sugimoto, K.; Mori, T.; Toyota, N.; Dunbar, K. R. *Journal of the American Chemical Society* **2010**, *132*, 1532.
- (39) Emge, T. J.; Wiygul, F. M.; Chappell, J. S.; Bloch, A. N.; Ferraris, J. P.; Cowan, D. O.; Kistenmacher, T. J. *Molecular Crystals and Liquid Crystals* **1982**, *87*, 137.
- (40) Heintz, R. A.; Zhao, H.; Ouyang, X.; Grandinetti, G.; Cowen, J.; Dunbar, K. R. *Inorganic Chemistry* **1999**, *38*, 144.
- (41) Neufeld, A. K.; Madsen, I.; Bond, A. M.; Hogan, C. F. *Chemistry of Materials* **2003**, *15*, 3573.
- (42) Harris, A. R.; Neufeld, A. K.; O'Mullane, A. P.; Bond, A. M.; Morrison, R. J. S. *Journal of The Electrochemical Society* **2005**, *152*, C577.
- (43) Harris, A. R.; Nafady, A.; O'Mullan, A. P.; Bond, A. M. *Chemistry of Materials* **2007**, *19*, 5499.
- (44) Zhao, C.; MacFarlane, D. R.; Bond, A. M. *Journal of the American Chemical Society* **2009**, *131*, 16195.
- (45) Le, T. H.; O'Mullane, A. P.; Martin, L. L.; Bond, A. M. *Journal of Solid State Electrochemistry* **2011**, *15*, 2293.
- (46) Nafady, A.; Bond, A. M.; O'Mullane, A. P. *Inorganic Chemistry* **2009**, *48*, 9258.
- (47) Kathirgamanathan, P.; Rosseinsky, D. R. *Journal of the Chemical Society, Chemical Communications* **1980**, 839.
- (48) Mahajan, M.; Bhargava, S. K.; O'Mullane, A. P. *RSC Advances* **2013**, *3*, 4440.
- (49) Lu, J.; Abrahams, B. F.; Winther-Jensen, B.; Martin, L. L.; Bond, A. M. *ChemCatChem* **2014**, *6*, 2345.
- (50) Mirkhalaf, F.; Tammeveski, K.; Schiffrin, D. J. *Physical Chemistry Chemical Physics* **2004**, *6*, 1321.
- (51) Scribner, R. M. *The Journal of Organic Chemistry* **1966**, *31*, 3671.

- (52) Emge, T. J.; Maxfield, M.; Cowan, D. O.; Kistenmacher, T. J. *Molecular Crystals and Liquid Crystals* **1981**, *65*, 161.
- (53) Mitchell Wiygul, F.; Ferraris, J. P.; Emge, T. J.; Kistenmacher, T. J. *Molecular Crystals and Liquid Crystals* **1981**, *78*, 279.
- (54) Wiygul, F. M.; Emge, T. J.; Ferraris, J. P.; Kistenmacher, T. J. *Molecular Crystals and Liquid Crystals* **1981**, *71*, 303.
- (55) Long, R. E.; Sparks, R. A.; Trueblood, K. N. *Acta Crystallographica* **1965**, *18*, 932.
- (56) Kistenmacher, T. J.; Wiygul, F. M.; Emge, T. J. In *Intermolecular forces*; Pullman, B., Ed.; Springer Netherlands: 1981, p 499.
- (57) Lieffrig, J.; Jeannin, O.; Frackowiak, A.; Olejniczak, I.; Swietlik, R.; Dahaoui, S.; Aubert, E.; Espinosa, E.; Auban-Senzier, P.; Fourmigue, M. *Chemistry (Weinheim an der Bergstrasse, Germany)* **2013**, *19*, 14804.
- (58) Murata, T.; Saito, G.; Nishimura, K.; Enomoto, Y.; Honda, G.; Shimizu, Y.; Matsui, S.; Sakata, M.; Drozdova, O. O.; Yakushi, K. *Bulletin of the Chemical Society of Japan* **2008**, *81*, 331.
- (59) Wang, Z. X.; Zhang, X.; Zhang, Y. Z.; Li, M. X.; Zhao, H.; Andruh, M.; Dunbar, K. *R. Angewandte Chemie (International ed. in English)* **2014**, *53*, 11567.

Chapter 2

Investigation of the redox and acid-base properties of TCNQF and TCNQF₂ – Electrochemistry, vibrational spectroscopy and substituent effects

Abstract

Electrochemistry and the acid-base chemistry of TCNQF and TCNQF₂ are reported and these results are compared to those reported previously with TCNQ and TCNQF₄. In acetonitrile solution, both mono- and di-fluorinated TCNQ derivatives show two well resolved, diffusion-controlled chemically and electrochemically reversible one-electron transfer processes under conditions of cyclic voltammetry. The reversible potentials of the mono and difluoro-TCNQ were determined for both the monoanion and dianionic processes, i.e. TCNQF^{0/-/2-} and TCNQF₂^{0/-/2-}. A Hammett plot shows a linear relationship of the potential difference between the three fluorinated derivatives and TCNQ and the sum of the Hammett constant for fluoro substitution. A significant positive shift in the reversible potential is found by increasing the number of fluoro substituents. Although the first TCNQF_n^{0/-} (n = 1, 2) reduction process is not affected by addition of trifluoroacetic acid (TFA), the dianions are more basic and rapidly protonated to form H₂TCNQF_n which explained the significant change detected in the electrochemistry of the second TCNQ(F)_n^{-/2-} redox process. The addition of TFA to solutions of the monoanionic form also gives rise to the disproportionation of TCNQF_n⁻ to TCNQF_n and H₂TCNQ(F)_n, as proved electrochemically and spectroscopically. Furthermore, the higher the number of fluoro substituents results in the reduced form of the molecule being more stable, as evidenced by both UV-Vis spectra and voltammetric measurements.

2.1. Introduction

TCNQ (TCNQ = 7,7,8,8-tetracyanoquinodimethane) and its halogenated derivatives can be reduced to the anion radical and the dianion, both which are good electron acceptors. The electrochemistry of TCNQX_n and the synthesis of TCNQX_n-based charge-transfer complexes were first reported in the 1970s with the most famous

example of an organic charge-transfer complex being TTF.TCNQ.¹⁻³ Halogenated derivatives, particularly the fluorinated ones (Figure 1) are of special interest since this substituent enhances the stability of the reduced forms of the charge transfer compounds.⁴⁻⁸

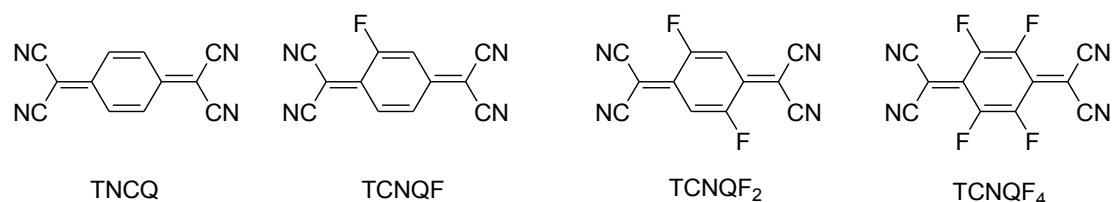


Figure 1: Structures of TCNQ, TCNQF, TCNQF₂ and TCNQF₄

In this study, the electrochemistry of the mono (TCNQF) and di-fluoro (TCNQF₂) derivatives of TCNQ have been investigated. In earlier studies with TCNQF₄, it was showed that with four fluorine substituents, the reversible potential shifted positively by ~360 mV and the stability of the dianion TCNQF₂²⁻ was greatly enhanced in comparison with TCNQ²⁻.⁴⁻⁶ The acid-base chemistry of TCNQF_n is also considered. With one and two fluorine substituents, intermediate properties are expected.

The Hammett equation has been used to assess the electronic effect of a substituent attached directly to an aryl system.^{9,10} Although originally based on proton dissociation constants of substituted benzoic acids, the Hammett equation is applicable to an equilibria of any substituted aromatic compounds. The Hammett equation is given in eq 1, where K is the equilibrium constant of a reaction involving a substituted aryl system, σ is the Hammett constant, ρ is the reaction constant and K_0 is the equilibrium constant for the unsubstituted parent compound.

$$\log K - \log K_0 = \log \frac{K}{K_0} = \sigma \rho \quad (1)$$

The equilibrium constant of a redox reaction can be expressed in term of its standard redox potential E^0

$$\log K = \frac{nFE^0}{2.303RT} \quad (2)$$

$$\log K - \log K_0 = \frac{nFE^o}{2.303RT} - \frac{nFE^o_0}{2.303RT} \quad (3)$$

$$\log \frac{K}{K_0} = \frac{nF}{2.303RT} \Delta E^o = \sigma \rho \quad (4)$$

According to equation 4, a linear relationship between the sum of σ for all the substituents and the potential difference ΔE^o between TCNQ and the fluorinated derivatives should be established.

It is well-known that protonation affects the electrochemistry of the quinone family.¹¹ This can also be applied to TCNQ derivatives.^{12,13} Protonation plays an important role in controlling the redox chemistry as well as the stability of the basic anions. Employing simulations, the two equilibrium constants associated with protonation of the dianions in the presence of trifluoroacetic acid (TFA), were determined to be 1×10^8 and 2×10^2 for TCNQ²⁻ compared with 3×10^3 and 1 for TCNQF₄²⁻.^{12,13} This is a great difference in the basicity of the TCNQ²⁻ and TCNQF₄²⁻ dianions. Therefore acid-base studies with TCNQF₂ and TCNQF, will provide a more complete understanding on the influence of the substituent effect within the TCNQF_n family.

In this report, the electrochemistry and acid-base chemistry of TCNQF and TCNQF₂ along with their radical anions and dianions have been investigated in the presence of TFA and the results have been compared with published data on TCNQ and TCNQF₄. Simulations of the cyclic voltammograms have been used to establish the details of the proton-coupled electron transfer mechanism and to extract the kinetic and thermodynamic parameters associated with these processes. Characteristic UV-Vis, IR and Raman spectroscopy are also employed as a diagnostic tool for further characterization.

2.2. Experiments

2.2.1. Chemicals

TCNQF and TCNQF₂ (98%, TCI Tokyo), acetonitrile (HPLC grade, Omnisolv) and acetone (suprasolv, Merch KGaA) were used as received from the manufacturer. Bu₄NPF₆ (Aldrich), used as the supporting electrolyte in electrochemical studies,

was recrystallized twice from 96% ethanol (Merck) and then dried at 100°C under vacuum for 24 hours prior to use.

2.2.2. Electrochemistry

Voltammetry experiments were studied at room temperature using a Bioanalytical systems (BAS) 100W workstation. A standard three electrode cell configuration, comprising of a glassy carbon (GC, 1 mm diameter) working electrode (WE), a Ag/Ag⁺ reference electrode (RE) and a 1.0 mm diameter platinum wire counter electrode, were employed in those experiments. The working electrode was polished with 0.3 μm alumina slurry on a microcloth polishing cloth, washed with water followed by sonication in an ultrasonic bath for 30 seconds before being used for voltammetric experiments. The WE was polished and washed after each run to ensure a fresh electrode surface. The RE was constructed of an Ag wire in contact with an acetonitrile solution of 0.1 M Bu₄NPF₆ containing 1.0 mM AgNO₃, which was separated from the solution under studied by a salt bridge. The relative potential of this reference electrode is -124 mV vs the ferrocene/ferrocenium, Fc^{0/+} couple. All the solutions under studied were purged with nitrogen gas for at least 10 min and a stream of nitrogen was maintained above the solutions during the course of the voltammetric experiments. In bulk electrolysis experiment, a Pt mesh was used as the working electrode rather the GC electrode.

Electrochemistry of the dianionic solution TCNQF_n²⁻ was performed in a glove box.

2.2.3. Simulation software

Digi Sim 3.0 software distributed by BAS was used to simulate the cyclic voltammograms.

2.2.4. DFT calculation of IR and Raman spectra

Geometry optimizations and harmonic vibrational frequency calculations were performed for gas-phase TCNQF_n and TCNQF using the B3LYP density functional theory^{14,15} in conjunction with the 6131G(2df,p) basis set¹⁶. This model is known to give good accuracy for the calculation of vibrational frequencies and is employed in G4 theory for the accurate calculation of zero-point energies.¹⁷ In each calculation the full symmetry of the molecule was used which is C_{2h} for TCNQF_n, TCNQF_n⁻ and TCNQF₂²⁻.

B3LYP/6131G(2df,p) vibrational frequencies are normally scaled by a factor of 0.9854¹⁸ to account for known deficiencies in the method¹⁹ (incomplete basis set, anharmonicity, etc.). This factor gives good agreement between theory and experiment for most frequencies below 2000 cm⁻¹. However the nitrile stretching frequencies (at ~2200 cm⁻¹) and the C-H stretching frequencies (at ~3050 cm⁻¹) are consistently over predicted. In earlier work,²⁰ a new scaling factor of 0.9556 was determined for nitrile stretching frequencies. In this study a revised the scaling factor of 0.9513 was used for all frequencies above 3000 cm⁻¹. This factor was determined by comparing the calculated C-H stretching frequencies with experimental values²¹.

2.2.5. Other instrumentation

UV-Vis spectra were recorded with a Varian Cary 5000 UV-Vis NIR spectrophotometer using a 1.0 cm path length quartz cuvette. A Varian UMA600 IR microscope and FTS7000 optics bench using 128 scans and a resolution of 8 cm⁻¹ was used to obtain IR spectra. Raman spectra were recorded with a Renishaw Invia Raman spectrograph using Argon ion laser excitation at 633 nm

2.3. Result and discussion

2.3.1. Electrochemistry of TCNQF and TCNQF₂ in CH₃CN in comparison with TCNQ and TCNQF₄

Cyclic voltammograms obtained with 1.0 mM solutions of TCNQF and TCNQF₂ in acetonitrile (0.1M Bu₄NPF₆) compared with those of TCNQ and TCNQF₄ in Figure 2. All exhibit two well resolved diffusion-controlled chemically and electrochemically reversible one -electron reduction processes, corresponding to the two steps:



The midpoint potentials (E_m , calculated from the average of the reduction and oxidation peak potentials recorded under these transient conditions) of both reduction processes for the four TCNQ derivatives are summarized in Table 1. E_m provides a very good approximation of E^0 , the reversible potential. The separation

between two processes (ΔE) increase^{12,13} and E_m values shift consistently to more positive values on the addition of each fluorine substituent.

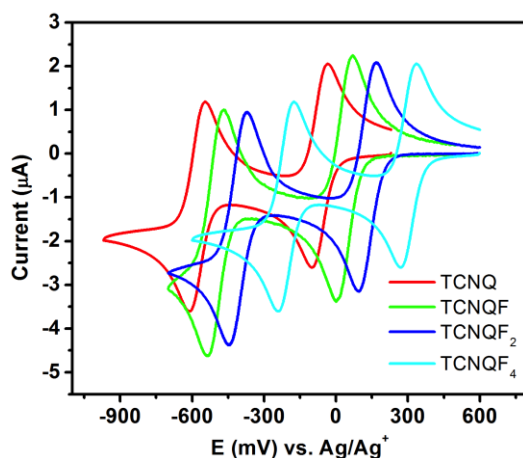


Figure 2: Cyclic voltammograms obtained at a scan rate of $100 \text{ mV}\cdot\text{s}^{-1}$ in acetonitrile solution ($0.1 \text{ M Bu}_4\text{NPF}_6$) for 1.0 mM TCNQ, TCNQF, TCNQF₂, and TCNQF₄ at a 1.0 mm diameter GC electrode.

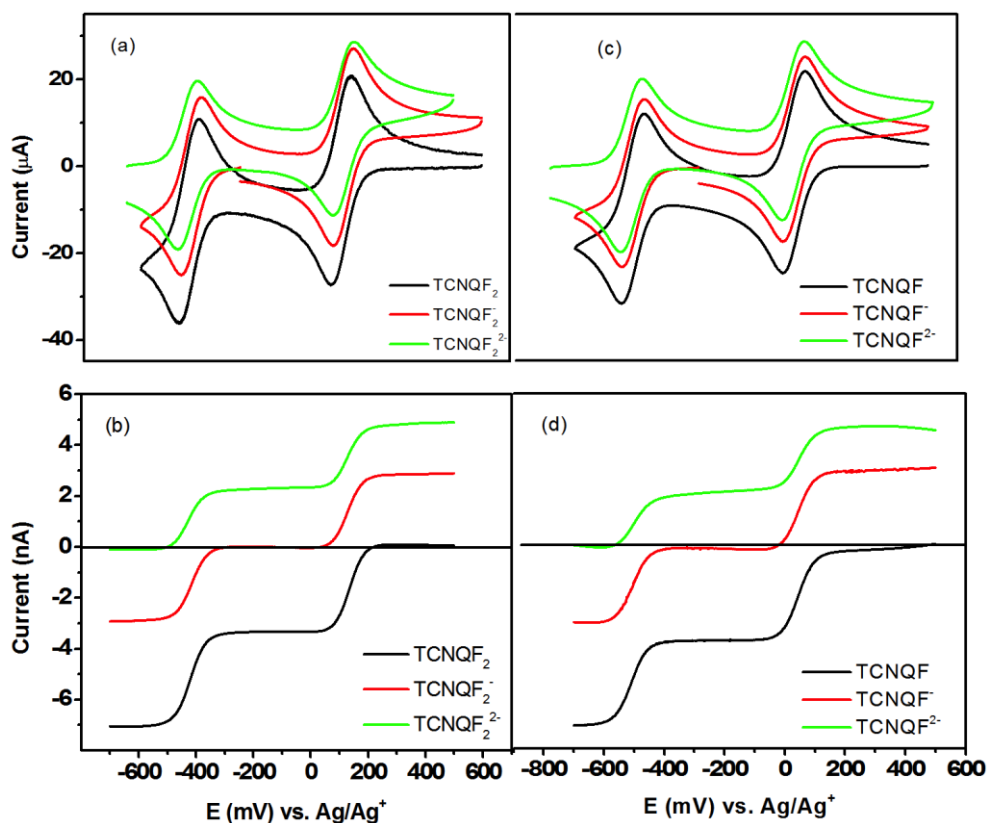


Figure 3: Voltammograms obtained from 1.0 mM TCNQF_n, TCNQF_n⁻ and TCNQF_n²⁻ in acetonitrile ($0.1 \text{ M Bu}_4\text{NPF}_6$); (a,c) Cyclic voltammograms with a 3.0 mm diameter GC electrode ($\nu = 100 \text{ mV}\cdot\text{s}^{-1}$) and (b,d) Near steady state voltammograms at a $10 \mu\text{m}$ diameter gold micro disc electrode ($\nu = 50 \text{ mV}\cdot\text{s}^{-1}$)

This reversible potential order is in agreement with the reported first electron affinities of the family, that are $EA_{TCNQ} = 2.85 \text{ eV} < EA_{TCNQF} = 2.95 \text{ eV} < EA_{TCNQF_2} = 3.02 \text{ eV} < EA_{TCNQF_4} = 3.20 \text{ eV}$.^{22,23}

Steady state and transient cyclic voltammograms of TCNQF_n, the monoanion and dianion solutions prepared by bulk electrolysis are shown in Figure 3. The two reduction steps of a solution containing neutral TCNQF_n are confirmed by the presence of purely negative current in the steady state voltammogram. The purely positive current obtained with TCNQF_n²⁻ confirms that both processes of the dianion are oxidation ones. Voltammograms of a solution of the monoanion results in negative current for the reduction to the dianion and positive current for the oxidation to neutral TCNQF_n. However, while TCNQF_n⁻ solutions were highly stable under N₂ purging after preparation by bulk electrolysis, TCNQF_n²⁻ was unstable as evidenced by the rapid decay in oxidation current signal on consecutive scans. The instability of the TCNQF_n²⁻ solution will be discussed further.

Table 1: Summary of midpoint potentials summary of TCNQ, TCNQF, TCNQF₂ and TCNQF₄

	E_{m1} (mV) vs Ag/Ag ⁺	E_{m2} (mV) vs Ag/Ag ⁺	ΔE (mV) vs Ag/Ag ⁺
TCNQ	-60	-610	550
TCNQF	35	-502	537
TCNQF ₂	129	-408	537
TCNQF ₄	305	-221	526

The substituent effect on the electrochemistry of TCNQF_n is well described by the Hammett equation referred to above. Thus ΔE_1^0 , the E_m potential differences (very similar to half-wave potential, $E_{1/2}$ or E^0 difference) between a derivative and TCNQ, for the first redox process are in linear relationship against the summation of the Hammett constant $\Sigma\sigma_m$ as shown in figure 4 with a correlation coefficient of 0.99. The Hammett constant for the fluorine substituent was taken from ref. 9. This

linear relationship confirms that an increase of the number of fluorine substituents, which is an electron-withdrawing substituent, enhances the electron affinity of the TCNQF_n derivatives.

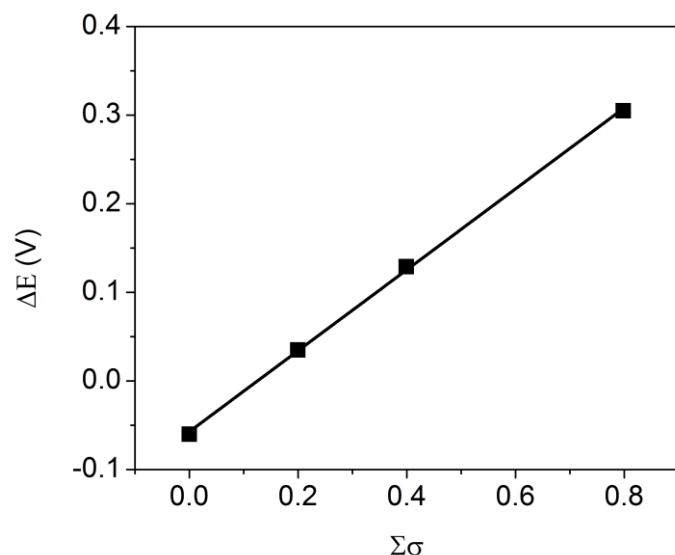


Figure 4: ΔE_1^0 vs $\Sigma\sigma$ Hammett plot of TCNQF_n (n = 0-2, 4)

The diffusion coefficients of TCNQF and TCNQF₂ were determined by applying the Randles-Sevcik equation which described the dependence of peak current in the voltammograms for a reversible process with scan rate as shown in equation 7.

$$\text{The Randles-Sevcik equation:}^{24} \quad i_p = 0.4463 nFA C \left(\frac{nFvD}{RT} \right)^{1/2} \quad (7)$$

where i_p : peak current, n: number of electrons transferred, A: electrode area (cm²), F: Faraday constant (C.mol⁻¹), D: diffusion coefficient (cm².s⁻¹), C: concentration (mol.cm⁻³), v: scan rate (V.s⁻¹), R: gas constant and T: temperature (°K).

As expected for a reversible diffusion controlled redox processes, the reduction peak current increases linearly with $v^{1/2}$. The diffusion coefficients of TCNQF and TCNQF₂ found by analysis of the scan rate dependence and use of equation 7 were $2.15 \pm 0.13 \times 10^{-5}$ and $2.10 \pm 0.17 \times 10^{-5}$ cm.s⁻¹ respectively and similar to those of TCNQF₄ (2.0×10^{-5} cm.s⁻¹) and TCNQ (1.9×10^{-5} cm.s⁻¹).^{13,25}

2.3.2. UV-Vis spectroscopy of TCNQF_n and the anions in acetonitrile

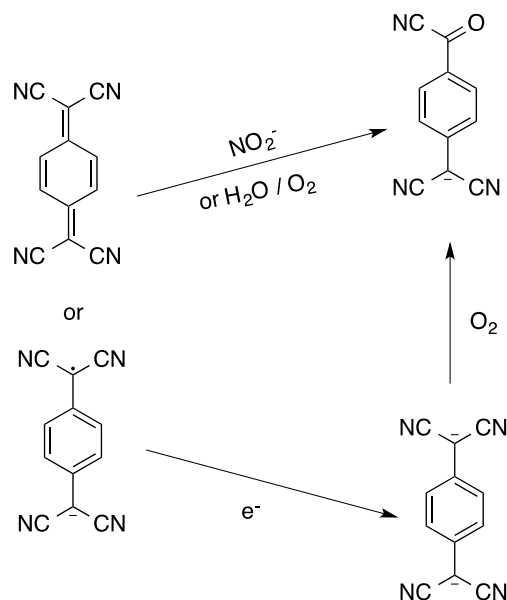
The neutral TCNQ and TCNQF₄,^{26,27} as well as their anions show a distinct absorption spectrum maxima which provides a useful tool to identify the oxidation state(s) present in solution. Hence, the UV-Vis spectroscopy of TCNQF and TCNQF₂

and their anions (Figure 5) was also recorded to identify their characteristic maxima in acetonitrile and are listed in table 2.

Table 2. λ_{\max} (nm) of TCNQF_n neutral and anions in acetonitrile

λ_{\max} (nm)	0	-1	-2
TCNQF	391	417, 744	311
TCNQF ₂	392	418, 742	323

Monitoring the time dependence of solutions using UV-Vis spectroscopy also provides information on the stability of TCNQ(F)_n and their anions in the presence of air. While the neutral and the monoanion of TCNQ(F)_n were found to be stable to aerial oxygen, the dianions are not. In the case of both TCNQF²⁻ and TCNQF₂²⁻ solutions, and in the presence of air, a peak at $\lambda_{\max} \sim 475$ nm increased in intensity with time (Figures 6 and 7). This maximum is associated with formation of the fluorinated dicyano-p-toluoylcyano anion (DTC⁻), a decomposition product of TCNQ and its derivatives, according to reaction in scheme 1:²⁸



Scheme 1: Decomposition of TCNQ to dicyano-p-toluoylcyano anion (DTC⁻) in the presence of air (Adapted from ref 11)

In the case of TCNQF₂²⁻, this decomposition absorption band only appeared after leaving the solution stand under open-air condition for 15 minutes. The aerial

stability of TCNQF_2^{2-} lies between that of TCNQ^{2-} , which only can be obtained under anaerobic conditions, and the tetrafluorinated TCNQF_4^{2-} which does not react with air. The TCNQF_2 confirms the substituent effect of two fluorines on the TCNQ parent, where the stability of the dianion increases with the number of fluorine atoms attached.

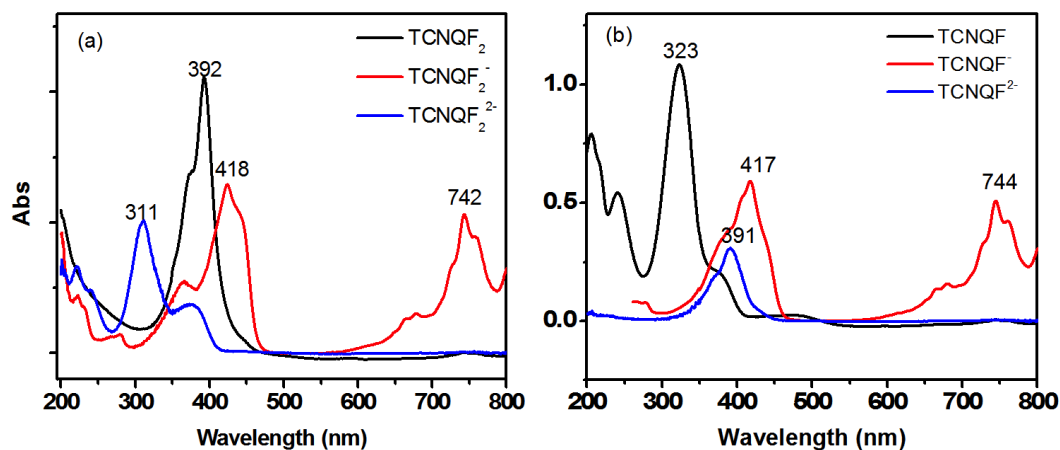


Figure 5: UV-Vis spectra of neutral $\text{TCNQ}(\text{F})_n$ (black) and their anions $\text{TCNQ}(\text{F})_n^-$ (red) and $\text{TCNQ}(\text{F})_n^{2-}$ (blue) in acetonitrile.

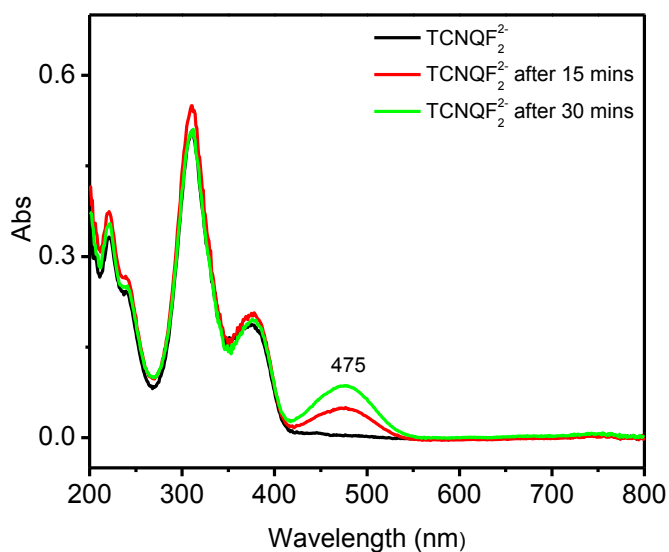


Figure 6: UV-Vis spectra of TCNQF_2^{2-} solution in acetonitrile (black), and exposed to the air for 15 (red) and 30 (green) minutes. Decomposition is indicated by the appearance of a new band at 475 nm.

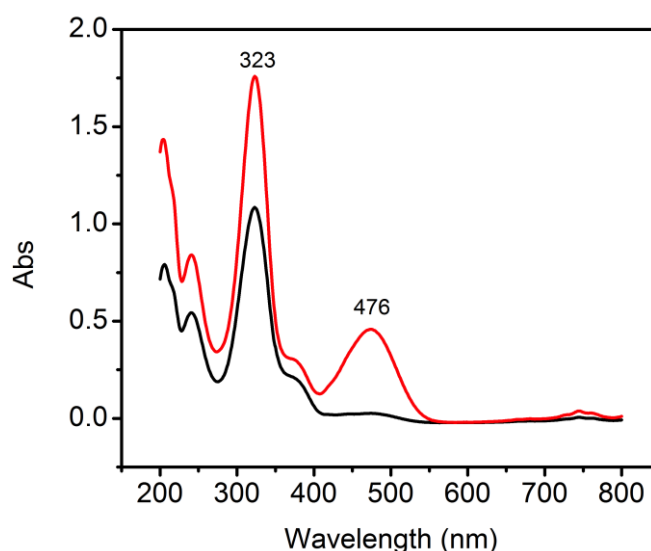


Figure 7: UV-Vis spectra of TCNQF₂²⁻ solution in acetonitrile (black), and exposed to the air for 15 mins (red).

2.3.3. Electrochemistry of TCNQF_n, TCNQF_n⁻ and TCNQF_n²⁻ in acetonitrile in the presence of trifluoroacetic acid (n = 1, 2)

Voltammetry of TCNQF_n in acetonitrile in the presence of TFA

The transient and steady state voltammetry of neutral TCNQF_n (n = 1, 2) and its anions were studied as a function of TFA concentration. The voltammograms obtained are presented in Figure 8. Addition of TFA over the concentration range of 0.3 mM to 10.0 mM into a 1.0 mM solution of TCNQF₂ shows that the first reduction process of TCNQF₂^{0/-} (Red1) is independent of TFA concentration (Figure 8a). In contrast, the second reduction process TCNQF₂^{-/2-} (Red2) initially at -470 mV changes dramatically. On addition of 0.3 mM TFA, the current magnitude of Red2 diminishes with the concomitant appearance of a new reduction process at much more positive potential of -274 mV (Red3). When the concentration of TFA exceeds 1 equivalent, Red2 process disappears and is completely replaced by Red3 with the peak potential of Red3 shifts positively from -274 mV to -188 mV as the concentration of TFA in the solution is increased from 0.3 to 10.0 mM. This behavior is characteristic of a proton-coupled electron transfer process (EC mechanism), which implies that TCNQF₂²⁻ reacts with protons in solution after formation by reduction of TCNQF₂⁻. On the reverse potential scan, upon adding TFA from 0.3 to 10.0 mM, the counterpart oxidation process of Red2, Ox2, decreases and disappears with Red2. An addition of TFA at the concentration equal

5.0 to 10.0 mM gives rise to an oxidation process Ox3 at 450 mV, concomitantly with the drop in current magnitude of Ox1 process. This suggests that TCNQF_2^{2-} is protonated in the presence of TFA and Ox3 process can be attributed to the oxidation of the protonation form.

An analogous behavior was observed with TCNQF. In this case, although E_p of Red1 does not shift, the current magnitude of the first reduction process $\text{TCNQF}^{0/-}$ markedly increases upon addition of TFA (Figure 8c). This is consistent with that the disproportionation of TCNQF^- , which produces TCNQF^0 , is more remarkable than that of TCNQF_2^- (eq. 8)



Also, on the positive scan, the decrease in current magnitude of Ox1 is more significant than that was observed with TCNQF_2 .

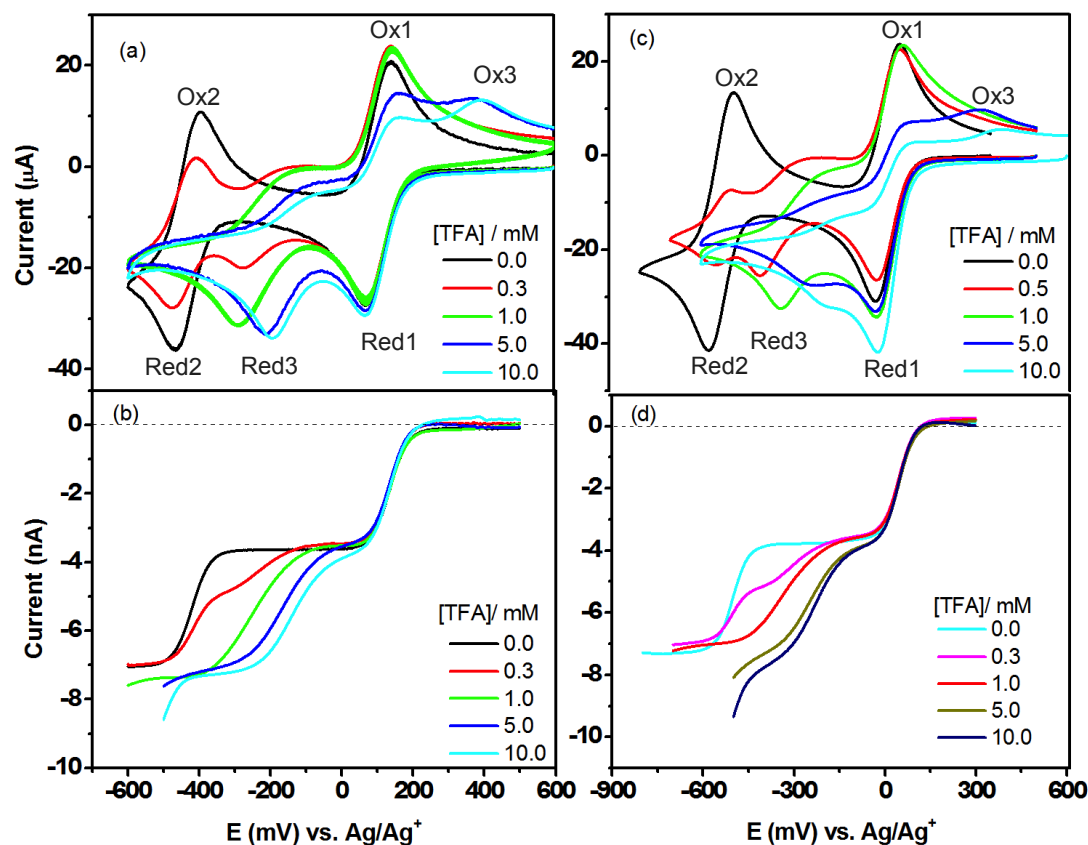


Figure 8. Voltammograms obtained from 1.0 mM TCNQF_n solution in the presence of designated TFA concentrations: Cyclic voltammograms with a 3.0 mm diameter GC electrode ($\nu = 100 \text{ mV}\cdot\text{s}^{-1}$) for (a) TCNQF_2 and (c) TCNQF; and steady state voltammograms using a $10\mu\text{m}$ diameter gold micro electrode ($\nu = 50 \text{ mV}\cdot\text{s}^{-1}$) for (b) TCNQF_2 and (d) TCNQF

The steady state voltammograms of TCNQF_n also confirm the independence of TCNQF_n^{0/-} reduction process on TFA concentration (Figure 8b,d). Indeed, the current magnitude and E_{1/2} values of this process remain virtually unchanged upon adding up to 10.0 mM TFA. In contrast, the second redox step changes dramatically. When 0.3 mM TFA was added into 1.0 mM TCNQF_n solution, a new irreversible wave appeared prior to the second process with an E_{1/2} value of -215 mV for TCNQF₂ and -337 mV for TCNQF; and the limiting current magnitude of the second process concomitantly decreased. At higher concentration of TFA, the TCNQF_n^{-/2-} process was replaced by the new one whose E_{1/2} value shifts to more positive potential as a function of the TFA concentration.

Direct protonation of TCNQF_n²⁻ in the presence of TFA

The protonation of TCNQF_n²⁻ dianion was confirmed by studying the voltammetry of TCNQF_n²⁻, which was prepared by exhaustive bulk reduction electrolysis of TCNQF_n, in the presence of TFA. Voltammograms obtained are presented in Figure 9. Under steady state condition (Figure 9b,d), right after adding 0.3mM TFA into 1.0 mM solution of TCNQF_n²⁻ the current magnitude of TCNQF_n^{2-/-} drops significantly. It diminishes and approaches zero when increasing the concentration of added TFA. This phenomenon can be explained by the direct protonation of TCNQF_n²⁻ in the presence of TFA which leaving less TCNQF_n²⁻ available in the solution. At high concentration of TFA, presumably when the TCNQF_n²⁻ was fully protonated, the limiting current of TCNQF_n^{2-/-} process drops to zero. At the same time, in contrast with what is observed in steady state voltammetry of neutral TCNQF_n in the presence of TFA, the process at positive potential becomes complicated in this scenario. Although the first process of TCNQF_n⁻/TCNQF_n is still visible at TFA/TCNQF_n²⁻ ratio is less than 0.5, there is another redox process at more positive potential. When increase the concentration of TFA to a higher ratio, the TCNQF_n⁻/TCNQF_n process was totally replaced by the new redox process at more positive potential. This implies that the protonation form of TCNQF_n²⁻ was oxidized at more positive potential.

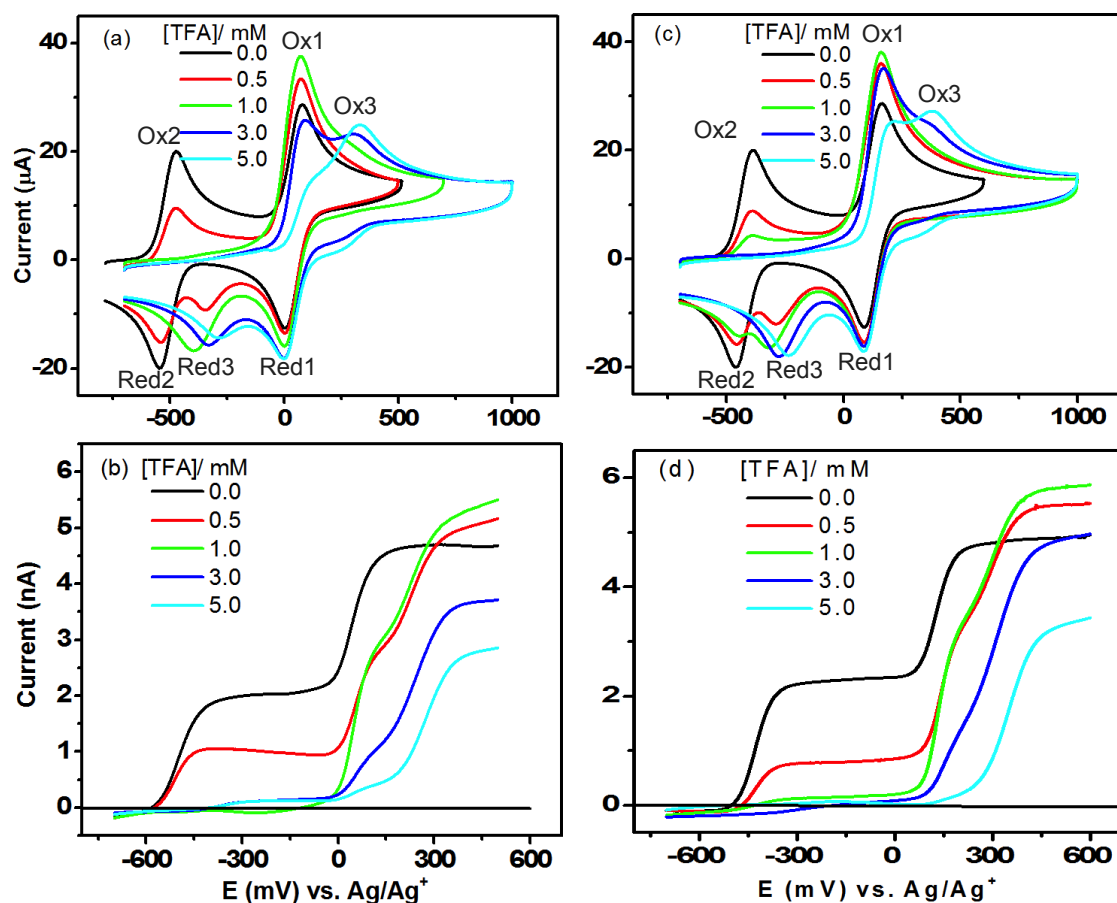


Figure 9. Cyclic voltammograms obtained from 1.0 mM TCNQF_n^{2-} solution in the presence of designated TFA concentration with a 3.0 mm diameter GC electrode ($v = 100 \text{ mV}\cdot\text{s}^{-1}$) for (a) TCNQF^{2-} and (b) TCNQF_2^{2-} and Near steady state voltammograms at a $10\mu\text{m}$ diameter gold micro electrode ($v = 50 \text{ mV}\cdot\text{s}^{-1}$) for (c) TCNQF^{2-} and (d) TCNQF_2^{2-} .

Similarly, the transient cyclic voltammetry of TCNQF^{2-} also describes a current drop of process Ox2 when increase the concentration of TFA in solution (Figure 9a). The current magnitude of Ox1, corresponding to the oxidation $\text{TCNQF}_n^{-/0}$, in the other hand increases when small TFA concentration is added (up to 1.0 mM) and then decreases at higher TFA levels with the concomitant arise of the new process Ox3. Also, when the potential is switched back to negative direction, the voltammetric waves obtained resembles to that of TCNQF solution with added TFA. This implies that in the voltammetric time scale, the protonated form of TCNQF_n^{2-} was oxidized to TCNQF_n if the potential was scanned to positive enough. Although, comparable behavior was observed for TCNQF_2^{2-} , it is noticeable that at

the addition of 1.0 mM of TFA into 1.0 mM TCNQF₂²⁻, Ox2 process is still detectable (Figure 9c) implying that the equilibrium constants of the protonation step differs for TCNQF₂²⁻ and TCNQF₂²⁻

From these observations, it is likely that although the TCNQF_n^{0/-} is independent on the addition of TFA, TCNQF_n²⁻ electrochemically produced from TCNQF₂²⁻ is protonated in two steps to form HTCNQF_n⁻ and H₂TCNQF_n with the equilibrium constant of K₁ and K₂ (equations 8, 9). It is assumed that H₂TCNQF_n is stable, similar to both H₂TCNQ and H₂TCNQF₄.^{12,13} Furthermore, HTCNQF_n⁻ is oxidized back to neutral TCNQF_n at a potential close to that of TCNQF_n⁻, supported by the fact that the oxidation current increases when up to 1.0 mM of TFA is added to 1.0 mM of TCNQF_n²⁻.



The appearance of the new oxidation peak Ox3, simultaneously with the reduction of peak current magnitude of Ox1 at high TFA concentration implies that HTCNQF_n⁻ is oxidized back to neutral TCNQF_n via two different steps depending on the TFA concentration.

Disproportion of TCNQF_n⁻ in the presence of TFA

In order to understand the effect of protonation to the monoanion, the voltammetric experiments of TCNQF_n⁻ were performed in the presence of TFA at different concentrations as presented in Figure 10. As expected, the transient cyclic voltammograms for 1.0 mM of TCNQF_n⁻ in the presence of increased TFA concentration resembled to those for the neutral TCNQF_n solution. At 0.5 mM of TFA, another oxidation step clearly happens prior the reduction of TCNQF_n⁻ to TCNQF_n²⁻. This is consistent with the protonation of TCNQF_n²⁻ right after it was formed from the reduction of TCNQF_n⁻. It is also consistent with the presence of 0.5mM of TFA which is equal to half of TCNQF_n⁻ concentration. Upon increase of the TFA concentration, the reversibility is totally lost at 1.0 mM of TFA up to 10.0 mM of TFA. Furthermore, the first process also loses its reversibility. Although the reduction current isn't modified, the oxidation wave not only decreases in magnitude but also changes in shape.

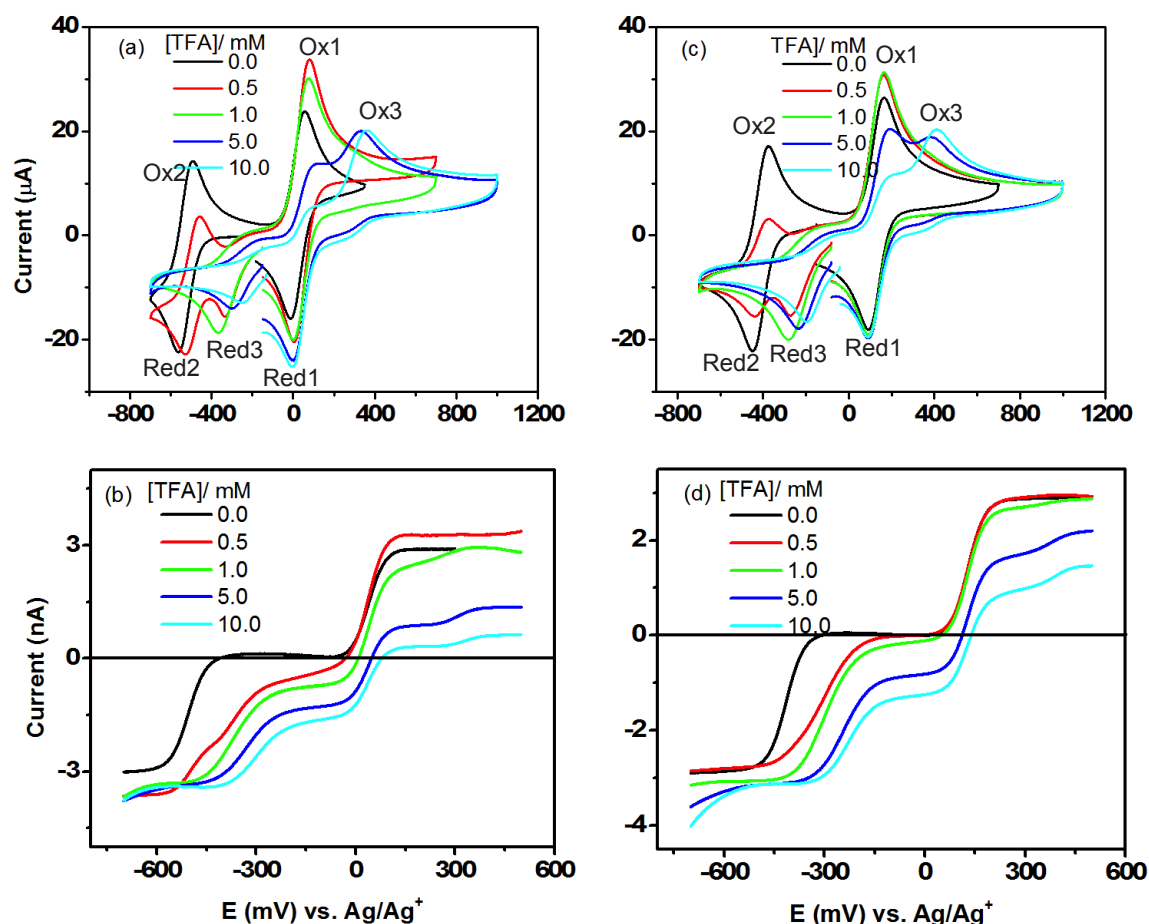


Figure 10. Voltammograms obtained from 1.0 mM $\text{TCNQ}(\text{F})_n^-$ solution in the presence of designated TFA concentration Cyclic voltammograms with a 3.0 mm diameter GC electrode ($\nu = 100 \text{ mV}\cdot\text{s}^{-1}$) for (a) TCNQF^- and (b) TCNQF_2^- and Near steady state voltammograms at a $10\mu\text{m}$ diameter gold micro electrode ($\nu = 50 \text{ mV}\cdot\text{s}^{-1}$) for (c) TCNQF^- and (d) TCNQF_2^-

The steady state voltammetry of TCNQF_n^- in the presence of TFA provides new information. Along with a positive shift in the $E_{1/2}$ value for the second process, the current density decreases as the TFA concentration increases. In addition, the current between the two major processes is no longer zero but becomes negative implying that TCNQF_n is now generated in the bulk solution. This is also consistent with the increase in current magnitude of Red1 when high concentration of TFA is added to TCNQF solution. These observations are in good agreement with the voltammetric results discussed above with equation 8. Furthermore, the limiting current also decreases as a function of added TFA, implying that in addition to the formation of TCNQF_n , the reaction of TCNQF_n^- with protons can also form another electro-inactive product. From observation of the steady state voltammograms, it

can be assumed that the equilibrium constant for the reaction between TCNQF_2^- and TFA is smaller than that of TCNQF^- and TFA. The result will be quantified in the Digital Simulation section.

The formation of neutral TCNQF_n when TFA is added to TCNQF_n^- was confirmed by the UV-Vis spectra shown in Figure 11. The absorption maxima at 424 and 743 nm, diagnostic of the mono radical anion, are replaced by a maximum at 393, characteristic for TCNQF_2 , upon increase of the concentration of TFA.

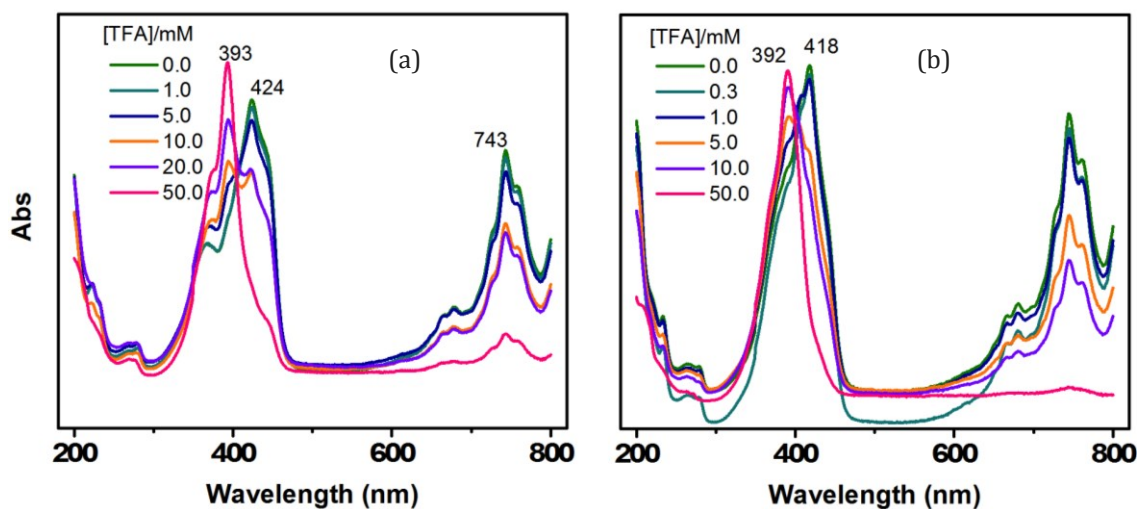
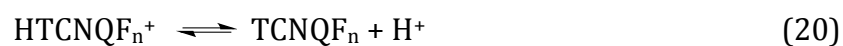
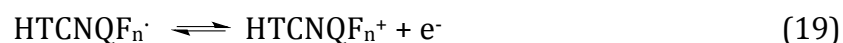
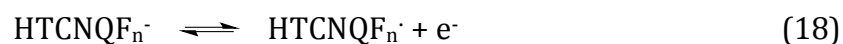
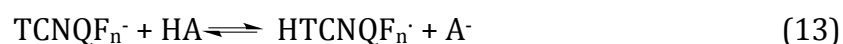
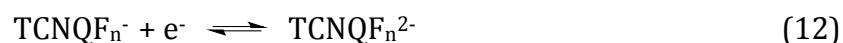
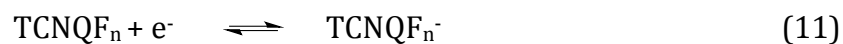


Figure 11. UV-Vis spectra obtained after the addition of designated TFA concentration to 1.0 mM (a) TCNQF_2^- and (b) TCNQF^- solution in acetonitrile (0.1 M Bu_4NPF_6) followed by a 60-fold dilution.

2.3.4. Simulation of the voltammetry of TCNQF_n and its anions in the presence of TFA

The mechanism of protonation of TCNQ and TCNQF_4 has been reported.^{12,13} A similar mechanism was proposed for simulation of the voltammetry of TCNQF and TCNQF_2 . These reactions are: (i) neutral TCNQF_n is not affected by TFA, (ii) TCNQF_n^- disproportionates in the presence of TFA forming TCNQF_n and H_2TCNQF_n , (iii) TCNQF_n^{2-} is protonated in two sequential steps to form HTCNQF_n^- and H_2TCNQF_n , (iv) HTCNQF_n^- is oxidized to HTCNQF_n^\bullet at the potential for TCNQF_n^- oxidation, (v) HTCNQF_n^\bullet is oxidized to HTCNQF_n^+ and then dissociates to TCNQF_4 and H^+ . The mechanism proposed occur via the reactions given in equations 11 to 20



This mechanism is supported by simulations of cyclic voltammograms obtained for TCNQF_n , TCNQF_n^- and TCNQF_n^{2-} over a range of concentrations and scan rates. It was a challenge to simulate such a complicated mechanism that requires estimations of many parameters. However, by applying the parameters listed in table 2, acceptable agreement was obtained with experiment for all experimental conditions used for both the mono and di-fluoro derivatives (Figures 12, 13).

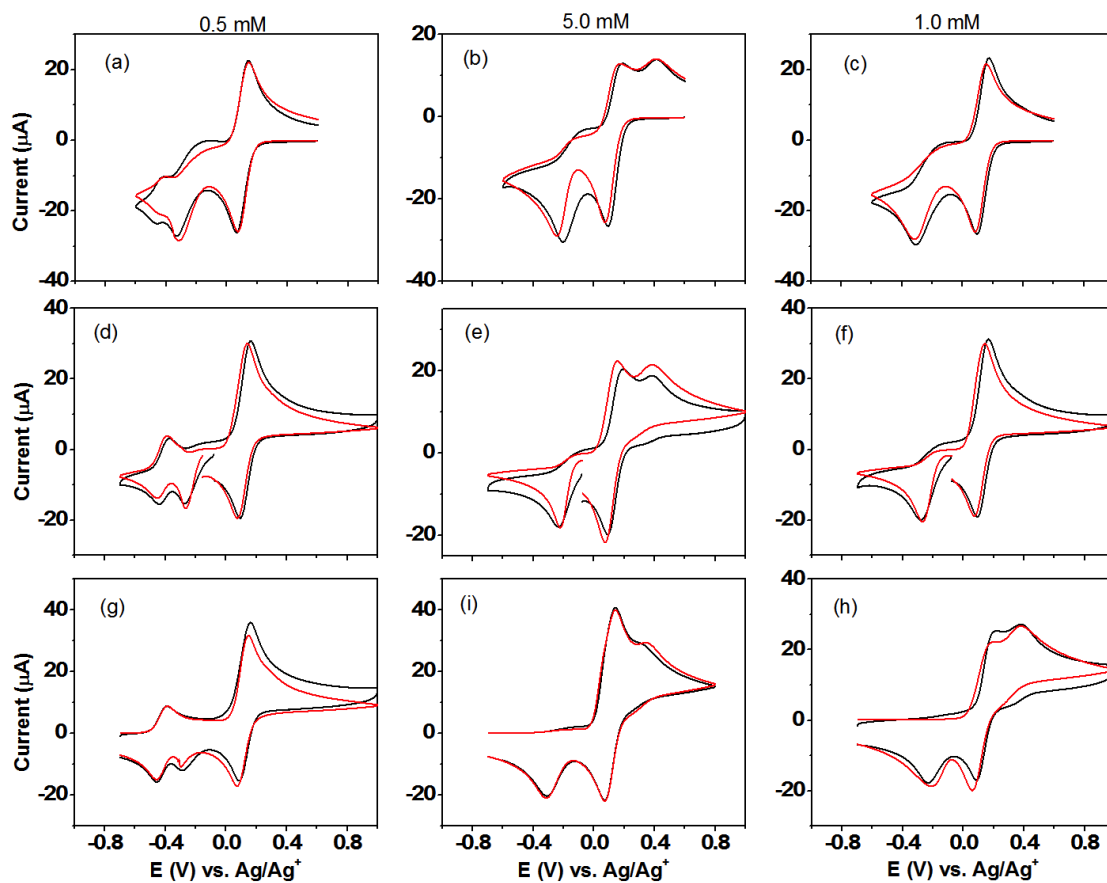


Figure 12. Experimental (black line) and simulated (red line) cyclic voltammograms obtained in acetonitrile (0.1M Bu_4NPF_6) with 1.0 mM (a-c) TCNQ, (d-f) $\text{TCNQ}^{\cdot-}$ and (g-i) $\text{TCNQ}^{2\cdot-}$ at designated TFA concentration at 100 mVs^{-1} using a 3.0 mm diameter GC electrode

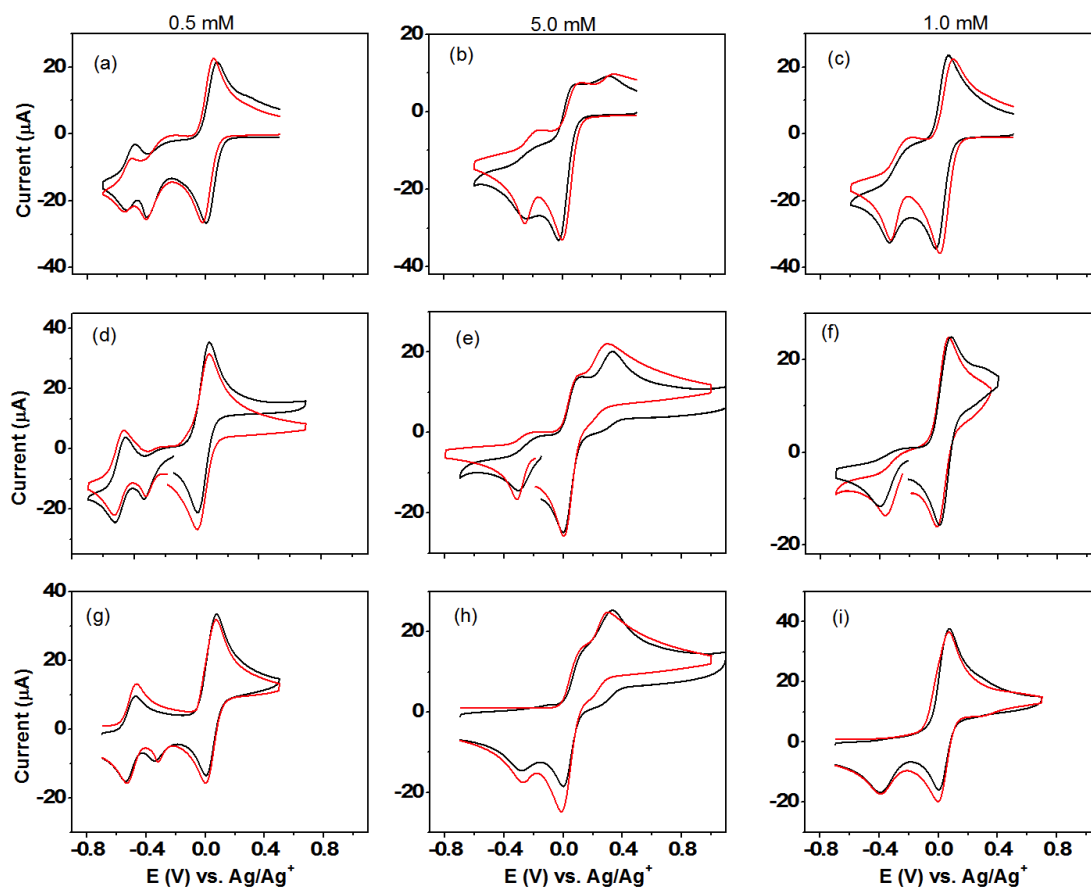


Figure 13. Simulated (red line) and experimental (black line) and cyclic voltammograms obtained in acetonitrile (0.1M Bu_4NPF_6) with 1.0 mM (a-c) TCNQF_2 , (d-f) $\text{TCNQF}_2^{\cdot-}$ and (g-i) $\text{TCNQF}_2^{2\cdot-}$ at designated TFA concentration using a scan rate of $100 \text{ mV}\cdot\text{s}^{-1}$ with a 3.0 mm diameter GC electrode

Table 2. Parameters used in the simulation of the cyclic voltammetry of TCNQF_n (n = 1, 2) and its anions in acetonitrile in the presence of TFA

Step	Reaction	TCNQF _n	E ⁰ /V		K _{eq}		k _s /cm s ⁻¹		k _f /M ⁻¹ s ⁻¹	
			1	2	1	2	1	2	1	2
1	TCNQF _n + e = TCNQF _n ⁻		0.04	0.11			0.1	0.1		
2	TCNQF _n ⁻ + e = TCNQF _n ²⁻		-0.50	-0.42			0.1	0.1		
3	TCNQF _n ⁻ + HA = HTCNQF _n [•] + A ⁻				1.5×10 ⁻²	8.8×10 ⁻⁴			5.0×10 ²	1.0
4	HTCNQF _n [•] + HTCNQF _n [•] = H ₂ TCNQF _n				3.0×10 ²	1.0×10 ³			1.0×10 ⁶	5.0×10 ⁷
5	TCNQF _n ²⁻ + HA = HTCNQF _n ⁻ + A ⁻				2.0×10 ⁷	8.0×10 ⁵			1.0×10 ¹⁰	1.0×10 ¹⁰
6	TCNQF _n ²⁻ + H ₂ TCNQF _n = HTCNQF _n ⁻ + HTCNQF _n ⁻				4.0×10 ⁶	1.3×10 ⁷			1.0×10 ¹⁰	1.0×10 ¹⁰
7	HTCNQF _n ⁻ + HA = H ₂ TCNQF _n + A ⁻				5.0	1.0			1.0×10 ⁴	6.0×10 ³
8	HTCNQF _n ⁻ = HTCNQF _n [•] + e		0.04	0.11					0.1	0.1
9	HTCNQF _n [•] = HTCNQF _n ⁺ + e		0.30	0.35					0.1	0.1
10	HTCNQF _n ⁺ + A ⁻ = TCNQF _n + HA				5.3×10 ⁶				1.0×10 ¹⁰	1.0×10 ¹⁰

The parameters used in the simulation are $\alpha = 0.50$, $T = 295^\circ\text{K}$, $D(\text{TCNQF}_2) = 2.1 \times 10^{-5} \text{ cm}^2.\text{s}^{-1}$, $D(\text{TCNQF}^{\cdot-}, \text{TCNQF}_2^{\cdot-}) = 1.9 \times 10^{-5} \text{ cm}^2.\text{s}^{-1}$, $D(\text{TCNQF}_2^{\cdot-}, \text{TCNQF}_2^{2\cdot-}) = 1.5 \times 10^{-5} \text{ cm}^2.\text{s}^{-1}$, $D(\text{TCNQF}) = 2.15 \times 10^{-5} \text{ cm}^2.\text{s}^{-1}$, $D(\text{HA}) = D(\text{A}^{\cdot-}) = 3 \times 10^{-5} \text{ cm}^2.\text{s}^{-1}$, area of electrode = 0.075 cm^2 , $R_u = 150 \Omega$, all potentials are versus Ag/Ag⁺. The electron transfers are assumed to be reversible, thus the k_s value of $0.1 \text{ cm}.\text{s}^{-1}$ was chosen. The k_f values were chosen to be fast but not exceed value for diffusion control limit of about $10^{10} \text{ M}^{-1}.\text{s}^{-1}$.

2.3.5. Comparison of the redox and acid base chemistry of the TCNQF_n derivatives

New data derived from voltammetric and spectroscopic studies on TCNQF and TCNQF₂ allow comparison to be made across the series of TCNQF_n derivatives. Firstly, all four derivatives undergo two diffusion-controlled, chemically and electrochemically reversible one electron reduction processed in acetonitrile. The reversible potentials for each of the TCNQF_n^{0/-} and TCNQF_n^{-/2-} couples shift positively with an increase in the level of fluorine substitution which was described by a linear relationship in the Hammett plot of the substituent effect and the redox potentials. Spectroscopic observation demonstrates an increased stability of the dianions in the order TCNQ²⁻, TCNQF²⁻, TCNQF₂²⁻ and TCNQF₄²⁻ on exposure to air to give decomposition product DCTC⁻ derivatives. This result also confirms the role of the strong electron-withdrawing effect associated with fluoro substitution in enhancing the stability of the dianions. Finally, voltammetric simulations provide data that allow a quantitative comparison of the protonation of the anions (Table 3). Thus, equilibrium constants for different protonation steps of monoanions and dianions in this specific condition decrease from TCNQ to TCNQF₄, i.e step 3 from 4.0×10^{-2} to 3.9×10^{-6} , step 5 from 1.0×10^8 to 3.0×10^3 and step 7 from 2.0×10^2 to 1. This outcome confirms the impact of an increase of the number of fluoro substituents on the stability of the anions, where TCNQF and TCNQF₂ are the intermediate between TCNQ and TCNQF₄.

Table 3. Summary of kinetics parameters of protonation steps

	TCNQ ^(a)	TCNQF ^(b)	TCNQF ₂ ^(b)	TCNQF ₄ ^(c)
$\text{TCNQF}_n^{\cdot-} + \text{HA} = \text{HTCNQF}_n^{\cdot-} + \text{A}^-$	4.0×10^{-2}	1.5×10^{-2}	8.8×10^{-4}	3.9×10^{-6}
$\text{TCNQF}_n^{2-} + \text{HA} = \text{HTCNQF}_n^- + \text{A}^-$	1.0×10^8	2.0×10^7	8.0×10^5	3.0×10^3
$\text{HTCNQF}_n^- + \text{HA} = \text{H}_2\text{TCNQF}_n + \text{A}^-$	2.0×10^2	5.0	1.0	1.0

a - ref 13¹³, *b* - this work, *c* - ref 12¹²

2.3.6. Vibrational spectroscopy of TCNQF_n (n=1,2)

The vibrational spectroscopy of TCNQ, its derivatives and their anions has been reported to be sensitive to their redox level. Although single crystal X-ray analysis provides an ideal approach to determine the redox level, growing crystals of TCNQ-based materials hasn't been always successful. Therefore understanding the spectroscopic behavior in both infrared and raman spectra would provide a useful tool to assess the reduction level of TCNQ moiety. Recently, calculation of the harmonic vibrational frequencies for TCNQF₄, TCNQF₄⁻ and TCNQF₄²⁻ has been reported with a large basis set and shown to provide an accurate band assignment of IR and Raman spectra of the three TCNQF₄ species and the diagnostics band to identify the redox level in unknown compounds.²⁰ Within the interest of this study, a DFT calculation has been performed on TCNQF₂ and TCNQF to produce a spectroscopic library on IR and Raman characteristic bands. However the mixing of $\delta(\text{C-H})$ and $\delta(\text{C-F})$ with $\nu(\text{C-C})$ becomes complicated in the case of TCNQF and TCNQF₂, compared to those of TCNQF₄ where there is lack of $\delta(\text{C-H})$ mode. The mixing between modes is even more complicated in reduced species, producing significantly new characteristic bands. The vibrational modes of neutral TCNQF_n and the trends in their anions can be summarized as followed:

1. The highest energy bands are C-H stretching modes, which absorb at approximately 3060 cm⁻¹ in both derivatives. Although this band shows a red shift in monoanion and dianion species, the intensity of this band in

both IR and Raman spectra in the reduced forms is low and would not be a good diagnostic for the change of redox level in the material.

2. The $\text{C}\equiv\text{N}$ stretching modes which are sensitive to redox level of TCNQF_n moieties are detected from 2234 to 2215 cm^{-1} . The band position is hardly distinguishable between TCNQF and TCNQF_2 . The $\text{C}\equiv\text{N}$ stretching band clearly shift to lower energy in TCNQF_n^- and TCNQF_n^{2-} . It shifts to approximately 40 cm^{-1} and 70 cm^{-1} lower in the monoanions and dianions, respectively.
3. A noticeable shift is of C=C stretching modes. The ring C=C stretching in neutral moiety absorb at approximately 1660 cm^{-1} and 1600 cm^{-1} for A_g and B_{2u} modes for TCNQF_2 and 1650 cm^{-1} and 1580 cm^{-1} for A_g and B_{2u} modes for TCNQF , respectively. Meanwhile, there is not much difference in the exocyclic C=C stretching band for both derivatives, where it appear at 1557 cm^{-1} (B_u) and 1481 cm^{-1} (A_g) in TCNQF_2 and at 1557 and 1477 cm^{-1} in TCNQF . These bands were found to also have a red-shift when TCNQF_n is reduced to TCNQF_n^- and TCNQF_n^{2-} . For TCNQF_2 , the ring C=C stretching bands were detected at 1645 (A_g) and 1638 (A_g) in monoanion, and 1553 (B_u) and 1509 (A_g) in dianion. For TCNQF , although the ring C=C B_u mode follows the same trend when it shifts to 1517 and 1443 cm^{-1} in the monoanion and dianion species, the A_g mode in TCNQF^{2-} does not show much difference to TCNQF^- , 1630 compared to 1628 cm^{-1} . A similar manner was observed with exocyclic C=C mode which was detected at 1472 cm^{-1} (B_u), 1403 cm^{-1} (A_g), TCNQF_2^- , 1416 cm^{-1} (B_u), 1353 cm^{-1} (A_g) TCNQF_2^{2-} , 1497 cm^{-1} (B_u), 1391 cm^{-1} (A_g) for TCNQF^- , 1307 (B_u), 1330 (A_g) for TCNQF^{2-} .
4. A series of stretching modes involves C-F and endocyclic C-C bonds were observed from about 1500 cm^{-1} to 1250 cm^{-1} . Most of the bands shift to lower energy region with the increase of redox level. Interestingly, the ... B_{3g} mode experiences a reversed trend with an increase of reduction level of TCNQF_n species with a blue shift from 1442 to 1501 and 1540 cm^{-1} in TCNQF_2 , TCNQF_2^- and TCNQF_2^{2-} respectively, and from 1443 to 1481 and 1537 cm^{-1} for TCNQF , TCNQF^- and TCNQF^{2-} respectively. This assembles the shifting behavior which was reported for TCNQF_4 recently.²⁰

5. The C-CN wing stretching modes absorb at approximately 1200 cm^{-1} and also shift toward lower energies in TCNQF_n^- and TCNQF_n^{2-} .
6. Interestingly, C-H out-of-plane bending modes were observed in calculated spectrum at 903 cm^{-1} (A_u) and 891 cm^{-1} (B_g) for TCNQF_2 and from 987 cm^{-1} (B_g), 904 cm^{-1} (B_u) and 844 cm^{-1} (A_u) to 850 cm^{-1} for TCNQF . All of the bands shift toward lower energies in reduced species.

Interestingly, the position of most of the vibrational bands in experimental IR and Raman spectra of TCNQF and TCNQF_2 are consistent with the calculations bands (Figure 14 and 15). This agreement confirms the accuracy of DFT calculation on these systems and hence, it can be used as a reference to determine the redox level of TCNQF_n species.

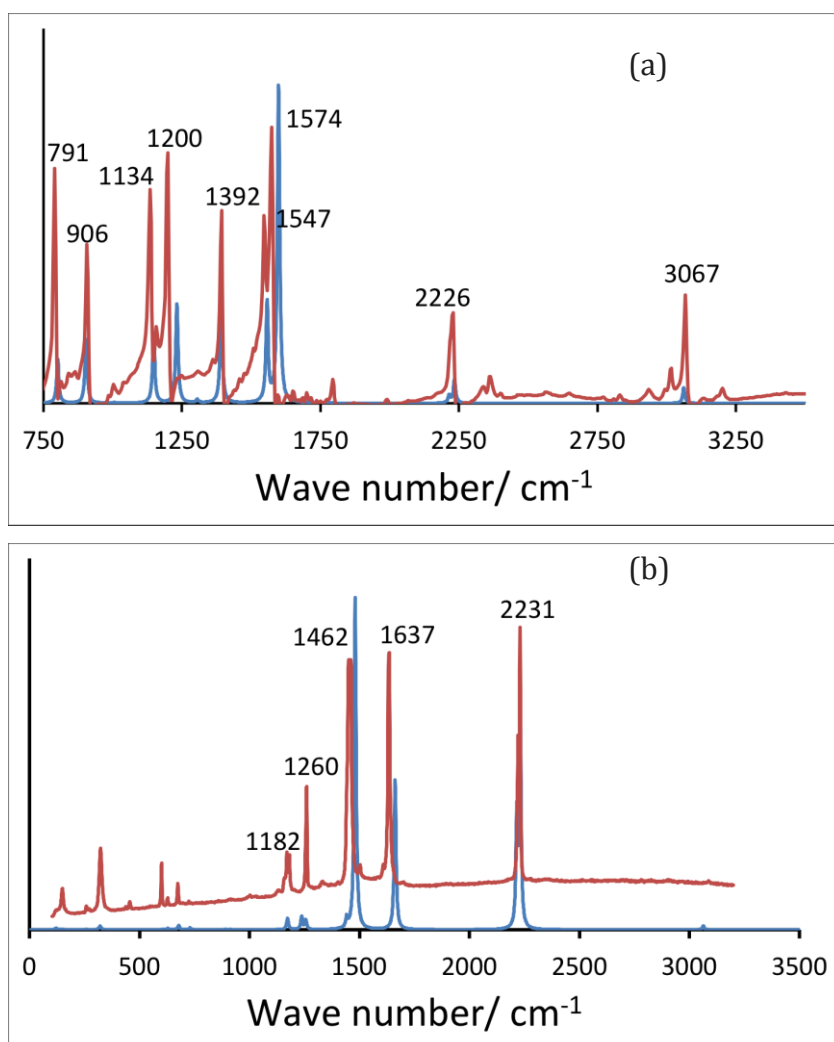


Figure 14. Calculated (blue) and experimental (red) (a) IR and (b) Raman spectra of neutral TCNQF_2

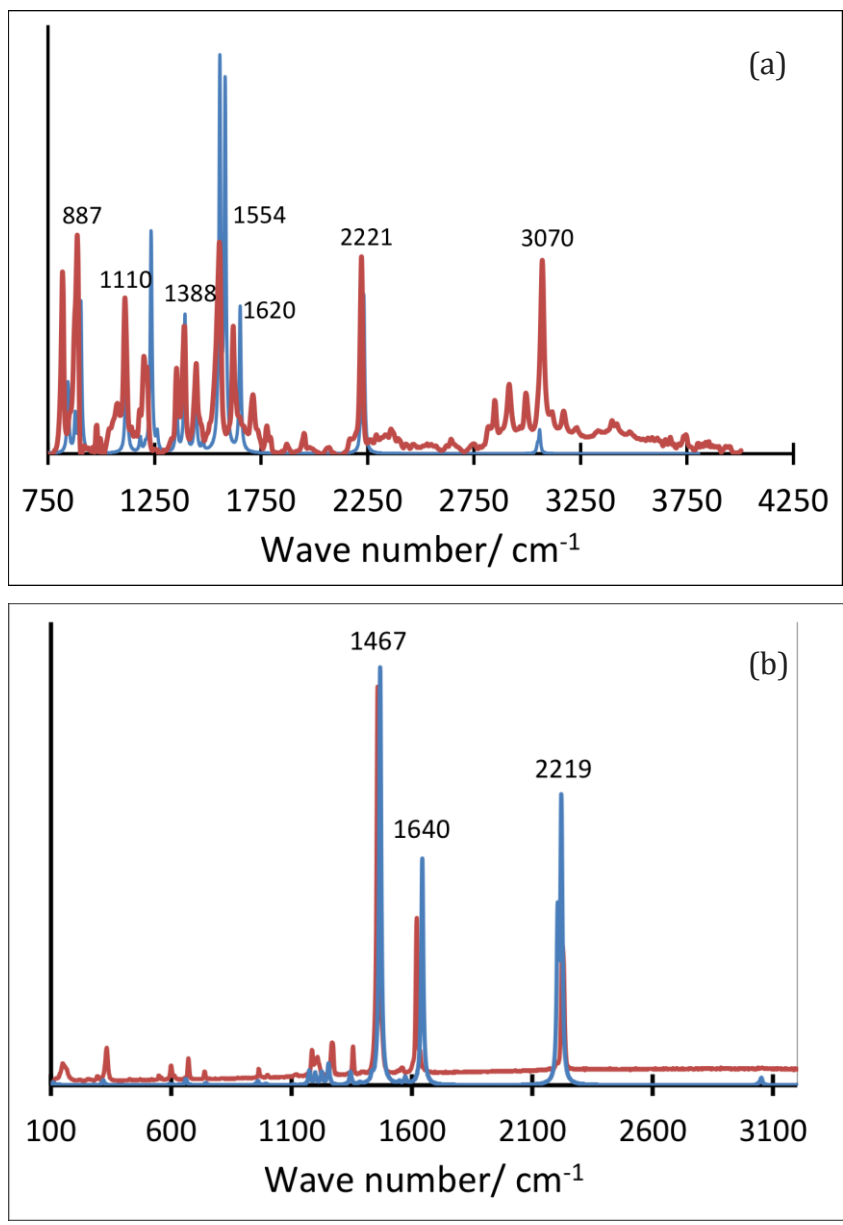


Figure 15. Calculated (blue) and experimental (red) (a) IR and (b) Raman spectra of neutral TCNQ

Table 4. Calculated harmonic vibrational frequencies of TCNQF₂, TCNQF₂⁻ and TCNQF₂²⁻ (above 800 cm⁻¹)

No.	Sym.	Mode	TCNQF ₂	IR	Ra	TCNQF ₂ ⁻	IR	Ra	TCNQF ₂ ²⁻	IR	Ra
1	A _g	C-H stretch	3063		w	3053		w	3033		w
2	B _u	C-H stretch	3062	w		3052	w		3032	w	
3	B _u	C≡N stretch	2234	w		2195	s		2168	m	
4	A _g	C≡N stretch	2231		s	2191		s	2156		s
5	A _g	C≡N stretch	2215		s	2159		s	2119		m
6	B _u	C≡N stretch	2215	w		2159	m		2118	s	
7	A _g	Ring C=C stretch	1662		s	1636		s	1638		s
8	B _u	Ring C=C stretch	1599	s		1530	s		1509	s	
9	B _u	Exocyclic C=C stretch	1557	m		1472	w		1416	m	
10	A _g	Exocyclic C=C stretch	1481		s	1403		s	1353		m
11	A _g	Ring C-C and C-F stretch	1442		w	1501		w	1540		-
12	B _u	Ring C-C and C-F stretch	1392	s		1338	m		1296	w	
13	B _u	Ring C-C and C-F stretch	1305	w		1290	w		1261	m	
14	A _g	Ring C-C and C-F stretch	1256		-	1252		w	1256		w
15	A _g	Ring C-C and C-F stretch	1237		w	1216		-	1217		-
16	A _g	C-CN stretch	1173		w	1186		w	1203		w
17	B _u	C-CN stretch	1148	m		1160	w		1179	w	
18	B _u	Ring mode	1005	-		1022	w		1163	w	
19	A _g	ring stretch	914		-	919		-	916		-
20	A _u	C-H out of plane bend	903	m		877	m		852	w	
21	B _g	C-H out of plane bend	891			865			841		
22	B _u	Ring mode	801	m		1220	m		1031	-	

Table 5. Calculated harmonic vibrational frequencies of TCNQF, TCNQF⁻ and TCNQF²⁻ (above 800 cm⁻¹)

No.	Sym.	Mode	TCNQF	IR	Ra	TCNQF ⁻	IR	Ra	TCNQF ²⁻	IR	Ra
1	A _g	C-H stretch	3061		w	3048		w	3024		w
2	B _u	C-H stretch	3058	w		3045	w		3018	w	
3	B _u	C-H stretch	3048	w		3030	w		3001	w	
4	B _u	C≡N stretch	2233	w		2189	s		2152	m	
5	A _g	C≡N stretch	2230		s	2193		s	2164		s
6	A _g	C≡N stretch	2216		s	2155		s	2114		s
7	B _u	C≡N stretch	2214	w		2158	s		2113	s	
8	A _g	Ring C=C stretch	1652	s	s	1628	w	s	1630	w	s
9	B _u	Ring C=C stretch	1582	s		1517	m		1307	w	
10	B _u	Exocyclic C=C stretch	1557	s		1497	w		1504	m	
11	A _g	Exocyclic C=C stretch	1477		s	1391		s	1330	-	s
12	A _g	Ring C-C and C-F stretch	1443		-	1481		-	1537		-
13	B _u	Ring C-C and C-F stretch	1393	s		1354	w		1504	s	
14	B _u	Ring C-C and C-F stretch	1354	m		1320	w		1291	-	
15	A _g	Ring C-C and C-F stretch	1263		-	1262		w	1256		w
16	B _u	Ring C-C and C-F stretch	1234	s		1218	m		1189	m	
17	A _g	C-CN stretch	1208		-	1209		-	1226		-
18	B _u	C-CN stretch	1189	w		1193	w		1210	-	
19	B _u	Ring mode	1118	s		1127	w		1124	-	
20	A _g	ring stretch	1002		-	1026		-	1041		-
21	B _u	C-H out of plane bend	987	-		942	-		901	-	
22	B _u	Ring stretch	969	-		987	-		997	-	
23	B _u	C-H out of plane bend	904	s		874	w		847	-	
24	B _u	ring stretch	878	w		878	-		872	-	

2.4. Conclusion

A variety of characterization methods for TCNQF and TCNQF₂ and their reduced forms have been reported, including electrochemistry, UV-Vis, IR and Raman spectroscopy. Electrochemically, these TCNQ derivatives undergo two well-resolved one-electron reversible reduction steps with the reversible potentials being in the order of $E_{\text{TCNQ}} > E_{\text{TCNQF}} > E_{\text{TCNQF}_2} > E_{\text{TCNQF}_4}$. The stability of TCNQF_n and its reduced anions was qualitatively assessed by UV-Vis spectra and showed a high stability of TCNQF_n neutral and TCNQF_n⁻ whereas TCNQF_n²⁻ decomposes rapidly to their DCTC analogues. TCNQF₄²⁻ is the most stable species and can be handled in air, while working with TCNQF²⁻ and TCNQF₂²⁻ requires dry box. Electrochemical data show that TCNQF_n²⁻ are strong bases and are readily protonated in the presence of TFA in two steps to form HTCNQF_n⁻ and H₂TCNQF_n. Simulations of cyclic voltammograms has been employed to understand the mechanism of the protonation reaction are in good agreement with experimental data. The equilibrium constants associated with the protonation steps decrease with the addition of fluorine atoms. This result supports the hypothesis on the enhancement of stability in fluorinated derivatives relative to parent TCNQ. A series of vibrational bands in IR and Raman spectra were generated from DFT calculations of TCNQF_n and their anions. These assignments will assist the characterization of newly synthesized TCNQF_n materials.

References

- (1) Harrer, W.; Grampp, G.; Jaenicke, W. *Chemical Physics Letters* **1984**, *112*, 263.
- (2) Jérôme, D. *Chemical Reviews* **2004**, *104*, 5565.
- (3) Kepler, R. G.; Bierstedt, P. E.; Merrifield, R. E. *Physical Review Letters* **1960**, *5*, 503.
- (4) Le, T.; O'Mullane, A.; Martin, L.; Bond, A. *J. Solid State Chem.* **2011**, *15*, 2293.
- (5) Le, T. H.; Nafady, A.; Lu, J.; Peleckis, G.; Bond, A. M.; Martin, L. L. *Eur. J. Inorg. Chem.* **2012**, 2889.
- (6) Le, T. H.; Nafady, A.; Vo, N. T.; Elliott, R. W.; Hudson, T. A.; Robson, R.; Abrahams, B. F.; Martin, L. L.; Bond, A. M. *Inorganic Chemistry* **2014**, *53*, 3230.
- (7) Lopez, N.; Zhao, H. H.; Prosvirin, A. V.; Wernsdorfer, W.; Dunbar, K. R. *Dalton Trans.* **2010**, *39*, 4341.
- (8) O'Kane, S. A.; Clérac, R.; Zhao, H.; Ouyang, X.; Galán-Mascarós, J. R.; Heintz, R.; Dunbar, K. R. *Journal of Solid State Chemistry* **2000**, *152*, 159.
- (9) Brown, H. C.; Okamoto, Y. *Journal of the American Chemical Society* **1958**, *80*, 4979.
- (10) Wheland, R. C.; Gillson, J. L. *Journal of the American Chemical Society* **1976**, *98*, 3916.
- (11) Alligrant, T. M.; Hackett, J. C.; Alvarez, J. C. *Electrochimica Acta* **2010**, *55*, 6507.
- (12) Le, T. H.; Nafady, A.; Qu, X.; Martin, L. L.; Bond, A. M. *Analytical Chemistry* **2011**, *83*, 6731.
- (13) Le, T. H.; Nafady, A.; Qu, X.; Bond, A. M.; Martin, L. L. *Analytical Chemistry* **2012**, *84*, 2343.
- (14) Becke, A. D. *Journal of Chemical Physics* **1993**, *98*, 5648.
- (15) Lee, C. T.; Yang, W. T.; Parr, R. G. *Physical Review B* **1988**, *37*, 785.
- (16) Curtiss, L. A.; Raghavachari, K.; Redfern, P. C.; Rassolov, V.; Pople, J. A. *Journal of Chemical Physics* **1998**, *109*, 7764.
- (17) Curtiss, L. A.; Redfern, P. C.; Raghavachari, K. *Journal of Chemical Physics* **2007**, *126*.
- (18) Curtiss, L. A.; Redfern, P. C.; Raghavachari, K.; Pople, J. A. *The Journal of Chemical Physics* **2001**, *114*, 108.

- (19) Scott, A. P.; Radom, L. *The Journal of Physical Chemistry* **1996**, *100*, 16502.
- (20) Haworth, N. L.; Lu, J.; Vo, N.; Le, T. H.; Thompson, C. D.; Bond, A. M.; Martin, L. L. *ChemPlusChem* **2014**, *79*, 962.
- (21) Girlando, A.; Pecile, C. *Spectrochimica Acta Part A: Molecular Spectroscopy* **1973**, *29*, 1859.
- (22) Emge, T. J.; Maxfield, M.; Cowan, D. O.; Kistenmacher, T. J. *Molecular Crystals and Liquid Crystals* **1981**, *65*, 161.
- (23) Mitchell Wiygul, F.; Ferraris, J. P.; Emge, T. J.; Kistenmacher, T. J. *Molecular Crystals and Liquid Crystals* **1981**, *78*, 279.
- (24) Bard, A. J.; Faulkner, L. R. *Electrochemical Methods: Fundamentals and Applications*; 2nd ed.; John Wiley & Sons, Inc.: New York, 2001.
- (25) Ekanayake, C. B.; Wijesinghe, M. B.; Zoski, C. G. *Analytical Chemistry* **2013**, *85*, 4022.
- (26) Le, T. H.; Lu, J.; Bond, A. M.; Martin, L. L. *Inorganica Chimica Acta* **2013**, *395*, 252.
- (27) Jonkman, H. T.; Kommandeur, J. *Chemical Physics Letters* **1972**, *15*, 496.
- (28) Gossel, M. C.; Duke, A. J.; Hibbert, D. B.; Lewis, I. K.; Seddon, E. A.; Horton, P. N.; Weston, S. C. *Chem. Mater.* **2000**, *12*, 2319.

Chapter 3

Electrochemistry of TCNQF₂ in acetonitrile in the presence of [Cu(CH₃CN)₄]⁺ - The formation of CuTCNQF₂ and its catalytic activity

Nguyen T. Vo, Lisandra L. Martin*, Alan M. Bond*

School of Chemistry, Monash University, Clayton, Victoria 3800, Australia

* Corresponding Authors: Lisa.Martin@monash.edu, Alan.Bond@monash.edu

Abstract Electrochemistry of the two redox processes of TCNQF₂ in the presence of [Cu(MeCN)₄]⁺ has been investigated and revealed the formation of the mono- and dianionic-based solids. CuTCNQF₂ has been synthesized chemically and electrochemically. For the chemical synthesis, CuTCNQF₂ was formed by the reaction between TCNQF₂ and CuI in MeCN, while in the latter approach, TCNQF₂⁻ was formed by bulk reduction electrolysis and [Cu(MeCN)₄]⁺ was then introduced. A dark blue precipitate was obtained using both methods. Spectroscopic characterisation of these products showed that they were identical. Powder X-Ray diffraction of CuTCNQF₂ describes an analogous pattern with CuTCNQ phase II. The conductivity was also examined on a film of CuTCNQF₂ on FTO glass revealed a conductivity of 6.0×10^{-6} S.cm⁻¹.

3.1. Introduction

Organic charge-transfer materials of TCNQ (TCNQ = 7,7,8,8-tetracyanoquinodimethane) have been widely investigated and exhibit a range of important properties.^{1,2} For example, charge-transfer complexes of TCNQ (see scheme in Figure 1) with transition metals ions such as copper or silver are semi-conductors, which have been exploited in optical, electrical and magnetic devices.³⁻⁸ TCNQF₄-based materials (TCNQF₄ = 2,3,5,6-tetrafluoro-7,7,8,8-tetracyanoquinodimethane) have also been studied recently.^{9,10} The presence of four fluorine atoms (see scheme in Figure 1) enhances the electron affinity of TCNQF₄, which facilitates reduction and increases the stability of the anions, especially the dianion. This property has offered a number of TCNQF₄²⁻-based materials have been electrochemically generated in the air,¹¹⁻¹⁴ while those of TCNQ²⁻ needed to be synthesized anaerobically.¹⁵⁻¹⁷ The enhanced stability of the

fluorinated derivative offers the prospect of new dianion materials with interesting properties. Dihalogenated dibromo, dichloro and difluoro TCNQF_x complexes also have been reported,¹⁸⁻²¹ but the difluorinated TCNQF₂ (see scheme in Figure 1) are relative rare.

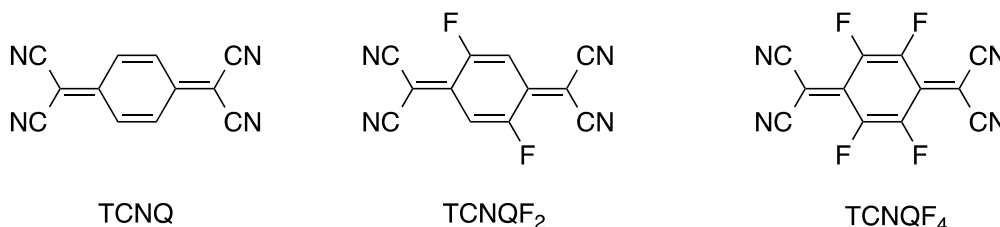


Figure 1: Structures of TCNQ, TCNQF₄ and TCNQF₂

TCNQF₂ (TCNQF₂ = 2,5-difluoro-7,7,8,8-tetracyanoquinodimethane) (Figure 1) based materials are expected to possess intermediate electrical properties between TCNQ and TCNQF₄. Its electron affinity is 3.02 eV, which lies midway between that of TCNQ and TCNQF₄, which are 2.85 and 3.20 eV, respectively.^{22,23} TCNQF₂⁻ salts of TTF derivatives have been reported¹⁹⁻²¹ and TCNQF₂-nucleobase, cytosine, material was synthesized and shown to be a fully ionic material derived from the monoanion TCNQF₂⁻ and cytosine cation.²⁴ However, studies on the interaction between TCNQF₂ and transition metals are limited. In this study, the reductive electrochemistry of TCNQF₂ in the presence of [Cu(CH₃CN)₄]⁺ is reported in acetonitrile. The formation of new TCNQF₂⁻-based material will be described along with their synthesis and spectroscopic characterization.

3.2. Experimental

3.2.1. Chemicals

TCNQF₂ (98%, TCI Tokyo), [Cu(CH₃CN)₄]PF₆ (98%, Aldrich), acetonitrile (HPLC grade, Omnisolv), isopropanol (BHD) and acetone (suprasolv, Merck KGaA) were used as received from the manufacturer. Bu₄NPF₆ (Aldrich), used as the supporting electrolyte in electrochemical studies, was recrystallized twice from 96% ethanol (Merck) and then dried at 100°C under vacuum for 24 hours prior to use.

3.2.2. Electrochemistry

Voltammetric experiments were studied at room temperature using a Bioanalytical Systems (BAS) 100W workstation. A standard three electrode cell

configuration, comprising a glassy carbon (GC, 1 mm diameter) working electrode, a Ag/Ag⁺ (1.0 mM Ag⁺) reference electrode (RE) and a 1.0 mm diameter platinum wire counter electrode, was employed in those experiments. Prior to each experiment the working electrode was polished with 0.3 μm Al₂O₃ slurry using polishing cloth, rinsed with water followed by sonication in an ultra sonic bath for 30 seconds and dried under a stream of nitrogen. The RE was constructed from Ag wire in contact with acetonitrile solution (0.1 M Bu₄NPF₆) containing 1.0 mM AgNO₃ and separated from the test solution by a salt bridge. The potential of this reference electrode was -124 mV vs the ferrocene/ferrocenium (Fc^{0/+}) couple. All solutions were purged with nitrogen gas for at least 10 min and a stream of nitrogen was maintained above the solutions during the course of the voltammetric experiments. In bulk electrolysis experiments, a three-compartments cell was used with each of the large area Pt mesh working electrode, Ag/AgCl reference electrode and Pt mesh counter electrode.

3.2.3. Synthesis of CuTCNQF₂

CuTCNQF₂ was prepared electrochemically as followed. Initially a solution of TCNQF₂⁻ was prepared quantitatively by the bulk reduction electrolysis of 10 ml solution containing 5.0 mM TCNQF₂ in acetonitrile (0.1 M Bu₄NPF₆). The potential of the Pt working electrode was held at -100 mV vs Ag/Ag⁺ until the current reached 1% of the initial value. A dark blue precipitate formed immediately upon an addition of a 0.75 ml solution of 100 mM [Cu(CH₃CN)₄]⁺. After stirring for 10 mins, the solid was collected by filtration and washed several times with CH₃CN. Finally, the solid was dried under vacuum overnight before further characterization.

The solid was also chemically synthesized by a reaction between TCNQF₂ and CuI (1:1.5 stoichiometric ratio) in acetonitrile for 3 hours. The resulted dark blue solid was filtered, washed with CH₃CN and dried as described above before characterization.

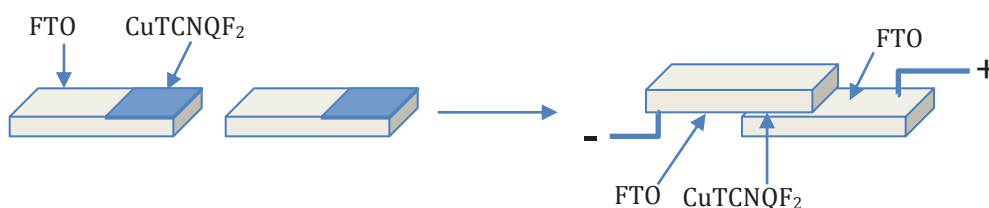
3.2.4. Conductivity measurement of CuTCNQF₂

The conductivity of CuTCNQF₂ was examined on a CuTCNQF₂ film formed on a FTO-coated glass. A Cu film was firstly sputter-coated with a Quorum Q150TS sputter coater machine over the area of 1.0 cm × 1.0 cm onto a FTO-coated glass

with an area of 1.0 cm × 3.0 cm. It was then soaked in an acetonitrile solution containing 10 mM of TCNQF₂ for 12 hours, and a CuTCNQF₂ film was formed as describe in equation 1.



The samples were rinsed briefly with acetonitrile to remove excess TCNQF₂ followed by copious water. They were dried under nitrogen stream and store under vacuum. For conductivity measurement, two CuTCNQF₂-coated FTO glasses were stacked together so that the two CuTCNQF₂ films are in contact. The FTO glasses were then clamped carefully to minimize force (see Scheme 1). Constant potential measurements were performed for 60 s at potentials from 50 to 500 mV with 50 mV intervals. The resistance (R) was calculated as $R=U/I$ (in which U (V) is the applied potential and I (A) is the measured current). The DC conductivity σ was calculated from the relationship $\sigma =t/R.S$ where t (cm) is the thickness of the layer formed by two CuTCNQF₂ film, and S (cm²) is the cross-sectional area. A VMP3 multi-channel potentiostat from BioLogic Instruments was used for the resistance measurements.



Scheme 1. Configuration of a conductivity measurement

The film thickness was measured using VeeCo Dektak 150 profilometer.

3.2.5. Other instrumentations

UV-Vis spectra were recorded with a Varian Cary 5000 UV-Vis NIR spectrophotometer with a 1.0 cm path length quartz cuvette. A Varian UMA600 IR microscope and FTS7000 optics bench using 128 scans and a resolution of 8 cm⁻¹ was used for IR spectra. Raman spectra were recorded on a Renishaw Invia Raman spectrograph with an Argon ion laser excitation at 633 nm. After being coated with Ir, SEM images were collected with a FEI Nova NanoSEM 450 FEGSEM

instrumentation using an accelerating voltage of 5.0 kV. The X-ray powder diffraction (XRD) pattern was collected using the Oxford Diffraction Suppernova diffractometer.

3.3. Result and discussion

3.3.1. Cyclic voltammetry of the TCNQF₂^{0/-} process in the presence of [Cu(CH₃CN)₄]⁺

In acetonitrile (0.1 M Bu₄NPF₆) solution, [Cu(CH₃CN)₄]⁺ can be reduced to metal and oxidized to Cu²⁺ (Figure 2a). The Cu⁺ to copper metal process at -900 mV and its counterpart Cu to Cu⁺ stripping process at -300 mV seen in the cyclic voltammogram correspond to the Cu^{+/0} redox couple, while the oxidation process at 800 mV and its reduction counterpart at -650 mV represents the Cu^{+/2+} couple. A comparison of cyclic voltammograms for [Cu(CH₃CN)₄]⁺ and TCNQF₂ in acetonitrile (see Figure 2) reveals that the potentials for reduction and oxidation of [Cu(CH₃CN)₄]⁺ are well-separated from the two reversible TCNQF₂^{0/-} and TCNQF₂^{-/2-} reduction steps. Therefore, the electrochemical reduction of TCNQF₂ in the presence of [Cu(CH₃CN)₄]⁺ can be investigated provided the applied potential lies in between the reduction and oxidation of [Cu(CH₃CN)₄]⁺.

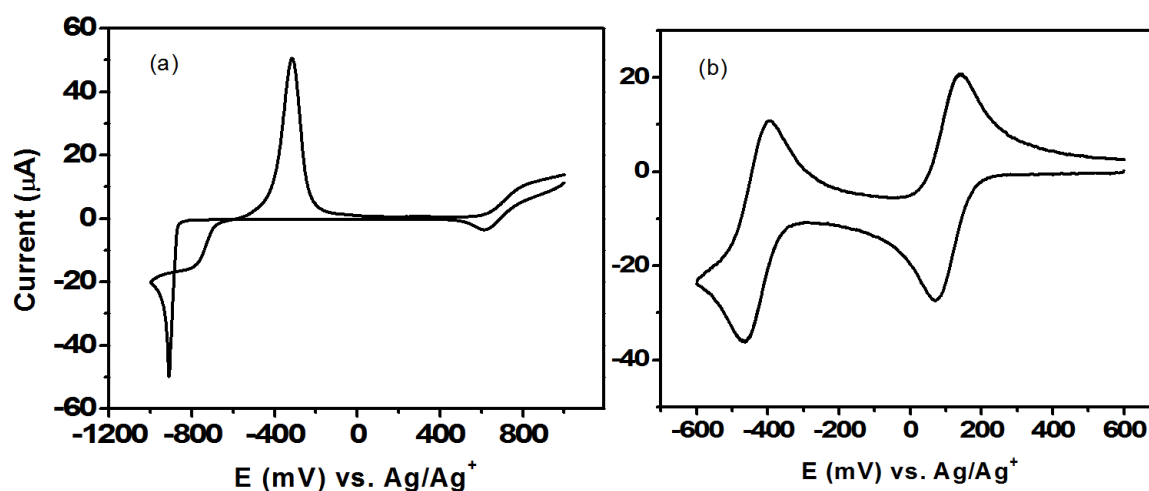


Figure 2: Cyclic voltammograms obtained at a scan rate of 100 mV.s⁻¹ in acetonitrile (0.1 M Bu₄NPF₆) for (a) 10.0 mM [Cu(CH₃CN)₄]⁺ with a 1 mm diameter GC electrode, (b) 1.0 mM TCNQF₂ with a 3 mm diameter GC electrode

Cyclic voltammograms for a series of solutions in acetonitrile (0.1 M Bu₄NPF₆) containing mixture of TCNQF₂ and [Cu(CH₃CN)₄]⁺ were recorded at a scan rate of

50 $\text{mV}\cdot\text{s}^{-1}$. For TCNQF₂ (1.0 mM), in the presence of either 5.0 mM or 10.0 mM [Cu(CH₃CN)₄]⁺, when scanning negatively, the TCNQF₂/TCNQF₂⁻ process retained its reversible diffusional characteristic (Figure 3a). However, upon increasing the concentration of TCNQF₂ to 2.0 mM, in the presence of 10.0 mM of [Cu(CH₃CN)₄]⁺ and scanning the potential showing only the TCNQF₂^{0/-} process, although the first reduction process is not modified, a new oxidation process at 385 mV, named Ox1 in Figure 3, was observed on the positive potential scan (Figure 3b). Process Ox1 was enhanced in solution containing 5.0 mM TCNQF₂ and 10.0 mM [Cu(CH₃CN)₄]⁺ (Figure 3b). On cycling the potential, the current ratio of i_{ox}/i_{red} for the TCNQF₂^{0/-} process decreased to less than unity as the oxidative current gradually decreased (Figure S1). Simultaneously, the current magnitude of Ox1 peak increased on cycling the potential. These observations imply that a chemical step is coupled to the TCNQF₂/TCNQF₂⁻ process, which consumes TCNQF₂⁻ as evidenced by the decrease of the oxidation current, when the potential was switch at -100 mV. Also, the new compound formed is electro-active and is oxidized at more positive potentials than that for TCNQF₂/TCNQF₂⁻ process (see process Ox1 in Figure 3b). After completion of the experiment a dark blue solid remained on the GC electrode surface.

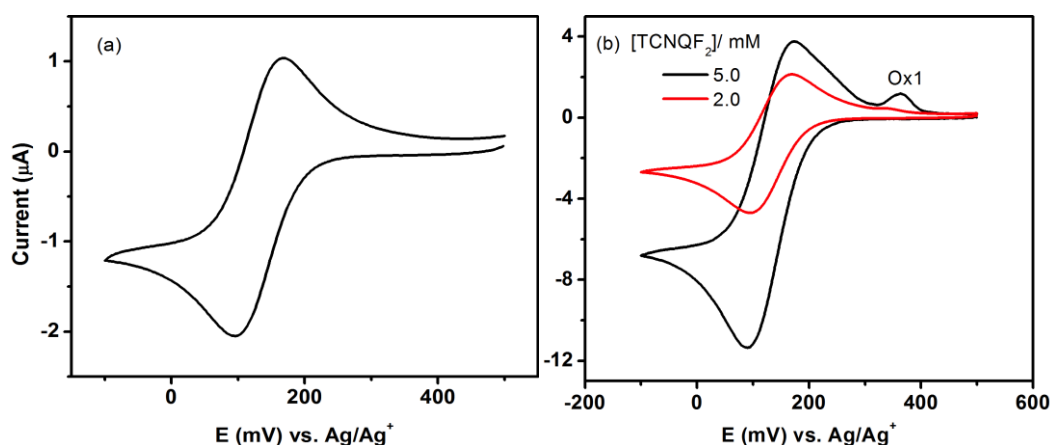


Figure 3: Cyclic voltammograms obtained at a scan rate of 50 $\text{mV}\cdot\text{s}^{-1}$ in acetonitrile (0.1M Bu₄NPF₆) with a 1 mm diameter GC electrode for (a) 1.0 mM TCNQF₂ in the presence of 10.0 mM of [Cu(CH₃CN)₄]⁺, (b) designated TCNQF₂ concentration in the presence of 10.0 mM of [Cu(CH₃CN)₄]⁺

Effect of scan rate

Figure 4a shows cyclic voltammograms in CH₃CN (0.1 M Bu₄NPF₆) containing 5.0 mM of TCNQF₂ and 10.0 mM of [Cu(CH₃CN)₄]⁺ in CH₃CN (0.1 M Bu₄NPF₆) at scan rates in a range 20-100 mV·s⁻¹. Process Ox1 at ~ 385 mV, which was detected at slow scan rates of 20 and 50 mV·s⁻¹, diminished at a scan rates ≥ 100 mV·s⁻¹. Moreover, at a slow scan rate 20 mV·s⁻¹, a shoulder is visible on the TCNQF₂⁻ oxidation peak, Ox2, implying another oxidation process occurs. Cu-TCNQ based materials can exist two phases with different morphologies.²⁵⁻²⁷ Thus CuTCNQF₂ also may exist in two phases. The existence of two phases of CuTCNQ has been reported in voltammetric experiment in acetonitrile previously when cycling the potential multiple times with a TCNQ-modified GC electrode in aqueous solution containing Cu²⁺.²⁷ In acetonitrile, two distinguishable reduction processes were observed, however, they are both associated to the formation of only CuTCNQ phase I during the voltammetric experiment.²⁸ Either branches of needle crystals were formed via nucleation-growth mechanism at discrete site or a continuous film of CuTCNQ was formed on the electrode surface. These two processes are independent to each other depending on the reduction potential. However, inspection the voltammograms in this study suggests that there is a conversion between two solids of CuTCNQF₂ during voltammetric experiment.

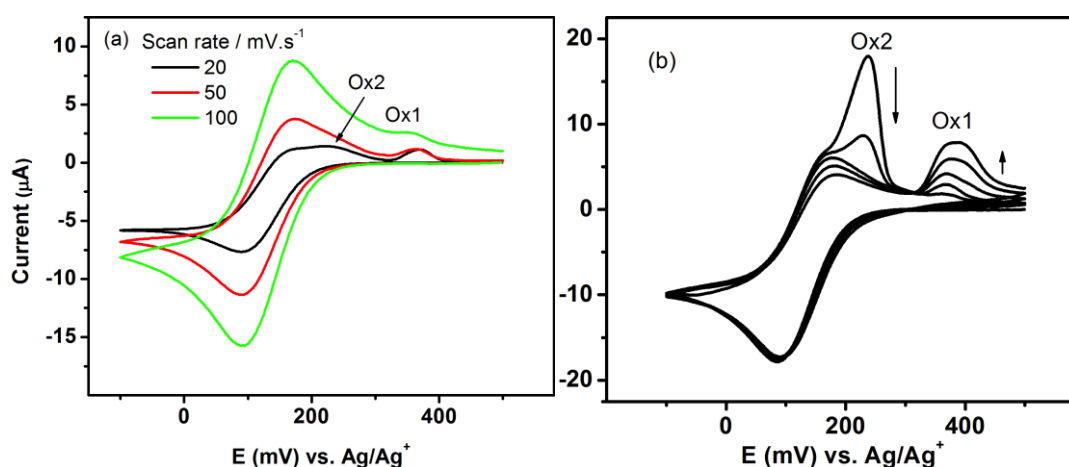


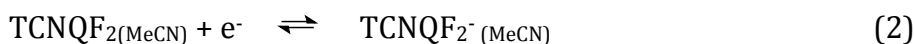
Figure 4. Cyclic voltammograms obtained with a 1 mm diameter GC electrode in acetonitrile (0.1M Bu₄NPF₆) for (a) 5.0 mM TCNQF₂ in the presence of 10 mM [Cu(CH₃CN)₄]⁺ at designated scan rates, (b) 8.0 mM TCNQF₂ in the presence of 8.0 mM [Cu(CH₃CN)₄]⁺ at a scan rate of 50 mV s⁻¹

Phases of CuTCNQF₂

In order to probe the origin of the second oxidation process a higher concentration solution containing 8.0 mM of TCNQF₂ and 8.0 mM of [Cu(CH₃CN)₄]⁺ was studied and the resultant cyclic voltammograms were shown in Figure 4b. At a scan rate of 50mV·s⁻¹, the anodic scan of the first cycle is dominated by the stripping peak Ox2 at 250 mV, with process Ox1 at 385 mV being less significant. However, on cycling the potential the magnitude of the Ox2 peak current decreases, and is not detected from the 3rd cycle. Simultaneously, the Ox1 peak current gradually increases in magnitude on cycling of the potential.

At the higher scan rate of 100 mV·s⁻¹, the Ox2 process was not detected (Figure S2). The clear scan rate dependence of Ox1 and Ox2 provides evidence for the existence of two different phases or morphologies of CuTCNQF₂ that are kinetic controlled with process Ox2 being derived from the thermodynamic favoured phase and only detected at slow scan rate, and Ox1 process corresponds to a kinetic favoured product, being dominant at high scan rate.

The mechanism for reduction of TCNQF₂ to TCNQF₂⁻ in the presence of Cu(MeCN)₄⁺ can be written as follows:



3.3.2. Cyclic Voltammetry of TCNQF₂ in the presence of [Cu(CH₃CN)₄]⁺, the second redox process

The second reduction step associated with the TCNQF₂^{-/2-} process was also investigated in the presence of [Cu(CH₃CN)₄]⁺ by scanning potential to more negative (600 to -600 mV). In order to prevent the precipitation of insoluble Cu-TCNQF₂⁻ material in the first reduction step, lower concentrations of TCNQF₂ and [Cu(CH₃CN)₄]⁺ were now used. Under the condition of 1.0 mM TCNQF₂ and 2.0 mM [Cu(CH₃CN)₄]⁺ and with a slow scan rate of 20 mV·s⁻¹, the reversible TCNQF₂^{-/0}

process was observed when the potential was switched at -120 mV and reversed before the second reduction of TCNQF_2^- to TCNQF_2^{2-} (Figure 5). That is no black CuTCNQF_2 material precipitate on the electrode surface, as in the case when the concentration of $[\text{Cu}(\text{CH}_3\text{CN})_4]^+$ are higher. These diluted conditions allow the second reduction step to be investigated without any interference from CuTCNQF_2 precipitate.

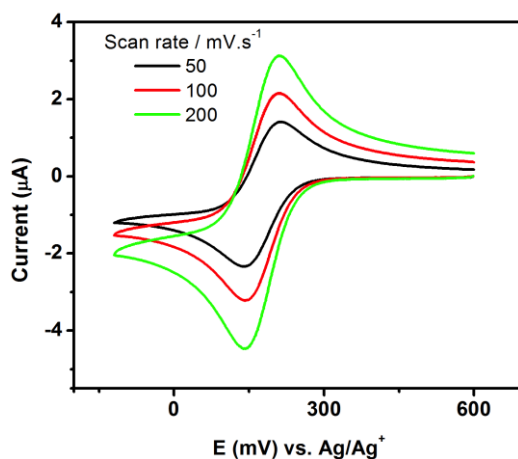


Figure 5. Cyclic voltammogram obtained with a 1 mm diameter GC electrode in acetonitrile (0.1M Bu_4NPF_6) containing 1 mM TCNQF_2^- and 2 mM $[\text{Cu}(\text{CH}_3\text{CN})_4]^+$ at at designated scan rate for the $\text{TCNQF}_2^{0/-}$ process.

The voltammogram of the $\text{TCNQF}_2^-/\text{TCNQF}_2^{2-}$ process in the presence of $[\text{Cu}(\text{CH}_3\text{CN})_4]^+$ changes dramatically over the wider range of the scanning potential from 600 mV to -600 mV. At a slow scan rate of 20 mV s^{-1} , the reduction of TCNQF_2^- to TCNQF_2^{2-} seen at -448 mV in the absence of $[\text{Cu}(\text{CH}_3\text{CN})_4]^+$ (*cf.* Figure 2) shifts to -275 mV in the presence of $[\text{Cu}(\text{CH}_3\text{CN})_4]^+$ (Figure 6a). Thus, it is now much easier to reduce the TCNQF_2^- to TCNQF_2^{2-} . Furthermore, a sharp oxidation process (Ox3) was observed at 169 mV when the potential was reversed, which replaced TCNQF_2^{2-} to TCNQF_2^- oxidation process that was at -373 mV (Figure 2). Once again, this voltametric behaviour strongly supported a chemical step was also involved with the second redox process.

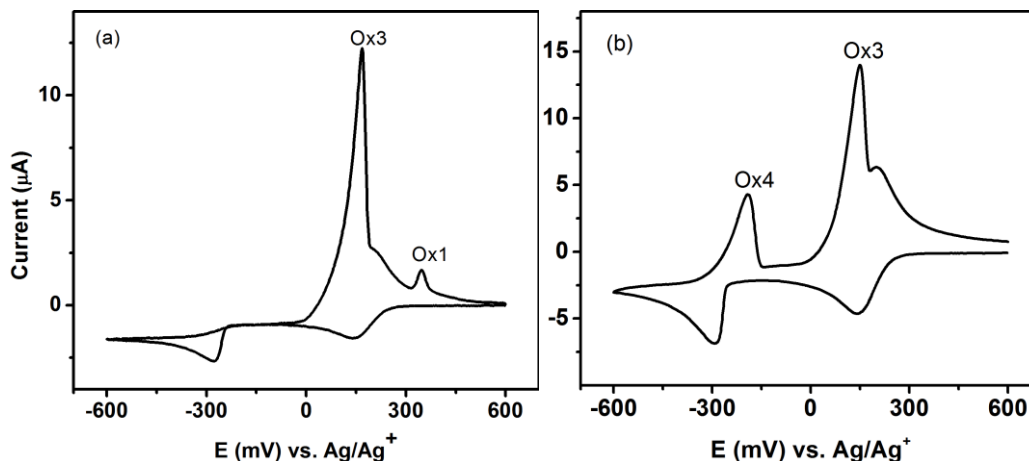
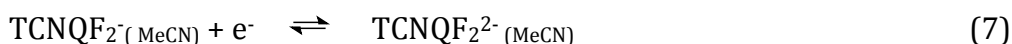
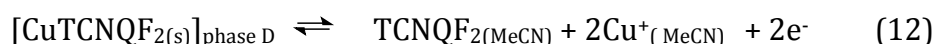


Figure 6. Cyclic voltammograms obtained with a 1 mm diameter GC electrode in acetonitrile (0.1M Bu₄NPF₆) containing 1 mM TCNQF₂ and 2 mM [Cu(CH₃CN)₄]⁺ at a scan rate of (a) 20 mV s⁻¹, and (b) 200 mV s⁻¹.

The sharp oxidation process at 169 mV (Ox3) has the characteristic of a 'stripping process' derived from oxidation of a solid Cu-TCNQF₂²⁻ material formed by reaction of TCNQF₂²⁻ with Cu⁺ on the electrode surface presumably to TCNQF₂⁻ and Cu⁺. In Figure 6a, a shoulder presents at 210 mV, which was the solution phase oxidation of TCNQF₂⁻ to TCNQF₂ and was not affected by Ox3. Interestingly, a second sharp oxidation wave was also observed at 348 mV (Ox1), which consistent with the oxidation process Ox1 of Cu-TCNQF_{2(s)} to Cu⁺ and TCNQF₂ observed previously. This behaviour can be explained if Cu-TCNQF₂²⁻ solid was oxidized to formed Cu-TCNQF_{2(s)}. On increasing the scan rate, a new oxidation process (Ox4) appears Ox4 at -192 mV (Figure 6b), which is consistent with the existence of two phases of Cu-TCNQF₂²⁻ based material. Similar process was observed for the Cu-TCNQF₄²⁻ materials,¹² in which one phase is thermodynamically favoured and the other is kinetic favoured, named phase C and phase D.

The mechanism for the reduction of TCNQF₂ to TCNQF₂²⁻ in the presence of [Cu(CH₃CN)₄]⁺ this process is proposed to be as follow;





The scan rate dependence of the anodic processes (Figure 7) illustrates well the inter-relationship of materials with a decrease in the Ox3 current and the simultaneous loss of the Ox1 wave. Thus, at scan rates $\geq 200 \text{ mV}\cdot\text{s}^{-1}$, there are only two major peaks in the voltammogram during the oxidative sweep, the Ox4 and Ox3 peaks. These results suggest that only the phase C solid can be oxidized to $\text{CuTCNQF}_2(\text{s})$ in solid state at the electrode surface, not both phases.

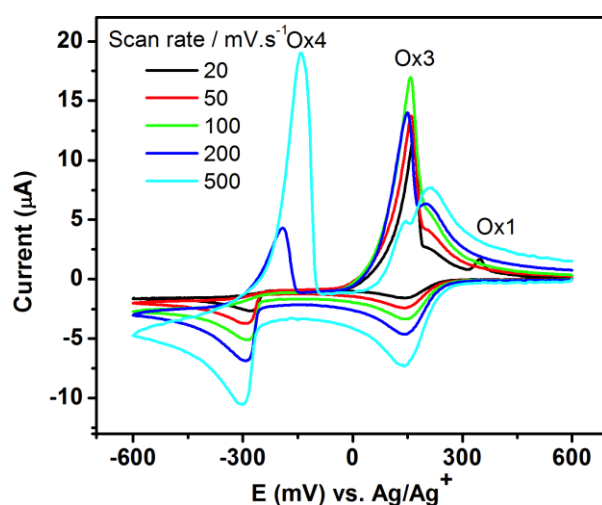


Figure 7. Cyclic voltammograms with a 1 mm diameter GC electrode in acetonitrile (0.1M Bu_4NPF_6) containing 1.0 mM TCNQF_2 and 2.0 mM $[\text{Cu}(\text{CH}_3\text{CN})_4]^+$ at designated scan rates.

Data are almost independent of electrode material (gold and platinum, data not shown).

3.3.3. Cyclic voltammetry of CuTCNQF_2^{2-} solid in the presence of $[\text{Cu}(\text{CH}_3\text{CN})_4]^+$

In order to further probe the solid-solid transformation of CuTCNQF_2^{2-} and CuTCNQF_2 , experiments were performed in CH_3CN (0.1 M Bu_4NPF_6) containing 50.0 mM $[\text{Cu}(\text{CH}_3\text{CN})_4]^+$, where solid CuTCNQF_2^{2-} was deposited on the electrode surface, and then the potential was swept positively. Representative voltammograms are shown in Figure 8.

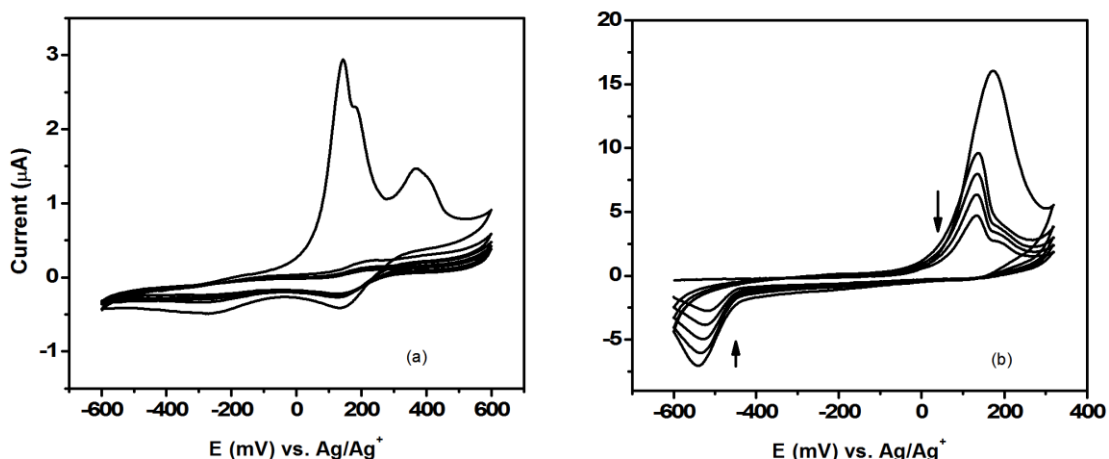


Figure 8. Cyclic voltammogram of Cu-TCNQF₂²⁻ material deposited onto a 3 mm diameter GC electrode in acetonitrile (0.1 M Bu₄NPF₆) containing 50.0 mM [Cu(CH₃CN)₄]⁺ at a scan rate of 50 mV s⁻¹ with the potential scan from -600 to (a) 600 mV, (b) 350 mV.

When the potential was cycled from the initial value of -600 mV to 600 mV and the concentration and that of [Cu(CH₃CN)₄]⁺ are not high enough to exceed the solubility of the Cu-TCNQF₂²⁻ solid, the first cycle contained a number of dominant oxidation processes. These processes diminished with subsequent scans until ultimately only the two TCNQ^{0/-/-2} diffusion controlled processes resembling that of neutral TCNQF₂ is generated. However, when the potential is switched at 300 mV, and hence before the oxidation of TCNQF₂⁻ to TCNQF₂, the solid-solid transformation of CuTCNQF₂ and Cu₂TCNQF₂ is detected. This solid-solid redox process remains clear for several cycles of potential, although the current magnitude decreases as Cu-TCNQF₂ solids slowly dissolve. Thus when the same experiment was performed but in the absence of [Cu(CH₃CN)₄]⁺, no oxidative current could be detected because now the dissolution is more rapid.

3.3.4. Powder X-Ray Crystallography

Although repeated attempts to grow single crystal of CuTCNQF₂ with high quality for single-crystal diffraction study were unsuccessful, XRD powder pattern of chemically synthesized material was obtained. Diffraction pattern of CuTCNQF₂ with broad peaks was compared to single crystal XRD pattern of phase II of CuTCNQ material as shown in Figure 9. It is interesting that although the peaks are

broadened, the position of most of them are almost identical to those of phase II CuTCNQ which crystallized in a monoclinic unit cell.²⁶

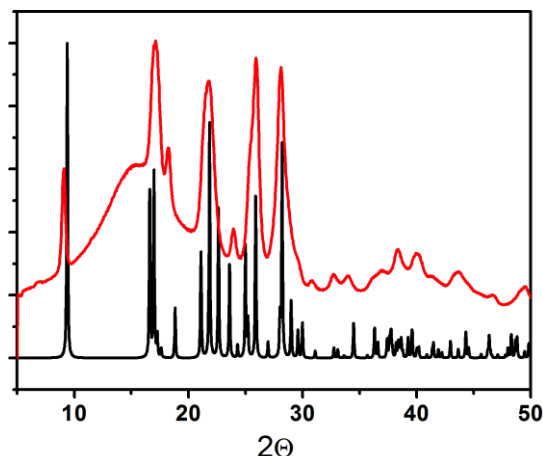


Figure 9. X-Ray diffraction pattern of CuTCNQF₂ synthesized chemically (red) and single crystal of phase II of CuTCNQF (black)²⁶

3.3.5. Spectroscopic characterization

For spectroscopic characterization, an ITO electrode was used to electrocrystallize CuTCNQF₂ when the potential was held at -100 mV for 10 minutes. The cyclic voltammetry was similar to that on GC, although the much larger surface led to large IR drop. Blue crystals of CuTCNQF₂ formed on the ITO surface. The ITO electrode containing the precipitate solid was washed with CH₃CN and dried under vacuum overnight before being characterised by vibrational spectroscopy and data compared with the material obtained by chemical synthesis.

Figure 10 provides comparison of FTIR and Raman spectroscopy of TCNQF₂ and electrocrystallized CuTCNQF₂. Bands can be identified that are characteristic for the TCNQ(F)_n family.^{10,29,30} The C-H stretch band is clearly visible at 3064 cm⁻¹ in the FTIR spectrum. The other major IR bands are the C≡N stretch at 2227 cm⁻¹, ring C=C stretch at 1574 cm⁻¹, exocyclic C=C stretch at 1548 cm⁻¹ and the C-F and ring C-C stretch at 1392 cm⁻¹. The Raman spectrum also provides characteristic bands for the C≡N stretch at 2230 cm⁻¹, the ring C=C stretch at 1633 cm⁻¹, and the exocyclic C=C stretch at 1453 cm⁻¹. These bands generally shift to lower energy in both IR and Raman spectra for the TCNQF₂⁻ radical anion presented in CuTCNQF₂, in which the IR bands for TCNQF₂⁻ are $\nu_{\max}/\text{cm}^{-1}$ 2214, 2182 (CN), 1515 (ring C=C), 1477 (exocyclic C=C), 1339 (C-F and ring C-C); Raman bands are $\nu_{\max}/\text{cm}^{-1}$ 2219 (CN), 1618 (ring C=C), 1401 (exocyclic C=C). Figure 11 compares the IR and

Raman spectra for the electrocrystallized and the chemically synthesized material confirming that they are identical, hence an alternative method to synthesize this new material. Similar data were obtained for the Raman spectrum using the two methods of preparation.

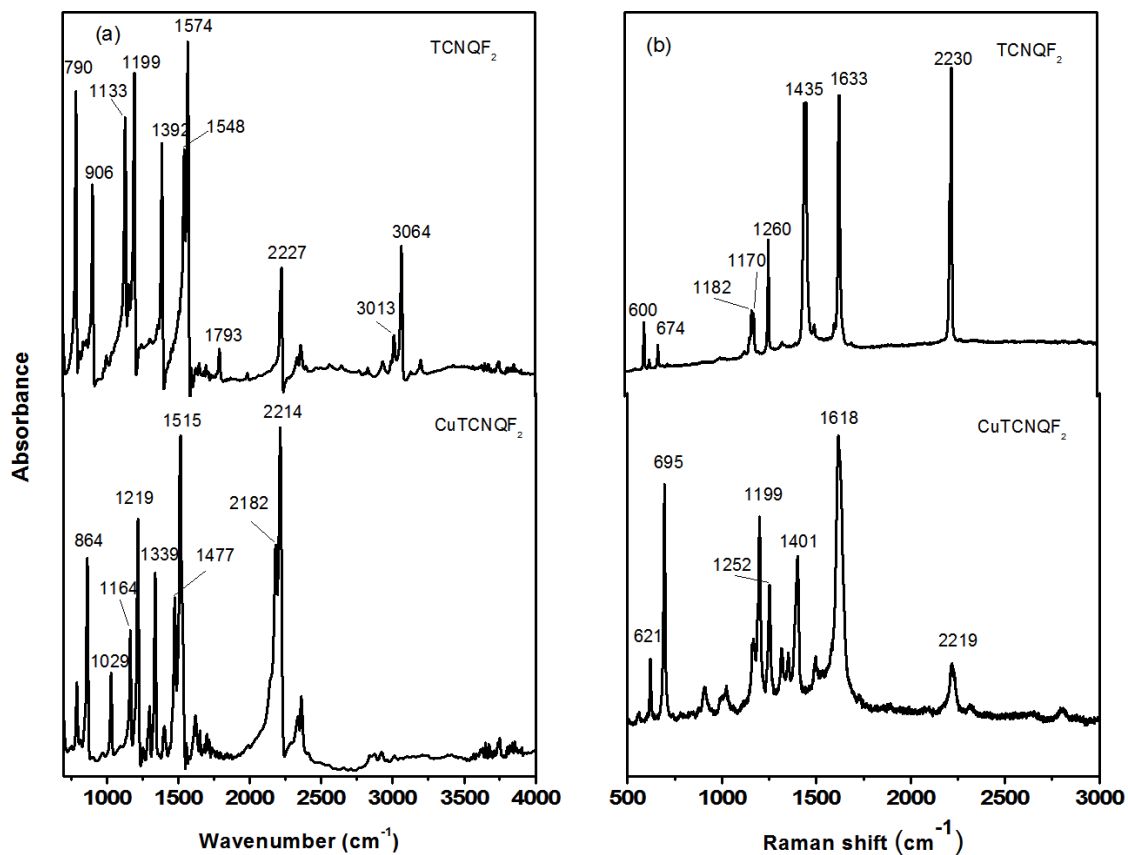


Figure 10. (a) FTIR spectra and (b) Raman spectra of neutral TCNQF₂ and bulk synthesized CuTCNQF₂

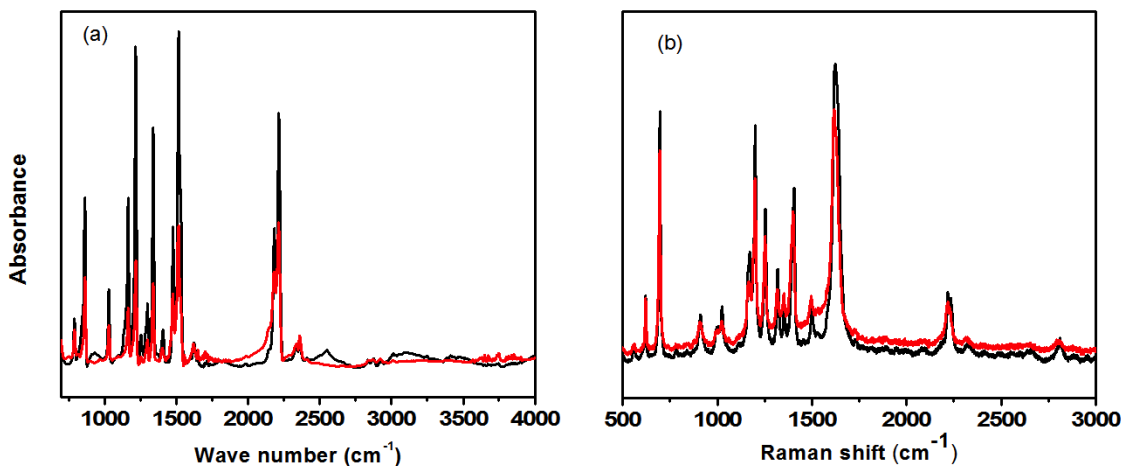


Figure 11. Comparison (a) FTIR spectra and (b) Raman spectra of (black) chemically synthesized and (red) electrocrystallized CuTCNQF₂ materials on an ITO electrode

3.3.6. Elemental microanalysis

The elemental analysis data are C= 46.76%, H = 0.82% and N = 18.18%, which consistent with the formulation being $\text{CuTCNQF}_2 \cdot 1/4\text{H}_2\text{O}$ (calculated: C = 46.66%, H = 0.86%, N =18.54%). This result implies that the there was a relative small amount of H_2O impurity retained as CuTCNQF_2 was precipitated.

3.3.7. Scanning electron microscopy

The morphologies of the chemically synthesized and electrochemically crystallized CuTCNQF_2 samples were probed using the SEM imaging technique (Figure 12). Two morphologies were observed with the electrochemically crystallized material, block-shaped microcrystals of micron size and clusters of platelet microcrystals. However, only blocked microcrystals, evenly distributed over the surface, were observed for the chemically synthesized sample. The two morphologies found by electrochemical crystallization are consistent with the phases identified and discussed above in the cyclic voltammetry. Furthermore, the block-shaped crystal confirms the similarity in morphology found in XRD powder pattern between CuTCNQF_2 and CuTCNQ phase II which was alternatively formed by an extensive reaction of CuTCNQ phase I with hot acetonitrile.²⁷

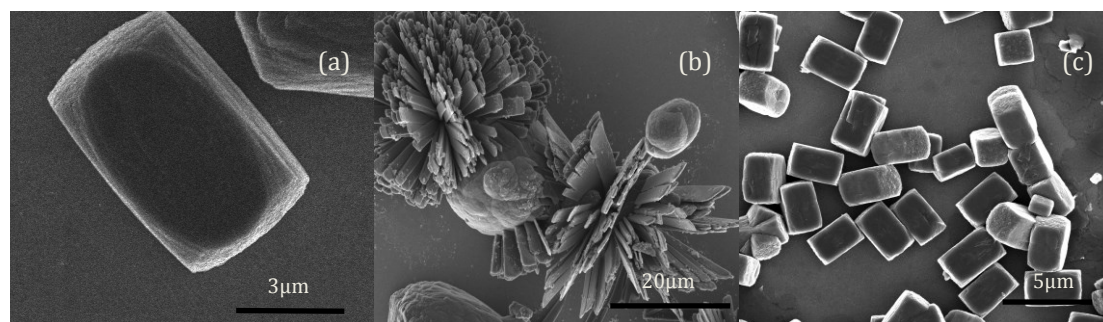


Figure 12. SEM images at different regions, (a) and (b) CuTCNQF_2 electrocrystallized onto an ITO electrode from an acetonitrile (0.1 M Bu_4NPF_6) solution containing 2.0 mM TCNQF_2 and 10.0 mM $[\text{Cu}(\text{CH}_3\text{CN})_4]^+$ at different spots; reductive electrolysis of TCNQF_2 was for 10 mins at -100 mV (vs Ag/Ag^+); and (c) CuTCNQF_2 synthesized by refluxing TCNQF_2 in acetonitrile solution containing 1.5 equivalent CuI .

3.3.8. Solubility of CuTCNQF₂

The solubility of the chemically synthesized CuTCNQF₂ solid was determined in the presence and absence of electrolyte Bu₄NPF₆ by steady state voltammetry and UV-Vis spectroscopy, respectively. For UV-Vis determination, CuTCNQF₂ solid was dissolved in 2.0 ml of acetonitrile in a vial followed by sonication for 5 min to achieve a saturated solution of TCNQF₂⁻. The solution was separated by centrifugation and then diluted 60 times prior to the UV-Vis measurement. The concentration of TCNQF₂⁻ was determined with the use of absorbance at the $\lambda_{\max} = 424$ nm by referring to a calibration curve. This calibration curve was prepared by plotting a graph of absorbance measured at 424 nm against concentration for a series of TCNQF₂⁻ solutions at concentration of 0.005, 0.01, 0.015, 0.02 and 0.03 mM. For steady state voltammetric determination, CuTCNQF₂ was dissolved in acetonitrile containing 0.1 M Bu₄NPF₆ to a saturation level. Steady state voltammogram was obtained with the saturated solution without any dilution. The final concentration of TCNQF₂⁻ and then the solubility of CuTCNQF₂ were then determined to be $5.25 \pm 0.13 \times 10^{-5}$ M and $9.05 \pm 0.09 \times 10^{-5}$ M in the absence and present of electrolyte, respectively. Thus the solubility products were calculated to be $2.75 \pm 0.21 \times 10^{-9}$ M² and $8.19 \pm 1.02 \times 10^{-9}$ M² in the absence and present of 0.1 M Bu₄NPF₆ electrolyte, respectively

3.3.9. Conductivity of CuTCNQF₂

The dependence of current on potential measured on a CuTCNQF₂ film on FTO-coated glasses is shown in Figure 13. The relationship between measured current and potential is ideally linear. DC resistivity of CuTCNQF₂ bulk materials was determined from the slope of the line and hence the average conductivity of 6.0×10^{-6} S.cm⁻¹ was derived which suggests CuTCNQF₂ has semiconducting properties although not a good one. This conductivity is lower than that found for CuTCNQ phase II, 1.3×10^{-5} S.cm⁻¹.²⁶ This similarity is also consistent with the resemblance of morphology between the two materials as discussed above.

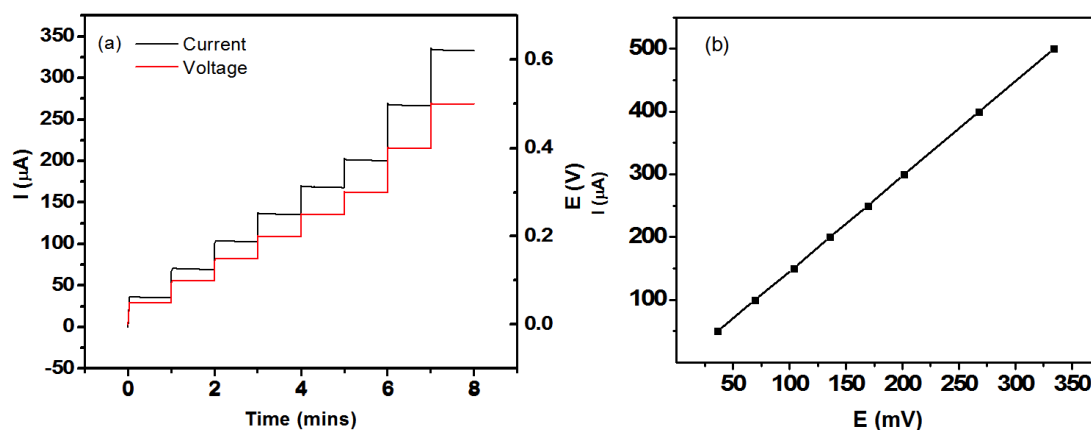


Figure 13. (a) Current and potential plot vs time obtained with CuTCNQF₂ films with a cross-sectional area of 0.82 cm² and a thickness of 840 nm, (b) Plot of current vs potential derived from (a).

3.4. Conclusion

New CuTCNQF₂ insoluble materials are formed during voltammetric experiments in an acetonitrile solution of TCNQF₂ in the presence of [Cu(CH₃CN)₄]⁺. The existence of two different phases was revealed by voltammetry at variable scan rates in both the TCNQF₂⁻ and TCNQF₂²⁻ insoluble materials. Due to the low solubility of CuTCNQF₂⁻ as well as Cu-TCNQF₂²⁻ solids, an interesting solid-solid transformation was observed which hasn't been previously detected in the analogous reaction with Cu(I) and TCNQF_n (n = 0, 4) analogues.

CuTCNQF₂ was both chemically and electrochemically synthesised and characterized using spectroscopic and imaging methods. XRD powder pattern of CuTCNQF₂ shows a similarity to that of CuTCNQ phase II which is in monoclinic unit cell structure. The conductivity determined on a film of CuTCNQF₂ shows a semiconductive property. The vibrational spectroscopies of material synthesized by both methods were identical implying that they can be generated via either methods.

Acknowledgement Financial support from the Australian Research Council is gratefully acknowledged by L.L.M. and A.M.B. N.T.V expresses her appreciation for the award of MGRS and MIPRS Monash University scholarships.

References

- (1) Nafady, A.; O'Mullane, A. P.; Bond, A. M. *Coordination Chemistry Reviews* **2014**, *268*, 101.
- (2) Lopez, N.; Zhao, H.; Prosvirin, A. V.; Wernsdorfer, W.; Dunbar, K. R. *Dalton Transactions* **2010**, *39*, 4341.
- (3) Nafady, A.; Bond, A. M.; Bilyk, A.; Harris, A. R.; Bhatt, A. I.; O'Mullane, A. P.; De Marco, R. *J. Am. Chem. Soc.* **2007**, *129*, 2369.
- (4) Nafady, A.; O'Mullane, A. P.; Bond, A. M.; Neufeld, A. K. *Chem. Mater.* **2006**, *18*, 4375.
- (5) Ran, C. B.; Peng, H. L.; Zhou, W.; Yu, X. C.; Liu, Z. F. *J. Phys. Chem. B* **2005**, *109*, 22486.
- (6) Peng, H. L.; Ran, C. B.; Yu, X. C.; Zhang, R.; Liu, Z. F. *Adv. Mater.* **2005**, *17*, 459.
- (7) Valade, L.; De Caro, D.; Malfant, I.; Ouahab, L., Yagubskii, E., Eds.; Kluwer Academic Publisher: Corfu, GREECE, 2003, p 241.
- (8) Yasuda, A.; Seto, J. *J. Electroanal. Chem.* **1988**, *247*, 193.
- (9) Le, T. H.; Lu, J.; Bond, A. M.; Martin, L. L. *Inorganica Chimica Acta* **2013**, *395*, 252.
- (10) Haworth, N. L.; Lu, J.; Vo, N.; Le, T. H.; Thompson, C. D.; Bond, A. M.; Martin, L. L. *ChemPlusChem* **2014**, *79*, 962.
- (11) Nafady, A.; Le, T. H.; Vo, N.; Haworth, N. L.; Bond, A. M.; Martin, L. L. *Inorganic Chemistry* **2014**, *53*, 2268.
- (12) Le, T. H.; Nafady, A.; Vo, N. T.; Elliott, R. W.; Hudson, T. A.; Robson, R.; Abrahams, B. F.; Martin, L. L.; Bond, A. M. *Inorganic Chemistry* **2014**, *53*, 3230.
- (13) Le, T.; O'Mullane, A.; Martin, L.; Bond, A. *J. Solid State Chem.* **2011**, *15*, 2293.
- (14) Le, T. H.; Nafady, A.; Bond, A. M.; Martin, L. L. *European Journal of Inorganic Chemistry* **2012**, *2012*, 5534.
- (15) Grossel, M. C.; Duke, A. J.; Hibbert, D. B.; Lewis, I. K.; Seddon, E. A.; Horton, P. N.; Weston, S. C. *Chem. Mater.* **2000**, *12*, 2319.
- (16) Lombardo, A.; Fico, T. R. *J. Org. Chem.* **1979**, *44*, 209.
- (17) Suchanski, M. R.; Vanduyne, R. P. *J. Am. Chem. Soc.* **1976**, *98*, 250.
- (18) Lopez, N.; Zhao, H. H.; Prosvirin, A. V.; Wernsdorfer, W.; Dunbar, K. R. *Dalton Trans.* **2010**, *39*, 4341.

- (19) Lieffrig, J.; Jeannin, O.; Guizouarn, T.; Auban-Senzier, P.; Fourmigué, M. *Crystal Growth and Design* **2012**, *12*, 4248.
- (20) Miyasaka, H.; Motokawa, N.; Matsunaga, S.; Yamashita, M.; Sugimoto, K.; Mori, T.; Toyota, N.; Dunbar, K. R. *Journal of the American Chemical Society* **2010**, *132*, 1532.
- (21) Emge, T. J.; Wiygul, F. M.; Chappell, J. S.; Bloch, A. N.; Ferraris, J. P.; Cowan, D. O.; Kistenmacher, T. J. *Molecular Crystals and Liquid Crystals* **1982**, *87*, 137.
- (22) Emge, T. J.; Maxfield, M.; Cowan, D. O.; Kistenmacher, T. J. *Molecular Crystals and Liquid Crystals* **1981**, *65*, 161.
- (23) Mitchell Wiygul, F.; Ferraris, J. P.; Emge, T. J.; Kistenmacher, T. J. *Molecular Crystals and Liquid Crystals* **1981**, *78*, 279.
- (24) Murata, T.; Saito, G.; Nishimura, K.; Enomoto, Y.; Honda, G.; Shimizu, Y.; Matsui, S.; Sakata, M.; Drozdova, O. O.; Yakushi, K. *Bulletin of the Chemical Society of Japan* **2008**, *81*, 331.
- (25) O'Mullane, A. P.; Neufeld, A. K.; Bond, A. M. *Analytical Chemistry* **2005**, *77*, 5447.
- (26) Heintz, R. A.; Zhao, H.; Ouyang, X.; Grandinetti, G.; Cowen, J.; Dunbar, K. R. *Inorganic Chemistry* **1999**, *38*, 144.
- (27) Neufeld, A. K.; Madsen, I.; Bond, A. M.; Hogan, C. F. *Chemistry of Materials* **2003**, *15*, 3573.
- (28) Harris, A. R.; Neufeld, A. K.; O'Mullane, A. P.; Bond, A. M.; Morrison, R. J. S. *Journal of The Electrochemical Society* **2005**, *152*, C577.
- (29) Bozio, R.; Girlando, A.; Pecile, C. *Journal of the Chemical Society, Faraday Transactions 2: Molecular and Chemical Physics* **1975**, *71*, 1237.
- (30) Takenaka, T. *Spectrochimica Acta Part A: Molecular Spectroscopy* **1971**, *27*, 1735.

Supporting Information

**Electrochemistry of TCNQF₂ in acetonitrile in the presence of [Cu(CH₃CN)₄]⁺ -
The formation of CuTCNQF₂ and its catalytic activity**

Nguyen T. Vo, Lisandra L. Martin*, Alan M. Bond*

School of Chemistry, Monash University, Clayton, Victoria 3800, Australia

* Corresponding Authors: Lisa.Martin@monash.edu, Alan.Bond@monash.edu

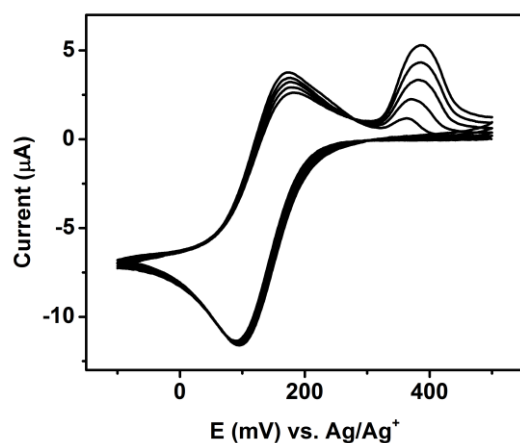


Figure S1. Voltammograms in acetonitrile solution (0.1M Bu₄NPF₆) at a 1 mm diameter GC electrode of 5.0 mM TCNQF₂ in the presence of 10 mM [Cu(CH₃CN)₄]⁺ at 50 mV s⁻¹

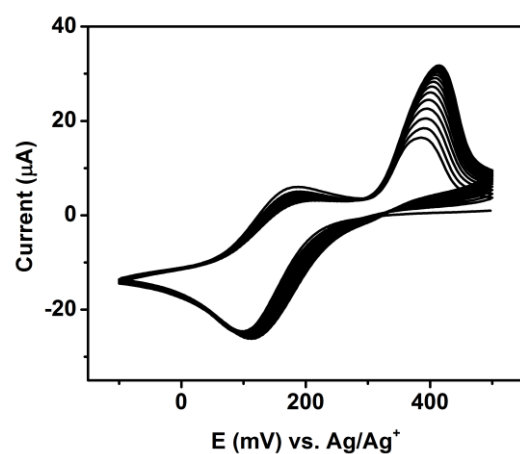


Figure S2. Voltammograms in acetonitrile solution (0.1M Bu₄NPF₆) at a 1 mm diameter GC electrode of 8.0 mM TCNQF₂ in the presence of 8.0 mM [Cu(CH₃CN)₄]⁺ at 100 mV s⁻¹

Chapter 4

Electrochemistry of TCNQF in the presence of [Cu(MeCN)₄]⁺- A comparative study of the catalytic activity of TCNQF_n derivatives

4.1. Introduction

CuTCNQ exists in two phases with different crystal packing and a significant difference in conductivity.¹ While phase I is a good semiconductor at room temperature with a resistivity of 0.2 S cm⁻¹, phase II is a poor one with a resistivity of 1.3 × 10⁻⁵ S cm⁻¹.¹ Significantly, CuTCNQ exhibits a reversible switching behavior between the conducting and insulating states upon application of optical irradiation or an electrical field.

The formation of CuTCNQ has been prepared voltammetrically by reducing TCNQ in the presence of Cu⁺ in acetonitrile media or Cu²⁺ in aqueous solution.^{2,3} The mechanism of the formation of CuTCNQ differs in these two media. In aqueous solution a solid-solid transformation mechanism with a complex charge transfer process including a TCNQ^{0/-} and Cu^{2+/+} reduction processes as shown in equation 1



The conversion from phase I to phase II material has been observed upon an extensive potential cycling.

However, only CuTCNQ phase I can be detected electrochemically in acetonitrile which gives rise to two redox processes at variable potential and voltammetric time scale relating to the formation of different sizes of crystal as well as morphologies. The formation of CuTCNQF₄ has also been reported.⁴ No crystal structure is available for CuTCNQF₄, however this material can be electrocrystallized and characterized on an electrode surface. An exciting finding with the Cu-TCNQF₄ material was that the formation of the more reduced TCNQF₄²⁻- based material can be detected on voltammetric time scale. The stable dianionic form has not been generated electrochemically for TCNQ. It needs to be stabilized in a coordination polymer with other ligands. For example, numbers of TCNQ²⁻ and TCNQF₄²⁻ coordination polymer were successfully synthesized chemically with the diruthenium ligands Ru₂(m-CH₃PhCO₂)₄ and Ru(o-CF₃PhCO₂)₄.^{5,6} Also, the dianionic complexes of TCNQ and TCNQF₄ have been

reported with Cu^+ in the presence of other coordination ligands such as 2,6-lutidine, quinone, 2-picoline, 2,2'-bipyridine with H_2TCNQ or H_2TCNQF_4 starting materials.⁷ The addition of fluorine substituents on TCNQ shifts the reversible potential to more positive values making the TCNQF_4^{2-} more accessible and enhancing its stability.

As part of systematic studies on the electrochemical behavior of fluoro derivatives of TCNQ, the electrochemistry of mono-fluoro TCNQF in the presence of $[\text{Cu}(\text{MeCN})_4]^+$ is now reported. In this study, reduction of TCNQF to TCNQF^- and TCNQF^{2-} in the presence of $[\text{Cu}(\text{MeCN})_4]^+$ is described over a range of concentrations and the catalytic activity of a CuTCNQ film on copper foil will be compared with that of the other fluoro-TCNQ derivatives.

4.2. Experimental

4.2.1. Chemicals

TCNQF (98%, TCI Tokyo), $[\text{Cu}(\text{CH}_3\text{CN})_4]\text{PF}_6$ (98%, Aldrich), acetonitrile (HPLC grade, Omnisolv), isopropanol (BHD) and acetone (suprasolv, Merck KGaA) were used as received from the manufacturer. Bu_4NPF_6 (Aldrich), used as the supporting electrolyte in electrochemical studies, was recrystallized twice from 96% ethanol (Merck) and then dried at 100°C under vacuum for 24 hours prior to use.

4.2.2. Electrochemistry

Voltammetric experiments were undertaken at room temperature ($22 \pm 2^\circ\text{C}$) using a Bioanalytical Systems (BAS) 100W electrochemical workstation. A standard three electrode cell configuration, comprising a glassy carbon (GC, 1 mm diameter) working electrode, a Ag/Ag^+ reference electrode (RE) and a 1.0 mm diameter platinum wire counter electrode, was employed in those experiments. The working electrode was polished with $0.3 \mu\text{m}$ Al_2O_3 slurry using polishing cloth, washed with water followed by sonication in an ultra sonic bath for 30 seconds prior each run to ensure a fresh electrode surface. The RE consisted of an Ag wire in contact with acetonitrile solution containing 0.1 M Bu_4NPF_6 and 1.0 mM AgNO_3 , which was separated from the test solution by a salt bridge. The relative potential of this reference electrode was -124 mV vs the ferrocene/ferrocenium, $\text{Fc}^{0/+}$ couple. All solutions were purged with nitrogen gas for at least 10 min and a stream of nitrogen was maintained above the solutions during the course of the

voltammetric experiments. For bulk electrolysis experiment, a Pt mesh electrode was used as the working electrode instead of a GC electrode.

4.2.3. Synthesis of CuTCNQF

CuTCNQF was prepared both electrochemically and chemically. A 5.0 ml solution of 0.5 mM TCNQF⁻ was quantitatively prepared by bulk reduction electrolysis of 5.0 mM TCNQF in acetonitrile (0.1 M Bu₄NPF₆). The potential at Pt mesh working electrode was held at -150 mV vs Ag/Ag⁺ until the current ratio reached 1% of the initial value. To this solution, 0.375 ml solution of 100 mM [Cu(CH₃CN)₄]⁺ was added. A dark blue precipitate formed immediately. The mixture was kept stirring was maintained for 10 minutes after which the solid was collected by filtration, washed several times with CH₃CN, dried and stored under vacuum overnight before further characterization.

CuTCNQF was also electrocrystallized on an ITO electrode by holding the potential at -150 mV for 5 mins. A dark precipitate deposited on the ITO electrode was rinsed with acetonitrile followed by acetone and stored under vacuum. All the samples generated via these different synthetic pathways were characterized and compared.

The solid was also chemically synthesized by a reaction between TCNQF and CuI at a 1:1.5 stoichiometric ratio in acetonitrile for 3 hours followed equation 2. A dark blue solid was obtained, filtered, washed with CH₃CN and dried at the same manner as described above before characterization.



4.2.4. Catalytic experiment

A piece of copper foil was used to prepare a film of CuTCNQF for catalytic experiment according to equation 2.



The foil was initially cleaned by immersion in HNO₃ (5%) to remove surface oxide, then washed with acetone and methanol and dried under a nitrogen stream. To form a layer of CuTCNQF, the copper foil was immersed in a 1.0 mM TCNQF solution in CH₃CN for 12 hours. Afterwards, the foil was removed from the

solution, rinsed briefly with CH₃CN to remove excess TCNQF and washed with copious amounts of water. The sample was then dried and stored under vacuum prior to use.

CuTCNQF₂-coated copper foils were prepared in the same manner as described for CuTCNQF.

Catalytic activity of CuTCNQF and CuTCNQF₂ in contact with copper foil (area of 0.16 cm²) was assessed on the reaction between S₂O₃²⁻ and [Fe(CN)₆]³⁻. A 30 ml solution of 0.1 M S₂O₃²⁻ and 1.0 mM [Fe(CN)₆]³⁻ was stirred in the presence of the CuTCNQF_n film. At regular time intervals 600 μl of solution was removed for UV-Vis measurement and the amount of [Fe(CN)₆]³⁻ remaining in the solution was determined by referring to a calibration curve.

Open circuit potential (OCP) experiments were performed using a CuTCNQF_n-coated copper foil as a working electrode. An aqueous Ag/AgCl (3.0 mM KCl) electrode (BAS) and platinum wire were used as reference and counter electrodes, respectively. 30 ml solution containing 1.0 mM [Fe(CN)₆]³⁻ was initially stirred for 10 min in the electrochemical cell and the OCP vs. time data was recorded during this period of time. 1.0 ml solution containing 3.0 M S₂O₈²⁻ was sequentially injected into the cell to give a final concentration of ~0.1 M. The OCP vs. time data was continuously recorded before being terminated at 31 min.

4.2.5. Other instrumentations

UV-Vis spectra were recorded with a Varian Cary 5000 UV-Vis NIR spectrophotometer with a 1.0 cm path length quartz cuvette. A Varian UMA600 IR microscope and FTS7000 optics bench using 128 scans and a resolution of 8 cm⁻¹ was used for IR spectra. Raman spectra were recorded on a Renishaw Invia Raman spectrograph with an Argon ion laser excitation at 633 nm. After being coated with Ir, SEM images were collected with a FEI Nova NanoSEM 450 FEGSEM instrumentation using an accelerating voltage of 5.0 kV.

4.3. Result and discussion

4.3.1. Voltammetry of TCNQF in the presence of $[\text{Cu}(\text{CH}_3\text{CN})_4]^+$, the first reduction process

The potentials of two reduction processes for TCNQF are well removed from the potentials for the reduction and oxidation of $[\text{Cu}(\text{CH}_3\text{CN})_4]^+$. Hence, the reduction of both reduction steps $\text{TCNQF}^{0/-}$ and $\text{TCNQF}^{-/2-}$ can be studied without any interference from $[\text{Cu}(\text{CH}_3\text{CN})_4]^+$.

The $\text{TCNQF}^{0/-}$ reduction process was studied in an acetonitrile solution containing 8.0 mM TCNQF and 8.0 mM $[\text{Cu}(\text{CH}_3\text{CN})_4]^+$. Voltammograms obtained when the potential was swept negatively to reduce TCNQF to TCNQF^- and then reversed at designated scan rates are shown in Figure 1. Upon increase the scan rate from 20 $\text{mV}\cdot\text{s}^{-1}$ to 300 $\text{mV}\cdot\text{s}^{-1}$ the reduction peak potential shift to more negative from -16 to -76 mV. Furthermore, although the peak current, i_p^{red} , is proportional to the square root of scan rate, $v^{1/2}$, a negative intercept on the current axis was derived which implies that the reduction $\text{TCNQF}^{0/-}$ is not totally diffusion-controlled in the presence of $[\text{Cu}(\text{CH}_3\text{CN})_4]^+$. In the positive scan direction, a new oxidation process, which is sharper and more symmetric, appears at more positive potential (Ox1) than the $\text{TCNQF}^{-/0}$ oxidation step. The Ox1 peak potential (E_p) and current magnitude highly depend on the scan rate as well as the switching potential. For example, E_p shifts positively from 123 to 176 mV when the scan rate increase from 20 to 300 $\text{mV}\cdot\text{s}^{-1}$. The loss of diffusion-controlled characteristics together with the appearance of the Ox1 step indicates a chemical step accompanied the reduction of TCNQF to TCNQF^- . It is most likely that solid CuTCNQF is formed via equations 3 and 4.



On this basis, Ox1 peak represents the oxidation of $\text{CuTCNQF}_{(\text{solid})}$ (A) to dissolved TCNQF.

Interestingly, when the potential was scanned to more negative potential before being reversed, i.e -250 mV, which still avoids the $\text{TCNQF}^{-/2-}$ reduction process found in the absence of Cu^+ , a second reduction process was observed with a small current magnitude (Red1) (see Figure 2). Simultaneously process Ox1 becomes

dominant in the positive potential scan with an enhanced current magnitude of Ox1 which suppresses the diffusion controlled TCNQF^{-/0} oxidation step. Moreover, a new small broad oxidation peak at 298 mV is now detected. Taken together, these data suggests that more negative potential increases the deposition of the Cu-TCNQF solid associated with the Ox1 step and also enables the formation of another solid which is oxidized at a more positive potential. As illustrated in Figure 2b, at faster scan rates, while the current magnitude of Ox1 increases, the Ox2 peak becomes more difficult to detect which implies that these reductions, leading to solid formation, are kinetically controlled.

The presence of the additional Red1 process is presumably due to the reduction of TCNQF⁰ to TCNQF⁻ at the Cu-TCNQF crystal sites that already formed in Red process followed by the reaction with Cu⁺ (equation 6). The two solids were then oxidized at different potentials.

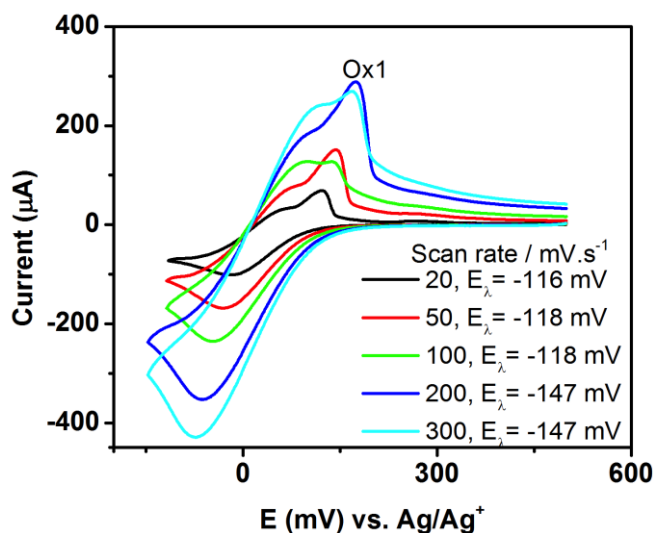


Figure 1 Cyclic voltammograms obtained in acetonitrile (0.1 M Bu₄NPF₆) for 8.0 mM TCNQF and 8.0 mM [Cu(CH₃CN)₄]⁺ with a 1 mm diameter GC electrode at designated scan rates

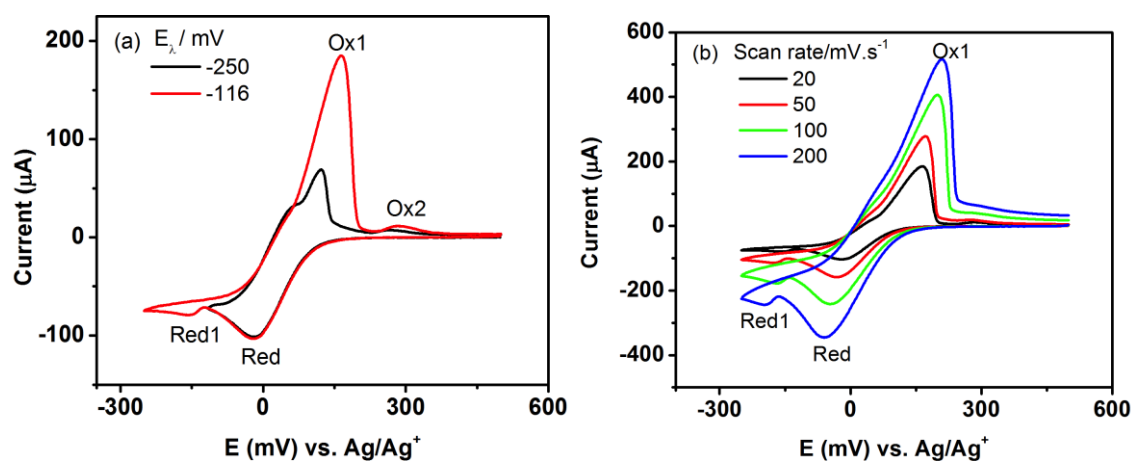


Figure 2 Cyclic voltammograms obtained in acetonitrile (0.1 M Bu_4NPF_6) for 8.0 mM TCNQF and 8.0 mM $[\text{Cu}(\text{CH}_3\text{CN})_4]^+$ with a 1 mm diameter GC electrode (a) at 20 $\text{mV}\cdot\text{s}^{-1}$ as a function of switching potential, (b) switched at -250 mV with designated scan rates

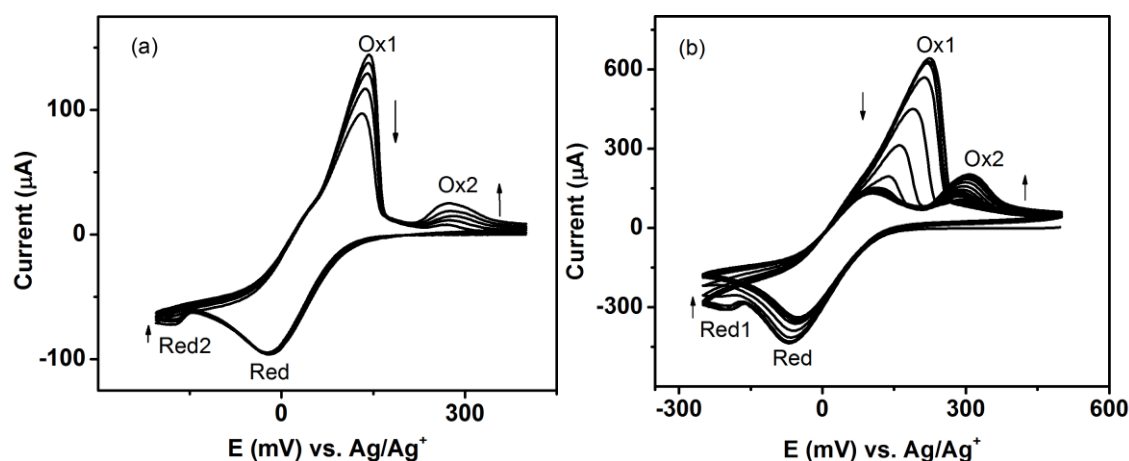


Figure 3 Cyclic voltammograms obtained in acetonitrile (0.1 M Bu_4NPF_6) for 8.0 mM TCNQF and 8.0 mM $[\text{Cu}(\text{CH}_3\text{CN})_4]^+$ with a 1 mm diameter GC electrode when the potential was switched at (a) -205 mV at a scan rate of 20 $\text{mV}\cdot\text{s}^{-1}$ (b) switched at -250 mV at a scan rate of 300 $\text{mV}\cdot\text{s}^{-1}$

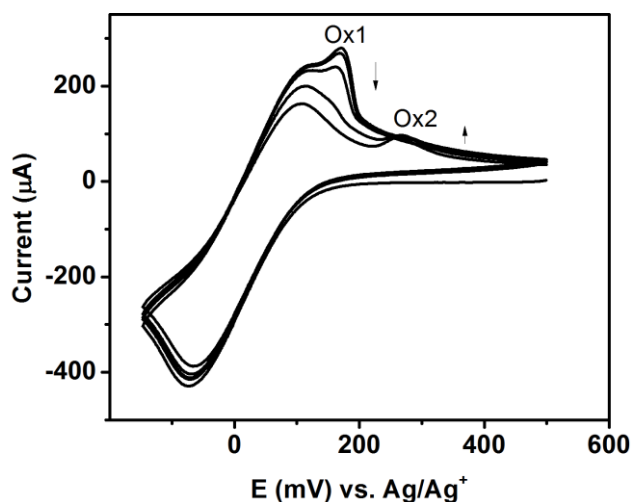


Figure 4 Cyclic voltammograms obtained in acetonitrile (0.1 M Bu_4NPF_6) for 8.0 mM TCNQF and 8.0 mM $[\text{Cu}(\text{CH}_3\text{CN})_4]^+$ with a 1 mm diameter GC electrode when the potential was switched at -146 mV at a scan rate of $300 \text{ mV}\cdot\text{s}^{-1}$

Moreover, on scanning multiple cycles, the nature of the accumulation of solid A (associated with Ox1) and solid B (associated with Ox2) varies. Thus, the Ox2 current magnitude gradually increases on cycling of the potential at scan rates of $20 \text{ mV}\cdot\text{s}^{-1}$ and $300 \text{ mV}\cdot\text{s}^{-1}$, and Ox1 decreases when the potential was switched at -146 mV (Figure 4) or at -250 mV (Figure 3b). At $300 \text{ mV}\cdot\text{s}^{-1}$, the current decay of Ox1 is rapid until it was no longer detected and neither was Red1. These data suggest that the solid product, giving rise to Ox2 oxidation process is thermodynamically more stable than that giving rise to Ox1 process.

Effect of deposition potential

A series of experiments were performed with a solution containing 8.0 mM TCNQF and 8.0 mM $\text{Cu}(\text{MeCN})_4^+$ in which the potential was held at either -118 or -250 mV vs. Ag/Ag^+ for designated periods of time to induce either the Red or Red1 step, respectively. The potential was then scanned positively at designated scan rates. When TCNQF was reduced at -118 mV for 2s and the potential was scanned positively at $20 \text{ mV}\cdot\text{s}^{-1}$, Ox2 process was the main oxidation step implying predominant formation of solid B (Figure 5a). The current magnitude of Ox2 increased when a longer deposition time of 5 s was applied which indicates that the accumulation of solid B occurred on the electrode surface using a longer deposition time. However, with 10 s of deposition, the Ox1 peak was detected concomitantly with a drop in peak current of Ox2. This can be explained if there

was a transformation of solid B to solid A during the longer time scale of 10 s. Interestingly, after 5 s of deposition and when the potential was scanned positively, the peak current of Ox1 increased significantly with faster scan rate relative to the Ox1 step (Figure 5b). However, with 10 s of deposition, both Ox1 and Ox2 steps are detected at all scan rates examined, although Ox2 peak increases at higher rate than that of Ox1 (Figure 5c).

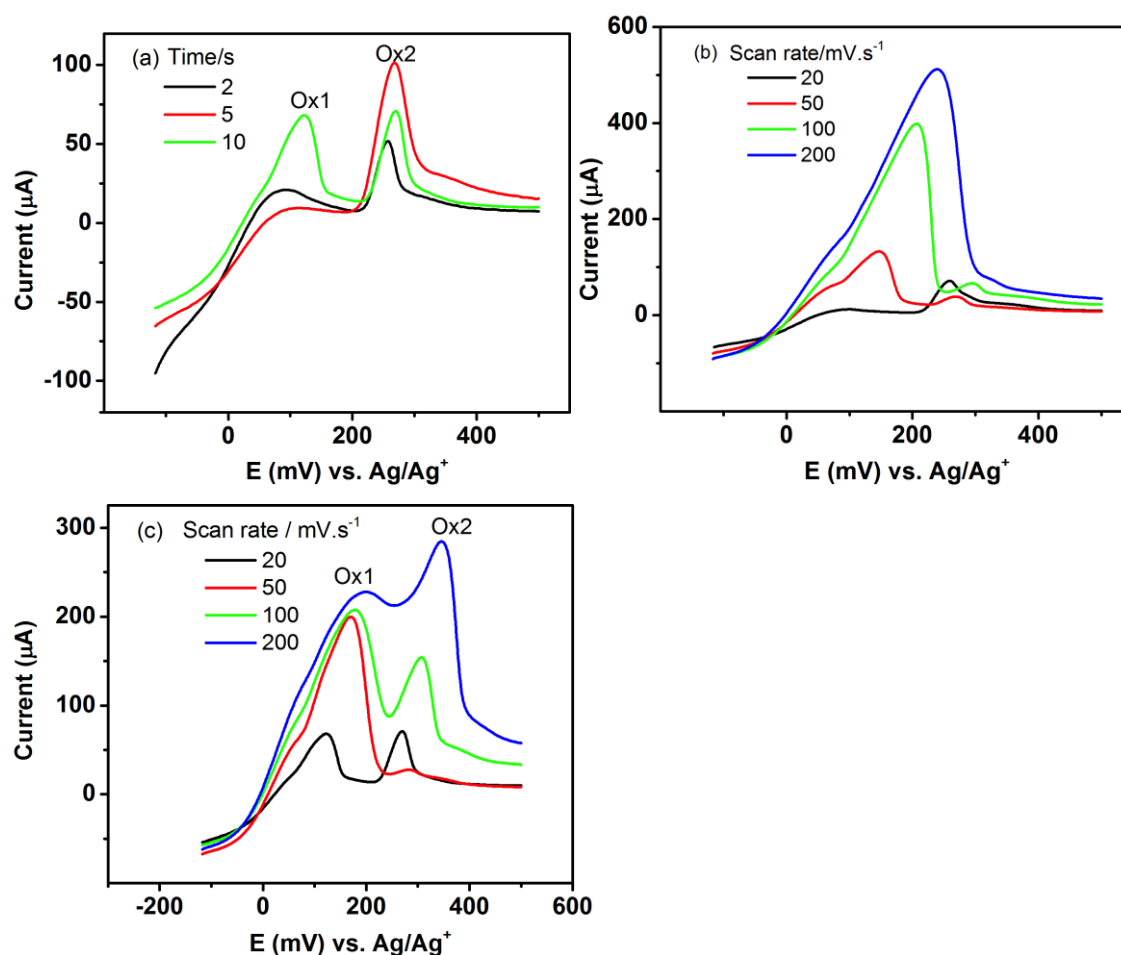


Figure 5. Voltammograms obtained in acetonitrile (0.1 M Bu_4NPF_6) for 8.0 mM TCNQF and 8.0 mM $[\text{Cu}(\text{CH}_3\text{CN})_4]^+$ with a 1 mm diameter GC electrode when potential was held at -118 mV before sweeping the potential to -500 mV (a) for designated times at a scan rate of 20 $\text{mV}\cdot\text{s}^{-1}$ (b) for 5 s at designated scan rates (c) for 10 s at designated scan rates

In contrast, when the potential was held at -250 mV and then scanned positively at 50 $\text{mV}\cdot\text{s}^{-1}$, the Ox1 process becomes more dominant on increasing the deposition time from 2 to 10 s (Figure 6a). With 5 s of deposition, both Ox1 and Ox2 can be detected despite the greater current magnitude of Ox1 compared to Ox2 (Figure

6b), whereas the Ox1 peak dominates in the voltammogram when 10 s is used for deposition. These data suggest that holding the potential at -250 mV creates an ideal condition for the growth of both solid A and solid B (Figure 6c). Furthermore, there is competition between scan rate and deposition time to detect either solid A or solid B product.

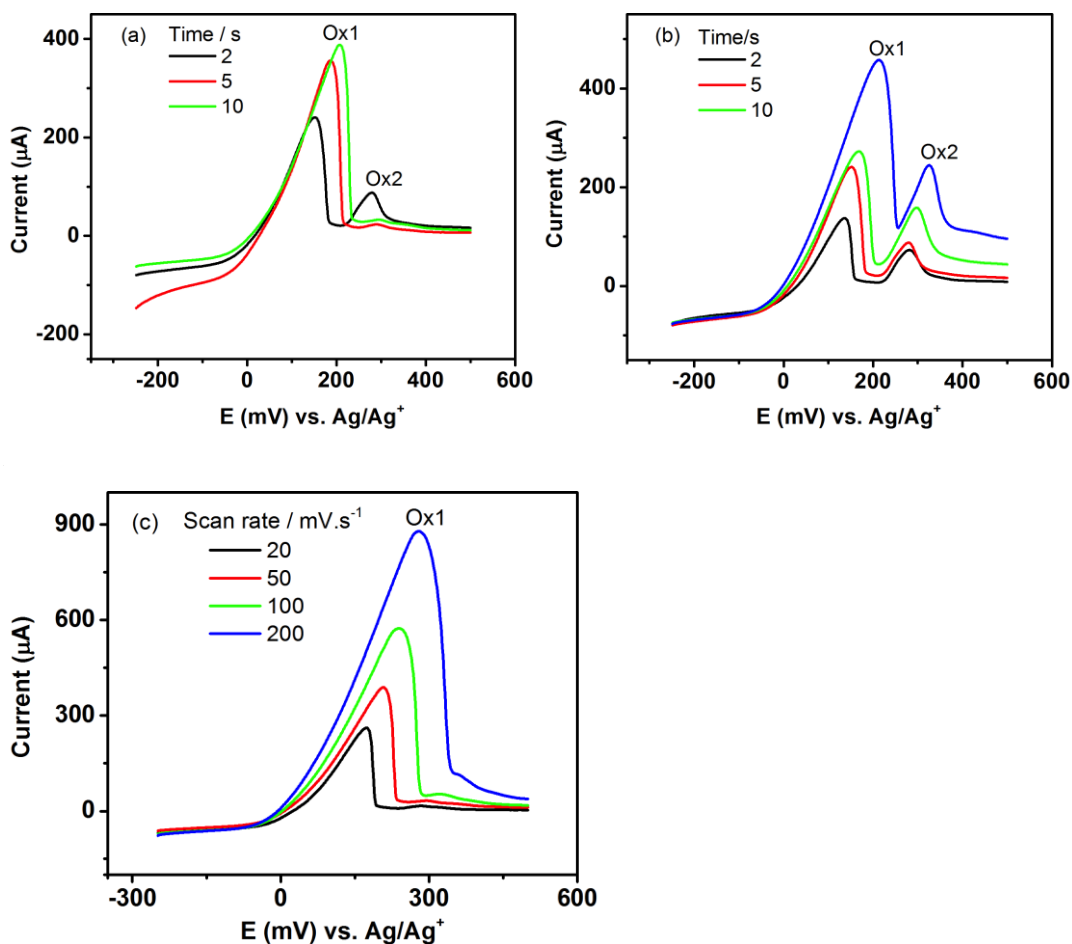


Figure 6 Voltammograms obtained in acetonitrile (0.1 M Bu₄NPF₆) for 8.0 mM TCNQF and 8.0 mM [Cu(CH₃CN)₄]⁺ with a 1 mm diameter GC electrode when potential was held at -250 mV before sweeping the potential to 500 mV (a) for designated times at a scan rate of 50 mV.s⁻¹ (b) for 5 s at designated scan rates (c) for 10 s at designated scan rates

4.3.2. Cyclic voltammetry of TCNQF^{-/2-} process in the presence of [Cu(MeCN)₄]⁺

Extending the potential range to more negative values provides an opportunity to explore the behavior of the second TCNQF^{-/2-} process in the presence of Cu⁺ provided that specific conditions are ensured to prevent the formation of CuTCNQF. As long as experiments performed at concentrations of Cu⁺ and TCNQF

lower than the value of the solubility of CuTCNQF, the precipitation can be avoided. On addition of 1.0 mM Cu⁺ into 1.0 mM TCNQF, the TCNQF^{0/-} process is not modified, however another reduction wave appears at -438 mV (Red') prior to the second TCNQF^{-/2-} reduction previously not present in the absence of Cu⁺. In the reversed scan, along with the TCNQF^{2-/-} oxidation, a sharp and symmetric peak appears at -267 mV (Ox'). At more positive potentials, the TCNQF^{-/0} process retains its diffusion-controlled nature. On increasing the concentration of Cu⁺ to 2.0 and then 3.0 mM, the solution phase TCNQF^{2-/-} process totally disappears and the reduction wave Red' becomes sharper and more symmetric, as does the Ox' peak (Figure 7)

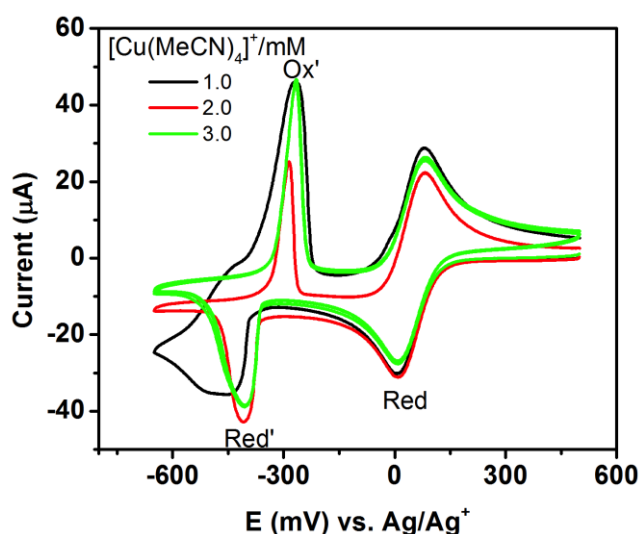
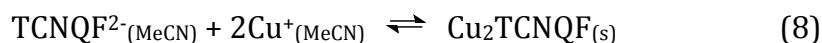
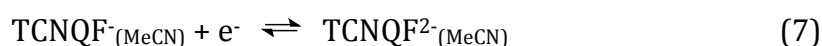
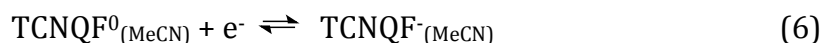


Figure 7. Cyclic voltammograms obtained in acetonitrile (0.1 M Bu₄NPF₆) for 1.0 mM TCNQF with designated [Cu(CH₃CN)₄]⁺ concentrations with a 1 mm diameter GC electrode at a scan rate of 100 mV.s⁻¹

Voltammograms obtained with 0.5 mM TCNQF and 1.0 mM [Cu(MeCN)₄]⁺ as a function of scan rate are shown in Figure 8. As can be seen, E_p^{red} shifts to more negative value from -454 to -475 mV over the scan rate from 50 to 500 mV.s⁻¹.

These observations suggest a formation of Cu-TCNQF²⁻ solid on the electrode surface during the voltammetric experiment as described in equations 6-8.



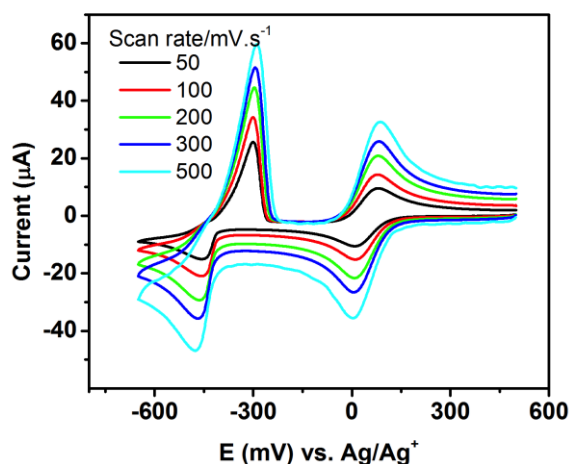


Figure 8 Voltammograms obtained in acetonitrile (0.1 M Bu_4NPF_6) for 0.5 mM TCNQF and 1.0 mM $[\text{Cu}(\text{CH}_3\text{CN})_4]^+$ with a 1 mm diameter GC electrode at designated scan rates

Nucleation growth mechanism

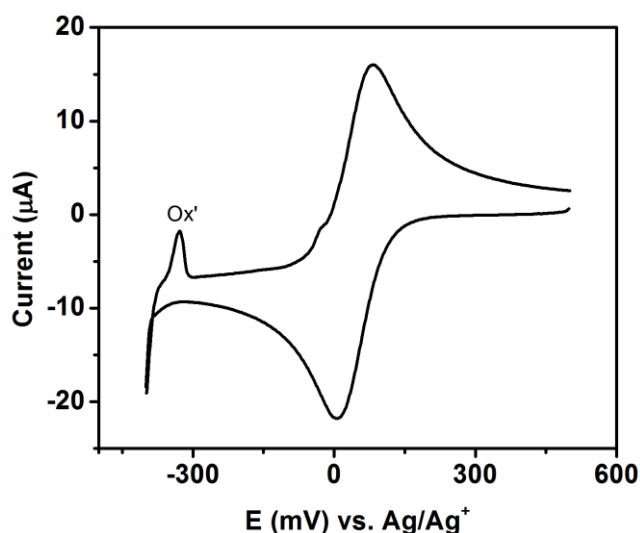


Figure 9 Voltammograms obtained in acetonitrile (0.1 M Bu_4NPF_6) for 1.0 mM TCNQF and 2.0 mM $[\text{Cu}(\text{CH}_3\text{CN})_4]^+$ with a 1 mm diameter GC electrode at a scan rate of 50 $\text{mV}\cdot\text{s}^{-1}$

Switching the potential at $E_\lambda = -400$ mV before scanning positively gave rise to a cross-over current and a symmetric oxidation peak Ox' which is characteristic of a nucleation-growth mechanism confirming formation of a solid on the electrode surface (Figure 9). The formation of Cu-TCNQF^{2-} material was confirmed by holding the potential at -700 mV to reduce TCNQF to TCNQF^{2-} in the presence of Cu^+ and then scanning the potential positively as shown in Figure 10a. The oxidation peak Ox' splits to two separate peaks at a scan rate of 300 $\text{mV}\cdot\text{s}^{-1}$. At the faster scan rate

of 700 mV.s^{-1} , the two processes are well resolved at -234 mV (Ox') and -120 mV (Ox'') indicating that two different forms of Cu-TCNQF_2 formed in this experimental condition. To further examine the presence of two different forms, the potential was held at -700 mV for various periods of time prior to the potential being scanned positively at a scan rate of 50 mV.s^{-1} or 500 mV.s^{-1} . The voltammograms are shown in Figure 10b (50 mV.s^{-1}), and Figure 10c (500 mV.s^{-1}). At 50 mV.s^{-1} scan rate, the amount of material formed on the electrode surface is independent on the deposition time evidenced by the mostly unchanged peak area of Ox' . However at 500 mV.s^{-1} , the appearance of two oxidation processes is highly dependent on the reduction time. The peak -120 mV was detected with high current magnitude when the potential was held for 10s, however when the reduction time increased to 30s, this peak disappeared. These observations suggest that there are in fact two forms of Cu-TCNQF_2 material which can be oxidized at different potentials. However, the material corresponding to Ox'' can only be detected with suitable scan rate and deposition times. This suggest that the formation of Ox'' is kinetic controlled.

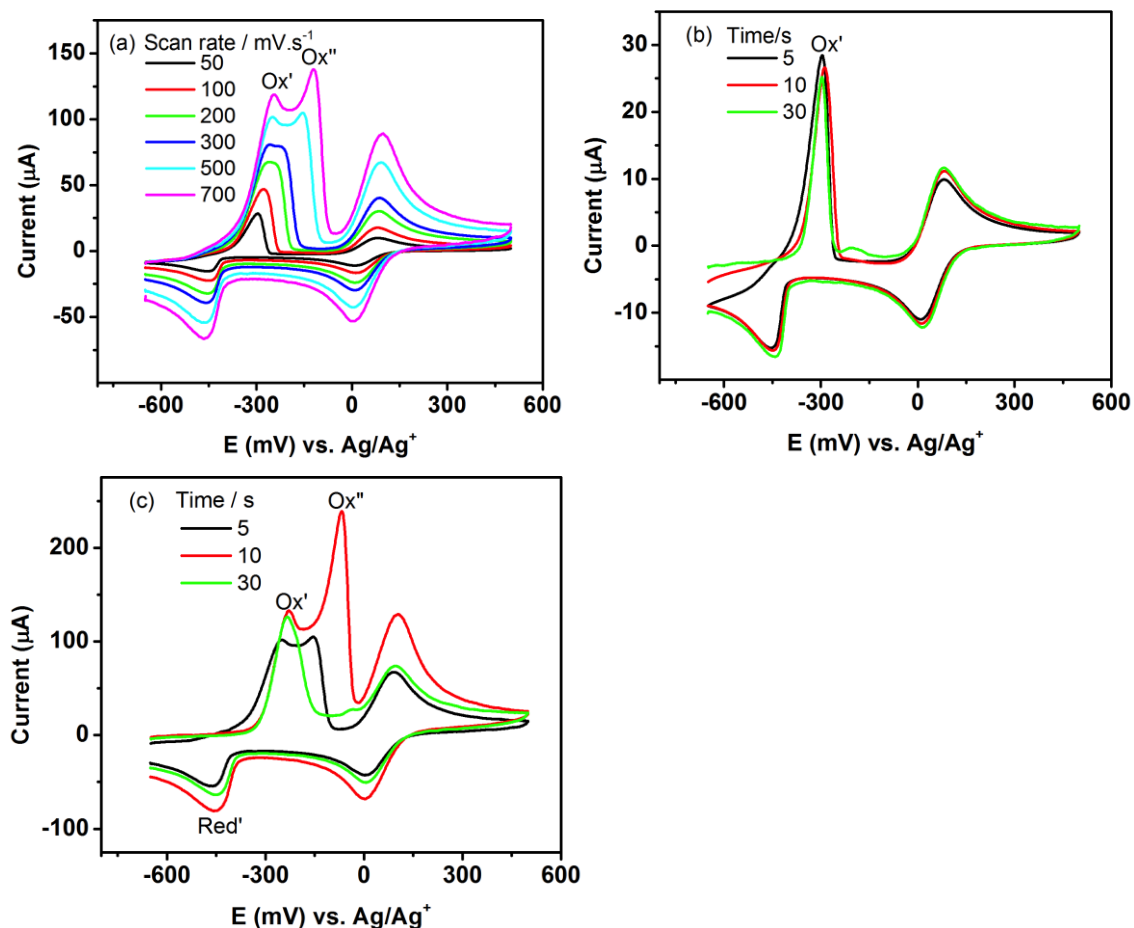
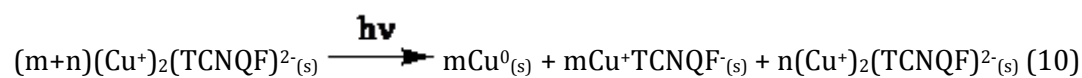


Figure 10. Cyclic voltammograms obtained in acetonitrile (0.1 M Bu_4NPF_6) for 0.5 mM TCNQF and 1.0 mM $[\text{Cu}(\text{CH}_3\text{CN})_4]^+$ with a 1 mm diameter GC electrode when the potential was held at -700 mV before sweeping the potential to 500 mV (a) for 5s at designated scan rates (b) for designated times at a scan rate of $50 \text{ mV}\cdot\text{s}^{-1}$ (c) for for designated times at a scan rate of $500 \text{ mV}\cdot\text{s}^{-1}$

4.3.3. Spectroscopic characterization

Figure 11 shows IR and Raman spectra of the samples synthesized both electrochemically and chemically. Characteristic IR vibrational bands were detected at 2205 and 2138 cm^{-1} for the $\text{C}\equiv\text{N}$ stretch, 1513 cm^{-1} for ring $\text{C}=\text{C}$ stretch, 1504 cm^{-1} for exocyclic $\text{C}=\text{C}$ vibration, 1350 cm^{-1} for the mixing mode of ring $\text{C}-\text{C}$ and $\text{C}-\text{F}$ stretch. The $\text{C}-\text{CN}$ stretch vibrational band was detected at 1196 cm^{-1} . Also, bands at 3343 and 1608 cm^{-1} imply the existence of water in these materials. Also, Raman absorptions were observed at 2214 cm^{-1} for the $\text{C}=\text{N}$ stretch, 1609 cm^{-1} for the ring $\text{C}=\text{C}$ stretch and 1391 cm^{-1} for the exocyclic $\text{C}=\text{C}$ stretch. These bands closely match those present in the calculated spectrum discussed in chapter 2.

TCNQF²⁻ material were also synthesized by adding 30.0 mM [Cu(MeCN)₄]⁺ to an acetonitrile solution containing 10.0 mM TCNQF²⁻ obtained by bulk electrolysis as described above. The yellow solid formed immediately after mixing and was collected and characterized by IR and Raman spectroscopy. However, the colour of this material gradually changed to green over several hours indicating that it decomposed in the air (Equation 10). Raman spectroscopy shown in Figure 12 reveal that the sample contained TCNQF⁻ deduced by Raman absorptions at 2220, 1614 and 1393 cm⁻¹ corresponding to C≡N stretch, ring C=C stretch and exocyclic C=C stretch, respectively.



4.3.4. Elemental microanalysis for CuTCNQF material

Elemental analysis results was found to be C 49.66, H 1.20 and N 19.56% which can rationalized by the existence of water with an overall composition of CuTCNQF.1/4H₂O (cal. C 49.66, H 1.22 and N 19.30%).

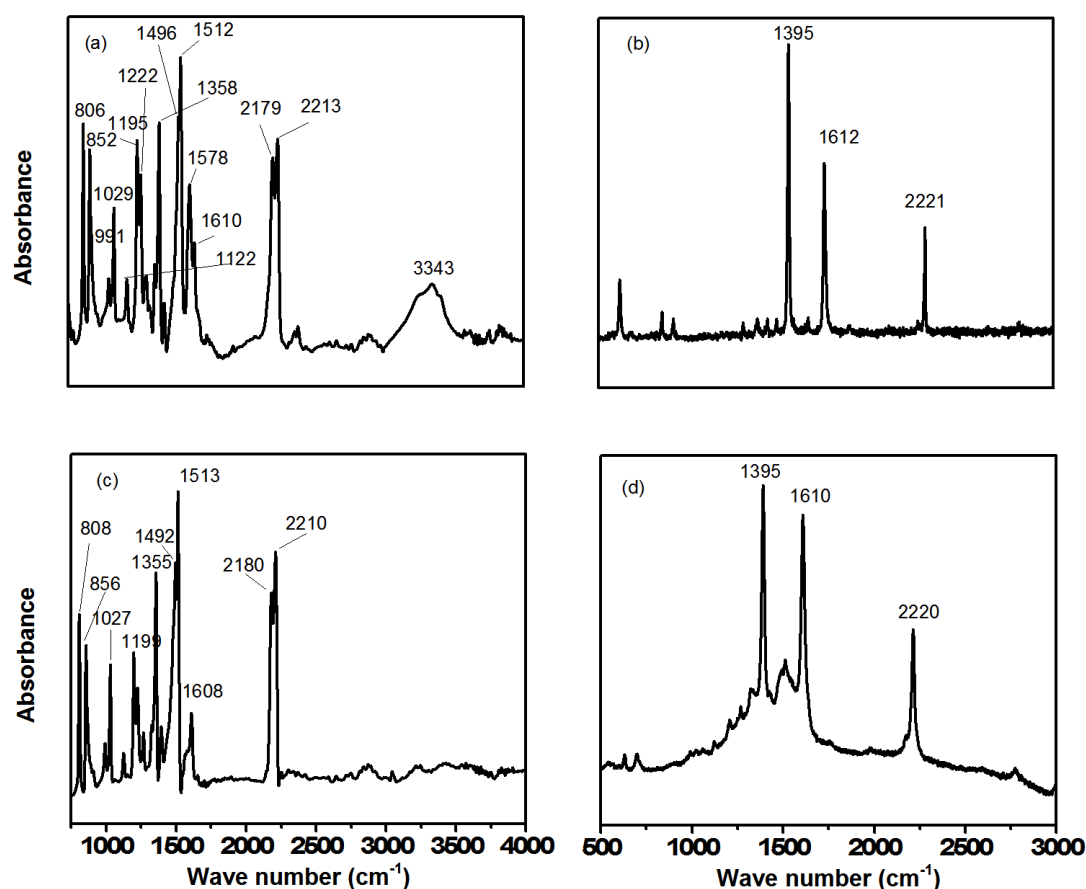


Figure 11 (a) IR and (b) Raman spectra of chemically synthesized CuTCNQF, (c) IR and (d) Raman spectra of electrochemically synthesized CuTCNQF

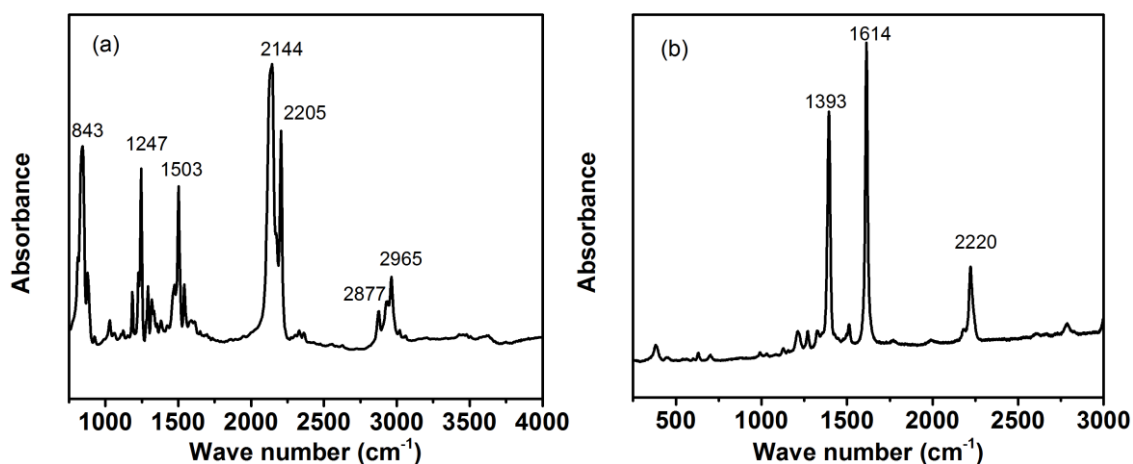


Figure 12 (a) IR and (b) Raman spectra of electrochemically synthesized CuTCNQF²⁻ based material

4.3.5. Morphology of CuTCNQF

Unfortunately, attempts to grow of CuTCNQF crystals suitable for X-ray single crystal structural analysis was unsuccessful. However, the morphology of these compounds can be probed by SEM. The voltammetric data indicates that the reduction of neutral TCNQF to TCNQF⁻ in the presence of Cu⁺ gave rise to the formation of two different morphologies as evidence as two separate stripping processes. Samples for SEM imaging were prepared with an acetonitrile solution containing 8.0 mM TCNQF and 8.0 mM [Cu(MeCN)₄]⁺ using electrocrystallization at an ITO electrode. In the first experiments, the potential was cycled 50 times with the potential switched at either -118 or -250 mV vs Ag/Ag⁺. In another experiment, the potential was held at -118 mV or -250 mV for 2 mins. The SEM images reveal that when the potential was held at -118 mV for 2 mins, crystals having three different morphologies were formed (Figure 13). They are plate-like crystals having a size of ~ 10 μm, clusters of smaller ordered platelet crystals with a size of ~ 50 nm and blocked crystals having a size of ~30 μm. In contrast, when the potential was held at a more negative value of -250 mV, only the 30 μm blocked crystals present (Figure 14). The pattern of variable crystal morphology for CuTCNQF solid suggests that the block-shaped crystal is the end point in the crystal growing process, representing a thermodynamic stable crystal. Apparently, the plate-like crystals initially formed at more positive potential (corresponding to the reduction peak present at 0 mV), are fragmented to smaller particles on increasing the

deposition time or applying more negative reduction potential. These smaller particles finally fused to generate the thermodynamically stable large block-like crystals.

Images of crystals obtained after 50 cycles of the potential confirmed the formation of small crystal clusters when switching the potential at -120 mV and larger block-like shaped crystals at -250 mV (Figure 15a, b). It is interesting to note that the multiple small crystals were structured to give the big block shape crystals. The cyclic voltammetric data can be interpreted as followed; the Ox1 peak corresponds to the oxidation of plate-like crystals which are kinetically favoured at positive potentials and shorter deposition times, while the Ox2 peak can be attributed to the oxidation of the larger block-like crystals which are thermodynamically favoured and are dominant at more negative potentials and longer deposition times. The current magnitude of these Ox1 and Ox2 peaks upon multiple scans is consistent with transformation of kinetically favoured plate-like crystals to thermodynamically favoured big square block crystals. Images obtained at a specific spots on the surface when holding the potential at -250 mV for 2 mins reveal the progression in the transformation from small thin crystals to big block crystals (see Figure 14b). Figure 15c shows the homogenous morphology of CuTCNQF synthesized from reaction of TCNQF and CuI in acetonitrile.

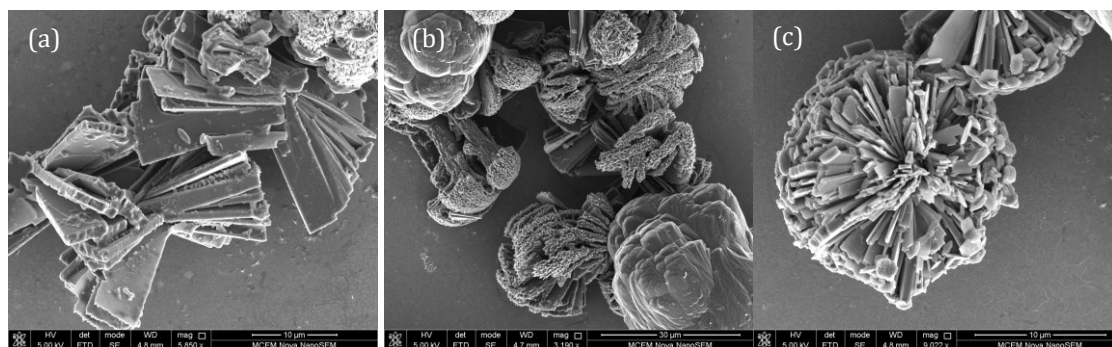


Figure 13. SEM images at different location on surface of CuTCNQF electrocrystallized on ITO electrode from an acetonitrile (0.1 M Bu₄NPF₆) solution containing 8.0 mM TCNQF and 8.0 mM [Cu(MeCN)₄]⁺. Reductive electrolysis of TCNQF to TCNQF⁻ was undertaken for 2 min at -118 mV

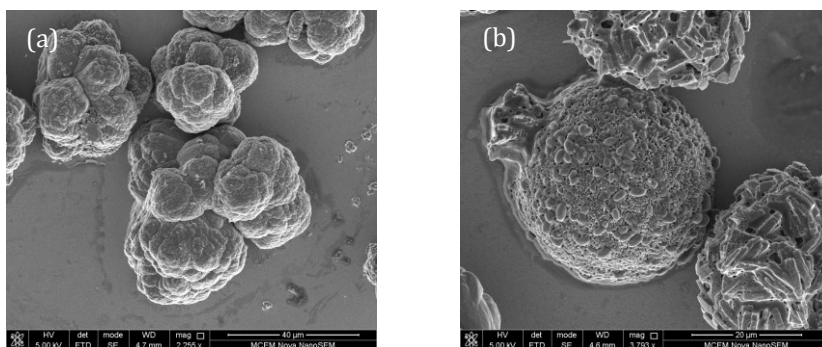


Figure 14. SEM images obtained at different location when CuTCNQF is electrocrystallized onto an ITO electrode surface from an acetonitrile (0.1 M Bu₄NPF₆) solution containing 8.0 mM TCNQF and 8.0 mM [Cu(MeCN)₄]⁺. Reductive electrolysis of TCNQF to TCNQF⁻ was undertaken for 2 min at -250 mV

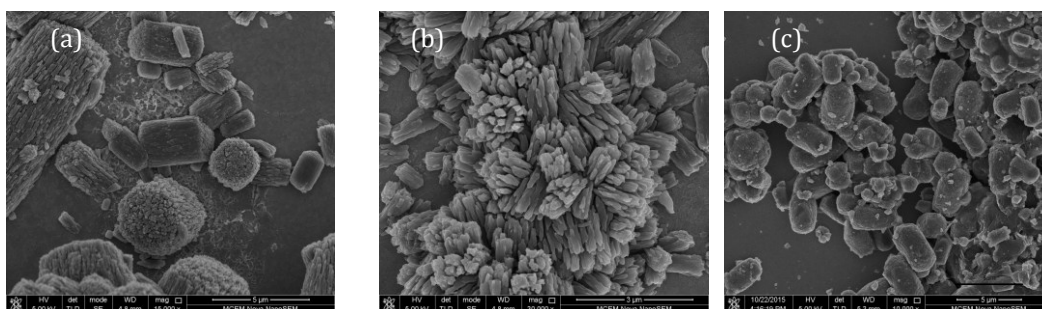


Figure 15. SEM images of (a, b)CuTCNQF electrocrystallized on ITO electrode by 50 cycles of potential from 500 to -118 mV from an acetonitrile (0.1 M Bu₄NPF₆) solution containing 8.0 mM TCNQF and 8.0 mM [Cu(MeCN)₄]⁺ at different magnification, (c) chemical synthesized CuTCNQF from TCNQF and CuI in acetonitrile

4.3.6. Catalytic activity

The redox reaction between ferricyanide and thiosulfate as shown below



was chosen to illustrate the catalytic activity that can be achieved when a CuTCNQF₂ or CuTCNQF layer on a copper foil presents in the solution.

The rate of the reaction can be monitored by UV-Vis spectrometry using the ferric absorption band at $\lambda_{\text{max}} = 420 \text{ nm}$ using a calibration curve.

This reaction has been shown to be catalysed by colloidal noble metals.^{8,9} Recently, O'Mullane *et al.* also reported the catalytic capability of MTCNQ and MTCNQF₄ (M = Cu, Ag).¹⁰

In order to compare the catalytic activity of CuTCNQF_n derivatives and explore the substituent effect on these catalysts, analogous catalytic experiments were performed by using a film of CuTCNQF₂ and CuTCNQF on a piece of Cu foil with an area of 0.16 cm². These foils were then added to the mixture of reactants shown in equation 2 while stirring. Aqueous solution of [Fe(CN)₆]³⁻ and S₂O₃²⁻ is yellow and in the absence of the catalyst, the colour does not change over a period of 2 hours. However the introduction of CuTCNQF₂ or CuTCNQF leads to rapid loss of the initial yellow colour as shown in Figure 16. This change was quantitatively determined by UV-Vis spectra. The absorbance at 420 was monitored at regular time intervals for both catalysts.



Figure 16. Colour change that takes place in a stirred aqueous solution containing 1.0 mM [Fe(CN)₆]³⁻ and 0.1 M S₂O₃²⁻ in the presence of CuTCNQF₂

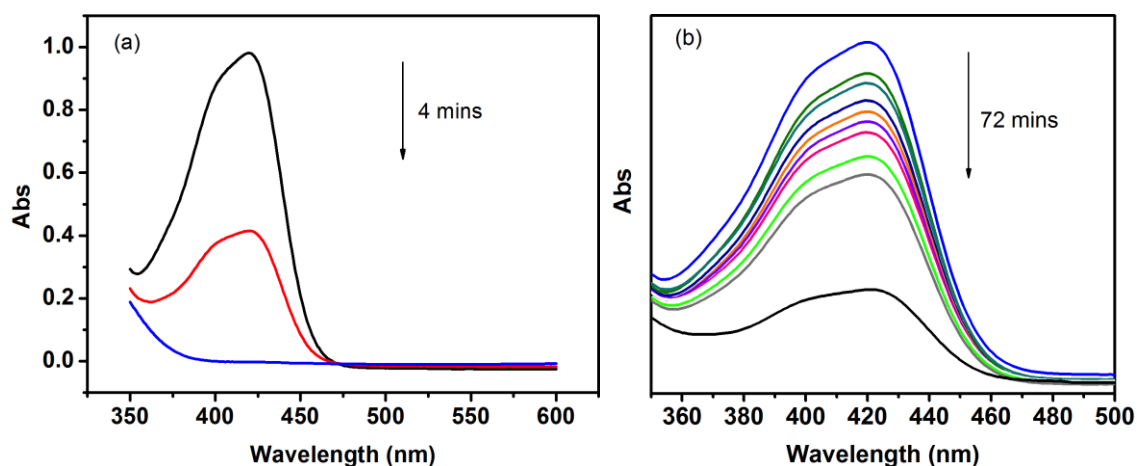


Figure 17. Time dependent UV-Vis spectra of a solution containing 1.0 mM [Fe(CN)₆]³⁻ and 0.1 M S₂O₃²⁻ catalysed by (a) CuTCNQF₂ and (b) CuTCNQF

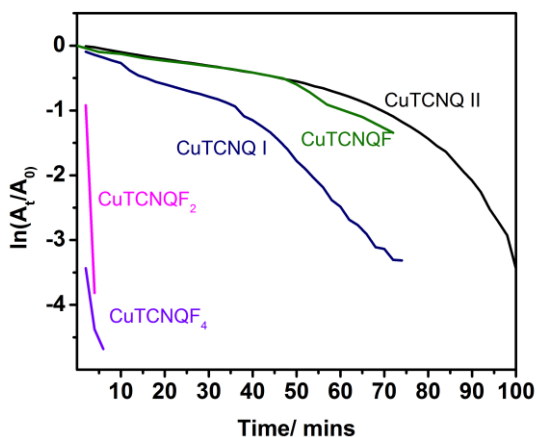


Figure 18. Plot of $\ln(A_t/A_0)$ versus time for CuTCNQ phase I and II, CuTCNQF, CuTCNQF₂ and CuTCNQF₄ (Data of CuTCNQ phase I and II and CuTCNQF₄ is reproduced from ref. 5)

As shown in Figure 17, CuTCNQF₂ significantly enhances the redox reaction as demonstrated by a rapid drop of the Abs at 420 nm. After 4 mins of reaction, the Abs reaches zero (Figure 17a). In contrast, the use of CuTCNQF drives the reaction to a completion state after more than 75 mins (Figure 17b). The reaction is assumed to be first order as thiosulfate presents in large excess, hence the kinetics of this reaction upon introduction of the two catalysts was determined by plotting $\ln(A_t/A_0)$ vs. time, where A_t is the absorbance at time t and A_0 is initial absorbance and taking the slope of the linear part of the graph in comparison with CuTCNQ and CuTCNQF₄ (Figure 18). The reaction rates on using CuTCNQF₂ and CuTCNQF catalyst calculated via the slope of a linear part on the plot are 0.95 min^{-1} and $1.05 \times 10^{-2} \text{ min}^{-1}$, respectively. It is surprising that the introduction of one fluorine atom in TCNQF does not enhance the catalytic activity of CuTCNQF. In contrast, the catalytic activity of CuTCNQF₂ is significantly increased. The catalytic activity among the derivatives are in an order of CuTCNQ phase II ($1.1 \times 10^{-2} \text{ min}^{-1}$) \sim CuTCNQF < CuTCNQ phase I ($2.6 \times 10^{-2} \text{ min}^{-1}$) < CuTCNQF₂ < CuTCNQF₄ (1.09 min^{-1}). However, the end point of the redox reaction of $[\text{Fe}(\text{CN})_6]^{3-}$ and $\text{S}_2\text{O}_8^{2-}$ in the presence of CuTCNQF was at shorter time than both phases of CuTCNQ were used. These results illustrate that the introduction of fluoro substituents, to some extent, affect the catalytic activity of CuTCNQ(F)_n but not necessarily in the order expected for the increase of substitution level.

The catalytic activity depends on several factors, including surface area, material's conductivity or solid-solution interface chemistry. In general, the catalytic reaction is enhanced with catalysts having larger surface area such as nano-materials. CuTCNQ crystal modified with gold nano particles significantly enhances the catalytic activity.¹¹⁻¹³ The morphology CuTCNQF and CuTCNQF₂ surfaces on the Cu foil were examined by SEM imaging. The images reveal a homogenous surface with analogous morphologies for both materials (Figure 19). The surfaces are covered CuTCNQF and CuTCNQF₂ dense blocks. The similar morphology of both catalyst surfaces is against the influence of high surface area on the catalytic activity in this scenario. This is also applied for other TCNQ and TCNQF₄ materials where CuTCNQ phase I although have greater surface area, the catalytic activity is lower than that of CuTCNQF₄.⁵

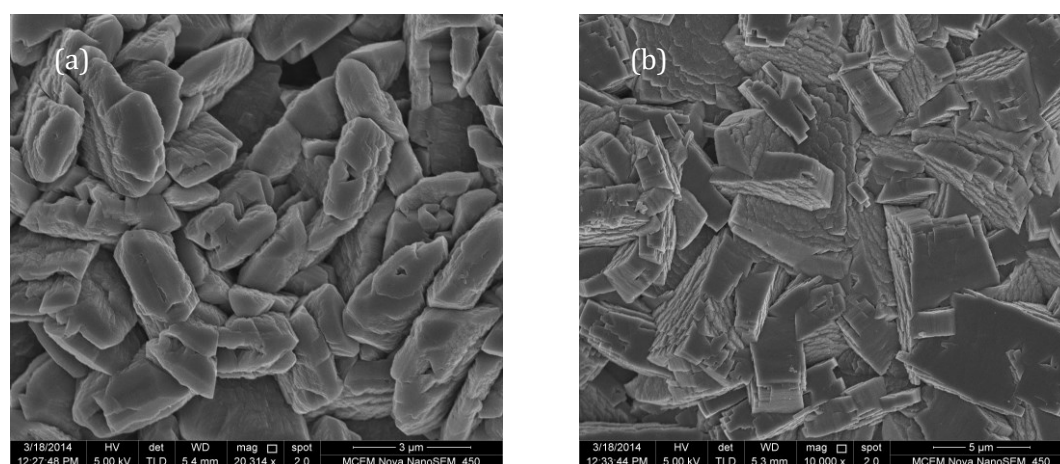


Figure 19. SEM images of (a) CuTCNQF and (b) CuTCNQF₂ surface on Cu foil

The mechanism of catalytic activity was also suggested to involve the charge accumulation on the catalyst surface. Results from open circuit potential experiments support this hypothesis. Comparing the OCP plots (Figure 20) between CuTCNQ, CuTCNQF, CuTCNQF₂ and CuTCNQF₄, shows that in all cases once thiosulphate is injected into the solution, the OCP value decreases which indicates that this process is either decrease in positive charge or increase negative charge on the surface. In this system the injection of thiosulphate should increase the negative charge on the surface. Interestingly, the trend of the decrease in OCP results is consistent with the catalytic activity order among these four derivatives. This suggests that the charge accumulation on those TCNQ derivatives films is

varied. The reason of different charge accumulation however requires further investigation.

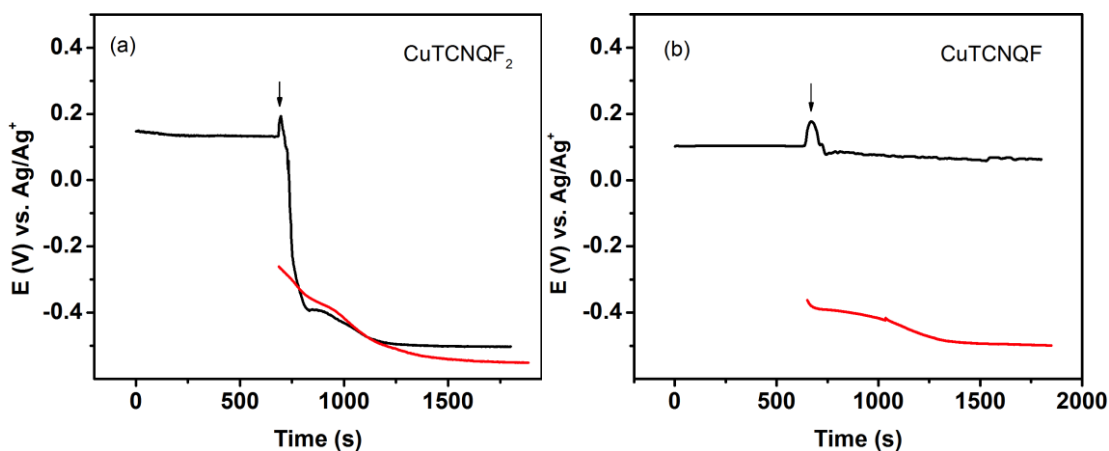


Figure 20 OCP vs. time recorded in 30 ml solution containing 1 mM $[\text{Fe}(\text{CN})_6]^{3-}$ (black) into which 0.1M $\text{S}_2\text{O}_3^{2-}$ was added after 600 s, indicated by an arrow, and containing 0.1 M $\text{S}_2\text{O}_3^{2-}$ (red) for (a) CuTCNQF_2 and (b) CuTCNQF

The composition of the CuTCNQF_n film was compared using IR spectra before and after the catalytic experiment and was found to be identical (Figure 21).

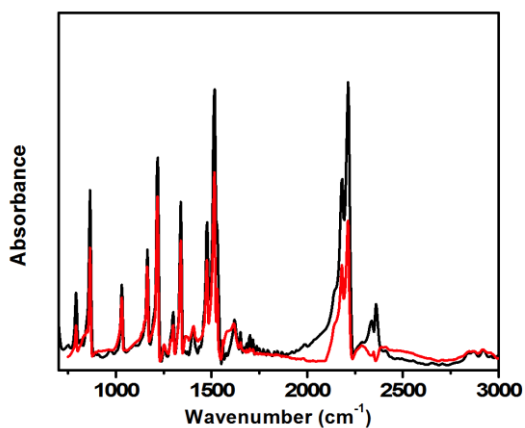


Figure 21. Comparison of the IR spectra of CuTCNQF_2 on a Cu foil before (black) and after (red) catalytic experiment.

4.3.7. Comparison between the four derivatives TCNQF_n ($n = 0, 1, 2, 4$)

The voltammetric behavior of TCNQ and its fluorinated derivatives in the presence of Cu^+ have some common features, although some are quite different. The common feature is that the formation of CuTCNQF_n can be probed on the voltammetric time scale if the concentration of the reactants exceeds their

solubility product. This is evident by the decrease in current ratio of the oxidation and the reduction peak of $\text{TCNQF}_n^{0/-1}$ process indicating the consumption of the soluble TCNQF_n^- into a solid material on the electrode surface during the experiment time scale. Also, a stripping peak observed during the oxidation scan implies that the oxidation removes the CuTCNQF_n material from the electrode surface.

The solubility of these solids can mask the observation of any change in the CV in each TCNQ(F)_n derivatives. While there was clear evidence of the formation of CuTCNQ , CuTCNQF and CuTCNQF_2 in the voltammetric time scale, there was no noticeable reduction or oxidation of CuTCNQF_4 even at a concentration of 10.0 mM of each reactant, although the solubility of CuTCNQF_4 is much lower than that of other derivatives-based materials. Two phases of CuTCNQ were reported with different crystal structures.¹ Voltammetric experiments enable the formation of CuTCNQ phase I in acetonitrile via two distinctly processes to be probe, where either discrete clusters of needles or smaller crystals were formed over the surface. For TCNQF_4 derivatives, evidence for the formation of CuTCNQF_4 comes from the decrease in current ratio between the oxidation and reduction process from 1.0 to approximately 0.7 when the concentration of TCNQF_4 is increased from 1.0 to 10.0 mM in the presence of 10.0 mM of Cu^+ in acetonitrile. Also, a broad peak was observed at more positive potential in the oxidation wave indicates the stripping of CuTCNQ while being oxidized. Interestingly, there was no oxidation peak close to the oxidation of soluble $\text{TCNQF}_4^{-/0}$ couple as was observed in the TCNQ case.

Interestingly, with TCNQF and TCNQF_2 , two oxidation processes were observed. These waves were scan rate dependent indicating that they are kinetic-controlled processes.

In a similar manner to TCNQ case, an additional redox process at more negative potential than the first redox process was observed which was attributed to the redox transformation of TCNQF into CuTCNQF material with a different morphology. Noticeably we are able to probe the morphology evolution voltammetrically and microscopically as discuss in this chapter.

4.4. Conclusion

Cyclic voltammetry of TCNQF in the presence of $[\text{Cu}(\text{MeCN})_4]^+$ in acetonitrile was investigated for both reduction processes $\text{TCNQF}^{0/-/2-}$ without any interference from one process to another by vary the concentration of TCNQF and $[\text{Cu}(\text{MeCN})_4]^+$. The formation of CuTCNQF was detected in voltammetric time scale at a concentration of 8.0 mM of TCNQF and $[\text{Cu}(\text{MeCN})_4]^+$. Crystal of two different morphologies corresponding to the two oxidation processes were probe using cyclic voltammetry as well as in microscopy by SEM. It was revealed that CuTCNQF was initially formed as plate-like crystals, before these crystals converted to smaller crystal and finally fused to form large block shape crystals when the potential was held at more negative value and longer period of time. CuTCNQF, unlike other fluoro derivatives, does not possess good catalytic activity on $\text{Fe}^{3+}/\text{S}_2\text{O}_8^{2-}$ redox reaction. This reaction rate with the presence of CuTCNQF is as slow as in the present of CuTCNQ phase II which is unexpected. The formation of TCNQF^{2-} -based material was also observed in voltammetric experiment, however this material is unstable in air, which are evidenced by IR and Raman spectroscopy.

References

- (1) Heintz, R. A.; Zhao, H.; Ouyang, X.; Grandinetti, G.; Cowen, J.; Dunbar, K. R. *Inorganic Chemistry* **1999**, *38*, 144.
- (2) Neufeld, A. K.; Madsen, I.; Bond, A. M.; Hogan, C. F. *Chemistry of Materials* **2003**, *15*, 3573.
- (3) Harris, A. R.; Neufeld, A. K.; O'Mullane, A. P.; Bond, A. M.; Morrison, R. J. S. *Journal of The Electrochemical Society* **2005**, *152*, C577.
- (4) Le, T. H.; Nafady, A.; Vo, N. T.; Elliott, R. W.; Hudson, T. A.; Robson, R.; Abrahams, B. F.; Martin, L. L.; Bond, A. M. *Inorganic Chemistry* **2014**, *53*, 3230.
- (5) Kosaka, W.; Morita, T.; Yokoyama, T.; Zhang, J.; Miyasaka, H. *Inorganic Chemistry* **2015**, *54*, 1518.
- (6) Miyasaka, H.; Morita, T.; Yamashita, M. *Chemical Communications* **2011**, *47*, 271.
- (7) Abrahams, B. F.; Elliott, R. W.; Hudson, T. A.; Robson, R.; Sutton, A. L. *Crystal Growth & Design* **2015**, *15*, 2437.
- (8) Li, Y.; Petroski, J.; El-Sayed, M. A. *The Journal of Physical Chemistry B* **2000**, *104*, 10956.
- (9) Jana, D.; Dandapat, A.; De, G. *Langmuir* **2010**, *26*, 12177.
- (10) Mahajan, M.; Bhargava, S. K.; O'Mullane, A. P. *RSC Advances* **2013**, *3*, 4440.
- (11) Pearson, A.; Bansal, V.; O'Mullane, A. P. *Electrochimica Acta* **2013**, *114*, 189.
- (12) Pearson, A.; O'Mullane, A. P.; Bhargava, S. K.; Bansal, V. *Inorganic Chemistry* **2012**, *51*, 8791.
- (13) Pearson, A.; O'Mullane, A. P.; Bansal, V.; Bhargava, S. K. *Inorganic Chemistry* **2011**, *50*, 1705.

Chapter 5

Electrochemical synthesis of M^{2+} -TCNQF materials ($M=Ni, Co$): Voltammetric, spectroscopic and microscopic evidence

5.1. Introduction

Transition metal-organic charge transfer salts, such as, CuTCNQ or AgTCNQ have been of wide interest because of their novel electronic and magnetic properties. (see Chapter 1). Much less research has been undertaken with the divalent cations metal organic salts, i.e. compounds compared to these 1:2 metal-(TCNQ⁻)₂ charge transfer materials. Thus, although Cu(TCNQ)₂ salt was synthesized in the 1960s and is diamagnetic,¹ TCNQ-based divalent metal salts have only reported in detail more recently. The chemical synthesis of M(TCNQ)₂(S)₂ complexes with M = Mn, Fe, Co or Ni and S = H₂O or MeOH have been described and these materials show to have diverse magnetic properties.²⁻⁵ The electrochemical formation of TCNQ-based material as M(TCNQ)₂ with Co²⁺, Ni²⁺, Zn²⁺ and Cd²⁺ has been reported.^{6,7} the TCNQ²⁻ compounds with similar M²⁺ cations are highly air-sensitive.⁸⁻¹⁰ However, the formation of TCNQF₄²⁻-based solids with Co²⁺ and Ni²⁺ was confirmed by the careful interpretation of cyclic voltammograms and vibrational spectroscopy.¹¹ As expected, the additional four fluorine atoms significantly enhances the stability of dianionic TCNQF₄²⁻-based materials. In this chapter, the electrochemistry of TCNQF in the presence of Co²⁺ and Ni²⁺ will be discussed and it is shown that by varying the concentrations of M²⁺ and TCNQF, the formation of both TCNQF⁻ and TCNQF²⁻ solids can be distinguished by their characteristic voltammetric behavior.

5.2. Experimental

5.2.1. Chemicals

TCNQF (98%, TCI Tokyo), Ni(ClO₄)₂.6H₂O (Aldrich), Co(ClO₄)₂.6H₂O (Aldrich), AgNO₃ (99.998%, Aldrich) acetonitrile (HPLC grade, Omnisolv), isopropanol (BHD) and acetone (suprasolv, Merch KGaA) were used as received from the manufacturer. Bu₄NPF₆ (Aldrich), used as the supporting electrolyte in electrochemical studies, was recrystallized twice from 96% ethanol (Merck) and then dried at 100°C under vacuum for 24 hours prior to use.

5.2.2. Electrochemistry

Voltammetric experiments were undertaken at room temperature using a Bioanalytical Systems (BAS) 100W electrochemical workstation. A standard three electrode cell (GC, 1 mm diameter) working electrode, a Ag/Ag⁺ (1.0 mM Ag⁺) reference electrode (RE) and a 1.0 mm diameter platinum wire counter electrode, was employed in those experiments. Prior to each experiment the working electrode was polished with 0.3 μm Al₂O₃ slurry using polishing cloth, rinsed with water followed by sonication in an ultra sonic bath for 30 seconds and dried under a stream of nitrogen. For electrocrystallization experiments Prazisions Glass and Optik GmbH indium tin oxide (ITO)-coated glass plates (0.1 – 0.2 cm²) with a resistance of 10 Ω/sq were used. The RE was constructed from Ag wire in contact with acetonitrile solution (0.1 M Bu₄NPF₆) containing 1.0 mM AgNO₃ and separated from the test solution by a salt bridge. The potential of this reference electrode was -124 mV vs the ferrocene/ferrocenium (Fc^{0/+}) couple. All solutions were purged with nitrogen gas for at least 10 min and a stream of nitrogen was maintained above the solutions during the course of the voltammetric experiments. For bulk electrolysis experiments, a large area Pt mesh was used as the working electrode instead of the GC electrode.

5.2.3. Synthesis of M(TCNQF)₂ and MTCNQF where M = Ni²⁺ and Co²⁺

TCNQFⁿ⁻ materials were prepared electrochemically by adding 100.0 mM M²⁺ in acetonitrile to a solution containing 10.0 mM of TCNQF⁻ or TCNQF²⁻ to form M(TCNQF₂)₂ or MTCNQF₂, respectively. In order to prepare TCNQF⁻, the potential at the working electrode was held at -200 mV, while TCNQF²⁻ was generated by further reduction of TCNQF⁻ at -600 mV vs Ag/Ag⁺. The potential was held until the current ratio decrease to 0.1% of the initial value. A precipitate formed immediately, although the solution was kept stirring for a further 10 mins and the solid was collected by filtration and washed several times with CH₃CN and dried under vacuum overnight before further characterization.

5.2.4. Other instrumentations

UV-Vis spectra were recorded with a Varian Cary 5000 UV-Vis NIR spectrophotometer with a 1.0 cm path length quartz cuvette. A Varian UMA600 IR microscope and FTS7000 optics bench using 128 scans and a resolution of 8 cm⁻¹

was used for IR spectra. Raman spectra were recorded on a Renishaw Invia Raman spectrograph with an Argon ion laser excitation at 633 nm. After being coated with Ir, SEM images were collected with a FEI Nova NanoSEM 450 FEGSEM instrumentation using an accelerating voltage of 5.0 kV.

5.3. Result and discussion

5.3.1. Cyclic voltammetry of the TCNQF^{0/-} process in the presence of M²⁺

Voltammetric experiments were performed in an acetonitrile solution containing 10.0 mM TCNQF and variable Ni²⁺ concentration, typically 5.0-50.0 mM. At concentration less than 5.0 mM Ni²⁺ and with a scan rate of 10 mV.s⁻¹, the cyclic voltammograms retained diffusion-controlled characteristics. However, as shown in Figure 1a when the Ni²⁺ concentration increases from 5.0 to 50.0 mM, even though the TCNQF^{0/-} reduction process remains unchanged, the reverse scan showed a new symmetric oxidation process (Ox1) appearing at a more positive potential (215 mV) than the diffusional peak for the TCNQF^{-/0} oxidation process at 112 mV. The oxidation current also increases with an increase in Ni²⁺ concentration. This behavior is consistent with an EC type mechanism which generates an insoluble material when the solubility product is exceeded at the electrode surface. Thus the solid is sequentially deposited on the electrode surface and is oxidized when the potential scan direction was reversed. Process label Ox1 corresponds to the stripping of the insoluble material. This oxidation peak current Ox1 is highly dependent on the scan rate. As shown in Figure 1b Ox1 diminishes on increase the scan rate and disappears at scan rates faster than 50 mV.s⁻¹. The scan rate dependence implies that the formation and deposition of the solid material that is kinetically controlled.

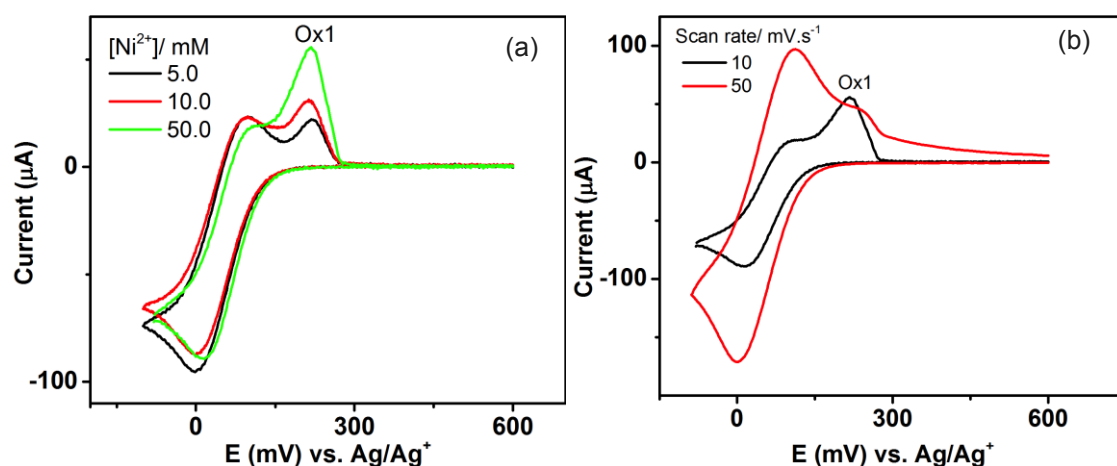


Figure 1. Cyclic voltammograms obtained with a 1 mm diameter GC electrode in acetonitrile (0.1M Bu_4NPF_6) containing 10.0 mM TCNQF, (a) designated Ni^{2+} concentrations. Scan rate = $10 \text{ mV}\cdot\text{s}^{-1}$, (b) 50.0 mM Ni^{2+} at designated scan rates

To further probe the formation of the solid material indicated by Ox1, the electrode potential was held at -80 mV for designated periods of time before scanning the potential in the positive direction.

The deposition time and scan rate dependence for the oxidation process were obtained in a solution containing 10.0 mM TCNQF and 50.0 mM Ni^{2+} as shown in Figure 2 and Figure 3. It is clear that the longer the deposition time, the larger Ox1. At 5 or 10 s of deposition, the oxidation of soluble TCNQF $^-$ remains visible, but at longer times of 30 or 50 s, Ox1 is the dominant oxidation wave (Figure 2).

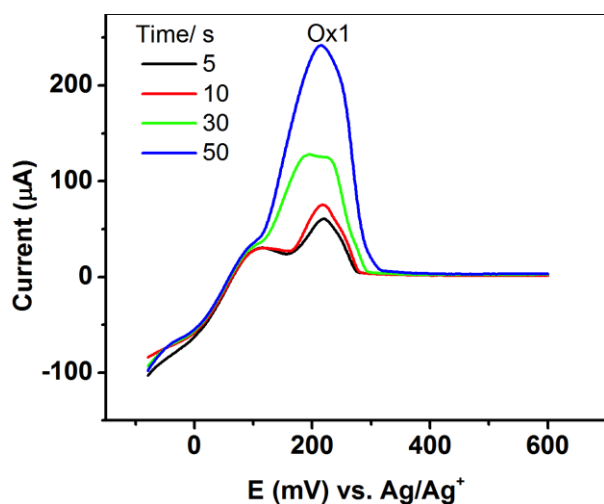


Figure 2. Voltammograms obtained with a 1 mm diameter GC electrode in acetonitrile (0.1M Bu_4NPF_6) containing 10.0 mM TCNQF and 50.0 mM Ni^{2+} when the potential was held at -80 mV for designated time before scan positively to 600 mV. Scan rate = $10 \text{ mV}\cdot\text{s}^{-1}$

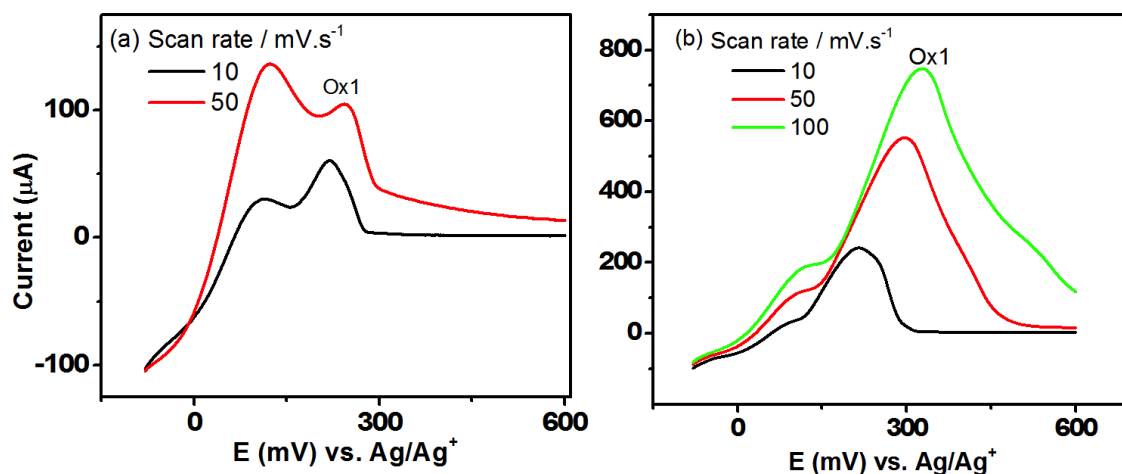


Figure 3. Voltammograms obtained with a 1 mm diameter GC electrode in acetonitrile (0.1M Bu₄NPF₆) containing 10.0 mM TCNQF and 50.0 mM Ni²⁺ when the potential was held at -80 mV for (a) 5 s and (b) 50 s before scan positively to 600 mV at designated scan rates

The scan rate dependence confirms the kinetic controlled nature of the formation of a Ni-TCNQF⁻ material. As can be seen in Figure 3a, at a deposition time 5 s, at a scan rate of 50 mV.s⁻¹, the ratio of peak currents for Ox1 peak and TCNQF^{-/0} oxidation peak has changed on varying the scan rate from 10 mV.s⁻¹ to 50 mV.s⁻¹. At faster scan rate, TCNQF^{-/0} oxidation peak dominates, while Ox1 dominates at slower scan rates. However, when the potential was held at -80 mV for much longer time of 50 s, the peak current magnitude as well as the peak area of Ox1 is significantly increased (Figure 4b) as multiple layer of solid has been formed.

Analogous voltammetric behavior was observed in the presence for Co²⁺. However, the lower solubility of Co-TCNQF material assists the observation of process Ox1 at slightly lower concentrations of both TCNQF and Co²⁺ ions. At concentration of 8.0 mM TCNQF and 8.0 mM Co²⁺, the reduction of TCNQF^{0/-} loses its reversible and diffusion-controlled voltammetric characteristics (Figure 4a). Moreover, the current magnitude TCNQF^{-/0} oxidation process is much smaller than the stripping peak that dominates at more positive potential. Similar to the Ni²⁺-TCNQF⁻ process, the Ox1 is related to the oxidation of Co-TCNQF⁻ material. The kinetically controlled formation of Co-TCNQF⁻ material is also illustrated by varying the switching potential while using a scan rate of 20 mV.s⁻¹ (Figure 4b).

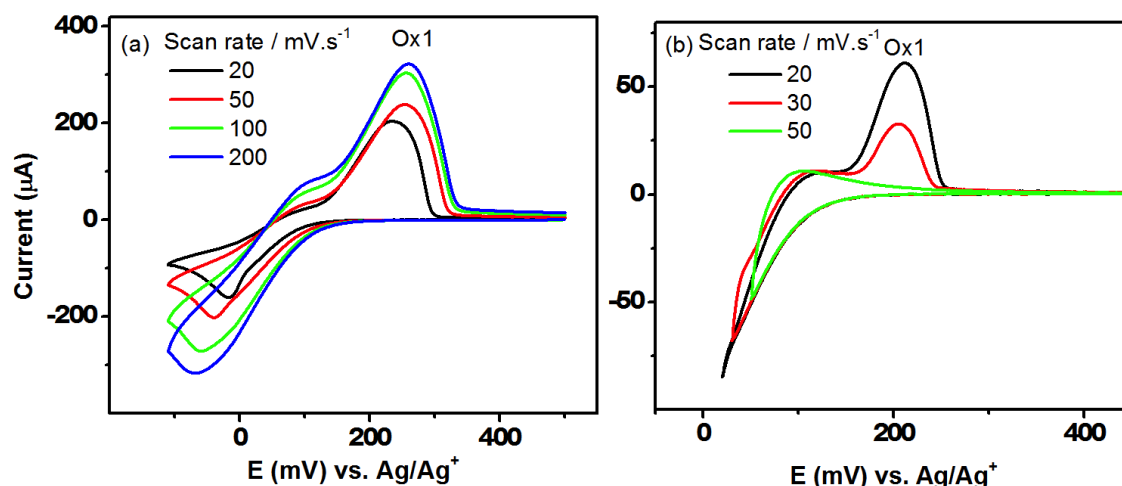


Figure 4. Cyclic voltammograms obtained with a 1 mm diameter GC electrode in acetonitrile (0.1M Bu₄NPF₆) containing 8.0 mM TCNQF and 8.0 mM Co²⁺ (a) at designated scan rates, (b) with designated switching potential at a scan rate of 20 mV.s⁻¹

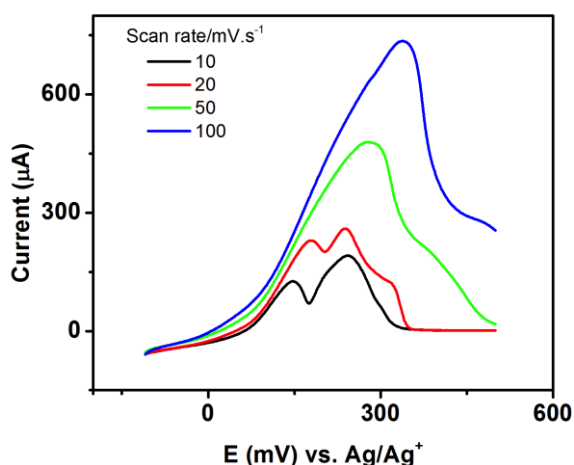


Figure 5. Voltammograms obtained with a 1 mm diameter GC electrode in acetonitrile (0.1M Bu₄NPF₆) containing 8.0 mM TCNQF and 8.0 mM Co²⁺ when the potential was held at -110 mV for 30 s before scan positively to 600 mV at designated scan rate

In order to confirm the formation of TCNQF⁻ solids on the electrode surface, TCNQF was reduced at -110 mV in the presence of Co²⁺ for selected times before scanning positively (Figure 5). Again, oxidation of materials formed on the electrode occurred and the current magnitude increased with scan rate. Thus, this formation is kinetic controlled.

5.3.2. Cyclic voltammetry of the TCNQF^{-/2-} process in the presence of M²⁺

The potential was scanned to the more negative value of -700 mV in order to investigate the behavior of the second redox TCNQF^{-/2-} process in the presence of M²⁺. In this case, more dilute solutions of TCNQF and M²⁺ were used to eliminate the formation of the M-TCNQF⁻ material. Upon addition of 0.5 mM Ni²⁺ to a solution containing 1.0 mM TCNQF, first reduction step TCNQF^{0/-} stays unchanged as found in the absence of M²⁺ (see Chapter 2). However, current magnitude of second reduction step TCNQF^{-/2-} decreases by half and a new reduction process appears at more positive potential -335 mV (Red'). Increasing the concentration of Ni²⁺ to 1.0 mM and higher, TCNQF^{-/2-} step diminishes and is replaced by Red' (see Figure 6). This implies that the reduction process at -335 mV can be attributed to a reduction of TCNQF⁻ to TCNQF²⁻ followed by rapid formation of TCNQF²⁻-M²⁺ material, which consumes TCNQF²⁻ immediately after its formation, by reduction TCNQF⁻. The formation of M²⁺-TCNQF²⁻ material can be described via equation 1-3

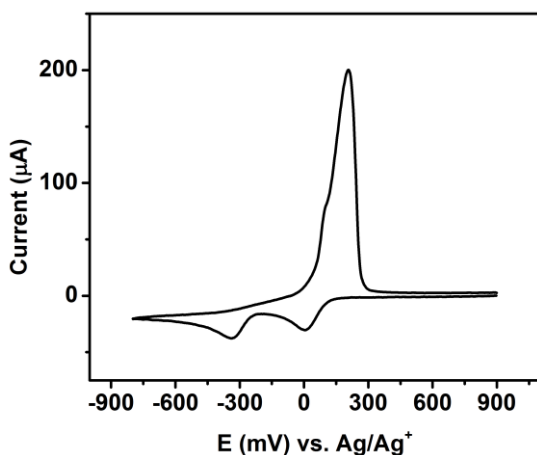
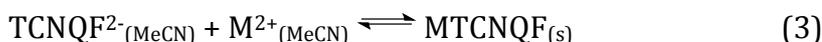
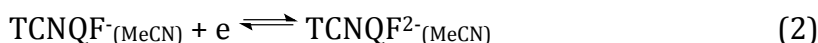
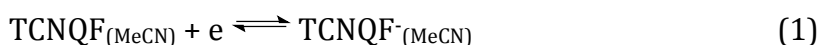
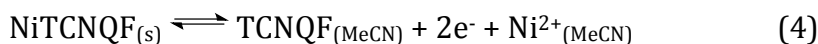


Figure 6. Cyclic voltammograms obtained with a 1 mm diameter GC electrode in acetonitrile (0.1M Bu₄NPF₆) containing 1.0 mM TCNQF and 1.0 mM Ni²⁺ (v = 50 mV.s⁻¹)

On reversing the scan direction, at a concentration ratio equal to 1.0 and higher, a stripping oxidation peak appears at 209 mV and overlaps with the TCNQF^{-/0} oxidation process. This oxidation process is given in equation (4)



The process of the Ox' oxidation counterpart to Red' was confirmed by varying the switching potential as shown in Figure 7. When the potential was switched at -258 mV, a cross-over current was observed at -172 mV and at more negative potential (-341 mV), the peak current significantly increased.

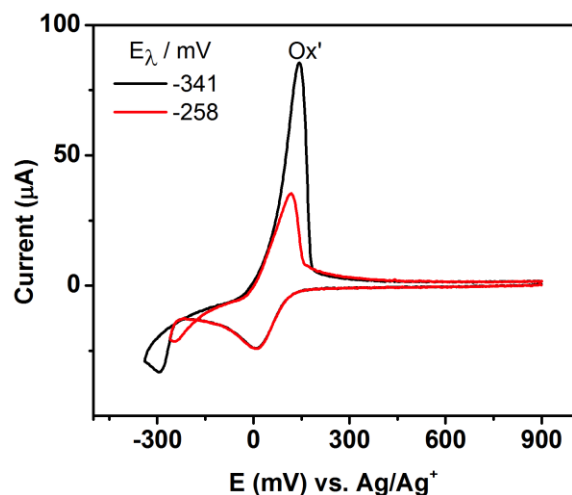


Figure 7 . Cyclic voltammograms obtained with a 1 mm diameter GC electrode in acetonitrile (0.1M Bu₄NPF₆) containing 1.0 mM TCNQF and 1.0 mM Ni²⁺ with different switching potential at 50 mV.s⁻¹

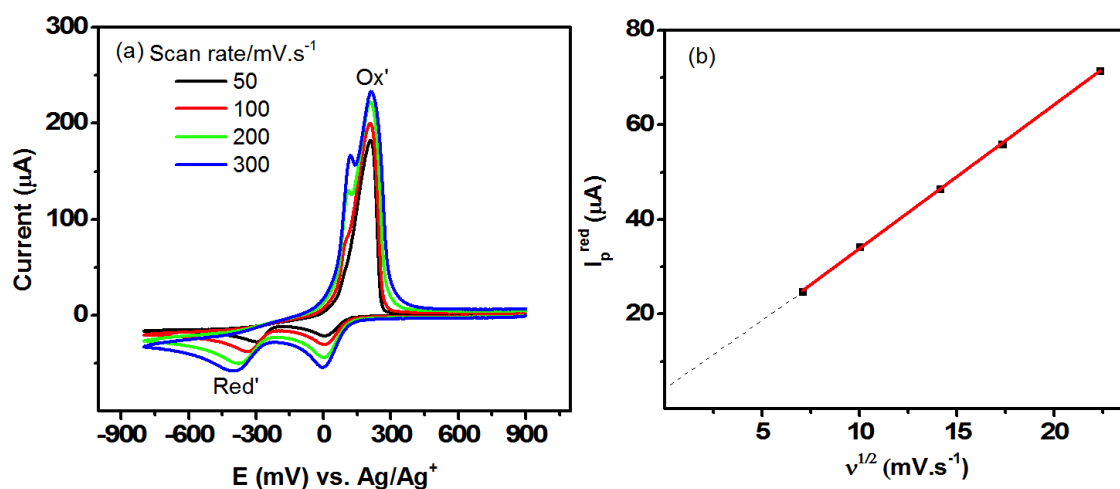


Figure 8 . (a) Cyclic voltammograms obtained with a 1 mm diameter GC electrode in acetonitrile (0.1M Bu₄NPF₆) containing 1 mM TCNQF and 1 mM Ni²⁺ at designated scan rates (b) Plot of I_p^{red} of Red' vs. square root of scan rate derived from (a).

The effect of scan rate is shown in Figure 8. As can be seen, while the TCNQF^{0/-} reduction retains its diffusion controlled characteristics, the E_p value of Red' shifts negatively from -296 to -402 mV upon increasing the scan rate from 50 mV.s⁻¹ to

300 $\text{mV}\cdot\text{s}^{-1}$. For Red', there is a linear relationship between the peak current $E_{\text{red}}^{\text{p}}$ and square root of scan rate $v^{1/2}$. However, the positive intercept from the plot of $E_{\text{red}}^{\text{p}}$ vs $v^{1/2}$ indicates a non-diffusion controlled component. At faster scan rates, two resolved-oxidation processes were observed with that at 116 mV being attributed to the diffusion-controlled oxidation of TCNQF^- to TCNQF^0 and that at ~ 213 mV (Ox') to the oxidation of Ni-TCNQF^{2-} solid to TCNQF^0 .

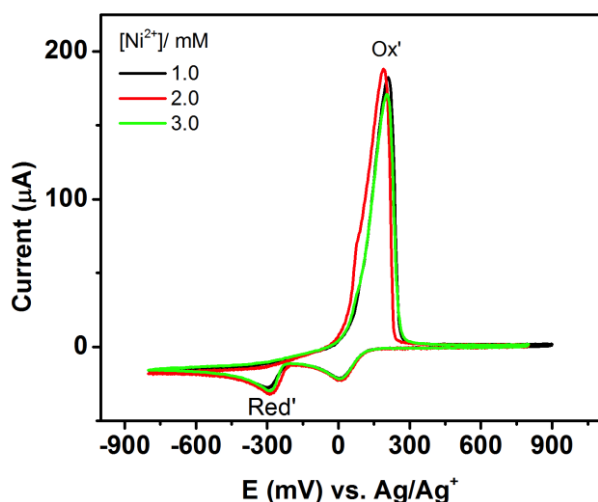


Figure 9. Cyclic voltammograms obtained with a 1 mm diameter GC electrode in acetonitrile (0.1M Bu_4NPF_6) containing 1.0 mM TCNQF and designated Ni^{2+} concentration at a scan rate of $50 \text{ mV}\cdot\text{s}^{-1}$

The influence of Ni^{2+} concentration on the voltammetry for solutions containing 1.0 mM TCNQF is shown in Figure 9 for a scan rate of $50 \text{ mV}\cdot\text{s}^{-1}$. Increasing the Ni^{2+} concentration from 1.0 to 3.0 mM did not significantly change the cyclic voltammograms which indicates that the formation of TCNQF^{2-} -based material is kinetically fast in this voltammetric time scale.

Evidence for the formation of Ni-TCNQF^{2-} material was also found when holding potential at -800mV for a period of time before commencing a positive potential scan (Figure 10a). When holding the potential for 2s, the current magnitude of Ox' increased at a relatively slower rate than that of Ox as the scan rate was increased. An increase in the reduction time led to a relative increase in the Ox' peak current magnitude, which means that there was more material deposited and stripped from the electrode surface.

An analogous behavior was observed in the presence of Co^{2+} indicating the formation of Co-TCNQF^{2-} solid during voltammetric time scale.

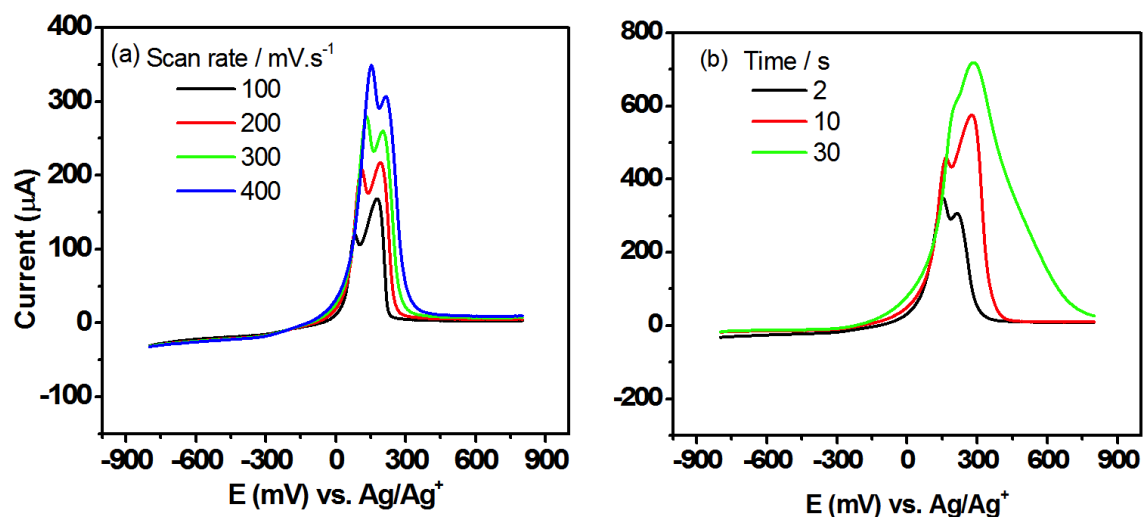


Figure 10. (a) Voltammograms obtained with a 1 mm diameter GC electrode in acetonitrile (0.1M Bu₄NPF₆) containing 1 mM TCNQF₂ and 2 mM Ni²⁺ when potential was held at -800 mV before scanning positively (a) for 2 s at designated scan rate (b) for designated times at 400 mV.s⁻¹

5.3.3. Elemental microanalysis

Microanalysis data for both Co- and Ni-TCNQF₂⁻ materials indicate the presence of H₂O in these materials. The results for Co material are C 52.97% (53.44%), H 1.96% (1.86%), N 19.48% (20.77%), which is consistent with a composition of Co(TCNQF)₂.2H₂O, for Ni material are C 52.98%(53.43%), H 1.97% (1.87%), N 20.14% (20.77%) which is consistent with a composition of Ni(TCNQF)₂.2H₂O. The coordination of two water molecules in the composition of M(TCNQF)₂.2H₂O is consistent with TCNQ complexes with other divalent metal cations has been reported with the coordination of either two H₂O or two MeOH.²⁻⁵ The TGA data also reveals a lost ~ 8.5% of the mass at the temperature below 120-150°C, confirming the existence of 2 water molecules (Figure 11).

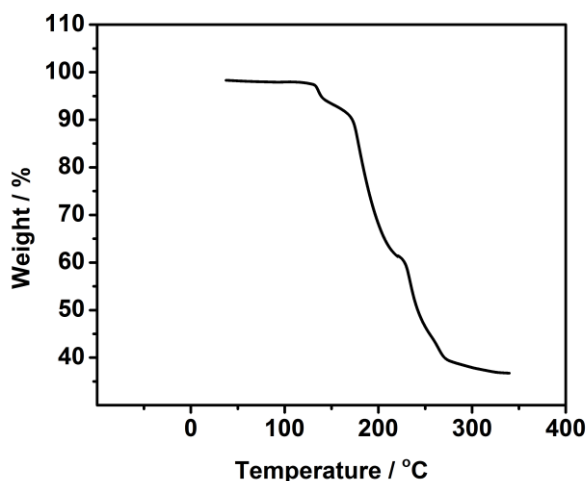


Figure 11. TGA data for electrochemically synthesized Ni(TCNQF)₂·2H₂O material

5.3.4. Solubility of M(TCNQF)₂ materials

The solubility of M(TCNQF)₂·2H₂O in acetonitrile was determined by monitoring the concentration of TCNQF₂⁻ using UV-Vis spectrophotometry and steady state voltammetry at a 125 μm diameter gold microelectrode. For Co(TCNQF)₂·2H₂O in the absence of electrolyte, the solubility was found to be 0.323 ± 0.005 mM. In the presence of 0.1 M Bu₄NPF₆, the solubility increased to 0.486 ± 0.009 mM which is a result of ion pairing with the electrolyte ions. The calculated solubility product of Co(TCNQF)₂·2H₂O is 1.14 × 10⁻¹⁰ M³ with electrolyte and 3.37 × 10⁻¹¹ M³ without electrolyte. For Ni(TCNQF)₂·2H₂O, the solubility was found to be 0.640 ± 0.008 mM and 0.177 ± 0.012 mM with and without the presence of electrolyte, respectively, which results in solubility products of 2.65 × 10⁻¹⁰ M³ in the presence and 5.54 × 10⁻¹² M³ in the absence of electrolyte.

5.3.5. IR and Raman spectroscopy

IR and Raman spectroscopy of materials synthesized electrochemically by direct addition M²⁺ in a solution containing TCNQF⁻ prepared by bulk electrolysis and electrocrystallized on an ITO electrode are shown in Figure 12. The characteristic bands of the TCNQ family are evident in their spectra. For the Co(TCNQF)₂ solid, the C ≡ N stretch at 2212, 2190 cm⁻¹, ring C=C stretch at 1510 cm⁻¹, 1264 cm⁻¹, exo C=C stretch at 1493 cm⁻¹, mixing endocyclic ring C-C and C-F stretch at 1353 and 1323 cm⁻¹ and C-CN stretch at 1196 cm⁻¹. These bands are closely resemble those in calculated spectrum described in Chapter 2. The presence of broad IR

absorption at $\sim 3400\text{ cm}^{-1}$ and a band at $\sim 1600\text{ cm}^{-1}$ supports the presence of H_2O found in the analytical data. Raman bands at 2232 cm^{-1} for the $\text{C}\equiv\text{N}$ stretch, 1613 cm^{-1} for ring the $\text{C}=\text{C}$ stretch and 1399 cm^{-1} for the exocyclic stretch are characteristic for monoanion TCNQF^- as discussed in chapter 2. A similar spectrum for $\text{Ni}(\text{TCNQF})_2$ solid was obtained.

In the case of TCNQF^- solid electrocrystallized on ITO electrode, IR and Raman spectra closely resemble those of bulk-synthesized solids, except that the broad band for water at $\sim 3400\text{ cm}^{-1}$ was absent. Small amount of material electrocrystallized on the ITO electrode under nitrogen blanket may assist the removal of water during rinsing and drying in vacuum, which is harder than with bulk-synthesized samples. This can cause the absent of 3400 cm^{-1} band in IR spectrum as found in bulk-synthesized material.

M- TCNQF^{2-} materials were also synthesized and characterized. Bright yellow colour precipitates formed immediately after adding 10.0 mM M^{2+} ($\text{M} = \text{Ni}^{2+}, \text{Co}^{2+}$) to 5.0 mM TCNQF^{2-} obtained by bulk electrolysis. However, it gradually changed to green. The IR and Raman spectra are shown in Figure 14 for the green solid. A red shift was expected if TCNQF^{2-} was present. In IR spectrum, absorption of $\text{C}\equiv\text{N}$ stretch was observed at $2230, 2130$ and 2064 cm^{-1} . The splitting in $\text{C}\equiv\text{N}$ absorption bands has been reported with TCNQF_4^{2-} -based materials due to the nature of metal-nitrile bond in the material.¹¹⁻¹³ The mixing mode of ring C-C and C-F stretch at 1504 and 1307 cm^{-1} also showed a shift to lower energy compared to TCNQF^- materials. However, absorption bands in the Raman spectra at 1617 and 1403 cm^{-1} are characteristic for a symmetric ring $\text{C}=\text{C}$ stretch mode and exocyclic $\text{C}=\text{C}$ mode respectively in monoanion material. These observations consistent with the colour change suggest that TCNQF^{2-} based materials are not stable in the presence of air and are slowly oxidized to the monoanion-based solids.

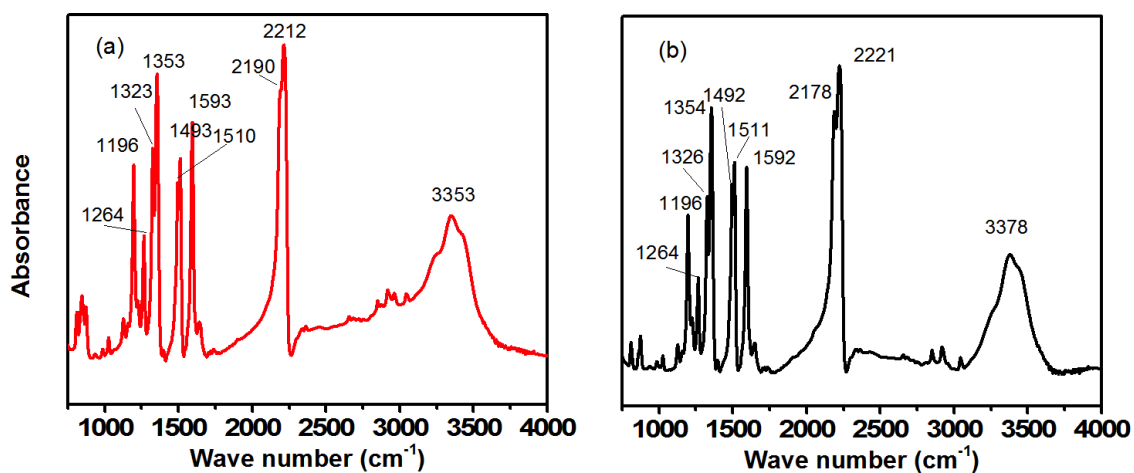


Figure 12. IR spectra for Co(TCNQF)₂ (a) and Ni(TCNQF)₂ bulk-synthesized solids

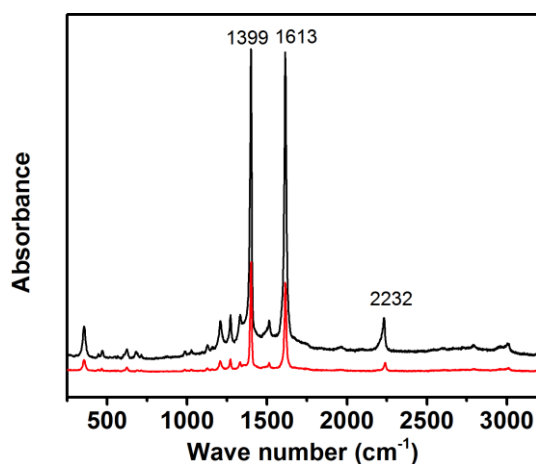


Figure 13. Raman spectra for bulk-synthesized solids of Co(TCNQF)₂ (red) and Ni(TCNQF)₂ (black) materials

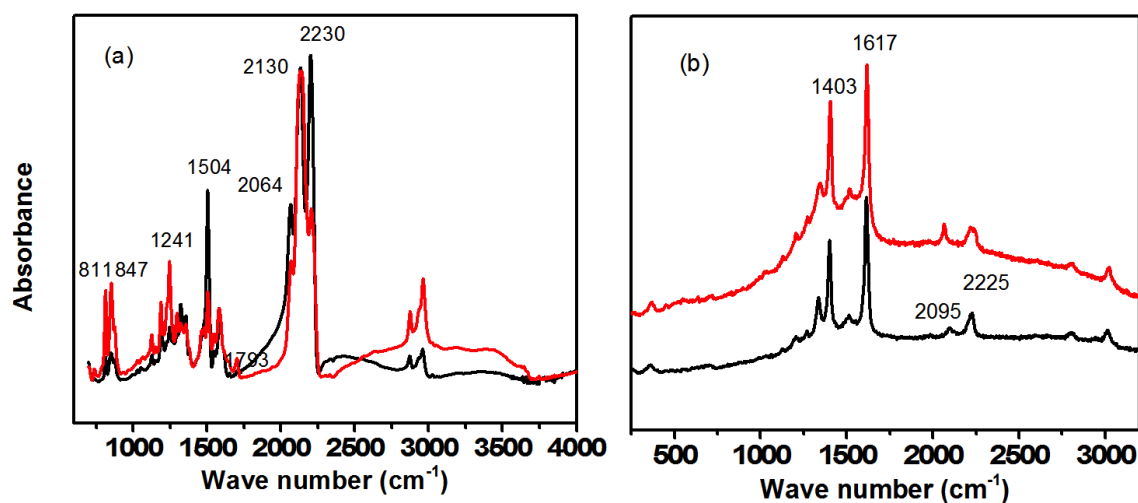


Figure 14. IR (a) and Raman (b) spectra for electrocrystallized Co(TCNQF)₂ (red) and Ni(TCNQF)₂ (black) materials on an ITO electrode

5.3.6. Morphology of TCNQF-based material

SEM imaging were used to examine the morphologies of the TCNQF⁻ and TCNQF²⁻-based materials electrocrystallized onto an ITO electrode. Ni(TCNQF)₂·2H₂O electrocrystallized in discrete ~ 2 μm long cylindrical crystal (see Figure 17a), while Co(TCNQF)₂·2H₂O crystal are long and sharp needle-like growing out of electrode surface (see Figure 17b). EDAX analysis of the composition of electrodeposited materials confirmed the presence of Co and Ni along with carbon and nitrogen as required for formation of M(TCNQF)₂·2H₂O (Figure 17).

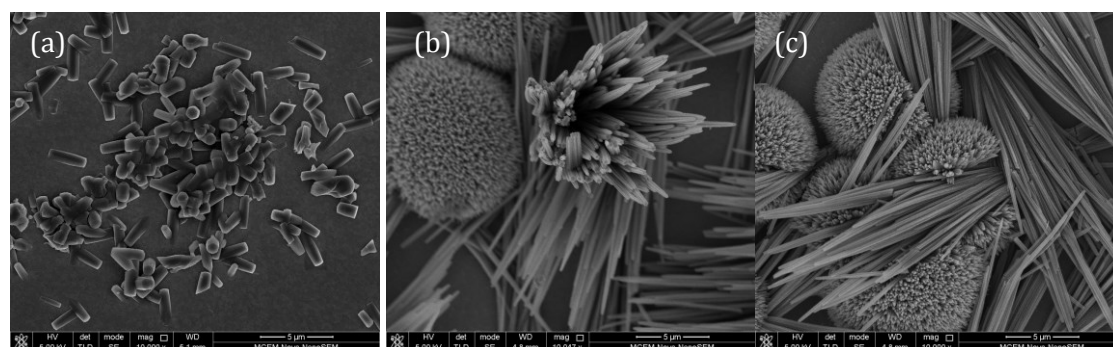


Figure 15. SEM image of electrocrystallized (a) Ni(TCNQF)₂·2H₂O (b,c) Co(TCNQF)₂·2H₂O obtained by reducing 10.0 mM TCNQF to TCNQF⁻ at -200 mV in the presence of M²⁺ for 3 mins with an ITO electrode

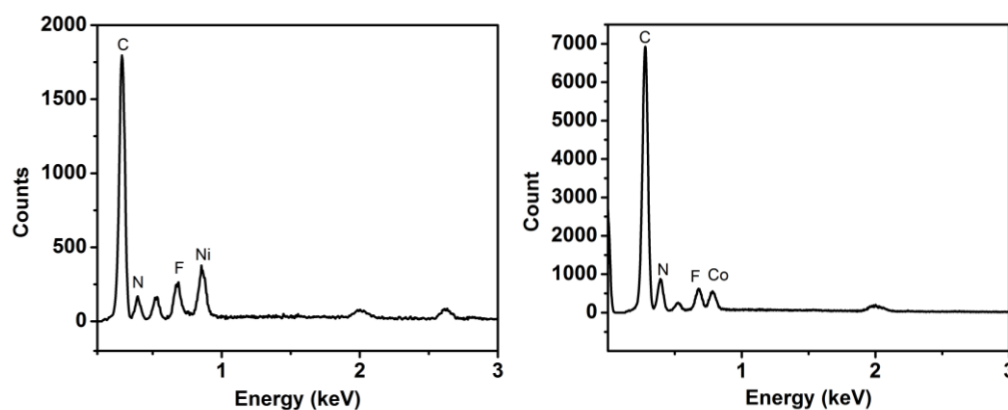


Figure 16. EDAX spectrum for (a) Ni(TCNQF)₂·2H₂O and (b) Co(TCNQF)₂·2H₂O

SEM images of TCNQF²⁻ materials electrocrystallized by holding the potential at -700 mV for 180s exhibit an entirely different morphology as shown in Figure 17. While discrete crystals were observed for monoanionic based materials of both cations, electrocrystallization of dianionic solids generated clusters of crystals with different sizes and shapes. Block-shaped crystals of Ni-TCNQF²⁻ were built up

during electrolysis experiment and covered the entire ITO electrode surface. Whereas, solids of Co-TCNQF²⁻ is longer and thinner in shape.

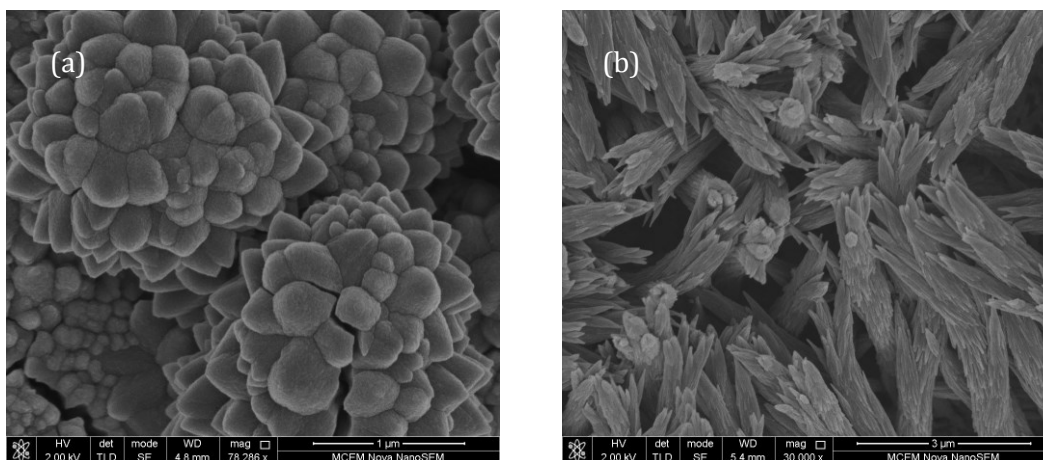


Figure 17. SEM image of electrocrystallized (a) Ni-TCNQF²⁻ (b) Co-TCNQF²⁻ obtained by reducing 1.0 mM TCNQF at -500 mV in the presence of M²⁺ for 3 mins with an ITO electrode

5.4. Conclusion

The electrochemistry of TCNQF in the presence of Ni²⁺ and Co²⁺ has been described with respect to the TCNQF^{0/-} and TCNQF^{-/2-} reduction processes. The formation of M(TCNQF)₂·2H₂O and its electrochemistry was probed by cyclic voltammetric experiments using a range of different concentrations. The formation of Co(TCNQF)₂ also can be detected using 8.0 mM for both M²⁺ and TCNQF but higher concentrations of TCNQF and Ni²⁺ are required to detect the nickel analogue (10.0 mM of TCNQF and 50.0 mM Ni²⁺). Voltammetric data also reveal that the formation of TCNQF⁻ solids is kinetically controlled. The second TCNQF^{-/2-} reduction step also change dramatically in the presence of M²⁺. The TCNQF⁻-based solid was characterized and is consistent with a formulae M(TCNQF)₂·2H₂O. Unfortunately, the TCNQF²⁻-based solids are easily oxidized in air to give M(TCNQF)₂ so they are not fully characterized.

References

- (1) Melby, L. R.; Harder, R. J.; Hertler, W. R.; Mahler, W.; Benson, R. E.; Mochel, W. E. *Journal of the American Chemical Society* **1962**, *84*, 3374.
- (2) Zhao, H.; Heintz, R. A.; Dunbar, K. R.; Rogers, R. D. *Journal of the American Chemical Society* **1996**, *118*, 12844.
- (3) Zhao, H.; Heintz, R. A.; Ouyang, X.; Dunbar, K. R.; Campana, C. F.; Rogers, R. D. *Chemistry of Materials* **1999**, *11*, 736.
- (4) Clérac, R.; O'Kane, S.; Cowen, J.; Ouyang, X.; Heintz, R.; Zhao, H.; Bazile, M. J.; Dunbar, K. R. *Chemistry of Materials* **2003**, *15*, 1840.
- (5) Vickers, E. B.; Giles, I. D.; Miller, J. S. *Chemistry of Materials* **2005**, *17*, 1667.
- (6) Nafady, A.; Bond, A. M.; Bilyk, A.; Harris, A. R.; Bhatt, A. I.; O'Mullane, A. P.; De Marco, R. *Journal of the American Chemical Society* **2007**, *129*, 2369.
- (7) Nafady, A.; O'Mullane, A. P.; Bond, A. M. *Coordination Chemistry Reviews* **2014**, *268*, 101.
- (8) Suchanski, M. R.; Vanduyne, R. P. *J. Am. Chem. Soc.* **1976**, *98*, 250.
- (9) Lombardo, A.; Fico, T. R. *J. Org. Chem.* **1979**, *44*, 209.
- (10) Grossel, M. C.; Duke, A. J.; Hibbert, D. B.; Lewis, I. K.; Seddon, E. A.; Horton, P. N.; Weston, S. C. *Chem. Mater.* **2000**, *12*, 2319.
- (11) Le, T. H.; Nafady, A.; Bond, A. M.; Martin, L. L. *European Journal of Inorganic Chemistry* **2012**, *2012*, 5534.
- (12) Haworth, N. L.; Lu, J.; Vo, N.; Le, T. H.; Thompson, C. D.; Bond, A. M.; Martin, L. L. *ChemPlusChem* **2014**, *79*, 962.
- (13) Nafady, A.; Le, T. H.; Vo, N.; Haworth, N. L.; Bond, A. M.; Martin, L. L. *Inorganic Chemistry* **2014**, *53*, 2268.

Chapter 6

Electrochemical synthesis of Ni²⁺ and Co²⁺ TCNQF₂-based in acetonitrile

6.1. Introduction

Electrochemical formation of TCNQ and TCNQF₄-based materials has been widely investigated, including comparisons to derivatives formed using a chemical synthesis approach.¹⁻⁹ Much of this work has been reviewed in Chapter 1. In chapter 5, details of electrochemistry of M²⁺-TCNQF materials are provided, where M²⁺ = Ni or Co ions. Of note, it was shown that the difference in solubility of TCNQF⁻ complexes has enabled an assessment of their electrochemical formation with Co²⁺ and Ni²⁺ and properties investigated, whereas, the M²⁺-derivatives of TCNQ⁻ and TCNQF₄⁻ haven't been described. Although detectable within voltammetric time scale, TCNQF₂²⁻-based materials are not stable on exposure to the air, as evident by spectroscopic analysis. In this Chapter, the electrochemical synthesis of Co²⁺ and Ni²⁺ derivatives of TCNQF₂⁻ and TCNQF₂²⁻ is described by carefully choice of the concentrations of M²⁺ and TCNQF₂. Again, as found for TCNQF₂²⁻, it has been found that TCNQF₂²⁻-derivatives decomposed in the air. Thus, only the tetrafluorinated TCNQF₄²⁻ could stabilize the cationic complexes, with Ni²⁺ and Co²⁺.

6.2. Experimental

6.2.1. Chemicals

TCNQF₂ (98%, TCI Tokyo), Ni(ClO₄)₂.6H₂O (Aldrich), Co(ClO₄)₂.6H₂O (Aldrich), AgNO₃ (99.998%, Aldrich) acetonitrile (HPLC grade, Omnisolv), isopropanol (BHD) and acetone (suprasolv, Merch KGaA) were used as received from the manufacturer. Bu₄NPF₆ (Aldrich), used as the supporting electrolyte in electrochemical studies, was recrystallized twice from 96% ethanol (Merck) and then dried at 100°C under vacuum for 24 hours prior to use.

6.2.2. Electrochemistry

Voltammetric experiments were studied at room temperature using a Bioanalytical Systems (BAS) 100W workstation. A standard three electrode cell configuration, comprising a glassy carbon (GC, 1 mm diameter) working electrode,

a Ag/Ag⁺ (1.0 mM Ag⁺) reference electrode (RE) and a 1.0 mm diameter platinum wire counter electrode, was employed in those experiments. Prior to each experiment the working electrode was polished with 0.3 μm Al₂O₃ slurry using polishing cloth, rinsed with water followed by sonication in an ultra sonic bath for 30 seconds and dried under a stream of nitrogen. For electrocrystallization experiments Prazisions Glass and Optik GmbH indium tin oxide (ITO)-coated glass plates (0.1 – 0.2 cm²) with a resistance of 10 Ω/sq. The RE was constructed from Ag wire in contact with acetonitrile solution (0.1 M Bu₄NPF₆) containing 1.0 mM AgNO₃ and separated from the test solution by a salt bridge. The potential of this reference electrode was -124 mV vs the ferrocene/ferrocenium (Fc^{0/+}) couple. All solutions were purged with nitrogen gas for at least 10 min and a stream of nitrogen was maintained above the solutions during the course of the voltammetric experiments. For bulk electrolysis experiments, a large area Pt mesh was used as the working electrode instead of the GC electrode.

6.2.3. Synthesis of M(TCNQF₂)₂ and MTCNQF₂, where M = Ni²⁺, Co²⁺

TCNQF₂ⁿ⁻ materials was prepared electrochemically by adding 100.0 mM M²⁺ (where M = Ni²⁺ or Co²⁺) in acetonitrile to a solution containing 10.0 mM of TCNQF₂⁻ or TCNQF₂²⁻ to form M(TCNQF₂)₂ or MTCNQF₂, respectively. In order to prepare TCNQF₂⁻, the potential at the working electrode was held at -100 mV, while TCNQF₂²⁻ was generated by further reduction of TCNQF₂⁻ at -500 mV vs Ag/Ag⁺. The potential was held until the current ratio decrease to 0.1% of the initial value. Precipitate formed immediately. The solution was kept stirring for 10 mins and the solid was collected by filtration and washed several times with CH₃CN and dried under vacuum overnight before further characterization.

6.2.4. Other instrumentation

UV-Vis spectra were recorded with a Varian Cary 5000 UV-Vis NIR spectrophotometer with a 1.0 cm path length quartz cuvette. A Varian UMA600 IR microscope and FTS7000 optics bench using 128 scans and a resolution of 8 cm⁻¹ was used for IR spectra. Raman spectra were recorded on a Renishaw Invia Raman spectrograph with an Argon ion laser excitation at 633 nm. After being coated with Ir, SEM images were collected with a FEI Nova NanoSEM 450 FEGSEM instrumentation using an accelerating voltage of 5.0 kV.

6.3. Result and discussion

6.3.1. Voltammetry of TCNQF₂ in the presence of M(ClO₄)₂ (M: Co, Ni)

Cyclic voltammetry was used to examine the M-TCNQF₂ solid materials which deposited on the electrode surface. Cyclic voltammograms were obtained for the reduction of TCNQF₂ in the absence and presence of M(ClO₄)₂ in acetonitrile (0.1 M Bu₄NPF₆) at a glassy carbon (GC) electrode. In the absence of M²⁺, TCNQF₂ undergoes two diffusion-controlled, one-electron, chemically and electrochemically reversible processes as described in Chapter 2. These processes correspond to reduction of TCNQF₂ to TCNQF₂⁻ and further to TCNQF₂²⁻. Furthermore, the reduction of M²⁺ in acetonitrile is much more negative than for TCNQF₂; hence the voltammetry of TCNQF₂ can be studied without interference from these metal ions.

Initially, cyclic voltammetric experiments were performed in acetonitrile solution containing 4.0 mM TCNQF₂ and 2.0 mM Co²⁺. The scan rate dependence on the voltammetric behavior of the TCNQF₂^{0/-} process is described in Figure . Using a slow scan rate of 10 mV.s⁻¹, the TCNQF₂^{0/-} reduction wave remains diffusion controlled. However, on reversing the scan direction, a new sharp and well defined oxidation process was observed at 251 mV (Ox1). At faster scan rates (50 or 100 mV.s⁻¹), the peak current magnitude of this process decreases and is absent at scan rates faster than 100 mV.s⁻¹.

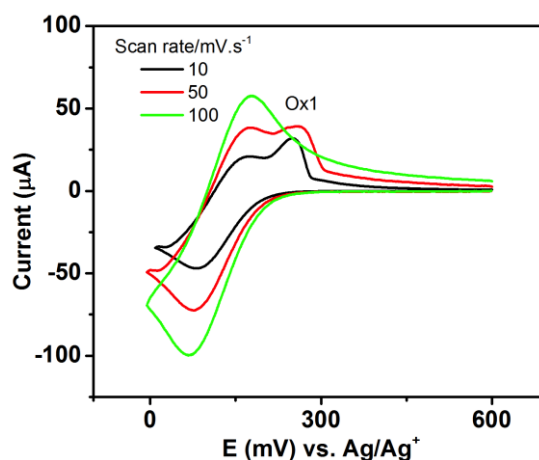


Figure 1. Cyclic voltammograms obtained with a 1 mm diameter GC electrode in acetonitrile (0.1M Bu₄NPF₆) containing 4 mM TCNQF₂ and 2 mM Co²⁺ at designated scan rate

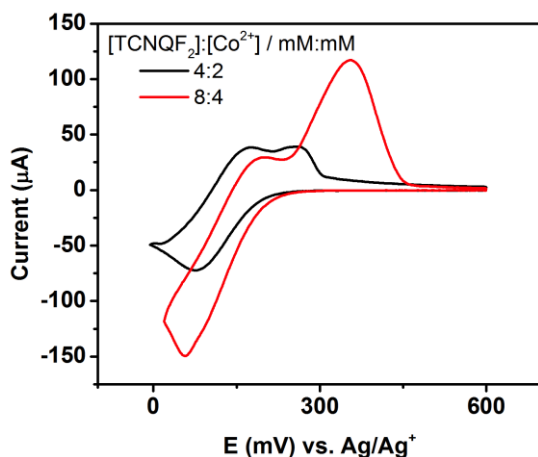


Figure 2. Cyclic voltammograms obtained with a 1 mm diameter GC electrode at a scan rate of 50 mV.s⁻¹ in acetonitrile (0.1M Bu₄NPF₆) containing 4 mM TCNQF₂ and 2 mM Co²⁺ (black), and 8 mM TCNQF₂ and 4 mM Co²⁺ (red)

At the higher concentration, with a solution containing of 8.0 mM TCNQF₂ and 4.0 mM Co²⁺ (Figure 2), current magnitude of the new process increases and the oxidation peak shifts to a more positive potential. This behavior is characteristic of the formation of a solid material upon reduction of TCNQF₂ to TCNQF₂⁻, accompanied by a stripping process on the oxidative reverse scan. Thus, TCNQF₂⁻ formed by the reduction of TCNQF₂ reacts with Co²⁺ and forms a solid which is precipitated onto the electrode surface. This solid material is then oxidized in the reverse scan to regenerate the neutral TCNQF₂.

Results obtained by varying the switching potential in an acetonitrile solution containing 8.0 mM Co²⁺ and 4.0 mM TCNQF₂ are shown in Figure 3. Switching the potential at a more negative potentials, from 100 to 50 to 17 mV, led to an increase in current magnitude of the oxidation stripping peak at 355 mV (Ox1). As described in Chapter 5, this is consistent with TCNQF₂⁻ formed by reduction of TCNQF₂ reacted with Co²⁺ to give a solid on the electrode. This Co-TCNQF₂ solid material can only be formed when the product of the concentration of Co²⁺ and TCNQF₂⁻ exceeds the solubility product, hence, the earlier the potential is switched, the less TCNQF₂⁻ formed.

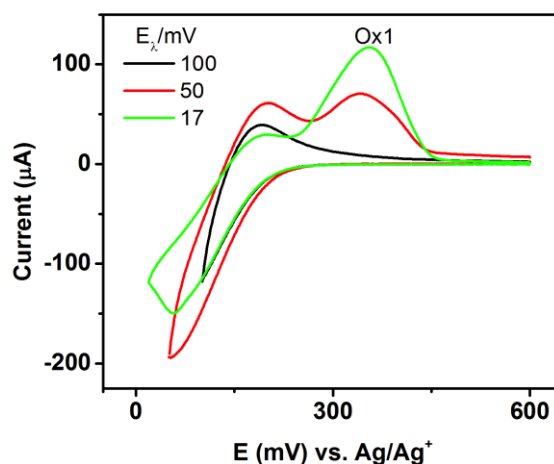


Figure 3. Cyclic voltammograms obtained with a 1 mm diameter GC electrode in acetonitrile (0.1M Bu₄NPF₆) containing 8 mM TCNQF₂ and 4 mM Co²⁺ at a scan rate of 50 mV.s⁻¹ at designated switching potential

In the presence of Ni²⁺ and with low concentrations of TCNQF₂ and Ni²⁺, the voltammogram of the TCNQF₂^{0/-} remains diffusion controlled without any evidence of solid formation on the electrode surface, i.e. unlike Co-TCNQF₂ system. However, a layer of green solution was observed close to electrode surface during the reduction scan which faded during the reverse oxidation scan. TCNQF₂^{0/-} process loses its reversible characteristics at low scan rates when an acetonitrile solution contains the higher concentrations 10.0 mM TCNQF₂ and 50.0 mM of Ni²⁺ (Figure 4). At a scan rate of 10 mV.s⁻¹, a new broad oxidation process appears at 347 mV (Ox1) which is associated with the stripping of a surface confined material. At faster scan rates, this stripping peak can't be observed. This implies that the kinetics for the precipitation of Ni²⁺-TCNQF₂⁻ is slow. Analogous voltammograms were also observed when using a semiconducting, indium tin oxide electrode.

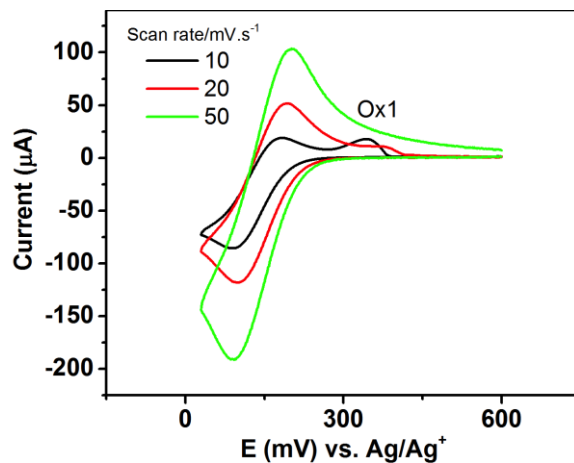


Figure 4. Cyclic voltammograms obtained with a 1 mm diameter GC electrode in acetonitrile (0.1M Bu₄NPF₆) containing 10 mM TCNQF₂ and 50 mM Ni²⁺ at designated scan rates

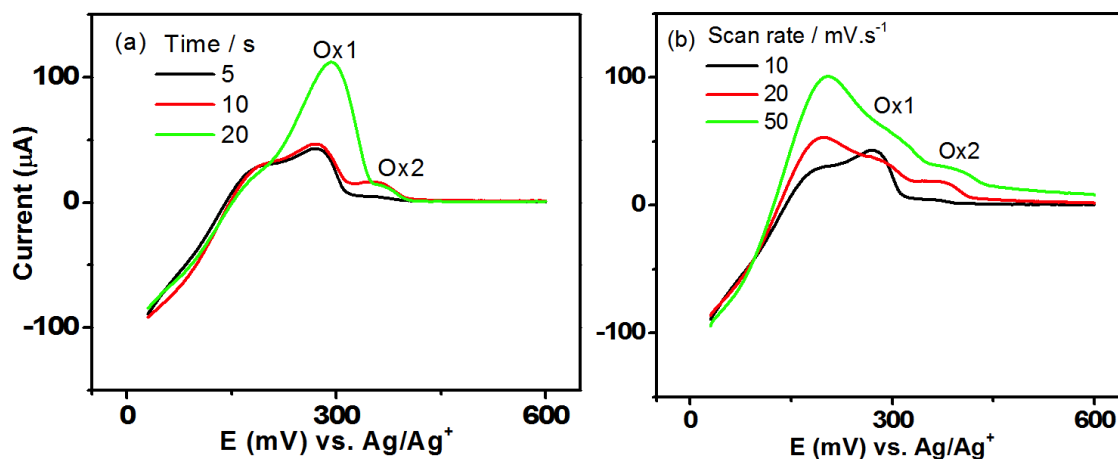


Figure 5. (a) Voltammograms obtained with a 1 mm diameter GC electrode in acetonitrile (0.1M Bu₄NPF₆) containing 10 mM TCNQF₂ and 50 mM Ni²⁺ when potential was held at 50 mV before scanning positively. (a) for designated time at a scan rate of 10 mV.s⁻¹ (b) for 5s at designated scan rates

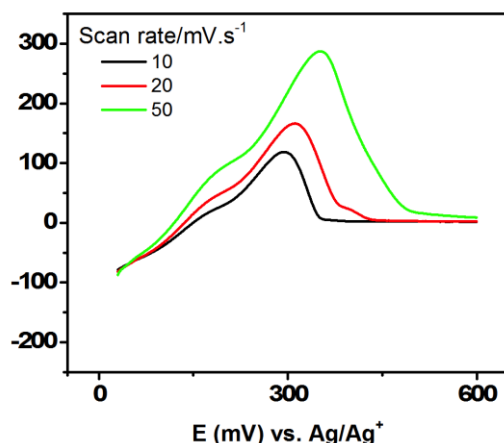


Figure 6. Voltammograms obtained with a 1 mm diameter GC electrode in acetonitrile (0.1M Bu₄NPF₆) containing 10 mM TCNQF₂ and 50 mM Ni²⁺ when the potential was held at 50 mV for 20 s before scanning positively at designated scan rates

6.3.2. Formation of M-TCNQF₂⁻ material on the electrode surface

The formation of TCNQF₂⁻ based material was further probed by holding the potential at 50 mV vs Ag/Ag⁺ prior to the positive potential scan. Results for an acetonitrile solution containing 10.0 mM TCNQF₂ and 50.0 mM Ni²⁺ are displayed in Figure 5. Both the deposition time and scan rate significantly affected not only the current magnitude, but also properties of the stripping wave. At a scan rate of 10 mV.s⁻¹, reducing TCNQF₂ for 5 s to 20 s gave rise to the oxidation stripping peak at ~292 mV and the current magnitude of this peak was enhanced when longer times were applied. The broad peak at ~ 379 mV (Ox2) which was observed during cyclic voltammetry experiments is small (Figure 5a). When the potential was held for 5s, it was hard to detect the stripping peaks and the diffusional wave of TCNQF₂^{-/0} became the main feature of the voltammogram presumably as the formation of the Ni-TCNQF₂⁻ solid is kinetically slow. The scan rate dependence was examined after 5 s and 20 s of deposition. For the shorter deposition time, although there is evidence of stripping process at ~ 272 mV (Ox1) and ~379 mV (Ox2) at scan rate of 10 mV.s⁻¹. However the diffusion controlled oxidation of TCNQF₂⁻ is the dominant feature in the voltammogram at 20 mV.s⁻¹ and 50 mV.s⁻¹, implying the stripping of the precipitate was kinetic controlled and not favoured under these conditions. However, when TCNQF₂ is reduced for 20 s the Ox1 oxidation peak increase in current magnitude at higher scan rate (Figure 6). Also

the peak potential shifts to more positive values. These observations suggest that the formation of Ni-TCNQF₂⁻ material could involve two different morphologies which are kinetically different and are oxidized at different potentials. Extensive electrolysis was performed in a solution containing 10 mM TCNQF₂ and 100 mM Ni²⁺ at different reduction potential, -40 or -65 mV. Figure 7 reveals the dependence of stripping process on the reduction potential. When the potential was held at -65 mV for 30 s, when scanning positively the Ox1 oxidation was observed. However, when the potential was held at -40 mV for the same period of time, oxidation of the soluble TCNQF₂⁻ was detected along with the Ox2 oxidation peak. These stripping peaks closely resemble the peaks at 292 and 349 mV discussed above. Thus, this behavior confirms the existence of two different morphologies of the Ni-TCNQF₂⁻ materials.

The growth of Co-TCNQF₂⁻ solid was studied in a similar manner confirming its formation via one oxidation stripping process, unlike in Ni²⁺ system (see Figure 8).

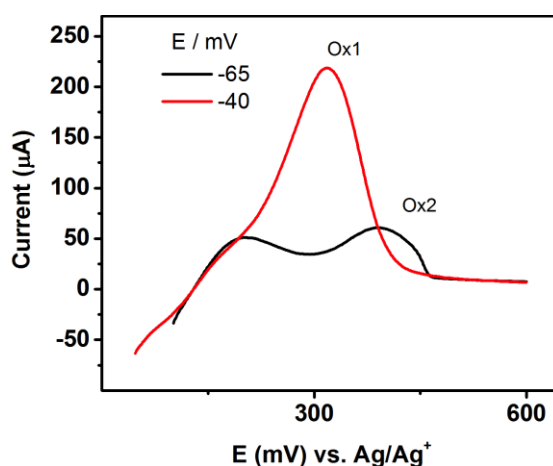


Figure 7. Voltammograms obtained with a 1 mm diameter GC electrode in acetonitrile (0.1M Bu₄NPF₆) containing 10 mM TCNQF₂ and 100 mM Ni²⁺ when potential was held at designated potential for 30 s before scanning positively at a scan rate of 50 mV.s⁻¹

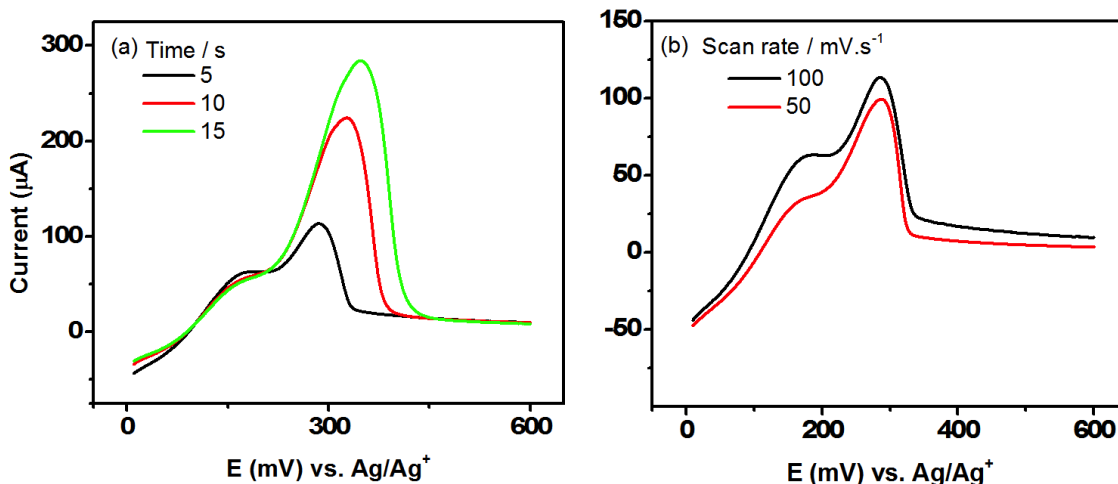
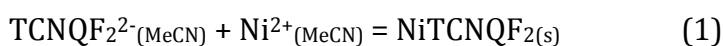


Figure 8. Voltammograms obtained with a 1 mm diameter GC electrode in acetonitrile (0.1M Bu₄NPF₆) containing 4 mM TCNQF₂ and 2 mM Co²⁺ when potential was held at 0 mV before scanning positively (a) for designated time at a scan rate of 100 mV.s⁻¹ (b) for 5s at designated scan rate

6.3.3. Cyclic voltammetry of TCNQF₂^{2-/2-} in the presence of M²⁺ - The formation of MTCNQF₂ solid

The TCNQF₂^{2-/2-} reduction step was also studied in the presence of M²⁺ (M = Ni, Co) by expanding the potential range to more negative values in order to include the second process. In these experiments, lower metal ion and TCNQF₂ concentrations were used to prevent any interference from the formation of TCNQF₂²⁻ material. Thus, voltammograms of the TCNQF₂^{0/-} process under these conditions show only the diffusion-controlled process even at a slow scan rate of 10 mV.s⁻¹.

Upon addition of 1.0 mM of Ni²⁺ to a 2.0 mM solution of TCNQF₂, a sharp reduction process was observed at a more negative potential (-96 mV) than for reduction of TCNQF₂^{0/-} and hence prior to the reduction of TCNQF₂^{2-/2-} (-450 mV). At the same time, the TCNQF₂^{2-/2-} reduction current diminished by ~ half relatively to what found in the absence of Ni²⁺ ions (Figure 9). This is consistent with the formation of TCNQF₂²⁻ - based material via equation



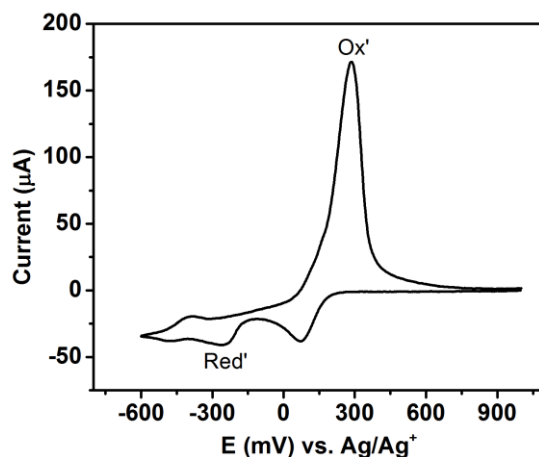


Figure 9. Cyclic voltammograms obtained with a 1 mm diameter GC electrode in acetonitrile (0.1M Bu₄NPF₆) containing 2.0 mM TCNQF₂ and 1.0 mM Ni²⁺ at a scan rate of 100 mV.s⁻¹

At this concentration ratio, close to 1.0 mM of TCNQF₂²⁻ remains unreacted, which generates the reduction wave at half of current magnitude in the absence of Ni²⁺. This TCNQF₂^{2-/-2-} response is completely absent when the concentration ratio of Ni²⁺: TCNQF₂ greater than or equal to 1.0 which is consistent with the formation of TCNQF₂²⁻ based material assuming that its formation is rapid on the voltammetric time scale. In the reverse scan, a sharp stripping peak is evident at 275 mV, which overlaps with the TCNQF₂^{2-/-0} process. This wave is close to a symmetric process and can be attributed to the oxidation of Ni-TCNQF₂²⁻ material on the electrode surface to TCNQF₂²⁻ which is then oxidized to TCNQF₂⁰. The scan rate dependence obtained in a solution containing 1.0 mM Ni²⁺ and 1.0 mM TCNQF₂ is shown in Figure 10a.

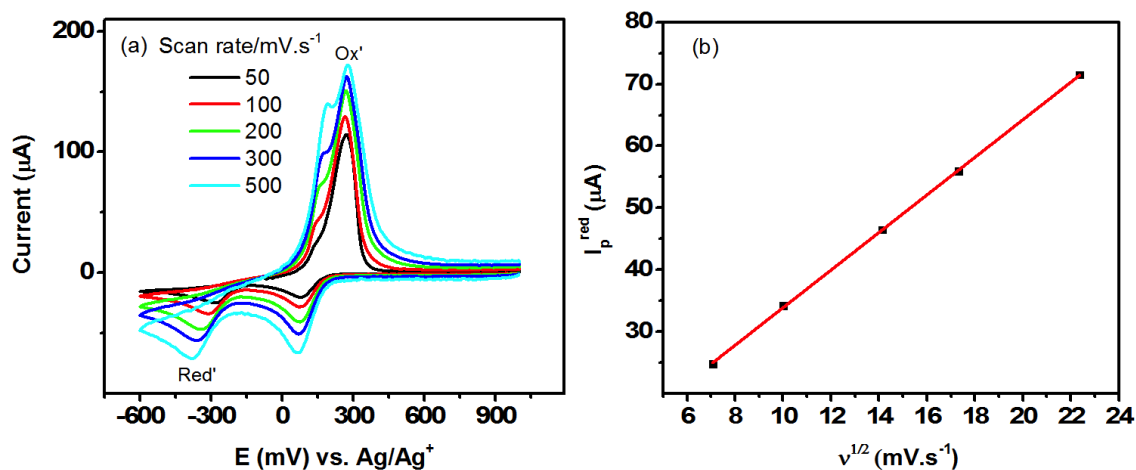


Figure 10 (a) Cyclic voltammograms obtained with a 1 mm diameter GC electrode in acetonitrile (0.1M Bu₄NPF₆) containing 1 mM TCNQF₂ and 2 mM Ni²⁺ at designated scan rate (b) Plot of I_p^{red} vs. square root of scan rate derived from Red' peak from (a)

The E_p value for the TCNQF₂^{0/-} process is almost independent of scan rate while the that for Red' shifts from -280 to -349 mV when the scan rate increased from 50 mV.s⁻¹ to 500 mV.s⁻¹. In the case of the oxidation stripping peak, there is a linear relationship between peak current of Red' and square root of scan rate (Figure 10b) with a positive intercept implying a nucleation growth mechanism is involved.¹⁰

The influence of switching potential on the stripping peak current is shown in Figure 11; the more negative E_λ value, the greater the magnitude of the stripping peak current. This confirms that the oxidation process at 275 mV (Ox') is coupled to the sharp reduction process at ~-280 mV (Red').

The formation of Ni²⁺-TCNQF₂⁻ is also supported by holding potential at -700 mV for 5 s to 30 s and then scanning the potential in the positive direction. As expected, the current magnitude of the stripping process increases with the scan rate and deposition time, as described previously.

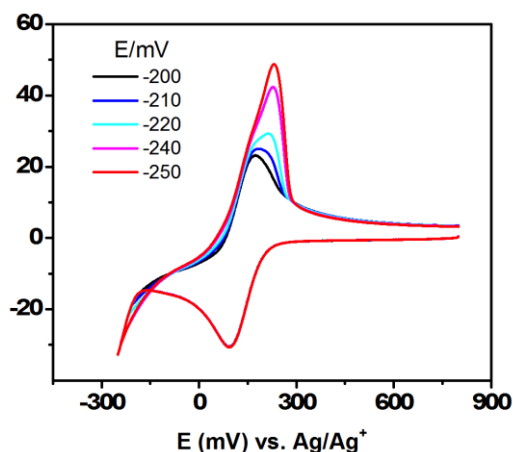


Figure 11. Cyclic voltammograms obtained with a 1 mm diameter GC electrode in acetonitrile (0.1M Bu₄NPF₆) containing 1 mM TCNQF₂ and 2 mM Ni²⁺ at designated switching potentials at a scan rate of 50 mV.s⁻¹

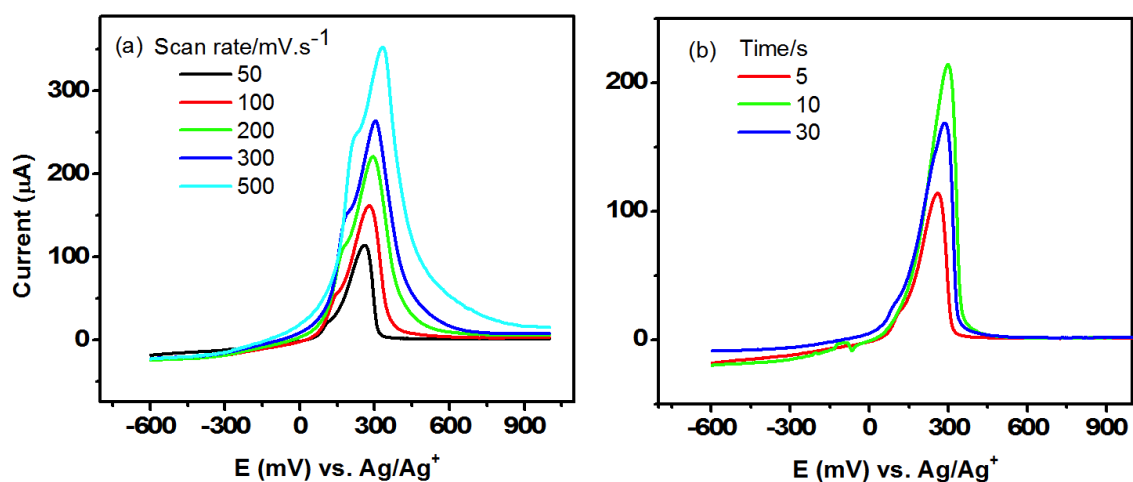


Figure 12. Voltammograms obtained with a 1 mm diameter GC electrode in acetonitrile (0.1M Bu₄NPF₆) containing 1 mM TCNQF₂ and 1 mM Ni²⁺ when the potential was held at -600 mV (a) for 5s at designated scan rate (b) for designated time before scanning positively at a scan rate of 50 mV.s⁻¹

Analogous voltammetric behavior is observed in the presence of Co²⁺ (Figure 13)

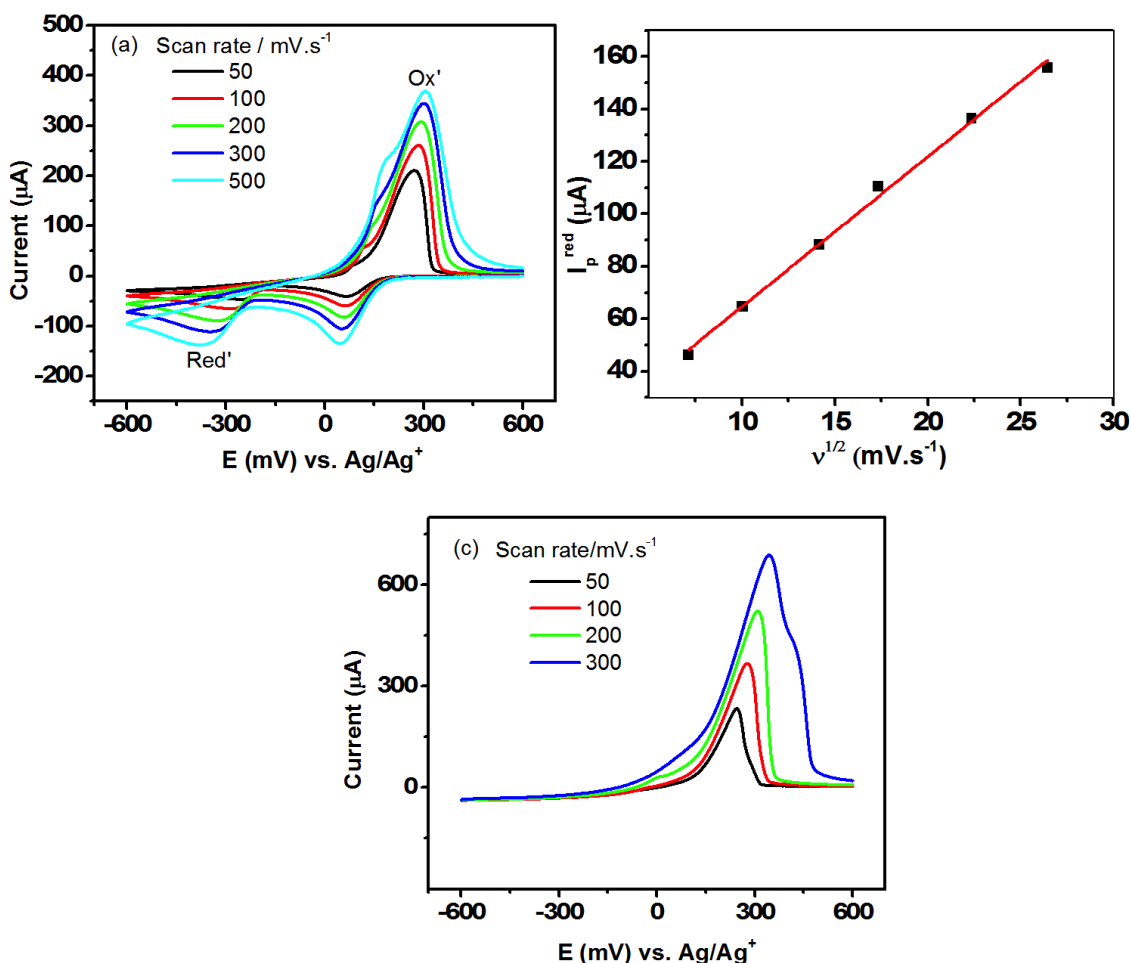


Figure 13 Voltammograms obtained with a 1 mm diameter GC electrode in acetonitrile (0.1M Bu_4NPF_6) containing 2 mM TCNQF_2 and 2 mM Co^{2+} (a) at designated scan rates, (b) Plot of I_p^{red} of Red' vs. square root of scan rate derived from (a), (c) as in (a) when the potential was held at -600 mV for 5s before scanning positively at designated scan rates.

6.3.4. IR and Raman characterization of TCNQF_2^- -based material

TCNQF_2^- -based solids were electrochemically synthesized by addition of M^{2+} , where $\text{M} = \text{Co}, \text{Ni}$, into a solution containing TCNQF_2^- obtained by bulk reductive electrolysis of TCNQF_2 and electrocrystallized on an ITO electrode as described in the Experimental section. IR and Raman spectra of Co (red) and Ni (black)-based materials are shown in Figure 14. The characteristic bands of TCNQ family were observed in the spectra. For the $\text{Co}(\text{TCNQF}_2)_2$ solid, the $\text{C}\equiv\text{N}$ stretch at 2217, ring $\text{C}=\text{C}$ stretch at 1512, exo $\text{C}=\text{C}$ stretch at 1476, mixing endocyclic ring $\text{C}-\text{C}$ and $\text{C}-\text{F}$

stretch at 1347 and 1249, C-CN stretch at 1164 cm^{-1} . A broad IR absorption at $\sim 3400 \text{ cm}^{-1}$ and the band at $\sim 1600 \text{ cm}^{-1}$ suggested the presence of H_2O in the sample. Raman band at 2232, 1623, 1406 cm^{-1} are characteristic for the monoanion TCNQF_2^- as discussed in chapter 2. A similar spectrum for NiTCNQF_2 solid was obtained.

For solid electrocrystallized on ITO electrode, both IR and Raman spectra mostly resemble those of the bulk-synthesized solids, except that the broad band for water was not present in the IR spectrum (Figure 15). It is interesting that this absence of H_2O band in IR spectrum has been observed with electrocrystallized $\text{M}(\text{TCNQF})_2$ material in previous chapter which was assumed to be due to the difference in synthesis conditions between electrocrystallization and bulk synthesis.

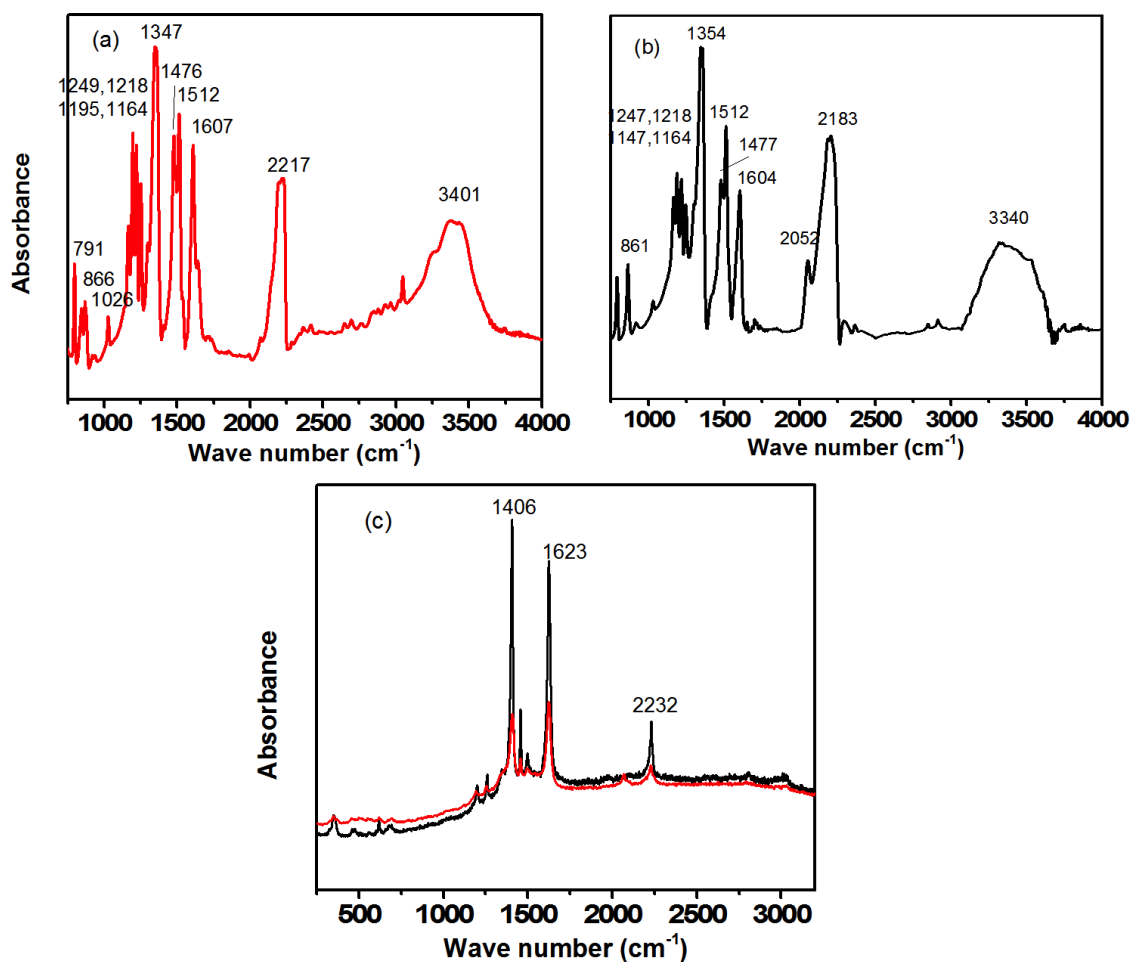


Figure 14. IR spectra of $\text{Co}(\text{TCNQF}_2)_2$ (a) and (b) $\text{Ni}(\text{TCNQF}_2)_2$ bulk-synthesized solids and (c) Raman spectra $\text{Co}(\text{TCNQF}_2)_2$ (red) and $\text{Ni}(\text{TCNQF}_2)_2$ (black)

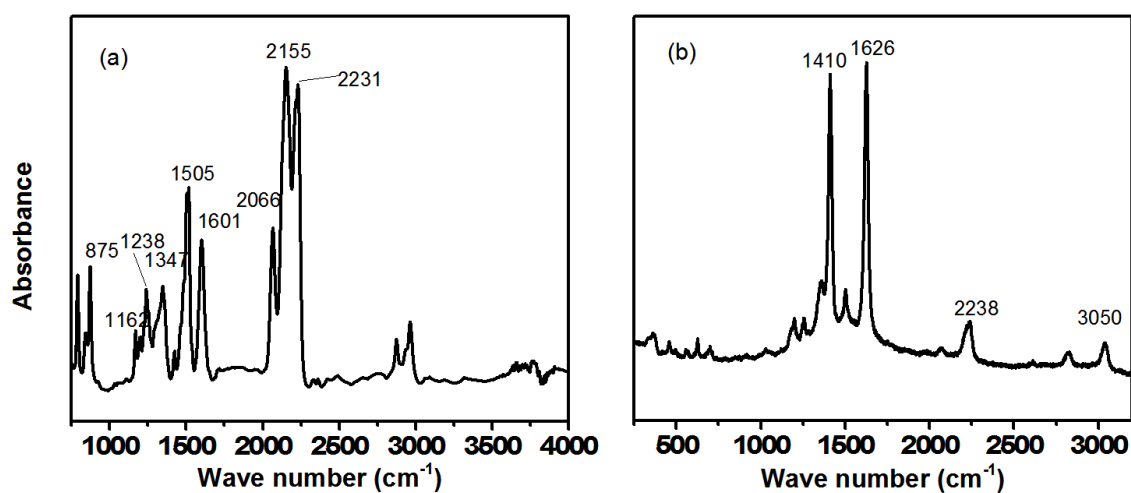


Figure 15. IR (a) and Raman (b) spectra of electrocrystallized $\text{Co}(\text{TCNQF}_2)_2$ on ITO electrode

M-TCNQF₂²⁻ (where M = Ni, Co) solids were also synthesized and characterized. Bright yellow coloured precipitates formed immediately after addition of 10.0 mM M²⁺ to 5.0 mM TCNQF₂²⁻ obtained by bulk electrolysis, which gradually turn to green in the air. The IR and Raman spectra are shown in Figure 16. It was expected that a red shift would be observed compared to the TCNQF₂⁻ material spectra. The C≡N stretch was observed at 2207, 2146 and 2074 cm⁻¹. The splitting of the C≡N absorption bands has been previously reported for TCNQF₄²⁻-based materials and is due to the coordination nature of metal-nitrile bond in these materials.^{8,11,12} The mixing mode of the ring C-C and the C-F stretches at 1306 and 1238 cm⁻¹ also showed a shift to lower energy compared to TCNQF₂⁻ materials. However, the ring C=C stretch at 1523 cm⁻¹ closely resembles that found in TCNQF₂⁻ spectrum. Furthermore, C-H out of plane bend band at 876 cm⁻¹ is also characteristic for the monoanion. Even stronger evidence for the existence of the monoanion came from the Raman absorption bands. The C≡N stretch shifts to higher energy at 2215 cm⁻¹, and other characteristic bands appear at 1629 and 1412 cm⁻¹ are also detected in M(TCNQF₂)₂·2H₂O solids. These observations suggest that TCNQF₂²⁻-based materials are not stable under ambient conditions and decomposed to the monoanion species which gives rise to a mixture of the mono and dianion diagnostic band in the vibrational spectra.

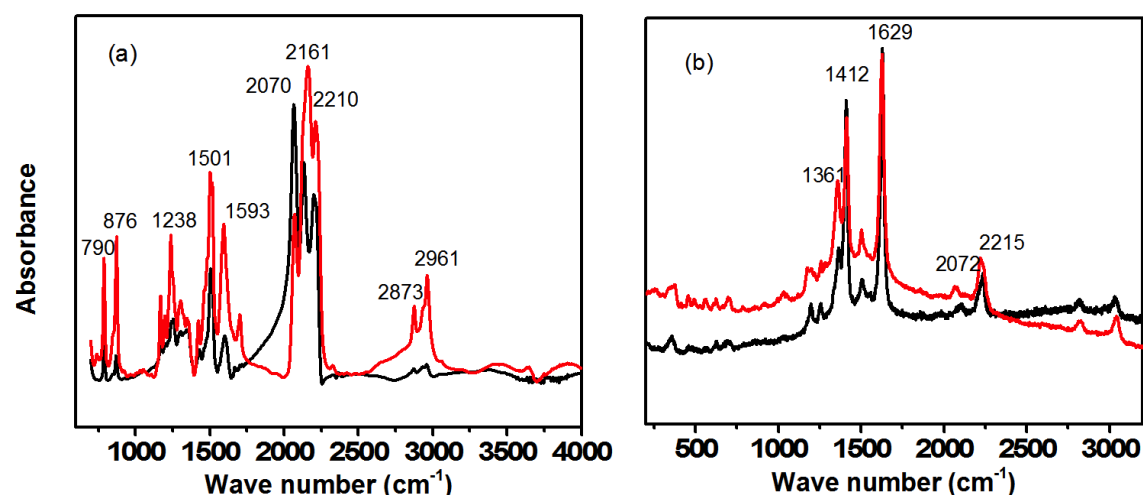


Figure 16. (a) IR and (b) Raman spectra of electrocrystallized Ni-TCNQF₂²⁻ (black) and Co-TCNQF₂²⁻ (red) materials

6.3.5. Elemental and thermogravimetric analysis

Elemental analysis data of both Ni and Co monoanionic TCNQF₂⁻ materials suggests a formulae of M(TCNQF₂)₂·2H₂O. The results for Co(TCNQF₂)₂·2H₂O are C 50.04% (50.10%), H 1.37% (1.40%) and N 19.44% (19.47%), and for Ni(TCNQF₂)₂·2H₂O material are C 50.68% (50.12%), H 1.23% (1.40%) and N 19.17% (19.48%). The TGA data also reveal a loss ~ 6% of the mass temperatures below 150°C, again is consistent with the presence of two water molecules. Once again, this formulae is consistent with other TCNQ⁻ and TCNQF⁻-based complexes with the presence of two solvent molecules.

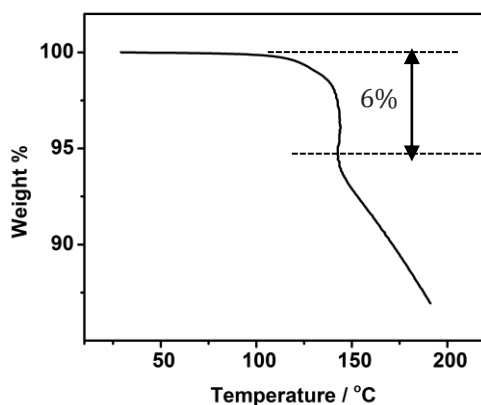


Figure 17 Thermogravimetric analysis for electrochemical synthesized Ni(TCNQF₂)₂·2H₂O material

6.3.6. Solubility measurements

The solubility of M(TCNQF₂)₂·2H₂O in acetonitrile was determined by monitoring the concentration of TCNQF₂⁻ using UV-Vis spectrophotometry and steady state voltammetry at a 125 μm diameter gold microelectrode. For Co(TCNQF₂)₂·2H₂O in the absence of electrolyte, the solubility was found to be 0.152 ± 0.007 mM. In the presence of 0.1 M Bu₄NPF₆, the solubility increased to 0.485 ± 0.012 mM which reflects the impact of ion pairing with the electrolyte ions. The calculated solubility product of Co(TCNQF₂)₂·2H₂O is 1.14 × 10⁻¹⁰ M³ with electrolyte and 3.51 × 10⁻¹² M³ without electrolyte. For Ni(TCNQF₂)₂·2H₂O, the solubility was found to be 0.222 ± 0.008 mM and 0.873 ± 0.012 mM with and without electrolyte, respectively, which results in solubility product of 6.65 × 10⁻¹⁰ M³ and 1.09 × 10⁻¹¹ M³. Clearly Ni(TCNQF₂)₂·2H₂O is slightly more soluble than Co(TCNQF₂)₂·2H₂O. This is consistent with the cyclic voltammetric observation where the formation of Ni-

TCNQF₂⁻ solid can only be detected electrochemically at higher Ni²⁺ and TCNQF₂⁻ concentrations compared with the Co-TCNQF₂ system. The higher solubility of TCNQF_n⁻-based materials could be used to explain the absence of precipitate where 100.0 mM of M²⁺ was added to a solution containing 2.0 mM of TCNQF₄⁻ to synthesize M-TCNQF₄⁻ material.⁸ TCNQF₄⁻-based materials also have much higher solubility as found with TCNQF₂⁻ where no precipitate could be achieved under voltammetric conditions.

6.3.7. Morphologies of M-TCNQF₂ materials

The morphologies of both TCNQF₂⁻ and TCNQF₂²⁻-based materials crystallized onto an ITO electrode were examined by the SEM technique. Only one morphology was observed for the Co-TCNQF₂⁻ material (Figure 18) where clusters of cylindrical blocks with a length of ~ 1 μm, presumably grow from the nucleation sites. However, the morphology of the Ni-TCNQF₂⁻ solid depends on the applied reduction potential. Figure 19a represents the image of an ITO electrode surface when a solution containing 10.0 mM TCNQF₂ and 100.0 mM Ni²⁺ is reduced at -76 mV for 3 min. Under these conditions, the electrode surface was covered evenly by a densely packed solid which was unlike Co(TCNQF₂)₂ where the crystals were found at discrete sites on the electrode surface. In contrast when TCNQF₂ was reduced at a more negative potential, i.e. -200 mV, this dense packing of crystals were replaced by interpenetrated thin sheets, see Figure 19b-c. Interestingly, the detection of two morphologies is consistent with the cyclic voltammetric data as discussed above. The oxidation peak at 434 mV can be attributed to the oxidation of crystal with cylindrical morphology, formed at a more positive potential, while the oxidation process at 345 mV corresponds to the oxidation of the thin-sheet morphology.

EDAX analysis of electrodeposited materials confirmed the presence of Co and Ni along with carbon and nitrogen as required for formation of M(TCNQF₂)₂·2H₂O.

Although spectroscopic data revealed that TCNQF₂²⁻ solids are not stable in air, it was still interesting to compare these morphologies. The TCNQF₂²⁻ materials were electrocrystallized onto an ITO electrode from an acetonitrile solution containing 0.5 mM Co²⁺ or Ni²⁺ and 0.5 mM TCNQF₂⁻ by holding the potential at -500 mV for 180 s. Images shown in Figure 20 reveal that the morphology is significantly

different from the TCNQF₂^{•-} materials described above. Here, cylindrical crystals of Co(TCNQF₂)₂ with thin needle-like morphology are observed (see Figure 20b). Needle-like crystals have commonly been reported for Co-TCNQ and TCNQF₄²⁻-based materials.^{8,13} On the other hand, the Ni material consist of stacks of block-shape crystals with a size of ~ 400 nm (Figure 20a). It is likely that although TCNQF₂²⁻ moiety was oxidized to TCNQF₂^{•-} in air with the morphology of TCNQF₂²⁻ solid being retained.

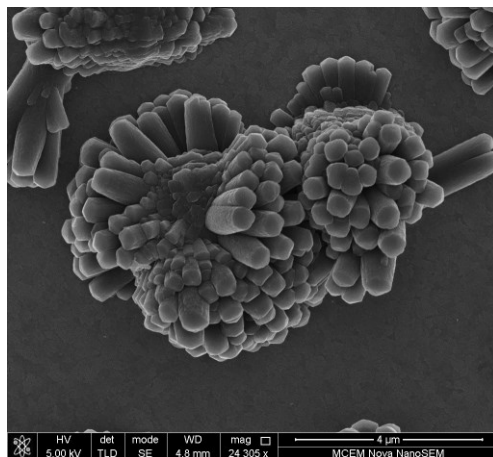


Figure 18. SEM image of Co(TCNQF₂)₂·2H₂O electrocrystallized onto an ITO electrode from an acetonitrile solution (0.1M Bu₄NPF₆) containing 8.0 mM TCNQF₂ and 8.0 mM Co²⁺ when the potential was held at -100 mV for 3 mins.

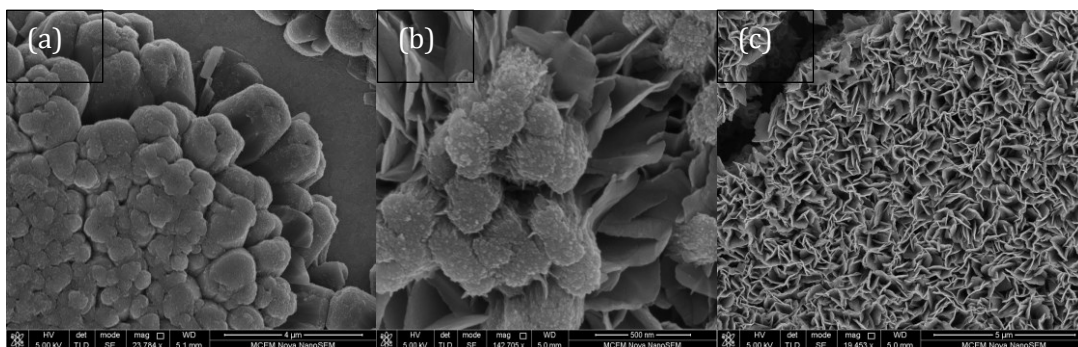


Figure 19. SEM image of Ni(TCNQF₂)₂·2H₂O electrocrystallized onto an ITO electrode from an acetonitrile solution (0.1M Bu₄NPF₆) containing 10.0 mM TCNQF₂ and 100.0 mM Ni²⁺ when the potential was held (a) -76 mV (b, c) -200 mV for 3 mins.

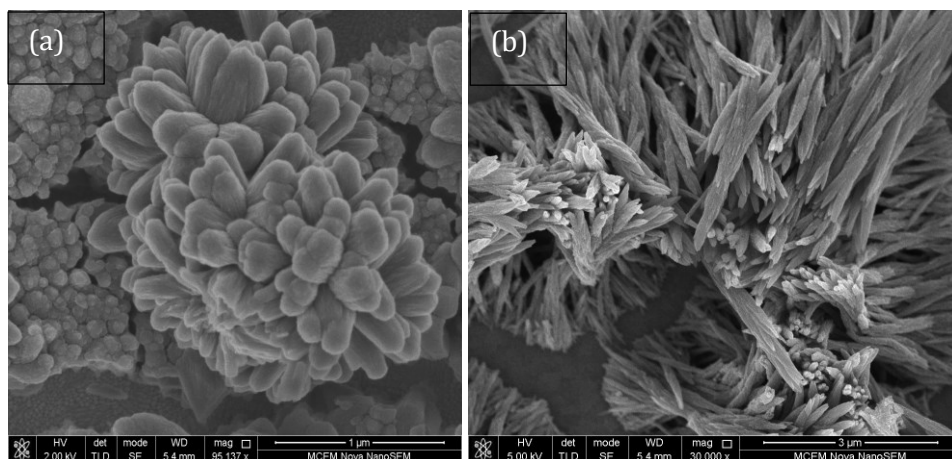


Figure 20. SEM image of (a) Ni-TCNQF₂²⁻ and (b) Co-TCNQF₂²⁻ solid electrocrystallized onto an ITO electrode from an acetonitrile solution (0.1M Bu₄NPF₆) containing 1.0 mM TCNQF₂ and 1.0 mM M²⁺ when the potential was held -600 mV for 3 mins.

6.3.8. Interpretation of the cyclic voltammetry of TCNQ in the presence of Co²⁺

Voltammetric evidence for the formation of both Co²⁺-TCNQF⁻ and TCNQF₂²⁻ was obtained by carefully choosing the Co²⁺ and TCNQF_n concentrations for each material. It is likely that the high solubility of Co²⁺-TCNQF_n⁻ materials compared to the monocationic Cu or Ag analogous has provided a significant challenge in probing the electrochemical behavior of this system. This also enabled the voltammetry of TCNQ in the presence of Co²⁺ to be re-examined.⁵ Provided the formation of Co-TCNQ⁻ is fast enough, at a concentration ratio Co:TCNQ of 1:2, according to equation 2 and 3, TCNQ⁻ will be totally consumed by Co²⁺, so the TCNQ^{-/2-} step should be absent. However, the current of the TCNQ^{-/2-} process decreases to approximately a half the magnitude, compared with that in the absence of Co²⁺ and remained detectable at the concentration up 1.2:1 (Figure 21), which suggests that the reduction of TCNQ⁻ to TCNQ²⁻ is accompanied by the formation of a Co-TCNQ²⁻ not TCNQ⁻ based material. The positive shift in the peak is consistent with Nernst equation where a decrease in concentration of TCNQ²⁻ will give a positive shift in peak potential.



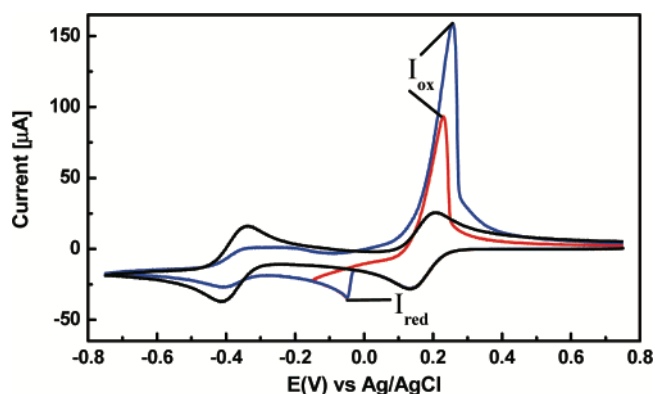


Figure 21. Cyclic voltammograms obtained in acetonitrile (0.1M Bu_4NClO_4) with a 3 mm diameter GC electrode and scan rate of $100 \text{ mV}\cdot\text{s}^{-1}$ for the reduction of 1.0 mM TCNQ in the absence (black curve) and in the presence of 0.5 mM $\text{Co}(\text{ClO}_4)_2\cdot 6\text{H}_2\text{O}$ at a 1:2 ratio and when the potential is switched before (red curve) and after (blue curve) the $\text{TCNQ}^{0/-}$ reduction process. Adapted from ref 13.¹³

Reviewing all the results from previous studies and within this thesis, it is strongly evidenced from the cyclic voltammetry of TCNQF_4 as well as TCNQF and TCNQF_2 in the presence of Co^{2+} and Ni^{2+} that the peak label as I_{red} in Figure 21 is associated with the $\text{TCNQ}^{0/-}$ reduction step, not $\text{TCNQ}^{0/-}$, accompanied with the formation of $\text{Co}\text{-TCNQ}^{2-}$ solid onto the electrode. Further evidence can be deduced from a voltammetric experiment was performed on a solution containing 2.0 mM Co^{2+} and 4.0 mM TCNQF_2 (Figure 22). In this condition, both the formation of TCNQF_2^- and TCNQF_2^{2-} material can be detected by varying experimental potential range. In this experiment the potential was switched at -7 mV, i.e prior to the Red' or -36 mV on Red' process. When the potential was switched at -7 mV and prior to the onset of the second process, on the reverse scan, an oxidation peak appeared at 263 mV (Ox1), which was attributed to the stripping of $\text{Co}(\text{TCNQF}_2)_2$ solid as described above, along with the diffusional $\text{TCNQF}_2^{2-/0}$ process. When the potential was switched at -36 mV, a cross-over current and three oxidation processes were observed on the reverse scan. The oxidation of soluble TCNQF_2^- was detected as a shoulder with two sharper peaks at 241 mV (Ox') and 294 mV (Ox1), which confirms that the TCNQF_2^- -based solid was actually formed prior to the Red' process. The same behavior should be true for other fluorinated derivatives provided that the concentrations of both M^{2+} and TCNQF_n are high enough to exceed the solubility products.

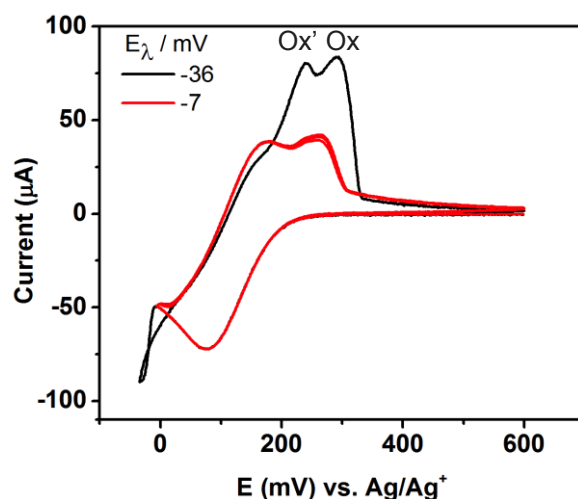


Figure 22 Voltammograms obtained with a 1 mm diameter GC electrode in acetonitrile (0.1M Bu₄NPF₆) containing 2 mM TCNQF₂ and 4 mM Co²⁺ at 50 mV.s⁻¹ at different switching potential

6.4. Conclusion

If the concentrations of M²⁺ and TCNQF₂ are carefully chosen, the cyclic voltammetry of both TCNQF₂^{0/-/2-} reduction processes can be investigated in the presence of Co²⁺ or Ni²⁺. Due to high solubility of Ni(TCNQF₂)₂ solid, 10.0 mM TCNQF₂ and 50.0 mM Ni²⁺ solution was required for voltammetric experiments to detect the formation of monoanion TCNQF₂⁻-based material on the voltammetric time scale. In contrast the less soluble Co(TCNQF₂)₂ formation can be detected with a much lower concentration of reactants. Cyclic voltammetric data suggest the existence of two Ni(TCNQF₂)₂ solid morphologies which gives rise to two stripping oxidation steps on the positive potential scan depending on scan rate and reduction potential. SEM images obtained using different electrolysis potential reveal two different morphologies for electrocrystallized Ni(TCNQF₂)₂ supporting the voltammetric results. The TCNQF₂^{0/-/2-} reduction step can be studied in the presence of M²⁺ by lowering the concentrations. However, the TCNQF₂²⁻-based materials are not stable in the air as evidence by a change in colour of the solid and spectroscopic data. Thus only the TCNQF₄²⁻ materials are air stable.

References

- (1) Neufeld, A. K.; Madsen, I.; Bond, A. M.; Hogan, C. F. *Chemistry of Materials* **2003**, *15*, 3573.
- (2) Harris, A. R.; Neufeld, A. K.; O'Mullane, A. P.; Bond, A. M.; Morrison, R. J. S. *Journal of The Electrochemical Society* **2005**, *152*, C577.
- (3) Nafady, A.; O'Mullane, A. P.; Bond, A. M.; Neufeld, A. K. *Chem. Mater.* **2006**, *18*, 4375.
- (4) Harris, A. R.; Nafady, A.; O'Mullan, A. P.; Bond, A. M. *Chemistry of Materials* **2007**, *19*, 5499.
- (5) Nafady, A.; Bond, A. M.; Bilyk, A.; Harris, A. R.; Bhatt, A. I.; O'Mullane, A. P.; De Marco, R. *J. Am. Chem. Soc.* **2007**, *129*, 2369.
- (6) Nafady, A.; Bond, A. M.; O'Mullane, A. P. *Inorganic Chemistry* **2009**, *48*, 9258.
- (7) Le, T.; O'Mullane, A.; Martin, L.; Bond, A. *J. Solid State Chem.* **2011**, *15*, 2293.
- (8) Le, T. H.; Nafady, A.; Bond, A. M.; Martin, L. L. *European Journal of Inorganic Chemistry* **2012**, *2012*, 5534.
- (9) Le, T. H.; Nafady, A.; Vo, N. T.; Elliott, R. W.; Hudson, T. A.; Robson, R.; Abrahams, B. F.; Martin, L. L.; Bond, A. M. *Inorganic Chemistry* **2014**, *53*, 3230.
- (10) Gunawardena, G.; Hills, G.; Montenegro, I. *Journal of Electroanalytical Chemistry and Interfacial Electrochemistry* **1985**, *184*, 371.
- (11) Haworth, N. L.; Lu, J.; Vo, N.; Le, T. H.; Thompson, C. D.; Bond, A. M.; Martin, L. L. *ChemPlusChem* **2014**, *79*, 962.
- (12) Nafady, A.; Le, T. H.; Vo, N.; Haworth, N. L.; Bond, A. M.; Martin, L. L. *Inorganic Chemistry* **2014**, *53*, 2268.
- (13) Nafady, A.; Bond, A. M.; Bilyk, A.; Harris, A. R.; Bhatt, A. I.; O'Mullane, A. P.; De Marco, R. *Journal of the American Chemical Society* **2007**, *129*, 2369.

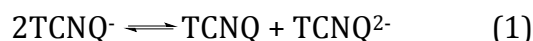
Chapter 7

Chemistry and electrochemistry of TCNQF and TCNQF₄ in the presence of Zn²⁺

7.1. Disproportionation of TCNQFⁿ⁻ in the presence of Zn²⁺ in acetonitrile

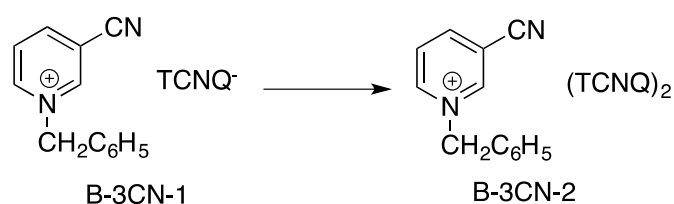
7.1.1. Introduction

In principle disproportionation of TCNQ^{•-} can generate TCNQ⁰ and TCNQ²⁻ as shown in the equation



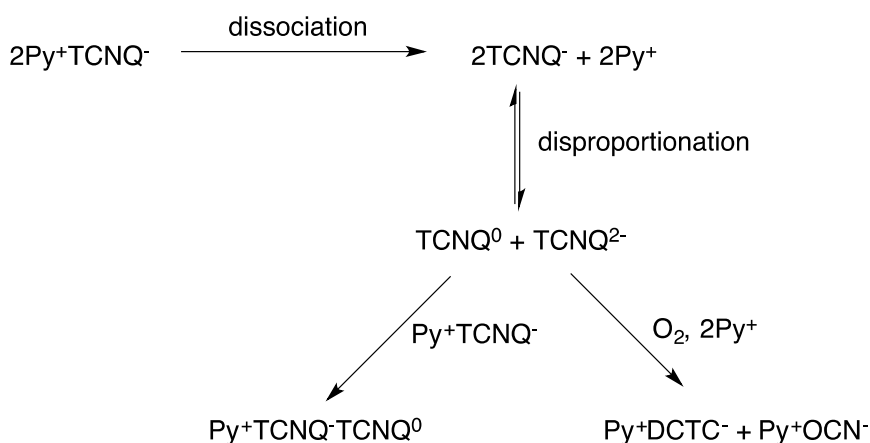
provided there is a driving force to stabilize the TCNQ²⁻ state.

This chemistry is known, for example, disproportionation of TCNQ^{•-} facilitates the conversion of 1:1 anion radical salts (1-benzyl-3-cyanopyridinium) TCNQ (B-3CN-1) and (1-benzyl-4-cyanopyridinium) TCNQ (B-4CN-1) to their 1:2 analogues (1-benzyl-3-cyanopyridinium)(TCNQ)₂ (B-3CN-2) and (1-benzyl-4-cyanopyridinium)(TCNQ)₂ (B-4CN-2), respectively as shown in Scheme 1.¹



Scheme 1. The disproportionation of TCNQ^{•-} illustrated using the B-3CN-1 complex.¹

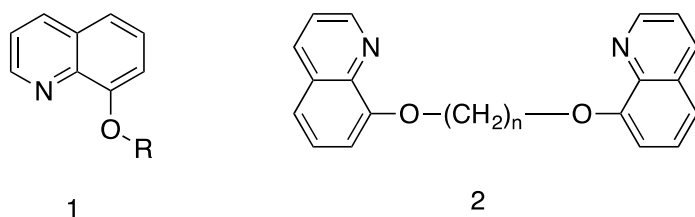
This conversion can be achieved by recrystallizing the initial material B-3CN-1 from pure acetonitrile in the presence of oxygen. It was proposed that during the recrystallization, B-3CN-1 slightly soluble, hence TCNQ^{•-} can be dissociated followed by the disproportionation to TCNQ⁰ and TCNQ²⁻. The neutral TCNQ⁰ is sequentially incorporated into initial crystals generating the (TCNQ)₂pyridinium salt. A representative mechanism for the conversion of simple pyridium salts (Py⁺TCNQ^{•-}) has been proposed as shown in Scheme 2.



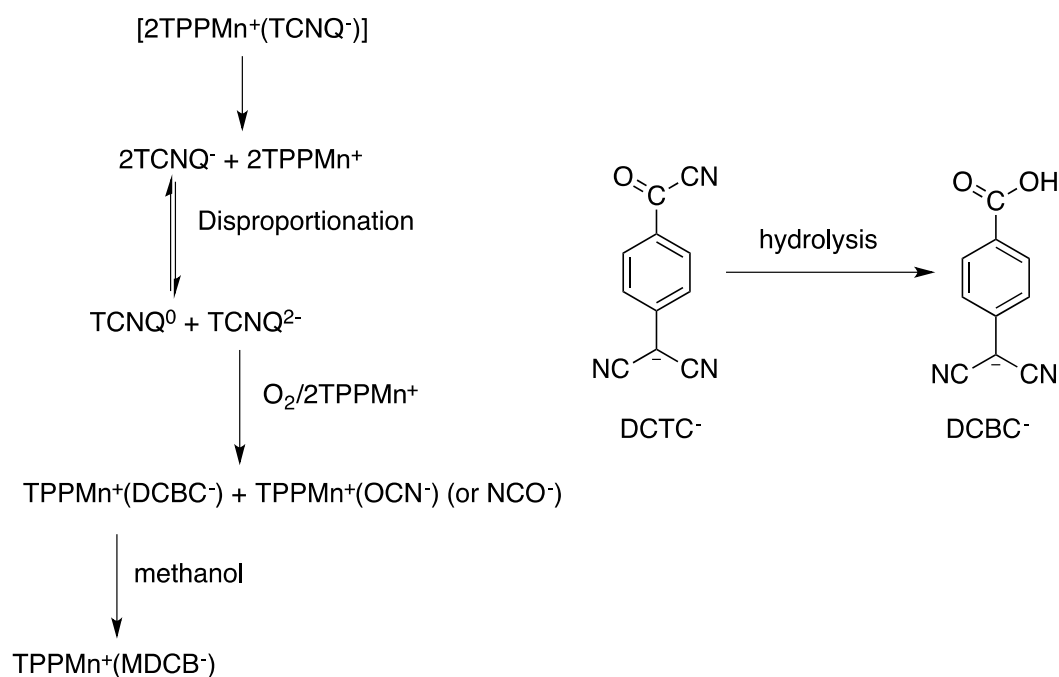
Scheme 2. A general mechanism proposed for the disproportionation of pyridium-TCNQ, where Py = pyridium¹

In this example, the irreversible oxidation of TCNQ²⁻ to DCTC⁻ is the driving force for the disproportionation of TCNQ⁻ reaction.

A similar disproportionation reaction was also observed in acetonitrile solution while preparing a conducting TCNQ salts with 8-hydroxyquinoline ethers and biethers (Scheme 3).² Although initial solid product is stable, it decomposed in acetonitrile solution. In another study, Hill and coworkers also exploited the disproportionation reaction to synthesize a six-coordinate 5,10,15,20-tetraphenylporphinatomanganese(III) complex (TPPMn⁺) with methyl 4-(dicyanomethylene)benzoate anion (MDCB⁻) which was resulted from the decomposition of TCNQ²⁻ followed by hydrolysis from the disproportionation of TCNQ⁻ in methanol (scheme 4).^{3,4}



Scheme 3. 8-hydroxyquinoline ethers (1) and biethers (2)



Scheme 4. The formation of 5,10,15,20-tetraphenylporphinatomanganese(III) complex (TPPMn^+) from the disproportionation of TCNQ^- where $\text{DCBC}^- = 4$ - (dicyanomethylene)benzoyl cyanide anion, $\text{MDCB}^- =$ methyl 4-(dicyanomethylene)benzoate anion

The electronic dynamics of $(\text{TCNQ}^-)_2^{2-}$ disproportionation was studied recently and revealed that it proceeds in a two step in which photoexcitation triggers an electron transfer ($<10\text{fs}$) followed by dissociation into two products TCNQ and TCNQ^{2-} within 350 fs.⁵

It is interesting that the disproportionation of TCNQ and TCNQF_4 in acetonitrile is shown to be facilitated by the presence of Zn^{2+} . Highly insoluble ZnTCNQF_4 is formed which drives the disproportionation. However, this disproportionation is reversed in the presence of water.⁶ Thus, the disproportionation of TCNQF^- and TCNQF_2^- in the presence of Zn^{2+} ions has been investigated here and compared with results for TCNQ^- and TCNQF_4^- .

7.1.2. Experimental

7.1.2.1. Chemicals

$\text{Zn}(\text{ClO}_4)_2 \cdot 6\text{H}_2\text{O}$ (Aldrich), ferrocene (98%, EGA-Chemie), acetonitrile (HPLC grade, Omnisolv), isopropanol (BHD) and acetone (Suprasolv, Merck), TCNQF and TCNQF_2 (98%, TCI) were used as received by the manufacturer. $(\text{Bu}_4\text{N})\text{PF}_6$ (Wako) was recrystallized twice from 96% ethanol (Merck) and then dried at 100°C under

vacuum for 24 h before being used as the supporting electrolyte in the electrochemical experiments.

7.1.2.2. Procedures

Acetonitrile solutions containing either 10.0 mM TCNQF₂⁻ or 10.0 mM TCNQF⁻ were quantitatively prepared by exhaustive electrochemical reduction of 10.0 mM TCNQF₂ or TCNQF in acetonitrile (0.1 M Bu₄NPF₆) at a Pt mesh working electrode at constant potentials of -100 mV (vs. Ag/Ag⁺) for the TCNQF₂ and -200 mV (vs. Ag/Ag⁺) for TCNQF. An analogous protocol was applied to prepare a 10.0 mM solution of TCNQF₂²⁻ and TCNQF²⁻ in which, after quantitative generation of the monoanion, potential was set to -550 mV and -650 mV to convert TCNQF²⁻ and TCNQF₂²⁻. Controlled potentials were maintained until the current decreased to 0.1% of its initial value. UV-Vis spectroscopy was utilized to confirm that all the starting material was reduced to the required product in the bulk electrolysis experiments. Zn-TCNQF_n material was obtained by mixing 10.0 mL solutions of the electrochemically generated TCNQF²⁻ or TCNQF₂²⁻ (10.0 mM) in acetonitrile (0.1 M Bu₄NPF₆) with 5.0 mL (2:1 ratio) or 10.0 mL (1:1 ratio) acetonitrile solutions containing 10.0 mM Zn²⁺, followed by stirring for 5 min. The rapidly formed precipitates were collected by centrifugation, washed with 5 × 2 mL of acetonitrile, dried and stored overnight under vacuum.

7.1.2.3. Electrochemistry

Voltammetric experiments were undertaken with a Bioanalytical Systems (BAS) Epsilon electrochemical workstation at room temperature (22±2°C) using a standard three-electrode cell configuration. The working electrode used in steady state voltammetric experiments was a BAS gold microelectrode (11±2 μm diameter). The counter electrode was 1.0 mm diameter Pt wire. The reference electrode consisted of a Ag wire placed in acetonitrile solution containing 1.0 mM AgNO₃ and 0.1 M Bu₄NPF₆, and separated from the test solution by a glass frit. Conversion to Fc/Fc⁺ reference scale can be achieved by addition of -135 mV. In the case of bulk electrolysis experiments, a three-compartment “H-type” cell configuration with Pt mesh working and counter electrodes and the same Ag/Ag⁺ reference electrode employed in voltammetric studies were used. Solutions for electrochemical measurements were purged with nitrogen gas for 10 min before

commencing the experiments.

7.1.2.4. Other Instrumentations

UV-vis and FT-IR instrumentation are as detailed in previous chapters.

7.1.3. Result and discussion

Voltammetric experiments were performed on an acetonitrile solution containing 10.0 mM of TCNQF_n^- ($n = 1, 2$) formed by one electron bulk reductive electrolysis of TCNQF_n . Near steady state voltammograms confirmed that all of the neutral TCNQF_n was reduced to TCNQF_n^- as evidenced from the zero current position. Prior to electrolysis TCNQF_n in acetonitrile generates two one-electron reduction steps as described in Chapter 2. In the case of TCNQF_n^- , the positive current represents the $\text{TCNQF}_n^{-/0}$ oxidation step and the negative current illustrates the $\text{TCNQF}_n^{-/2-}$ reduction step (see Chapter 2).

Upon adding addition Zn^{2+} to a 5.0 mM TCNQF_n^- in acetonitrile, the green colour of the solution associated with the monoanion gradually became yellow, which is the colour of neutral TCNQF_n^0 in acetonitrile and precipitate also was formed.

In a series of experiments, 1.25, 2.5 and 5.0 mM Zn^{2+} was added to a 5.0 mM solution of TCNQF_n^- to give 0.5:2, 1:2 and 2:2 $\text{Zn}^{2+}:\text{TCNQF}_n^-$ stoichiometric ratios. At the lowest ratio, it took longer for green colour to disappear and for the precipitate to appear with the rate being slower for TCNQF^- than for TCNQF_2^- . All the solutions were stirred for 5 mins to enable the reaction to go to completion before centrifugation to separate the solids. The supernatant solution was then diluted 200-fold with acetonitrile and examined by UV-Vis spectroscopy (Figure 1). At the 0.5:2 ratio, characteristic absorption bands for both neutral TCNQF_2^0 (TCNQF^0) and TCNQF_2^- (TCNQF^-) were observed at 392 (391) and 424 (417), respectively (see Chapter 2).

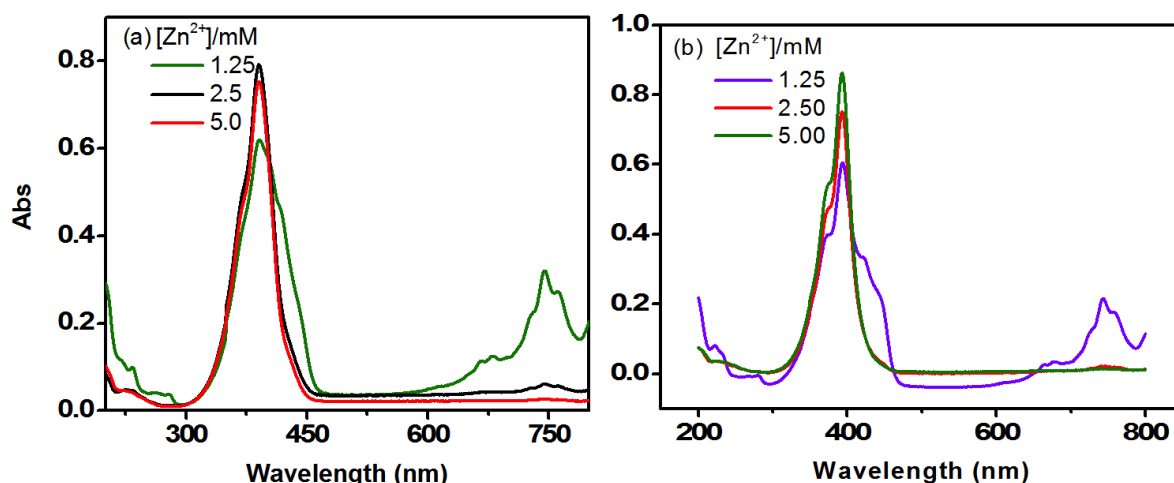
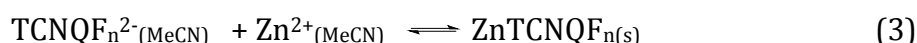


Figure 1. UV-Vis spectra obtained from the supernatant solution after mixing acetonitrile solutions containing 5.0 mM of (a) TCNQF₂⁻ and (b) TCNQF⁻ and Zn²⁺ at designated concentrations with 200 fold dilution with acetonitrile

However, when the ratio was increased to 1:2 or 2:2, the band for TCNQF_n⁻ was barely detected (420 and 742 nm), with the dominant absorption band being for neutral TCNQF_n at ~390 nm. The concentration of TCNQF_n and unreacted TCNQF_n⁻ was quantitatively determined by reference to calibration curves for each species. The results are summarized in Table 1. These UV-Vis data confirmed the generation of neutral TCNQF_n by reaction of TCNQF_n⁻ with Zn²⁺ at a of 1:2 stoichiometric ratio to afford TCNQF_n⁰ neutral and a Zn-TCNQF_n based solid via equations 2 and 3



The overall reaction is therefore:



Table 1. TCNQF_n and unreacted TCNQF_n⁻ concentrations formed upon mixing TCNQF_n⁻ and Zn²⁺ in CH₃CN (0.1 M Bu₄NPF₆) as derived from UV-Vis spectroscopy

Experiment	Initial [TCNQF _n ⁻] (mM)	Initial [Zn ²⁺] (mM)	[TCNQF _n ⁻]:[Zn ²⁺]	Produced [TCNQF ₂] ([TCNQF]) (mM)	Unreacted [TCNQF ₂] (TCNQF ⁻) (mM)
1	5.0	1.25	4:1	1.60 (2.02)	2.26 (3.53)
2	5.0	2.5	2:1	2.33 (2.12)	0.10 (0.12)
3	5.0	5.0	1:1	2.26 (2.46)	0.07 (0.08)

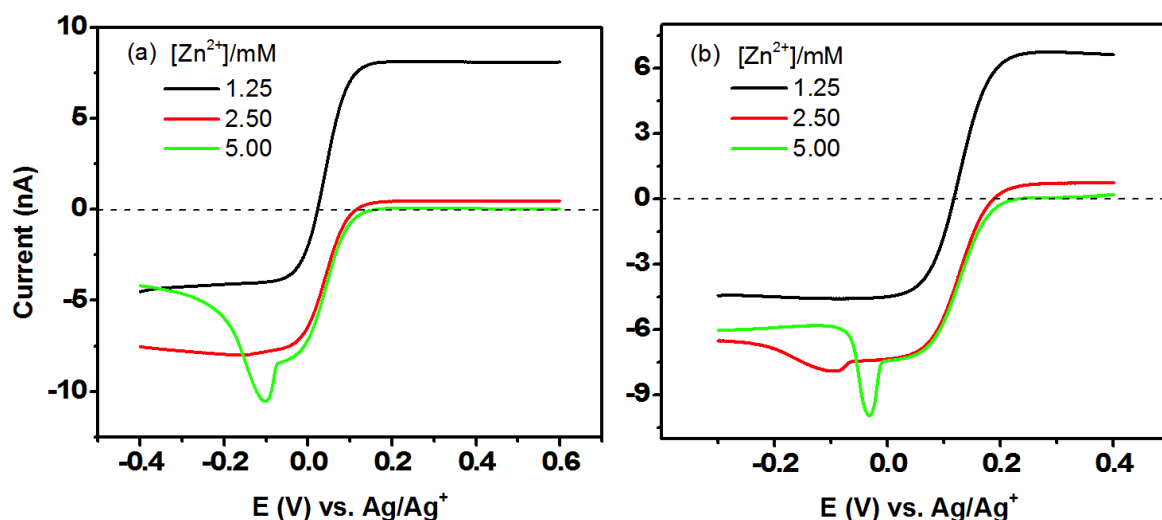


Figure 2. Near steady state voltammograms obtained with a gold microelectrode (25 μ m) at a scan rate of 20 mV.s⁻¹ after mixing acetonitrile solutions (0.1 M Bu₄NPF₆) of (a) TCNQF[·] and (b) TCNQF₂[·] and Zn²⁺ at designated concentration

Near steady state voltammogram obtained from 5.0 mM TCNQF_n⁻ solution in the presence of Zn²⁺ are shown in Figure 2. Upon addition of 1.25 mM Zn²⁺ into 5.0 mM TCNQF_n⁻, the position of zero current no longer lies between the reduction and oxidation steps. The position of zero current confirms the concurrent existence of TCNQF_n⁻ and TCNQF_n in the solution. The ratio of TCNQF_n⁻/TCNQF_n derived from the current magnitudes of the oxidation of reduction steps is 1.5 for TCNQF₂ and 2.0 for TCNQF, which suggests that the equilibrium constant for the reaction of TCNQF[·] and Zn²⁺ to form ZnTCNQF is larger than that of TCNQF₂[·]. When the concentration ratio of Zn²⁺ and TCNQF_n⁻ was increased to 2:2, almost no TCNQF_n⁻

was present with TCNQF_n^0 neutral being the main soluble species in solution. At a concentration ratio of 2:2, along with evidence of TCNQF_n^0 , a current drop was observed at more negative potentials which due to the formation of Zn-TCNQF_n solid on the electrode surface.

7.1.3.1. Characterization of the solid products of $\text{Zn}^{2+}\text{-TCNQF}_n$ ($n = 1, 2$)

IR and Raman spectra were used to determine the degree of charge transfer in the green material precipitated and collected from the reaction. The spectra are shown in Figure 3. Bands characterized of ZnTCNQF_2 material are present as: 2222, 2120 cm^{-1} for the C=N stretch, 1499 cm^{-1} for ring C=C stretch, 1425 cm^{-1} for exocyclic C=C stretch and 1302 cm^{-1} for ring C-C and C-F stretches. These absorption bands are therefore consistent with TCNQF_2^{2-} as discussed in Chapter 3. However, absorbance in Raman spectrum absorption bands at 2196, 1614 and 1394 cm^{-1} resembled those expected for TCNQF_2^- . Moreover, almost identical spectra were obtained by directly mixing TCNQF_2^{2-} and Zn^{2+} and the precipitate formed when mixing a solution of TCNQF_2^- and Zn^{2+} (Figure 4). These spectra closely resemble those expected for TCNQF^- materials with bands at 2226, 2159, 1513 and 1256 cm^{-1} . Thus, although there was a significant shift in the $\text{C}\equiv\text{N}$ stretch at 2138 cm^{-1} , the other peaks are close to those expected for TCNQF^- -based materials. Raman spectra showed bands at 2198, 1614 and 1397 cm^{-1} were also consistent for a Zn-TCNQF^- material. This is the same behavior described for other TCNQF_2^- based materials (see Chapter 5). Again the TCNQF_2^- solid is not stable enough for characterization. Synthesis of ZnTCNQF_n was performed inside the glove box and could be stored under vacuum. However on exposure to air the colour change to bright yellow colour to green and spectra for TCNQF_n^- are obtained. Again, the presence of four fluorine atoms in TCNQF_4 significantly enhances the stability of the dianion species.

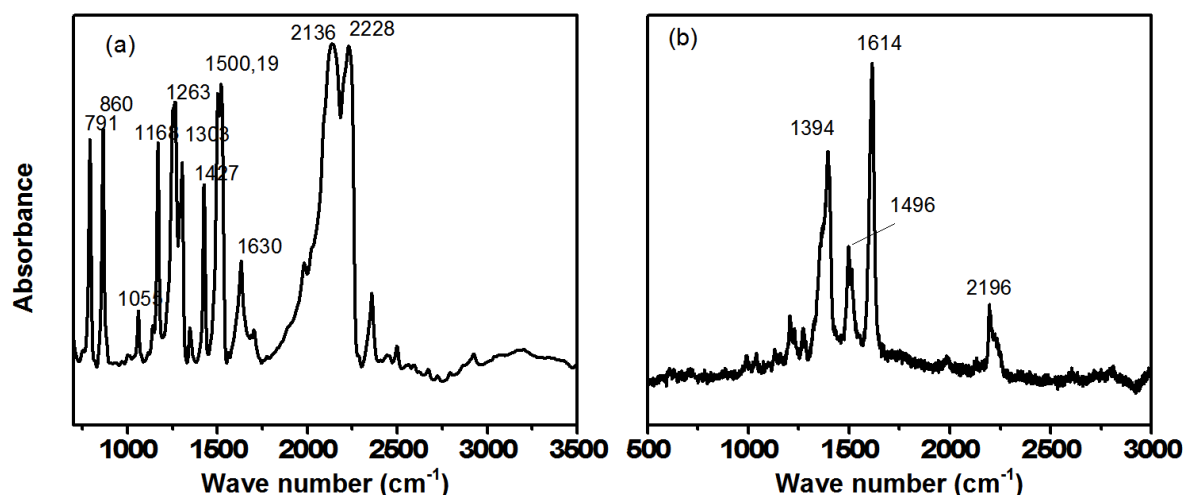


Figure 3 (a) IR and (b) Raman spectra for the solid obtained by mixing 5.0 mM Zn^{2+} with 5.0 mM $TCNQF_2^-$ in acetonitrile

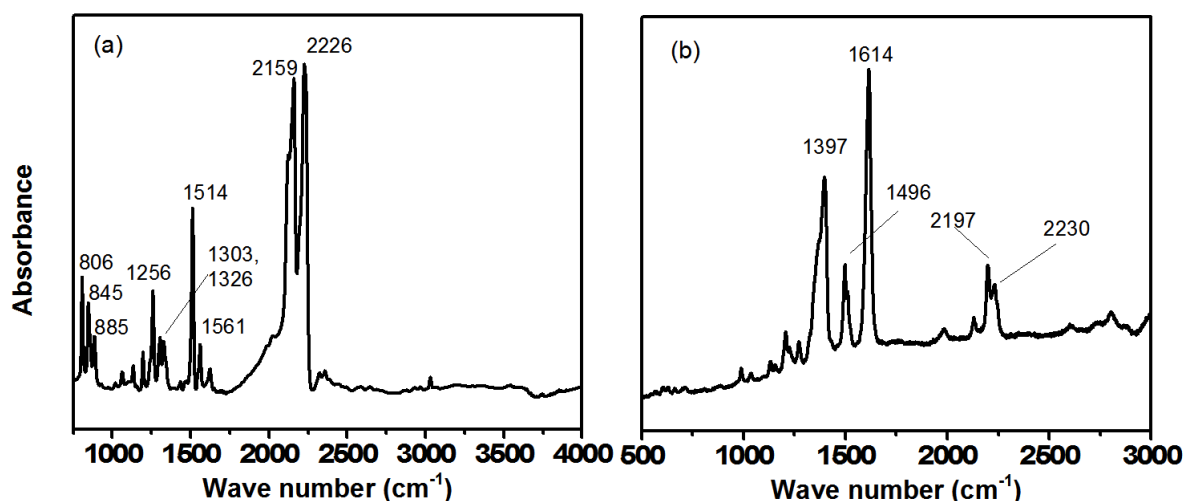


Figure 4 (a) IR and (b) Raman spectra for the solid obtained by mixing 5.0 mM Zn^{2+} with 5.0 mM $TCNQF^-$ in acetonitrile

The equilibrium constants for the disproportionation reaction given in equation 1 for TCNQ and $TCNQF_4$ analogs are very small.⁶ Similarly small equilibrium constants for TCNQF and $TCNQF_2$ are also calculated from the difference in the formal potentials for $TCNQF_n^{0/-}$ and $TCNQF_n^{-/2-}$ processes (537 mV for both derivatives) leading to a K_{eq} value of 6.16×10^{-10} (where $K_{eq} = 10^{\frac{E_1^0 - E_2^0}{0.0585}}$ at 22°C, and E_1^0 and E_2^0 are the reversible formal potentials for $TCNQF_n^{0/-}$ and $TCNQF_n^{-/2-}$ in acetonitrile). Thus, disproportionation is driven by the precipitation of $ZnTCNQF_n$

as in equation 3. A similar phenomenon was not observed in the presence of Ni^{2+} or Co^{2+} which can be attributed to their higher solubilities in acetonitrile.

Disproportionation of TCNQ^- and TCNQF_4^- in the presence of Zn^{2+} is not favoured when water is present in solution as also applied with TCNQF_n ($n=1, 2$). Figure 5 provides UV-Vis spectra of solutions containing 5 mM TF_n^- and 5 mM Zn^{2+} along with added water. Upon addition of H_2O , the absorbance at 390 nm for TCNQF_n^0 decreased while bands for TCNQF_n^- increased.

At the same time, the green solids gradually dissolved and when enough water was added, completely disappeared. This suggests that in the presence of water the equilibrium position of the reaction in equation lies the left so that disproportionation of TCNQF_n^- no longer is favoured.

The synthesis of $\text{Zn}(\text{TCNQ})_2 \cdot 2\text{H}_2\text{O}$ has been reported chemically and electrochemically in aqueous or acetonitrile solution respectively,^{7,8} where the Zn^{2+} source was $\text{Zn}(\text{NO}_3)_2 \cdot 6\text{H}_2\text{O}$, however there was no disproportionation reported in these scenario. This implies that there was a competition between reaction occurs in equation 4 and the formation of $\text{Zn}(\text{TCNQF}_n)_2 \cdot 2\text{H}_2\text{O}$ via equation 5, in which the formation of $\text{Zn}(\text{TCNQF}_n)_2 \cdot 2\text{H}_2\text{O}$ prevents the disproportionation of TCNQF_n^- .

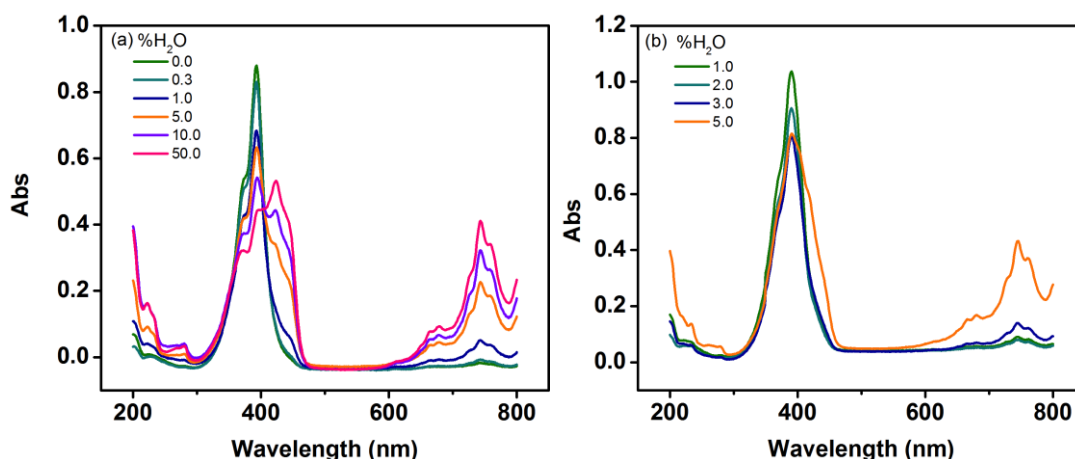
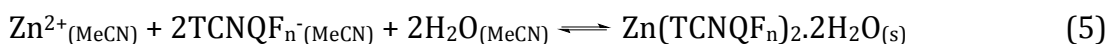


Figure 5 UV-Vis spectra for solutions obtained after mixing 5.0 mM (a) TCNQF_2^- and (b) TCNQF^- with 5.0 mM Zn^{2+} in acetonitrile upon addition designated amount added water

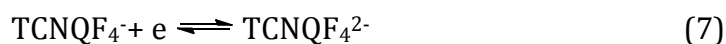
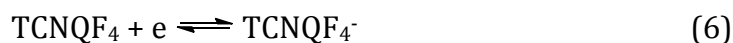
7.1.4. Conclusion

An analogous disproportionation of TCNQF⁻ and TCNQF₂⁻ was observed in acetonitrile in the presence of Zn²⁺, compared to TCNQ and TCNQF₄⁻. Although no kinetics or thermodynamic data has been derived from the study, it confirms the influence of Zn²⁺ on the disproportionation of TCNQF_n⁻ across the family.

7.2. The preparation of [M(DMF)₂TCNQF₄].2DMF materials

7.2.1. Introduction

As noted in previous chapters TCNQF₄ is a strong electron acceptor and can be reduced through two chemically and electrochemically reversible processes



Results in previous chapters suggest only TCNQF₄²⁻ and the two electron reduced materials are air stable. Thus dianionic TCNQF₄²⁻ derivatives were all characterized.

Herein, the electrochemistry of TCNQF₄ in the presence of Zn²⁺, Co²⁺ and Mn²⁺ in the mixed solvent of acetonitrile (MeCN) and dimethylformamide (DMF) is investigated to reveal the formation of an insoluble material on the electrode surface. These materials were then synthesized by mixing TCNQF₄²⁻ chemically or electrochemically generated with a solution of a metal cation. Crystals were obtained using the chemical synthesis approach but not from electrochemical synthesis and these complexes were characterized using X-ray diffraction, IR, UV-Vis and electrochemical methods.

The single crystal X-ray diffraction (XRD) was obtained for the Zn materials which have 2D sheet structures. Their formula is [Zn(DMF)₂TCNQF₄].2DMF in which two DMF molecules are coordinated to the metal ions and the other two act as solvents of crystallization within the lattice. In this case both chemical and electrochemical methods generated the same material as confirmed by IR and powder XRD methods, although the electrochemical approach does not afford highly crystalline samples. Moreover, IR spectra contained bands which distinguished between coordinated and uncoordinated mode DMF. The IR, UV-Vis and electrochemical

data also confirmed the existence of only TCNQF₄²⁻ when the solids are dissolved in DMF solution. Interestingly, these new materials have solvent exchangeability, as soaking the DMF derivative in MeCN resulted in solvent exchange.

7.2.2. Experimental

7.2.2.1. Chemicals

Zn(ClO₄)₂·6H₂O (Alfa Aesar), Co(ClO₄)₂·6H₂O (Aldrich), Mn(ClO₄)₂·6H₂O (Aldrich), AgNO₃ (Aldrich), acetonitrile (MeCN) (HPLC grade), dimethylformamide (DMF) was stored over molecular sieves. Acetone, iso-propanol were used as received from the manufacturer. TCNQF₄ (97% Aldrich) was recrystallized from dichloromethane prior to use. Tetrabutylammonium hexafluorophosphate (Bu₄NPF₆) (Wako) was recrystallized twice from 96% ethanol prior to use.

7.2.2.2. Electrochemistry

Voltammograms were recorded at room temperature with a Bioanalytical Systems (BAS) 100W electrochemical workstation. A standard three-electrode cell was employed with glassy carbon (1 and 3 mm diameter) or indium tin oxide (ITO) coated glass plated working electrodes. A silver wire in contact with acetonitrile containing 1.0 mM AgNO₃ and 0.1 M Bu₄NPF₆ was used as a Ag/Ag⁺ reference electrode. The reversible potential of this electrode is -0.122 V versus ferrocene/ferrocenium couple. The counter electrode was a Pt wire (1.0 mm diameter). The solutions were purged with nitrogen for 10 minutes before the experiments and a stream of nitrogen was maintained on top during the experiments.

Bulk electrolysis experiments employed Pt meshes as working electrode and counter electrode. All the electrodes were placed in an H-type three-compartment cell. The studied solution was stirred and purged with nitrogen during the course of the bulk electrolysis. A potential of 160 mV was applied to a designated concentration TCNQF₄ solution in acetonitrile (0.1 M Bu₄NPF₆) to reduce TCNQF₄ to TCNQF₄⁻. Then TCNQF₄²⁻ was sequentially generated at a potential of -350 mV. The bulk electrolysis experiment was stopped when the current decreased to 0.1% of the initial value.

7.2.2.3. *Synthesis of [ZnTCNQF₄(DMF)₂](DMF)₂*

A solution of Li₂TCNQF₄ (43.4mg, 0.15 mmol) in CH₃OH (10 ml) was layered over a solution of Zn(ClO₄)₂.6H₂O (55.9 mg, 0.15 mmol) in DMF (10 ml). Colourless crystals which were suitable for crystallographic studies were formed after one day at room temperature (32.5 mg). UV/vis (nm)(CH₃CN): 333 (TCNQF₄²⁻), 220 (TCNQF₄²⁻). Anal. Calcd. for [ZnTCNQF₄(DMF)₂](DMF)₂ [C₂₄H₂₈N₈F₄O₄Zn]: C 45.47%, H 4.45%, N 17.68%. Found: C 45.24 %, H 4.75 %, N 17.98%.

7.2.2.4. *Crystallography*

Crystal structure data were collected on an Oxford Diffraction Supernova diffractometer. The structure was solved using direct methods and refined using a full-matrix least-squares procedure, using all data, within the WinGX program system. The X-ray powder diffraction (XRD) pattern also was collected using the Oxford Diffraction Supernova diffractometer.

7.2.2.5. *Other instrumentation*

UV-Vis spectra were recorded with a Varian Cary 5000 UV-Vis NIR spectrophotometer with a 1.0 cm path length cuvette. FTIR spectra were obtained with a Perkin Elmer FTIR spectrometer 100 or a Varian UMA600 IR microscope and FTS7000 optics bench using 128 scans and a resolution of 8 cm⁻¹.

7.2.3. Results and discussion

7.2.3.1. *Cyclic Voltammetry of TCNQF₄ in the presence of M²⁺ in the mixed MeCN/DMF solvents*

The electrochemical behavior of TCNQF₄ in the presence of some transition metal cations has been well-investigated in neat MeCN.⁹⁻¹¹ However, the introduction of DMF into an MeCN solution of TCNQF₄ led to some changes in the electrochemical response in the presence of Zn²⁺, Co²⁺, Mn²⁺ (M²⁺) ions.

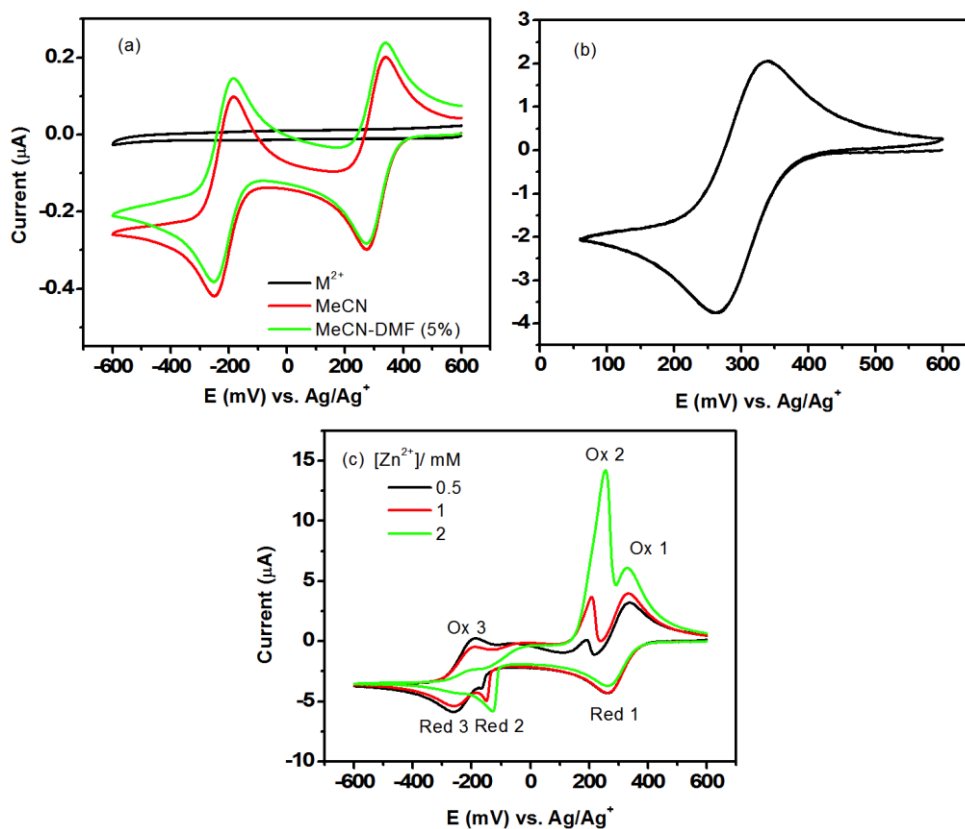


Figure 3. Cyclic voltammograms measured in MeCN and MeCN/DMF (5%) (0.1 M Bu_4NPF_6) with a GC electrode at a scan rate of 50 mV s^{-1} : (a) 1.3 mM TCNQF₄, 0.1 M M^{2+} ; (b) 2.0 mM TCNQF₄ in the presence of 0.1 M Zn^{2+} , (c) 2.0 mM TCNQF₄ with designated Zn^{2+} concentration

TCNQF₄ was examined initially using a MeCN/DMF mixture with 5% DMF. Under these conditions TCNQF₄ still undergoes two electrochemically reversible one-electron reduction processes. Cyclic voltammograms derived from 1.3 mM TCNQF₄ in the MeCN-DMF mixed solvent (0.1 M Bu_4NPF_6) exhibit TCNQF₄⁰/TCNQF₄⁻ and TCNQF₄⁻/TCNQF₄²⁻ processes at 253.5 mV and -217.5 mV, respectively. These are very similar to that observed if TCNQF₄ is dissolved in neat MeCN. Cyclic voltammograms of TCNQF₄ in a 0.1 M M^{2+} solution (MeCN/DMF) over the potential range where TCNQF₄ is reduced (Figure 3a) confirm that M^{2+} is not electroactive in this potential range. Hence, electrochemical experiments on TCNQF₄^{0/-/2-} can be performed without interference from M^{2+} electrochemistry.

In the presence of 0.1 M Zn^{2+} , cyclic voltammograms over the potential range of 600 mV to 50 mV which covers TCNQF₄^{0/-} process, are unchanged (Figure 3b). This implies that Zn^{2+} -TCNQF₄⁻ solid does not electrocrystallize under these conditions.

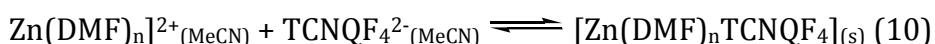
However, significant changes are found in extending the potential window to values that include the second TCNQF₄^{-/2-} process. Cyclic voltammograms obtained for the reduction of 2 mM TCNQF₄ in the presence of 0.5 mM Zn²⁺ over a wide potential range are illustrated in Figure 3c. When the potential was scanned negatively, three reduction processes were observed. In addition to the first two processes (Red1 and Red3) associated with the sequential reduction of TCNQF₄ to TCNQF₄¹⁻ and then to TCNQF₄²⁻, a new sharp process present prior to the second reduction process at -166 mV (Red2). This peak became dominant while the Red3 peak almost disappeared upon increasing the concentration of Zn²⁺ from 0.5 mM to 2 mM (Figure 3c). This behaviour is consistent with an EC mechanism, where an electrochemical reaction (E step) is coupled with a chemical reaction (C step) as shown in equation 5 and 6.¹² The consumption of B after the reduction step (equation 5) followed by the reaction in equation (6) decreases the concentration of B near the electrode surface. This makes reduction easier according to Nernst equation (equation 7) so that reduction can occur at a less negative potential, i.e it is easier to reduce TCNQF₄⁻ to TCNQF₄²⁻.



$$E_p = E^0 + 0.056 \log \frac{[A]}{[B]} \quad \text{at } 23^{\circ}\text{C} \quad (7)$$

here, E⁰ is the formal potential, E_p is peak potential, [A] and [B] are the concentrations of the reduced and oxidized forms of the couple, respectively.

On reversing the scan direction, a third well-resolved oxidation process (Ox2) is detected at 214 mV associated with Red2 which has a greater peak current magnitude than Ox1 or Ox2. The relationship of Ox2 and Red2 is confirmed below. The peak-to-peak separation ($\Delta E_p = |E_{p^{ox}} - E_{p^{red}}|$) is expected to be 56 mV for a reversible diffusional process, but for Red2 and Ox2 are 374 mV at scan rate of 50 mV.s⁻¹. This indicates that this couple is irreversible. Red2 process is attributed to the reduction of TCNQF₄⁻ to TCNQF₄²⁻ accompanied by reaction with Zn²⁺ to form an insoluble material on the electrode surface. And process Ox3 is attributed to the oxidation of Zn-TCNQF₄²⁻ material to TCNQF₄⁻ giving rise to a stripping of the insoluble material off the electrode surface according to equations 8-10.



Effect of switching potential

The coupling of the process Ox2 and Red2 was further supported by varying the switching potential. When the potential was switched at a value less negative than -110 mV, process Ox2 was not observed on the reverse scan. However, when switching potential to more negative value of -115 mV, and hence at the onset of Red2, the Ox2 process was detected (Figure 4). Furthermore, a current loop was observed. The presence of current loops when the scan direction is reversed at the foot of a process is a characteristic feature of a nucleation growth mechanism.^{13,14} This observation is consistent with the deposition of Zn-TCNQF₄ material on the electrode surface.

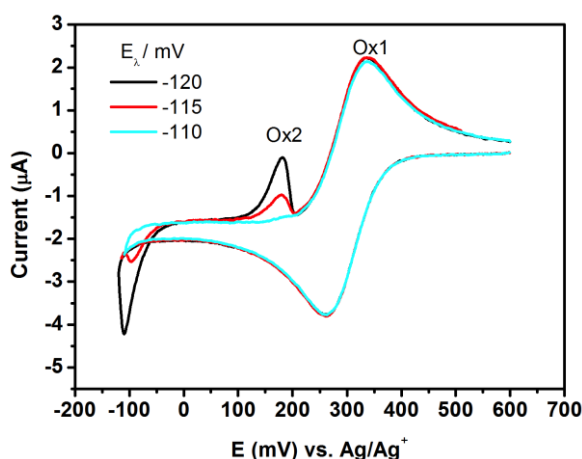


Figure 4. Cyclic voltammograms obtained at a GC electrode at 50 mV.s⁻¹ in MeCN/DMF (5%) (0.1 M Bu₄NPF₆) solution containing 2 mM TCNQF₄ and of 2 mM Zn²⁺ using designated switching potentials.

Effect of scan rate

The nucleation-growth mechanism is also supported by the scan rate dependence on cyclic voltammograms (Figure 5). The peak potential for Ox1 and Red1 are independent of scan rate as expected and IR drop is insignificant. In contrast, Ox3 and Red3 peak potential show a great increase on scan rates, E_p^{ox3} becomes slightly more positive when the scan rate increases from 20 to 200 mV.s⁻¹ while

the E_{p}^{red3} becomes 21 mV more negative (-119 mV to -140 mV). Moreover, the residue at faster scan rates emerge from of residue at lower scan rate. This is also consistent with nucleation-growth mechanism where mathematical modeling predicts that the gradients of the current-voltage curves are steeper at low scan rates than at high scan rates.¹³ All data are therefore consistent with insoluble Zn-TCNQF₄ formation.

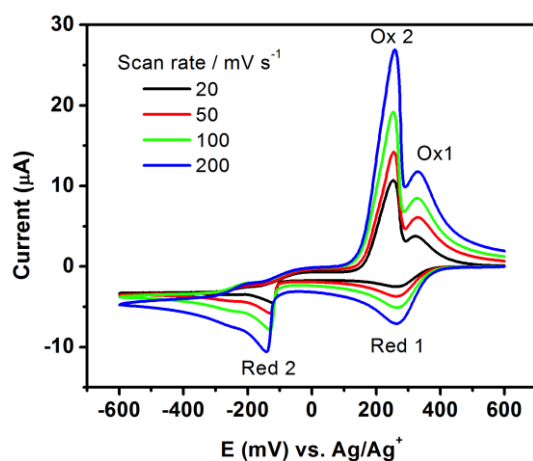


Figure 5. Cyclic voltammograms obtained at a GC electrode at 50 mV.s⁻¹ in MeCN/DMF (5%) (0.1 M Bu₄NPF₆) solution containing 2 mM TCNQF₄ and of 2 mM Zn²⁺ at designated scan rates.

Concentration effect of Zn²⁺ and TCNQF₄

The influence of both TCNQF₄ and Zn²⁺ concentration on the cyclic voltammetric behaviour was investigated.

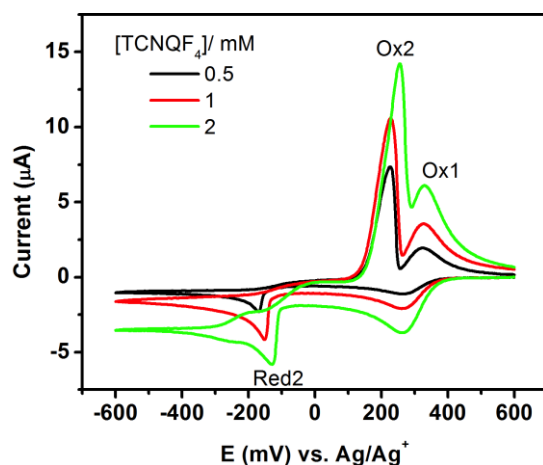


Figure 6. Cyclic voltammograms obtained at a GC electrode in MeCN/DMF (5%) (0.1 M Bu₄NPF₆) solution containing 2 mM Zn²⁺ and designated concentrations of TCNQF₄ at a scan rate of 50 mV s⁻¹

Increasing the Zn^{2+} concentration from 0.5 mM to 2 mM in the presence of 2 mM of TCNQF₄ did not lead to a change in the Ox1 and Red1 processes. However, the peak potential for the Red3 process shifted positively (Figure 3c) by 36.7 mV. Similar behaviour was observed when the concentration of TCNQF₄ was varied from 0.5 mM to 2.0 mM and the concentration of Zn^{2+} was maintained at 2 mM (Figure 6). This potential shift is consistent with an EC mechanism mentioned above. The formation of Zn-TCNQF₄ material was again supported by results shown in Figure 7a. In this experiment, the potential was held at -600 mV for known period of times before scanning the potential in the positive direction. When the potential is held at -600 mV, TCNQF₄⁰ is reduced to TCNQF₄²⁻ which then combined with Zn^{2+} to form an insoluble “film” on the electrode surface which is oxidized when the potential is scanned in the positive direction giving rise to oxidation current Ox3. Only one phase of Zn-TCNQF₄ complex was observed which should be thermodynamically stable under the electrochemical conditions.

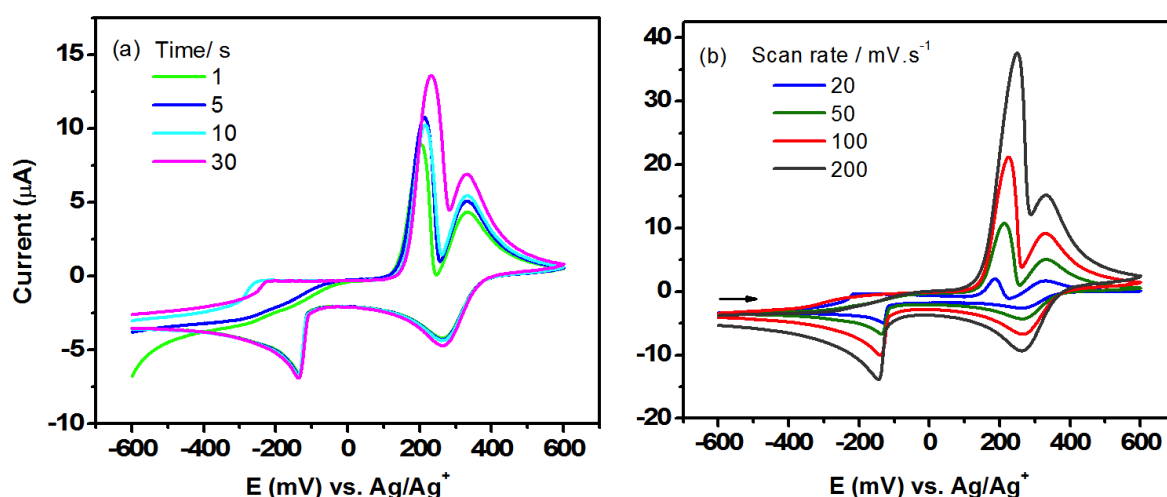


Figure 7. Cyclic voltammograms obtained at a GC electrode at 50 $\text{mV}\cdot\text{s}^{-1}$ in MeCN/DMF (5%) (0.1 M Bu_4NPF_6) solution containing 2 mM TCNQF₄ and of 2 mM Zn^{2+} when potential was held at -600 mV for: (a) designated times followed by a positive scan of potential, (b) for 5s and scan times followed by a positive scan of potential at designated scan rates

Cyclic voltammetry of TCNQF₄ in the presence of Zn^{2+} :

In neat MeCN solvent, disproportionation occurred upon addition of Zn^{2+} to a TCNQF₄⁻ solution leading to the formation of ZnTCNQF₄ solid and neutral TCNQF₄ as described earlier and shown in equation¹⁵



However, when a stoichiometric amount of Zn^{2+} in DMF solution was added to a 2.0 mM solution of TCNQF_4^- in MeCN to produce a MeCN/DMF (5%) mixture, no precipitate was detected. Moreover, the cyclic voltammograms of a 2.0 mM TCNQF_4^- solution in the presence of 2.0 mM Zn^{2+} was identical to that for the TCNQF_4^- solution, indicating that the disproportionation is not favoured in MeCN/DMF mixed solvent media (Figure 8). Thus, the presence of DMF has a significant influence on the chemistry of this system. The formation of strongly solvated $\text{Zn}(\text{DMF})_n^{2+}$ cation is suggested to hinder disproportionation found in neat MeCN.

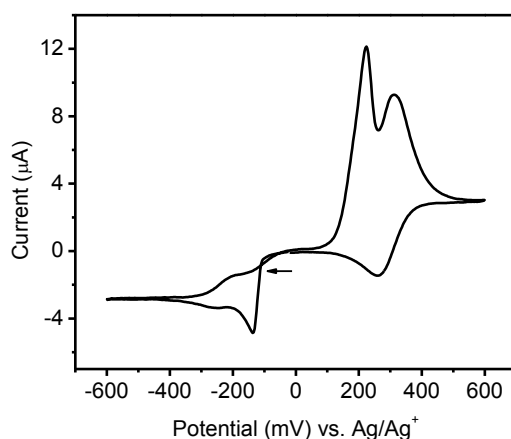


Figure 8. Cyclic voltammograms obtained at a GC electrode with a scan rate of $50 \text{ mV}\cdot\text{s}^{-1}$ in MeCN/DMF (5%) ($0.1 \text{ M Bu}_4\text{NPF}_6$) solution containing 2 mM TCNQF_4^- and of 2 mM Zn^{2+}

Importantly, cyclic voltammograms remained consistent upon multiple cycles of the potential, indicating that the regeneration of TCNQF_4^0 and Zn^{2+} is quantitative in each cycle.

Similarly, cyclic voltammetric behaviour was observed in the presence of Co^{2+} (Figure 9,10) and Mn^{2+} (Figure 11) in a MeCN/DMF solution containing TCNQF_4^- . However, a slight difference was observed for the Co^{2+} - TCNQF_4^- system. Unlike the Zn^{2+} example, following reduction of TCNQF_4^- to TCNQF_4^{2-} , the current stayed constant as the potential was scanned more negatively. This is consistent with the formation of an insoluble film on the electrode surface that blocks the current flow.

A further interesting feature for Co^{2+} in MeCN/DMF is that there was no evidence of a formation of a second phase of Co-TCNQF₄ as reported in neat MeCN.⁹

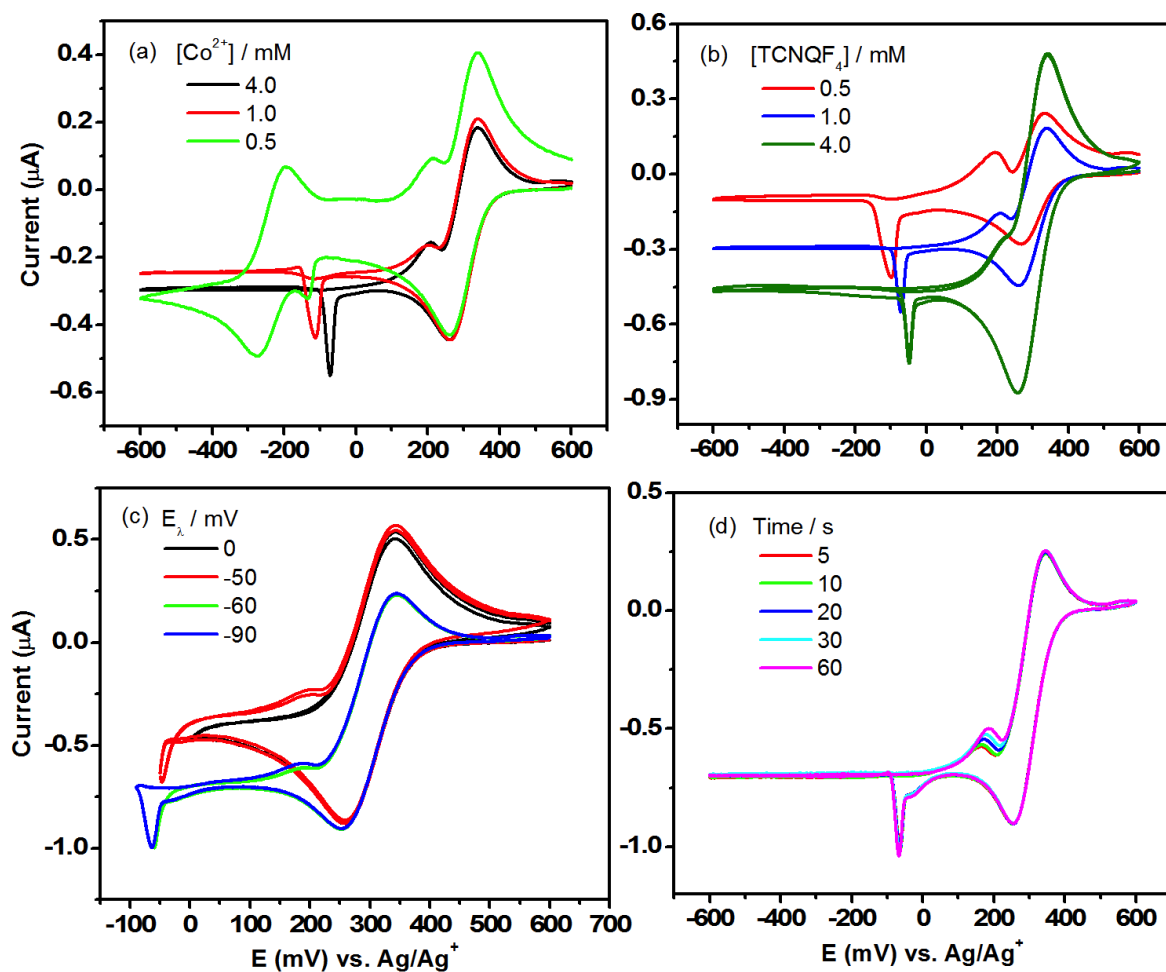


Figure 9. Cyclic voltammograms obtained at a GC electrode with a scan rate of 50 $\text{mV}\cdot\text{s}^{-1}$ in MeCN/DMF (5%) (0.1 M Bu_4NPF_6) solution containing: (a) 2 mM TCNQF₄ designated Co^{2+} concentrations; (b) 4 mM Co^{2+} and designated TCNQF₄ concentrations; (c) 4 mM TCNQF₄ and 4 mM Co^{2+} at designated switching potentials; (d) the same conditions as (c) but the potential was held at -600 mV for the designated time before the potential was reversed.

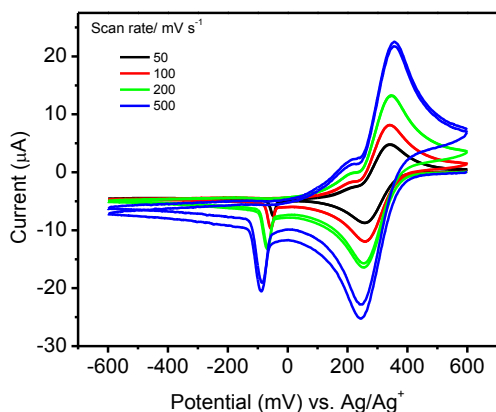


Figure 10. Cyclic voltammograms obtained at a GC electrode in MeCN/DMF (5%) (0.1 M Bu₄NPF₆) solution containing 4mM Co²⁺ and 4 mM TCNQF₄ at designated scan rates

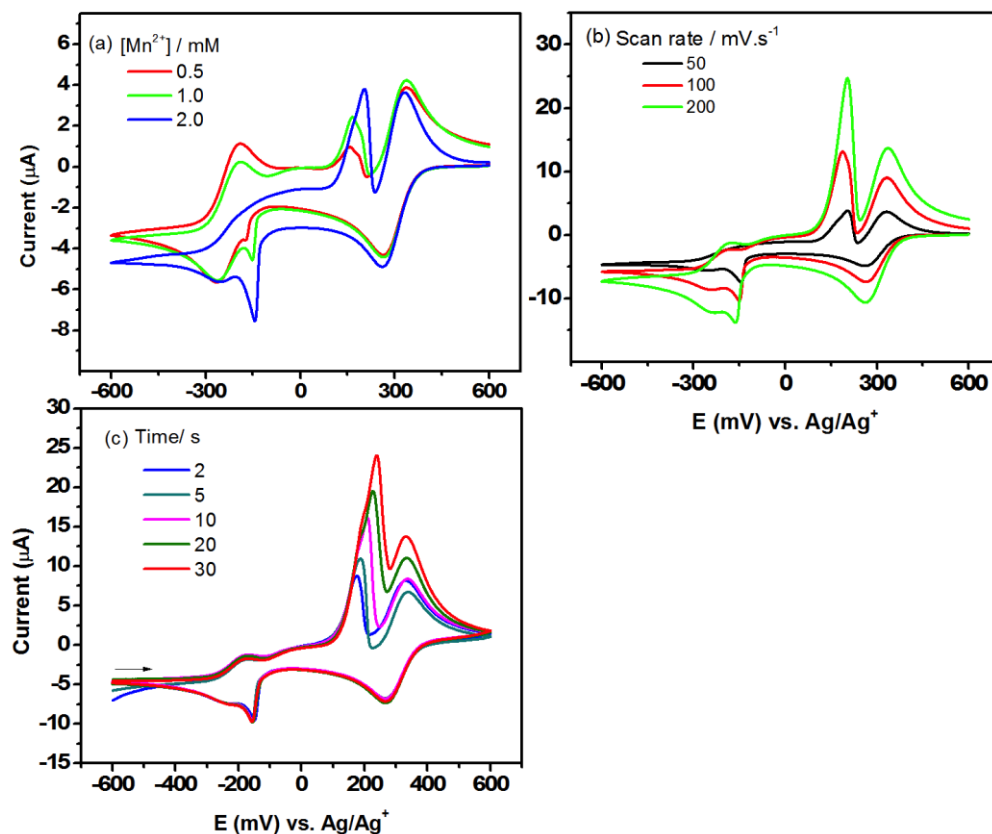


Figure 11. Cyclic voltammograms obtained at a GC electrode with a scan rate of 50 mV.s⁻¹ in MeCN/DMF (2.5%) (0.1 M Bu₄NPF₆) solution containing: (a) 2 mM TCNQF₄ designated Mn²⁺ concentrations; (b) 2 mM Mn²⁺ and designated TCNQF₄ concentrations; (c) 2 mM TCNQF₄ and 2 mM Mn²⁺ when the potential was held at -600 mV for the designated time before being reversed.

7.2.3.2. X-ray structural characterization of $\text{ZnTCNQF}_4(\text{DMF})_2 \cdot 2\text{DMF}$

Colourless crystal of $\text{Zn}(\text{DMF})_2\text{TCNQF}_4 \cdot 2\text{DMF}$ crystallized in the monoclinic space group $P2/c$ with unit cell parameters of $a = 8.9848(18)$, $b = 11.592(2)$, $c = 26.181(7)$ Å, $\beta = 101.22(3)^\circ$, $V = 2674.68$ Å³. Crystal structure is shown in Figure 12.

The asymmetric unit includes two halves of two crystallographic distinct TCNQF_4^{2-} moieties which orient differently in the lattice, two coordinate DMF and two uncoordinated DMF. Those two different oriented TCNQF_4^{2-} moieties form two different TCNQF_4^{2-} layers in the crystal lattice. The distance between two adjacent TCNQF_4^{2-} moieties in each layer is too far for any pi-pi stacking interaction.

The degree of charge transfer (ρ) on the TCNQF_4 moieties in both crystal structures have been estimated by the mean bond lengths of TCNQF_4 (Table 1) using Kistenmacher relationship, $\rho = A[c/(b+d)] + B$, ($A = -46.729$ and $B = 22.308$, A , B were determined from neutral TCNQF_4 ($\rho = 0$)¹⁶ and TCNQF_4^{2-} monoanion in $n\text{-Bu}_4\text{N}\text{TCNQF}_4$ ($\rho = -1$).¹⁷ The calculated ρ values of -2.17 and -2.18 support the assignment of TCNQF_4^{2-} . The structural parameters are closely consistent with those for TCNQF_4^{2-} complexes reported previously.

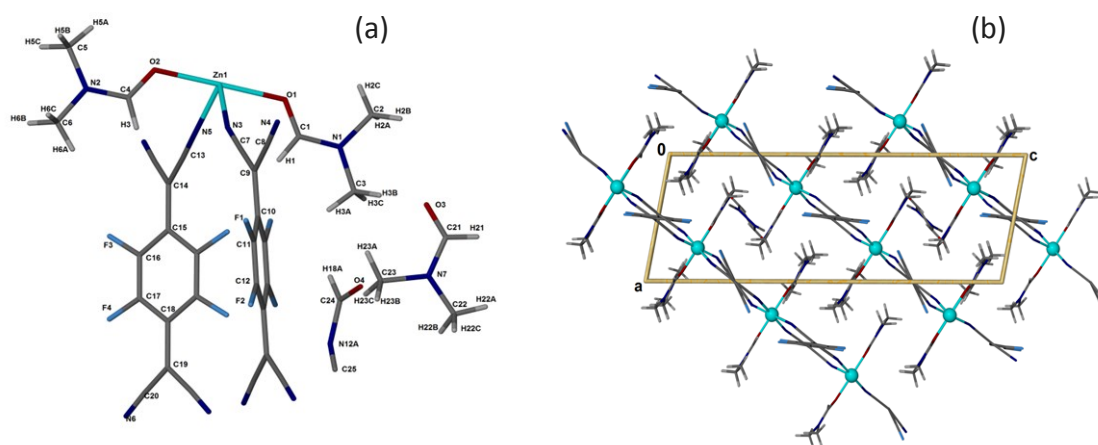
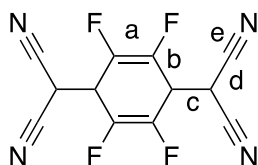


Figure 12. Single crystal X-ray structures; (a) asymmetric unit of $[\text{ZnTCNQF}_4(\text{DMF})_2] \cdot 2\text{DMF}$, (b) packing diagram viewed along the b-axis

Table 1. Degree of charge transfer (ρ) calculated from mean bond length in different complexes



	$a/\text{\AA}$	$b/\text{\AA}$	$c/\text{\AA}$	$d/\text{\AA}$	$e/\text{\AA}$	ρ	Ref.
TCNQF ₄ ⁰	1.334	1.437	1.372	1.437	1.140	0.00	19
Zn(DMF) ₂ TCNQF ₄ .2DMF	1.373	1.387	1.462	1.402	1.151	-2.18	This work
(Bu ₄ N) ₂ TCNQF ₄	1.377	1.403	1.456	1.406	1.161	-1.92	20
[(Me ₅ Cp) ₂ Fe] ₂ TCNQF ₄	1.373	1.398	1.457	1.403	1.154	-2.00	19

7.2.3.3. Bulk electro-generation of the M²⁺-TCNQF₄ material in the MeCN/DMF mixture

TCNQF₄²⁻ was generated by exhaustive reductive electrolysis in MeCN (0.1 M Bu₄NPF₆) solution as described in section 3.1.2. A solution with a stoichiometric amount of M²⁺ was prepared separately in an appropriate volume of DMF. The two solutions were then mixed together resulting in a white precipitate in the case of Zn²⁺ or an orange precipitate when Co²⁺ is present. In the case of Mn²⁺, a pale green precipitate formed after stirring for 5 minutes. All the solutions were stirred for 10 minutes before the precipitates were collected by centrifugation. The products were then washed with MeCN-DMF (5%) mixture three times to remove electrolyte and then dried under vacuum for further characterization. Attempts to generate single crystals rather than powders via electrochemical method were unsuccessful.

The IR spectra for the ZnTCNQF₄ solid are shown in Figure 13. Both chemically and electrochemically generated materials exhibit identical IR bands showing the presence of free and coordinated-DMF at 1688 and 1647 cm⁻¹, respectively.¹⁸ The

IR spectra also show the existence of TCNQF_4^{2-} via the characteristic $\text{C}\equiv\text{N}$ stretching vibration bands of the dianion at 2142, 2164 and 2211 cm^{-1} .¹⁹

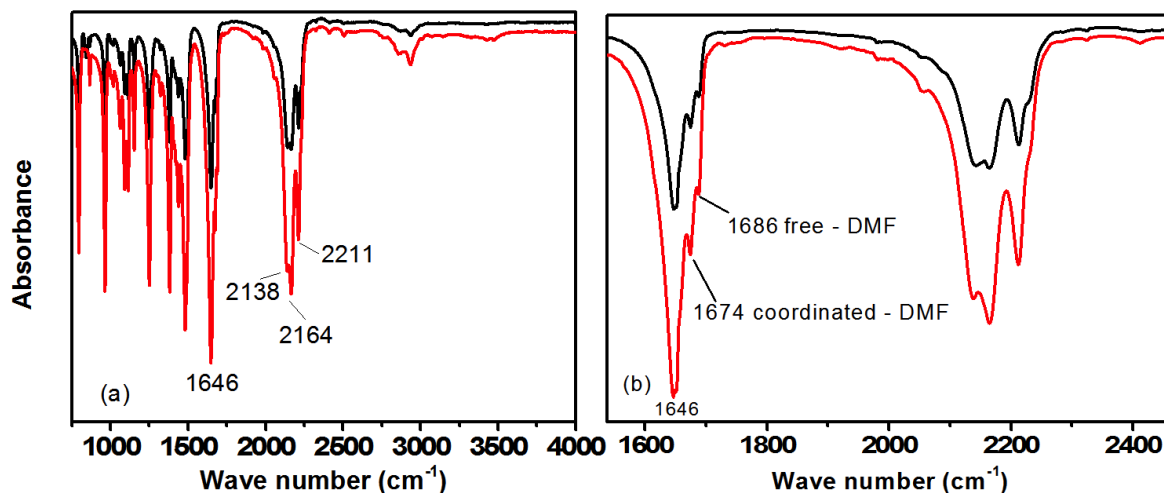


Figure 13. IR spectra of (black) chemically generated and (red) electrochemically generated $[\text{ZnTCNQF}_4(\text{DMF})_2].2\text{DMF}$, (a) full spectra, (b) close up to 1600 to 2400 cm^{-1} range

Furthermore, the X-Ray diffraction powder spectrum of materials synthesized by the electrochemical method was identical to that prepared using chemically, except that materials in former case were not as crystalline as evident by broader diffraction peaks (Figure 14).

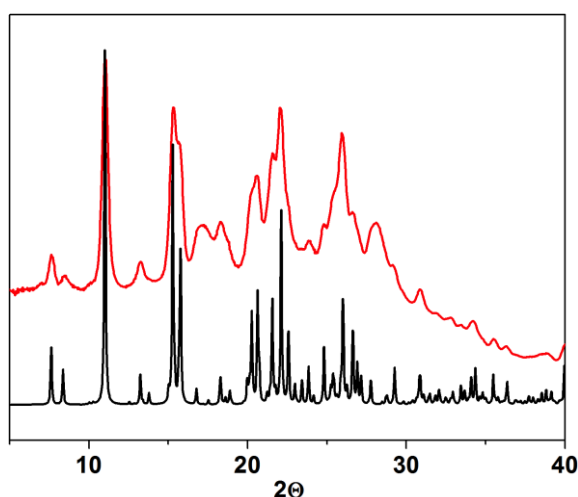


Figure 14. XRD spectrum of chemically synthesized (black) and electrochemically synthesized $[\text{Zn}(\text{DMF})_2\text{TCNQF}_4].2\text{DMF}$

Solution phase characterization of the new complexes was undertaken in neat DMF. UV-Vis spectra and steady state electrochemical methods both confirmed the

existence of the dianion TCNQF_4^{2-} (Figure 15). The band at 333 nm in the UV-Vis spectrum in DMF is characteristic of the dianion TCNQF_4^{2-} .²⁰ Furthermore, steady state voltammogram of these dissolved materials in DMF (0.1M TBAPF_6) exhibits two oxidation processes of TCNQF_4^{2-} .

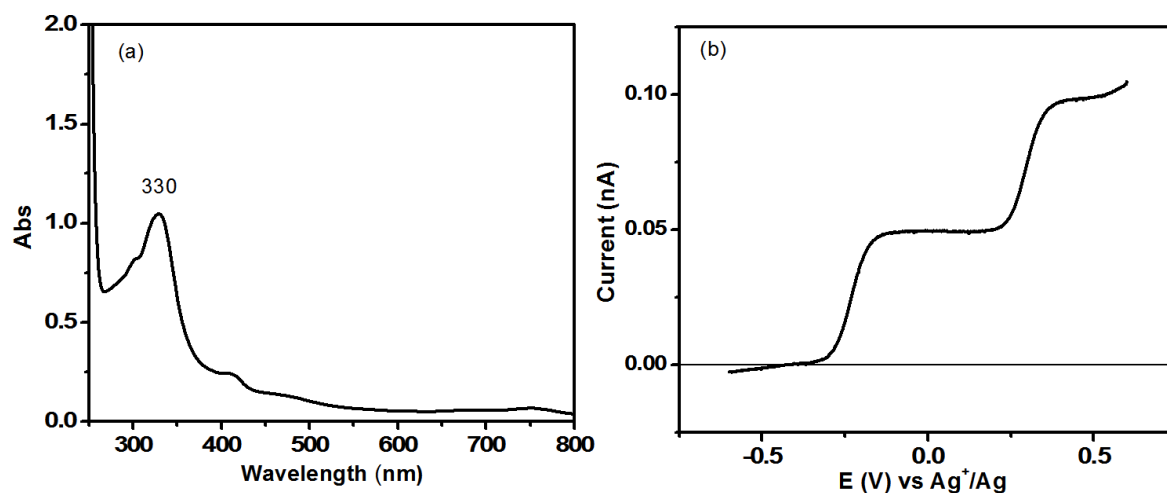


Figure 15. UV-Vis spectrum (a) and steady state voltammogram (b) of $[\text{M}(\text{DMF})_2\text{TCNQF}_4].2\text{DMF}$ dissolved in DMF (0.1M TBAPF_6)

$[\text{M}(\text{DMF})_2\text{TCNQF}_4].2\text{DMF}$ complexes is able to exchange solvent. The IR spectra shown in Figure 16 illustrate the change in the IR bands when that occurs. $[\text{Zn}(\text{DMF})_2\text{TCNQF}_4].2\text{DMF}$ complex is soaked in MeCN.

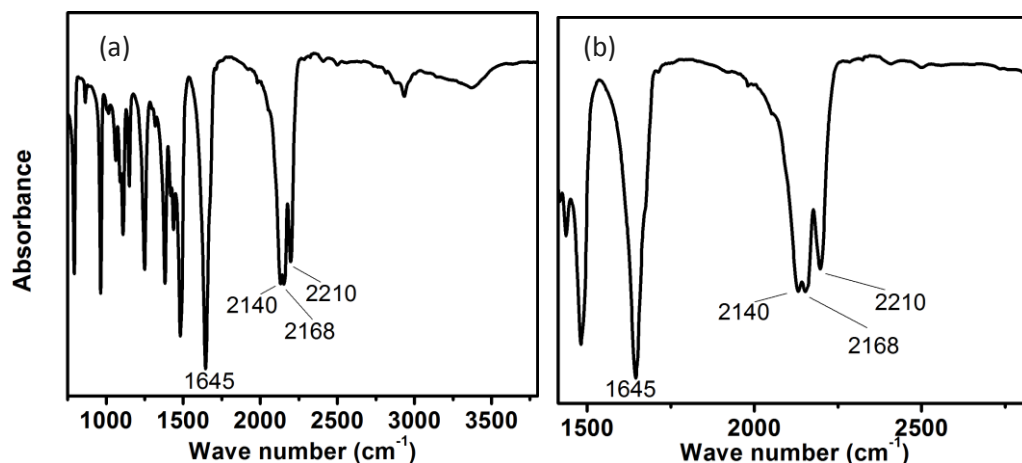


Figure 16. IR spectra of electrochemically generated $[\text{Zn}(\text{DMF})_2\text{TCNQF}_4].2\text{DMF}$ before (red) and after (black) soaked in MeCN, (a) full range spectrum, (b) close up to 1500 to 2600 cm^{-1} range.

The IR spectrum of the $[\text{Zn}(\text{DMF})_2\text{TCNQF}_4].2\text{DMF}$ solid obtained after soaking in neat MeCN showed the disappearance of free DMF band at 1686 cm^{-1} ; meanwhile,

the strong C=O band for coordinated DMF at 1646 cm^{-1} is retained. This implies that the coordinated DMF – metal bond is sufficiently strong to be maintained in neat MeCN.

7.2.4. Conclusion

The addition of DMF into conventional MeCN solvent for electrochemical experiment of TCNQF_n has a significant effect on the electrochemistry of TCNQF₄ in the presence of Zn²⁺. The disproportionation of TCNQF₄⁻ was not observed in the presence of 5% (w/w) of DMF. The formation of TCNQF₄²⁻-based materials with Zn²⁺, Co²⁺, Mn²⁺ were detected in voltammetric time scale in this mixed solvent. Interestingly, although [Zn(DMF)₂TCNQF₄].2DMF single crystal can not be obtained electrochemically, chemical approach produces good quality single crystal. The powder X-Ray diffraction pattern shows good agreement between the structures of these two materials. IR data also confirms this similar structure. An interesting property of [Zn(DMF)₂TCNQF₄].2DMF is the solvent exchangeability. IR spectrum reveals the disappearance of uncoordinated DMF band at 1686 cm^{-1} after the crystal being soaked in MeOH.

References

- (1) Lombardo, A.; Fico, T. R. *The Journal of Organic Chemistry* **1979**, *44*, 209.
- (2) Lindner, W.; Fugnitto, R.; Strzelecka, H.; Rivory, J. *Synthetic Metals* **1984**, *9*, 71.
- (3) Hill, J. P.; Santiago, J.; Sugino, T.; Shiro, M.; Shimizu, Y. *Inorganica Chimica Acta* **2001**, *315*, 107.
- (4) Hertler, W. R.; Hartzler, H. D.; Acker, D. S.; Benson, R. E. *Journal of the American Chemical Society* **1962**, *84*, 3387.
- (5) Hashimoto, S.; Yabushita, A.; Kobayashi, T.; Iwakura, I. *Chemical Physics Letters* **2016**, *650*, 47.
- (6) Nafady, A.; Le, T. H.; Vo, N.; Haworth, N. L.; Bond, A. M.; Martin, L. L. *Inorganic Chemistry* **2014**, *53*, 2268.
- (7) Fadly, M.; El Gandoor, M. A.; Sawaby, A. *Journal of Materials Science* **1992**, *27*, 1235.
- (8) Veder, J.-P.; Nafady, A.; Clarke, G.; De Marco, R.; Bond, A. M. *Australian Journal of Chemistry* **2012**, *65*, 236.
- (9) Le, T. H.; Nafady, A.; Bond, A. M.; Martin, L. L. *European Journal of Inorganic Chemistry* **2012**, *2012*, 5534.
- (10) Le, T.; O'Mullane, A.; Martin, L.; Bond, A. *Journal of Solid State Electrochemistry* **2011**, *15*, 2293.
- (11) Le, T. H.; Nafady, A.; Lu, J.; Peleckis, G.; Bond, A. M.; Martin, L. L. *European Journal of Inorganic Chemistry* **2012**, *2012*, 2889.
- (12) Bard, A. J.; Faulkner, L. R. *Electrochemical methods: Fundamentals and applications*; 2 nd ed.; John Wiley & Sons, INC: New York, 2001.
- (13) Fletcher, S.; Halliday, C. S.; Gates, D.; Westcott, M.; Lwin, T.; Nelson, G. *Journal of Electroanalytical Chemistry and Interfacial Electrochemistry* **1983**, *159*, 267.
- (14) Bond, A. M.; Fletcher, S.; Marken, F.; Shaw, S. J.; Symons, P. G. *Journal of the Chemical Society, Faraday Transactions* **1996**, *92*, 3925.
- (15) Le, T. H., Monash University, 2012.
- (16) Emge, T. J.; Maxfield, M.; Cowan, D. O.; Kistenmacher, T. J. *Molecular Crystals and Liquid Crystals* **1981**, *65*, 161.

- (17) O'Kane, S. A.; Clérac, R.; Zhao, H.; Ouyang, X.; Galán-Mascarós, J. R.; Heintz, R.; Dunbar, K. R. *Journal of Solid State Chemistry* **2000**, *152*, 159.
- (18) Sathyanarayana, D. N. *Vibrational Spectroscopy: Theory And Applications*; New Age International (P) Limited: New Delhi, 2004.
- (19) Nafady, A.; Bond, A. M.; Bilyk, A.; Harris, A. R.; Bhatt, A. I.; O'Mullane, A. P.; De Marco, R. *Journal of the American Chemical Society* **2007**, *129*, 2369.
- (20) Le, T. H.; Lu, J.; Bond, A. M.; Martin, L. L. *Inorganica Chimica Acta* **2013**, *395*, 252.

Conclusions and future work

Fluorinated derivatives of TCNQ have already been identified as having enormous potential for electronic devices and material applications. In particular the tetrafluorinated TCNQF₄ has a rich chemistry of the dianion, not previously observed in TCNQ. This thesis focuses on the redox and synthetic chemistry of two derivatives which are TCNQF and TCNQF₂. The use of electrochemistry as the primary method of exploration along with synthesis and spectroscopic and structural characterization, studies on TCNQF and TCNQF₂ have been described. The effect of fluorine substituents on the electrochemistry, acid-base properties and overall stability of complexes among the four derivative of TCNQF_n (n = 0-2, 4) was examined. In acetonitrile, TCNQF_n (n = 1, 2) undergo two one-electron reversible reduction processes as found in the other TCNQF_n (n = 0, 4) derivatives. However, the reversible potentials are highly dependent on the number of fluorine substituents, shifting to more positive potential as the number of F increases. Electrochemistry of TCNQF and TCNQF₂ in the presence of several transition cations was investigated for M = Co, Ni, Cu, Zn. These studies revealed some differences from similar complexes of TCNQ and TCNQF₄. Although the formation of both mono- and dianionic TCNQF_n solids was detected on the voltammetric time scale, the monoanion-based materials are considerably more stable than the dianionic complexes. The dianion-based materials readily decomposed in the air as evidence by visual inspection and/or spectroscopic data. The studies in this thesis cover four general topics areas as described below.

8.1. Investigation of the redox and acid-base properties of TCNQF and TCNQF₂ – Electrochemistry, vibrational spectroscopy and substituent effects

The redox and acid-base properties of TCNQF, TCNQF₂ and their mono- and dianions have been studied in comparison with the parent TCNQ and fully fluorinated TCNQF₄. Electrochemically, both fluorinated TCNQF_n (n = 1, 2) derivatives undergo two well-resolved one-electron reversible reductions steps in acetonitrile. The reversible potentials of two redox processes are in the order $E_{TCNQ} > E_{TCNQF} > E_{TCNQF_2} > E_{TCNQF_4}$ which are in good agreement with substituent effect of increasing the fluorines on TCNQ. The E^0 are also in good

linear relationship with the sum of Hammett constant of fluorine substituent in each derivatives implying a greater substituent effect on the redox properties across TCNQF_n family (n = 0, 1, 2, 4). The substituent effect was also found to affect the basicity as well as the stability of the anions, especially dianions in the presence of TFA. The dianions TCNQF_n²⁻ are readily protonated in TFA in a two step process to form HTCNQF_n⁻ and H₂TCNQF_n. The use of simulations allowed quantitative determination of both thermodynamic and kinetic parameters of the protonation reaction using cyclic voltammetric data. The equilibrium constants for the protonation of TCNQF_n²⁻ as shown in equation 1 were found to be 2.0×10⁷, and 8.0×10⁵ for TCNQF²⁻ and TCNQF₂²⁻, respectively, compared with 1.0×10⁸ and 3.0×10³ for TCNQ²⁻ and TCNQF₄²⁻, respectively. These results support the substituent effect of fluorine on the stability and basicity of the dianions of TCNQF_n.



The calculated vibrational spectroscopy of TCNQF and TCNQF₂ and their anions generated from DFT calculations were also discussed giving a useful spectroscopic reference for further characterization of TCNQF and TCNQF₂-based materials.

8.2. Electrochemistry of TCNQF and TCNQF₂ in acetonitrile in the presence of [Cu(MeCN)₄]⁺ - The formation of Cu-TCNQF_n⁻ materials and a comparative study on the catalytic activity of TCNQF_n derivatives

Cyclic voltammetry of TCNQF_n in the presence of [Cu(MeCN)₄]⁺ was investigated for both reduction processes, TCNQF_n^{0/-/2-}, without any interference from each other possible by varying the concentration of TCNQF_n and [Cu(MeCN)₄]⁺. The formation of materials based on the mono anionic TCNQF_n⁻ were detected on the voltammetric time scale using higher concentrations of TCNQF_n and [Cu(MeCN)₄]⁺ compared with that required for the formation of TCNQF_n²⁻-based products. The existence of different crystalline phases was observed and characterized by varying scan rates in the voltammetry of both the TCNQF_n⁻ and TCNQF_n²⁻-based materials. Although good quality single crystals could not be synthesized, the X-Ray powder diffraction pattern of CuTCNQF₂ closely resembles that of the CuTCNQ phase II material with a monoclinic unit cell. Interestingly, the conductivity of

CuTCNQF₂, which was determined using a CuTCNQF₂ film on a FTO coated glass, is in semiconducting range and close to that of CuTCNQ phase II. Variable structural and spectroscopic characterization methods have been used to characterize solid CuTCNQF_n confirming the presence of TCNQF_n⁻ moieties in the compound. SEM imaging confirmed the presence of different morphologies that were observed in the voltammetric experiments.

Voltammetry was also able to detect the formation of two morphologies for TCNQF_n²⁻- based solids and synthesize these electrochemically. However these were not stable upon exposure to the air as demonstrated by IR and Raman spectra.

The catalytic activity of a CuTCNQF_n layer on a piece of copper foil was investigated and compared with that of CuTCNQ and CuTCNQF₄. It is interesting that for Fe³⁺/S₂O₈²⁻ redox reaction the catalytic activity on of CuTCNQF₂ was close to CuTCNQF₄, however the mono fluorine substituent CuTCNQF did not exhibit significant catalytic activity of. The reaction rate with the present of CuTCNQF is almost as slow as observed CuTCNQ phase II which was unexpected. These results suggest that although a substituent effect exists in the catalytic activity for these catalyst, it is not the only factor contributing to the properties of CuTCNQF_n materials.

8.3. Electrochemical synthesis of M(TCNQF_n)₂ and MTCNQF_n (M=Ni, Co): Voltammetric, spectroscopic and microscopic evidence

The electrochemistry of TCNQF_n in the presence of Ni²⁺ and Co²⁺ has been described for both the TCNQF_n^{0/-} and TCNQF_n^{-/2-} reduction processes. The formation of M(TCNQF_n)₂.xH₂O was probed using cyclic voltammetric experiments using a wide range of metal and TCNQF_n concentrations. The voltammetric data supported the formation of TCNQF_n⁻-based materials with divalent metal cations at high concentration of both TCNQF_n and M²⁺ in the solution, typically more than 8.0 mM of each reactant. Furthermore, this finding enabled a new understanding and re-interpretation of the previously reported voltammetric data for TCNQ to be gained. Unfortunately, it was not possible to obtain a challenge generating single crystal of these materials for structural analysis. However, SEM imaging assisted

visualization of the morphology of $M(\text{TCNQF}_n)_2$ material. Several morphologies were observed on the ITO electrode surface depending on the electrolysis potential and time of deposition. Also, $M\text{TCNQF}_n$ materials could be synthesized electrochemically. However, once again, they decompose in aerobic conditions to form TCNQF_n^- .

8.4. Disproportionation of TCNQF_n^- in the presence of Zn^{2+} - The preparation of $[\text{M}(\text{DMF})_2\text{TCNQF}_4].2\text{DMF}$ materials

Similar to the chemistry of TCNQ and TCNQF_4^- , an analogous disproportionation of TCNQF_n^- and TCNQF_2^- was observed in acetonitrile in the presence of Zn^{2+} . Although no kinetics or thermodynamic data has been derived from this study, it confirmed the influence of Zn^{2+} on the disproportionation of TCNQF_n^- was a general reactivity across the family.

The inclusion of DMF into the conventional choice of MeCN solvent for electrochemical experiment of TCNQF_n was found to have a significant effect on the electrochemistry of TCNQF_4 in the presence of Zn^{2+} . The disproportionation of TCNQF_4^- was no longer observed in the presence of 5% (w/w) of DMF. However, the formation of new TCNQF_4^{2-} -based materials with Zn^{2+} , Co^{2+} , Mn^{2+} were detected on voltammetric time scale in this mixed solvent system. The powder X-Ray diffraction patterns showed high agreement between single crystals synthesized chemically and the bulk materials synthesized electrochemically. An interesting property of $[\text{Zn}(\text{DMF})_2\text{TCNQF}_4].2\text{DMF}$ is that the solvent was exchangeable using IR spectral analysis to reveal the disappearance of uncoordinated DMF band at 1686 cm^{-1} following treatment of the crystal with MeOH.

To summarize, it has been shown in this thesis that

- i) The substituent effect of fluorine on TCNQ derivatives has a significant influence on the redox chemistry of TCNQF_n where the redox potentials increase in an order that matches the addition of fluorine atoms on the TCNQ. The presence of more fluorine atoms also enhances the stability of the dianions as well as disfavours the disproportionation of the monoanions.

- ii) Vibrational spectra for TCNQF, TCNQF₂ and their anions have been reported providing a diagnostic tool for the characterization of their complexes and derivatives.
- iii) Electrochemistry of TCNQF and TCNQF₂ in the presence of both monovalent (Cu⁺) and divalent (Ni²⁺, Co²⁺) metal cations has been investigated. Some differences in the redox properties compared to those of TCNQ and TCNQF₄ has been reported.
- iv) TCNQF and TCNQF₂-based materials have been synthesized electrochemically and chemically and fully characterized. The results show that TCNQF_n⁻-based materials are stable as found for TCNQ and TCNQF₄ derivatives, the presence of one and two fluorine substituents does not enhance the stability of TCNQF_n²⁻ complexes. TCNQF₄²⁻ has been the only derivatives that can form stable complexes in the air.

8.5. Future work

Electrochemical synthesis has been a valuable method to prepare a number of new TCNQF and TCNQF₂ materials. However, it didn't prove possible to grow single crystals that are suitable for X-ray crystallography using electrochemical method. In future the chemical method could be investigated further. For example, lithium precursors of TCNQF and TCNQF₂, such as LiTCNQF_n or Li(TCNQF_n)₂ could be used as starting materials to grow single crystals.

Conductivity of CuTCNQF_n materials is a potentially interesting subject for future studies. For example, in this thesis, a sample of bulk synthesized CuTCNQF₂ material had a similar conductivity to that of CuTCNQ phase II. However, SEM imaging revealed two morphologies. Thus it would be intriguing to explore both morphologies independently to establish whether they have different conductivities.

Investigation of the remaining substituted TCNQF₃ and the other two isomers of TCNQF₂ (2,3- and 2,6-difluoro-TCNQ) would be insightful and could provide further understanding on the influence of the fluoro substitution pattern on the chemical and electrochemical properties of TCNQF_n.

Appendix

Table 1. Frequencies for IR Bands Associated with the $\nu(\text{C}\equiv\text{N})$, $\nu(\text{C}=\text{C})$ ring and exocyclic Stretches and mixed $\delta(\text{C-F,C-C})$ mode in TCNQF_n-Based Materials (n=1,2)

Compound	TCNQF ₂ charge	$\nu(\text{C}\equiv\text{N})$ (cm ⁻¹)	Ring $\nu(\text{C}=\text{C})$ (cm ⁻¹)	Exocyclic $\nu(\text{C}=\text{C})$ (cm ⁻¹)	$\delta(\text{C-F,C-C})$ (cm ⁻¹)
TCNF ₂	0	2227	1574	1548	1392
CuTCNQF ₂	-1	2214, 2182	1515	1477	1339
Ni(TCNQF ₂) ₂	-1	2183	1512	1477	1354
Co(TCNQF ₂) ₂	-1	2217	1512	1476	1347
TCNQF	0	2221	1582	1557	1393
CuTCNQF	-1	2205, 2138	1513	1504	1350
Co(TCNQF) ₂	-1	2212, 2190	1510	1493	1353
Ni(TCNQF) ₂	-1	2221, 2178	1511	1492	1354

Table 2. Frequencies for Raman Bands Associated with the $\nu(\text{C}\equiv\text{N})$, $\nu(\text{C}=\text{C})$ ring and exocyclic Stretches and mixed $\delta(\text{C-F,C-C})$ mode in TCNQF_n-Based Materials (n=1,2)

Compound	TCNQF ₂ charge	$\nu(\text{C}\equiv\text{N})$ (cm ⁻¹)	Ring $\nu(\text{C}=\text{C})$ (cm ⁻¹)	Exocyclic $\nu(\text{C}=\text{C})$ (cm ⁻¹)
TCNF ₂	0	2230	1633	1453
CuTCNQF ₂	-1	2219	1618	1401
Ni(TCNQF ₂) ₂	-1	2232	1623	1406
Co(TCNQF ₂) ₂	-1	2232	1623	1406
TCNQF	0	2230	1652	1477
CuTCNQF	-1	2221	1612	1395
Co(TCNQF) ₂	-1	2232	1613	1399
Ni(TCNQF) ₂	-1	2232	1613	1399

Table 3. Solubility of TCNQF_n-based materials

Compound	Solubility product in the presence of 0.1 M TBAPF ₆	Solubility product in the absence of 0.1 M TBAPF ₆
CuTCNQF ₂	$8.19 \pm 1.02 \times 10^{-9} \text{ M}^2$	$2.75 \pm 0.21 \times 10^{-9} \text{ M}^2$
Ni(TCNQF ₂) ₂	$6.65 \times 10^{-10} \text{ M}^3$	$1.09 \times 10^{-11} \text{ M}^3$
Co(TCNQF ₂) ₂	$1.14 \times 10^{-10} \text{ M}^3$	$3.51 \times 10^{-12} \text{ M}^3$
Ni(TCNQF) ₂	$2.65 \times 10^{-10} \text{ M}^3$	$5.54 \times 10^{-12} \text{ M}^3$
Co(TCNQF) ₂	$1.14 \times 10^{-10} \text{ M}^3$	$3.37 \times 10^{-11} \text{ M}^3$